Materials Science & Engineering R 162 (2025) 100877

Contents lists available at ScienceDirect

Materials Science & Engineering R

journal homepage: www.elsevier.com/locate/mser

A review on additive manufacturing of piezoelectric ceramics: From feedstock development to properties of sintered parts

Subhadip Bhandari [a,*], Gaurav Vajpayee [b,c], Lucas Lemos da Silva [b], Manuel Hinterstein [b], Giorgia Franchin [a], Paolo Colombo [a,d,**]

[a] *Department of Industrial Engineering, University of Padova, Via Marzolo 9, Padova 35131, Italy*
[b] *Fraunhofer IWM, Freiburg 79108, Germany*
[c] *Institute for Applied Materials, Karlsruhe Institute of Technology, Karlsruhe 76131, Germany*
[d] *Department of Materials Science and Engineering, The Pennsylvania State University, University Park, PA, USA*

ARTICLE INFO

Keywords:
Additive manufacturing
Piezoelectric ceramics
$BaTiO_3$
PZT
Debinding
Sintering
Dielectric

ABSTRACT

Piezoelectric ceramics are extensively used in several engineering applications in the field of sensors, actuators, energy harvesting, biomedical, and many more. Traditional ways of manufacturing piezoelectric devices result in better piezoelectric/ferroelectric performance. However, they are restricted to only simple shapes. With the widespread influence of additive manufacturing (AM), it is now possible to fabricate complex structures which were not possible by conventional technologies. In order to fabricate such complex structures with precision, it is necessary to understand in detail the factors influencing the feedstock preparation and the challenges associated with different AM technologies. With an emphasis on the most commonly used AM techniques (direct ink writing, fused filament fabrication, vat photopolymerization, binder jetting, and selective laser sintering) for

---

Abbreviation: d_{10}, 10 % of particles in the powder are smaller than this size; d_{50}, 50 % of particles in the powder are smaller than this size; d_{90}, 90 % of particles in the powder are smaller than this size; Ec, Critical energy density; T_c, Curie temperature; C_d, Curing depth; Tanδ, Dielectric loss; T_g, Glass transition temperature; ε_r,, Permittivity; d_{33}, Piezoelectric coefficient; P_r, Remanent polarizarion; G'_{eq} / G, Storage modulus; τ_y, Yield stress; ABS, Acrylonitrile Butadiene Styrene; ACMO, Acryloylmorpholine; $Al(H_2PO_4)_3$, Aluminium dihydrogen phosphate; AM, Additive manufacturing; APA, Ammonium salt of polyacrylic acid; APS, Average particle size; Ar, Argon; $BaCl_2$, Barium chloride; $BaCO_3$, Barium carbonate; BaO, Barium oxide; BAPO, Bis 2,4,6-trimethylbenzoyl-phenyl phosphine oxide; $BaSnO_3$, Barium stannate; $BaSrTiO_3$ or BST, Barium strontium titanate; $BaTiO_3$ or BT, Barium titanate; $BaZrO_3$, Barium zirconate; BCTZ, $(Ba_{0.85}Ca_{0.15})(Ti_{0.9}Zr_{0.1})O_3$; BCZT, Barium calcium zirconium titanium oxide; BEEA, 22-butoxyethoxy-ethyl acetate; $Bi_2Mo_2O_9$, Bismuth molybdate; $BiFeO_3$, Bismuth ferrite; BiT, Bismuth titanate; BJ, Binder jetting; Ca, Calcium; $CaTiO_3$, Calcium titanate; CNT, Carbon nanotubes; Co, Cobalt; CP, Ceramic particle; CuO, Copper oxide; DIW, Direct ink writing; DLP, Digital light processing; DMF, Dimethylformamide; DPPHA, Dipentaerythritol penta/hexa-acrylate; DTG, Derivative Thermogravimetry; Er, Erbium; ETPTA, Ethoxylated trimethylolpropane triacrylate; EVA, Ethylene vinyl acetate; F, Lotgering factor; FDC, Fused deposition of ceramics; FF, Fast firing; FFF, Fused filament fabrication; FS, Field strength; FTIR, Fourier transform infrared spectroscopy; HBA, 4-hydroxybutyl acrylate; HDDA, 1,6-Hexanediol diacrylate; HDODA, 1,6-Hexanediol; HNO_3, Nitric acid; HPMC, Hydroxypropyl methylcellulose; IEP, Isoelectric point; KNN, Potassium sodium niobate; La, Lanthanum; Li, Lithium; LVR, Linear viscoelastic region; MDEA, N-methyl diethanolamine; MEHQ, 4-Methoxyphenol; DSC, Differential scanning calorimetry; Mn, Manganese; N_2, Nitrogen; Na, Sodium; Nb, Niobium; Nb_2O_5, Niobium pentoxide; NH_4, Ammonium ion; NH_4Cl, Ammonium chloride; NH_4OH, Ammonium hydroxide; Ni, Nickel; OPPEOA, Oligo propylene glycol ethoxy triacrylate; PAA, Polyacrylic acid; PAA-NH_4, Ammonium polyacrylate; PAAS, Sodium polyacrylate homopolymer; Pb_3O_4, Lead (II,IV) oxide; PCL, Polycaprolactone; PE, Polyethylene; PEG, Polyethylene glycol; PEGDA, Polyethylene glycol diacrylate; PEI, Polyethylenimine; PEMA, Polyethyl methacrylate; PET, Polyethylene terephthalate; PFA, Pore forming agent; PI, Photoinitiator; PIN-PMN-PT, $PbIn_{1/2}Nb_{1/2}O_3$-$PbMg_{1/3}Nb_{2/3}O_3$-$PbTiO_3$; PLA, Polylactic acid; PMMA, Polymethyl methacrylate; PMN-PT or PMNT, Lead magnesium niobate-lead titanate; PNZT, Lead niobium zirconate titanate; POE, Phenoxyethanol; PP, Polypropylene; PPG, Polypropylene glycol; PPTTA, Ethoxylated pentaerythritol tetraacrylate; PS, Polystyrene; PSD, Particle size distribution; P-SPS, Pressureless spark plasma sintering; PTC, Positive temperature coefficient; PTFE, Polytetrafluoroethylene; PUA, Polyurethane acrylate; PVA, Polyvinyl alcohol; PVB, Polyvinyl butyral; PVDF, Polyvinylidene fluoride; PVP, Polyvinylpyrrolidone; PZT, Lead zirconate titanate; RC, Robocasting; RH, Relative humidity; RI, Refractive index; RT, Room temperature; S, Strain; Sb, Antimony; SEM, Scanning electron microscopy; SLS, Selective laser sintering; SLA, Stereolithography; $SrTiO_3$, Strontium titanate; SS, Soluble starch; Ta, Tantalum; TCP, Tricalcium phosphate; TGA, Thermogravimetric Analysis,; TiO_2, Titanium dioxide; TMPTA, Trimethylolpropane triacrylate; TPGDA, Tripropylene Glycol Diacrylate; TPMS, Triply periodic minimal surface; TPO, Diphenyl 2,4,6-trimethylbenzoylphosphine oxide; TPU, Thermoplastic polyurethane; TTIP, Titanium isopropoxide; UHS, Ultra-fast high temperature sintering; UV, Ultraviolet; VP, Vat photopolymerization; $Zn(CH_3CO_2)_2$, Zinc acetate; ZrO_2, Zirconia.

[*] Corresponding author.

[**] Corresponding author at: Department of Industrial Engineering, University of Padova, Via Marzolo 9, Padova 35131, Italy.

E-mail addresses: subhadip.bhandari@phd.unipd.it (S. Bhandari), paolo.colombo@unipd.it (P. Colombo).

https://doi.org/10.1016/j.mser.2024.100877
Received 27 August 2024; Received in revised form 25 October 2024; Accepted 31 October 2024

Piezoelectric
Ferroelectric

fabricating ceramic parts, this review paper intends to provide a deep insight into the factors affecting the feedstock preparation as well as post-processing conditions required to develop a high-performance piezoelectric device. The summarized tables detailing the various piezoelectric ceramic compositions and additives or ingredients used in formulating a printable feedstock, along with the optimum printing and post-processing conditions, will aid the readers in developing their own printable formulations and determining the best post-processing parameters to achieve the best performance out of the fabricated piezoelectric device. The advantages and disadvantages of the AM technologies are analyzed with specific reference to piezoceramic materials and the remaining challenges that require further research are emphasized. Furthermore, with the ongoing and continuous developments in additive manufacturing of piezoelectric materials, it is expected that such advancements will progressively transition towards commercialization, with the ultimate goal of widely incorporating additively manufactured devices into practical applications.

1. Introduction

Global energy consumption expanded considerably during the last half-century due to industrialization, technological advancements and population growth. It approximately doubled between 1971 and 2019, reaching 14,421 Mtoe (million tons of oil equivalent) in 2019 [1]. This rising demand highlights the critical need for long-term energy solutions based on materials that can efficiently harness, store, and transform energy. A wide range of functional materials including ceramics, polymers and composite materials can be used to meet such requirements [2]. However, among these options, piezoelectric ceramics stand out due to their intrinsic properties, such as high permittivity, robust mechanical strength, high-temperature stability and excellent electromechanical coupling coefficients [3].

When subjected to mechanical stress, piezoelectric ceramics generate an electric charge, directly converting mechanical energy into electrical energy and vice versa. The most common and traditionally used piezoelectric material belongs to the family of lead zirconate titanate (PZT) due to its superior piezoelectric coefficient (d_{33}) [4]. However, the use of lead is considered dangerous due to health and environmental hazards as well as concerns regarding recycling and disposal [5]. Following this, in the year 2002 legislations were introduced in the European Union, governing the use of lead and other harmful elements in commercial products [6,7]. The restriction on using such hazardous substances has emphasized the urgency to eliminate lead from these ceramics. Environmental concerns associated with lead have driven research towards lead-free alternatives [8–11]. Materials such as barium titanate ($BaTiO_3$ or BT), BT-based solid solutions such as BT doped with calcium and zirconium (BCZT), potassium sodium niobate (KNN) and bismuth ferrite ($BiFeO_3$) etc., are being researched intensively as a potential alternative to PZT [12]. Although there have been advancements in lead-free compositions, it is important to note that these ceramics still do not possess the same level of high piezoelectric characteristics as PZT ceramics.

Subsequently, further research efforts were aimed at enhancing the piezoelectric characteristics of lead-free compositions. The strategies to achieve better piezoelectric properties include microstructure optimization, texturing and addition of suitable dopants [12]. The dielectric and piezoelectric characteristics are significantly influenced by the grain size [13–16] as well as the domain size [17]. A ferroelectric domain is a region of a ferroelectric material in which the spontaneous electric polarization is oriented in a specific direction [18]. For example, BT exhibits optimum piezoelectric properties when the grain size is in the order of 1 – 2 μm with domain sizes of around 100 nm [16,19–22]. In contrast, decreasing the grain size below 100 nm induces a paraelectric state [23,24]. In addition, texturing also helps in enhancing the piezoelectric and dielectric characteristics by increasing the proportion of domains aligned in the direction of the electric field [25]. Ceramics with templated-grain growth along certain directions such as [001], [110] and [111] have been reported to exhibit better piezoelectric properties than randomly oriented polycrystalline materials [26–28]. One of the most widely exploited techniques to enhance the piezoelectric properties to date is the addition of dopants which substitute the A– or B–site cations [12]. A summary of promising doped BT compositions with d_{33} more than 200 pC/N has been reported in the literature [12].

A wide range of conventional ceramic processing technologies such as slip casting [29], tape casting [30], die pressing [31], injection molding [32], etc. have been utilized to fabricate piezoceramics. However, these conventional techniques have certain limitations. These include time-consuming manufacturing processes, extremely high wear rates of expensive machining tools, difficulties in producing complex geometries with high accuracy, and related high labour costs[33]. Additionally, the mechanical stress applied during the conventional processing techniques often leads to grain loss, strength degradation and depolarization of the near-surface area in piezoelectric elements [34]. This deterioration significantly impacts the overall performance of the fabricated component. A solution to these problems came with the evolution of innovative three-dimensional (3D) printing technologies or additive manufacturing (AM) that enables the manufacture of complex structures with high accuracy and increased production costs. Perhaps the most important reason for resorting to AM techniques is the promise of creating shapes that may increase the functional value beyond what is currently possible with conventional ceramic fabrication methods [35].

The AM technologies for metallic and polymeric components have grown and developed significantly in the last several years. In fact, these technologies have now been commercialized and are ready to be used in industrial applications. On the contrary, the use of AM technologies in the field of ceramics has been sluggish [36]. The present technical delay may be attributed to the intricate nature of ceramics processing rather than a lack of technological enthusiasm. Indeed, one might argue that AM has particular advantages for the fabrication of ceramics compared to any other material families. When considering ceramics, justifications for using AM are particularly compelling due to the challenges posed by their inherent hardness and brittleness. These challenges limit the feasibility of subtractive manufacturing methods, making 3D printing a viable alternative for enhancing and broadening the range of applications for functional ceramics.

Fig. 1(a) reports the most widely used AM technologies concerning piezoelectric ceramics over the past 20 years. This includes vat photopolymerization (VP), direct ink writing (DIW), fused filament fabrication (FFF), binder jetting (BJ), and selective laser sintering (SLS) [35]. Fig. 1(b) illustrates the distribution of research publications that have been published to date, categorizing them according to the various AM techniques. The distribution of research publications demonstrates how widely in particular VP and DIW are being used, which highlights their importance in pushing the boundaries of AM for piezoelectric ceramics. In terms of materials, there has been a progressive shift from lead-based compositions to lead-free compositions including pure BT, doped BT, KNN, BCZT, etc., as depicted in Fig. 1(c). One can also clearly notice in Fig. 1(a) that SLS is a single-step process, eliminating the need for an additional debinding step before sintering, unlike the other techniques reviewed here.

Several review articles have been published to date on the additive manufacturing (AM) of piezoceramics, as reported in Table 1. These papers primarily focus on various AM technologies related to piezoceramics and discuss the piezoelectric and ferroelectric properties of the fabricated components. However, an essential aspect of additive manufacturing – the preparation of the feedstock and the factors influencing it, has not been adequately addressed in any of the existing review papers. Additionally, the different factors influencing the functional properties of these materials are also missing. Further, there have been significant developments and achievements in the past couple of years involving AM of piezoceramic materials that need to be highlighted to the research community.

In this aspect, this review paper aims to summarize the latest state of the art of research concerning AM of piezoelectric ceramics, with a major focus on the feedstock development, which is a key parameter for the success of the fabrication process. In fact, the structural integrity and the quality of the final fabricated component mostly depends on the preparation of the feedstock, hence plays a vital role in the complete fabrication process chain. Additionally, we discuss the piezoelectric and ferroelectric characteristics of the sintered components and analyze how these characteristics are influenced by variations in density, microstructure, and design. A comprehensive analysis of the additive manufacturing techniques specifically applied to the fabrication of piezoceramic components has also been carried out. It is important to mention that this review study only focuses on research papers that include debinding and sintering of piezoelectric ceramics after the fabrication. However, recent studies on FFF technology lacks sufficient investigation into pure ceramics (Tables 3, 9), resulting in the inclusion of polymer-ceramic composites in the review.

Table 1
Review papers published on AM of piezoceramic materials.

Sl. No.	Year of publication	Title	Reference
1	2020	Additive Manufacturing of Piezoelectric Materials	[35]
2	2020	Progress and challenges of 3D-printing technologies in the manufacturing of piezoceramics	[2]
3	2022	A Review on Additive Manufacturing of Functional Gradient Piezoceramic	[37]
4	2023	A Review on Recent Advances in Piezoelectric Ceramic 3D Printing	[38]
5	2023	Review of the applications of 3D printing technology in the field of piezoelectric ceramics	[39]

2. Additive manufacturing (AM)

2.1. Direct ink writing (DIW) / Robocasting (RC)

2.1.1. Basics of the technology

Direct ink writing (DIW) or robocasting (RC) is an extrusion-based AM technique in which a non-newtonian viscous ceramic ink with suitable viscoelastic properties is extruded through a nozzle and deposited on the print bed following the printing path at room temperature. It is one of the most widely used AM technology, thanks to its flexibility, simplicity, and cost-effectiveness in fabricating relatively

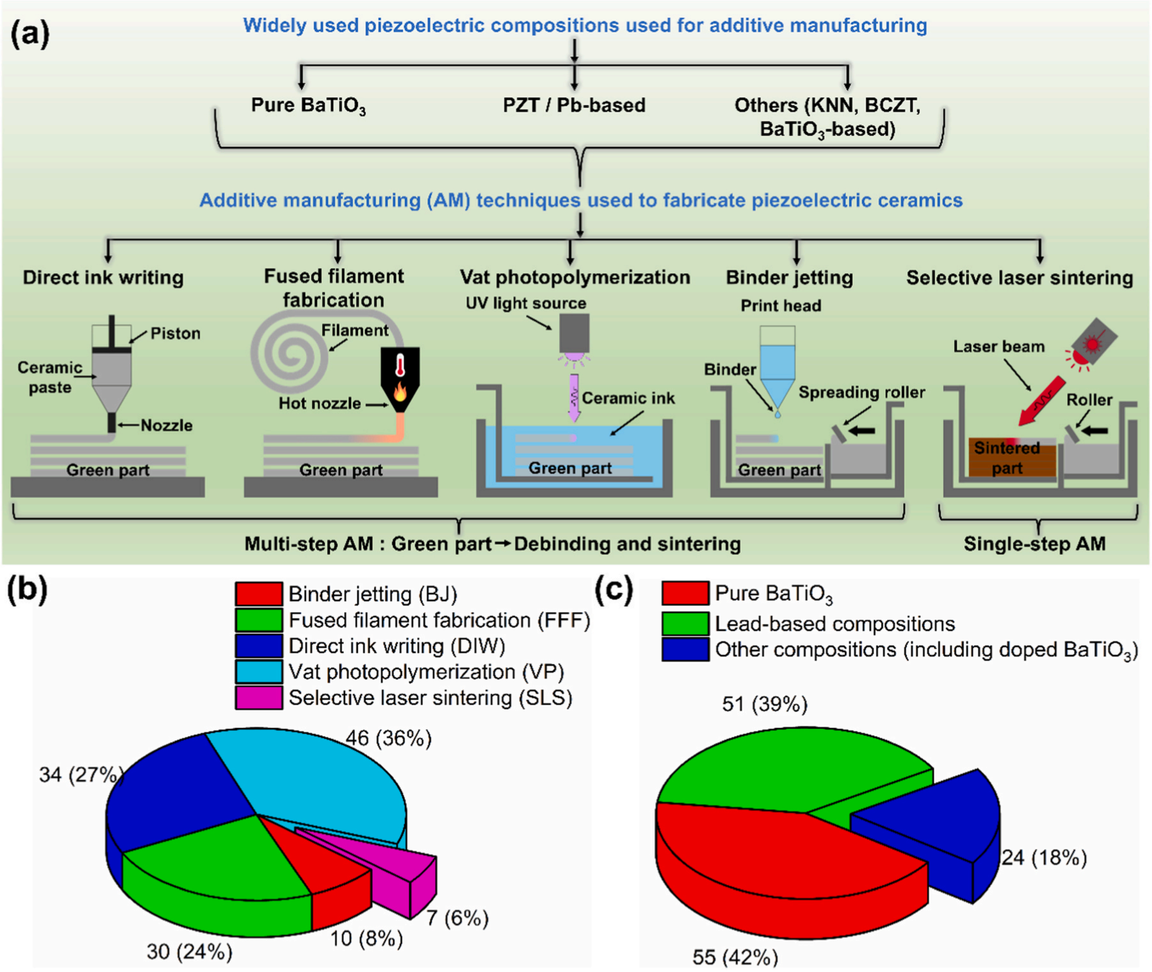

Fig. 1. (a) Overview of the piezoelectric compositions and the additive manufacturing techniques used to fabricate them. Graphical representation of: (b) Research papers reviewed in this study, categorized by the most widely used AM technologies, and (c) Various piezoelectric materials used with different AM technologies.

simple geometries and larger structures, without the need of ultraviolet (UV) curing or laser radiation [33,40]. These features significantly broaden the versatility in the range of powders that can be utilised as it is independent on the optical properties of the starting powder or the laser power required for consolidation. Additionally, DIW allows preparation of small amounts of ink, thereby minimizing the waste and making it more efficient. However, this comes at the expense of poor accuracy and surface finish, as it is constrained by the nozzle diameter (mostly > 400 μm as evidenced in Table 2) which limits the resolution of the printed components. Ceramic inks for such extrusion-based processes demand high ceramic loading (> 50 vol%) with a suitable solvent and appropriate amount of additives such as dispersant, coagulant, binder and humectant (solvent trap) [41]. High ceramic loadings in the ink are often associated with nozzle clogging and rapid drying of the ink, therefore limiting the upscaling of this technology.

One of the primary prerequisites for having a smooth flow of ink through the nozzle is the use of ink with optimized rheological properties [41,42]. The ink should possess a suitable viscoelastic behaviour; viscous when stress is applied so that it can easily exit from the nozzle without employing high pressure and, once the ink is extruded, it should have sufficient viscosity to keep the integrity of the fabricated structure without deformation or sagging, linked to the elastic part.

Maintaining tight control over the rheology of DIW pastes is crucial in order to manufacture printed ceramics of superior quality. It is thus of the utmost importance to review the factors that influence the rheology of the prepared ceramic ink.

2.1.2. *Effect of zetapotential and pH*

Most of the lead-free and lead-containing piezoceramics are highly sensitive to water, usually undergoes hydrolysis and dissolution [43–46]. This leads to: 1) leaching of metallic ions into the solution, and 2) reprecipitation of the leached metallic ions thereby affecting the stoichiometry. The concept of ion leaching is somewhat related to the ionic field strength (FS), which considers the charge and size of the concerned ion, defined as [47]:

$$FS = \frac{ionic\ charge}{\sqrt{ionic\ radius(\text{Å})}} \tag{1}$$

The lower FS, the easier is the dissolution due to weak bonding and vice versa. These solid-liquid interactions impose restrictions on the maximum solid loading that can be achieved and result in unstable suspensions that are unsuitable for further ink production and storage. All of these issues can be easily solved by either adjusting the pH value or by the addition of surfactants.

The stability of colloidal suspensions is dictated by the zeta potential of the solid particles in the solution. This parameter serves as an indicator of the magnitude of electrostatic forces, either repulsive or attractive, that exist between particles within a dispersion. A common way to figure out the stability of a colloidal solution is to look at how the zeta potential changes with pH. Generally speaking, a high zeta potential indicates that particles are highly charged (positive, 30 mV or negative, -30 mV) and repel each other, thereby stabilizing the dispersion [48]. It is interesting to note that the plot passes through a value of 0 zeta potential (as shown in Fig. 2(a, c)) known as the isoelectric point (IEP), indicating that in those conditions the suspension is least stable with a high possibility of aggregation or flocculation. Lower zeta potential values (in between 30 mV to -30 mV) may also cause such instabilities.

When employing a ceramic ink for robocasting, which requires a stable and smooth flow of ink with high solid loading through the nozzle, it is important to understand the correlation between zeta potential and pH in order to achieve and maintain the stability of colloidal suspensions. In order to accomplish a homogeneous dispersion of the pure BT and polyacrylic acid (PAA)-coated BT nanoparticles, Li *et al.* studied the variation of zetapotential as a function of the pH [49]. The zeta potential measurement revealed that the BT particles are positively charged and PAA-coated BT particles are negatively charged at pH 9 (Fig. 2(a)). Electrostatic interaction between opposing charges causes PAA to adsorb onto BT particles, thereby stabilizing the suspension. In addition, the isoelectric point also shifts to lower pH after addition of PAA; similar behaviour has been also reported for BT powder coated with ammonium polyacrylate (APA) [50] and BCZT powder coated with aluminium dihydrogen phosphate ($Al_2(H_2PO_4)_3$)) [51]. Such shift in the isoelectric point indicates that the surface modifiers are effective in promoting stability within the suspension.

The stability of the surface treated powder as a function of time was further investigated by Nan *et al.* [51]. The untreated and treated BCZT powders were subjected to an aging period of 64 h, during which pH values were measured. It was observed that the pH values of the treated powder remain almost constant with highly homogeneous dispersion (left image in Fig. 2(b)). In contrast, the untreated powders demonstrated inadequate wetting (caking) and significant agglomeration with increasing pH value with aging period (right image in Fig. 2(b)). The untreated powder in contact with water undergoes dissolution reaction and the rate of ion leaching is determined by the ionic field strength values which follows the order: Ba^{2+}>Ca^{2+}>Zr^{4+}>Ti^{4+}. This means that, for every divalent ion leached into the water, there is a simultaneous uptake of H^+ ions to maintain the electroneutrality. So, the increasing pH is due to the absorption of H^+ ions from the solution in order to maintain electro-neutrality, leading to an imbalance between H^+/OH^- ions.

In contrast to BT and BCZT, PIN-PMN-PT ($Pb(In_{1/2}Nb_{1/2})O_3$-$Pb(Mg_{1/3}Nb_{2/3})O_3$-$PbTiO_3$) exhibits a dual IEP characteristic, as shown in Fig. 2 (c) [52]. Such duality imposes complexity in the system. The complex metal oxides involved in PIN-PMN-PT are incongruent as a function of pH [53]. The addition of an acrylic-based binder causes the particles to lose their dual isoelectric point and the suspension is stabilized at a pH of 5 (~ -25 mV). At pH 12, the zeta potential value is no longer affected by the presence of PAA chains and the value is almost same for the pure powder and the powder with the acrylic binder.

Several studies have reported the variation of the rheological properties as a function of pH. For instance, Li *et al.* observed that for PZT ink lower pH led to suitable viscoelastic properties for a smooth extrusion process [54]. In another study, the effect of the pH on rheological and extrusion behaviour was also reported for PIN-PMN-PT ink [52]. The ink prepared at pH 1 and 13 were found to be almost identical, characterized by a high storage modulus, yield stress and inconsistent flow of the ink through the nozzle (Fig. 3(a)). It has been claimed that PAA exists in many configurations and has varying net charges depending on the pH [55]. At a lower pH, PAA is reported to exist in globular configuration without possessing any overall charge and the PIN-PMN-PT powder has positive zeta potential values. As a result, the PAA does not interact with the powder, thereby leading to flocculation. However, at higher pH levels, PAA chains are unfolded with negative charges on it and the powder has negative zeta potential values. Repulsion between ceramic particles and PAA chains create a homogenous dispersion. At the same time, the hydrogen bonding between the ionized PAA chains dominate [55], resulting in enhanced rheological properties. In contrast to the ink formulated at pH 1 (Fig. 3(b)) and 13, the ink prepared at pH 5 demonstrated the capability of being extruded into filaments with a uniform width (Fig. 3(c)). While the inks at pH 1 and 13 exhibited a gradual decrease in storage modulus, the pH 5 ink showed a sharp decrease, suggesting more effective interactions of PAA with the powder at pH 5. This is evident from the analysis in Fig. 3(a), where the yield stress decreased from over 1400 Pa to 530 Pa.

A study on the shape retention ability of a calibration (V-shaped) structure with spanning elements was carried out by Smay *et al.* [56]. The authors observed that the rheological properties were strongly affected by the change in pH. The ink with a pH of 8.05 ($G'_{eq} = 27$ kPa, $\tau_y = 3$ Pa) showed significant deformation even at small spanning lengths

Table 2
Feedstock preparation and optimized printing parameters for Direct ink writing (DIW).

Feedstock	Particle size and morphology	Solvent	Additives	Ceramic loading	Ink type	Printing parameters				Reference
						Nozzle size (mm)	Speed (mm/s)	Layer height (mm)	Additional information	
PIN-PMN-PT	Monomodal, d_{50} = 280 nm	Distilled water	WB4101,PL008, DS001, DF002, CuO (< 50 nm), HNO_3/NH_4OH	28 – 35 vol%	Colloidal		5		Extrusion pressure: 880 – 1250 kPa, Samples dried in 95 % R.H for 4 days	[52]
$BaTiO_3$ platelet	Width:2 – 40 µm, Thickness: 0.5 – 1 µm			1 – 10 vol% relative to PIN-PMN-PT powder						
Hard PZT	$d_{50} \sim 0.60$ µm	Distilled water	DISPERBYK−180, Glycerol, PVA	50 – 55 vol%	Colloidal	0.15 – 0.90	0 – 10	$\frac{h}{D} \sim 1$ $\frac{h}{D} \sim 0.8$	Extrusion pressure:0 – 0.20 MPa, Samples dried in 80 °C for 12 h	[74][a]
Barium acetate, TTIP		Isopropyl, Triple distilled water, Acetic acid, Isopropanol	$BaTiO_3$ (> 3 µm)	30 – 80 wt%	Sol-gel	1.5	5 – 30	0.3	Heated bed: 50 °C	[78]
$BaTiO_3$ Hydrothermally synthesized	Nano particles	DMF	PVDF	65 – 80 wt%	Colloidal	0.26, 0.41	~ 2.7		Extrusion pressure: 0.8 – 1 MPa, Samples dried in 80 °C for 6h, Printed on PET film	[69]
BCZT	Bi-modal, d_{50} = 0.17 µm, d_{90} = 0.38 µm	Deionized water	$Al(H_2PO_4)_3$, Dispex A40, HPMC, PEI	40 – 44 vol%	Colloidal	0.41			Samples dried in 40 °C for 8h, Printed in glycerin oil	[51,84]
$BaTiO_3$	d_{50} = 1.2 µm	Distilled water	Bermocol E 320 FQ, Darvan 821-A, PEI	50, 52 vol%	Colloidal	Square 1.5	5	1.35	Printed in oil bath, Samples dried at RT °C for 24 h	[70]
$BaTiO_3$	100 nm, 300 nm, 500 nm	Deionized water	PVA	28.5 vol%	Colloidal	1	10	0.6	Printed on aluminum plate at −40 °C, Samples dried in −60 °C for 2h, Samples dried in 40 °C for 24 h	[58]
$BaTiO_3$	100 nm, 300 nm	Deionized water	PVA	70 wt%	Colloidal	0.8 – 1.6	10 – 20		Printed on frozen plate at −40°C, Samples dried in −60 °C for 2h, Samples dried in 40 °C for 24 h	[59]
$BaTiO_3$ doped La, Mn PTC		Deionized water	Darvan 821-A, HPMC	33, 43 vol%	Colloidal	0.56	5	0.40	Print bed 20 – 80 °C, PTFE spray on print bed	[71]
PZT		Deionized water	PVA, Trisodium citrate, Polyacrylamide, glycerol	86.21 wt%	Colloidal	0.5	8		Extrusion pressure: 0.2 MPa	[85]
$BaTiO_3$	15 – 60 nm Nano particles	Deionized water	PAA, Cellulose, NH_4Cl, $Zn(CH_3CO_2)_2$, NH_4OH/ HNO_3	50 vol%	Colloidal	0.03 – 0.1	1	0.9D	Printed in oil bath	[49]
$BaTiO_3$	APS = 1.02 µm	Deionized water	NH_4OH/ HNO_3, $BaCl_2$,APA, HPMC, PEI	49 vol%	Colloidal	0.1 – 0.5			Printed in oil bath, Samples dried at RT for 12 h	[50]
$Bi_2Mo_2O_9$	APS < 10 µm	Distilled water	Ethylene glycol diacetate, Propylenecarbonate, Ethyl cellulose, Diisononyl phthalate, Ammonium lauryl sulphate	85 wt%	Colloidal	0.5	5	0.2	Samples dried at RT for 24 h	[60]
$BaTiO_3$	100 nm, 400 nm	Distilled water	PVA, PAA	28.5 vol%	Colloidal	0.6			Extrusion pressure: 58 MPa, Samples dried at −5 °C for 24 h and 40 °C for 24 h	[61]
PZT	Spherical agglomerates of 0.5 µm particles	Deionized water	PVA	86 – 89 wt%	Colloidal	1.5	10	0.8	Print bed 40 °C, Samples dried in 40 °C for 8 h	[77]
PZT	APS = 0.225 µm, spherical	Xylene, Ethanol	Triethyl phosphate, PEG, PVB	79 – 80.5 wt%	Colloidal	0.21 – 0.26			Samples dried at 60 °C for 1 h	[72]
PIN-PMN-PT	Monomodal, d_{50} = 280 nm	Distilled water	WB4101, PL008, DS001, DF002	28 vol%	Colloidal	Customized nozzles	5, 10, 20		Extrusion pressure: 275 – 1100 kPa	[91][b]

(*continued on next page*)

Table 2 (*continued*)

Feedstock	Particle size and morphology	Solvent	Additives	Ceramic loading	Ink type	Printing parameters				Reference
						Nozzle size (mm)	Speed (mm/s)	Layer height (mm)	Additional information	
$BaTiO_3$ platelet	Width = 2 – 40 µm, Thickness = 0.5 – 1 µm			2.6 vol% of total paste						
$BaTiO_3$, $SrTiO_3$, $BaZrO_3$, Ni		Deionized water	APA, HPMC, PEI	47 vol%	Colloidal					[92]
Nb, Ca, Co- doped $BaTiO_3$	Mean diameter = 0.5 µm	Terpineol	BEEA, PEG, PVB	80 wt%	Colloidal	1	2 – 3		Print bed 60 °C, Samples dried at 60 °C for 3 h	[80]
TTIP, MDEA, Glycerol, Water, BaO			$BaTiO_3$	30 – 40 vol%	Sol-gel	0.41	5		Extrusion pressure: 40 kPa	[73]
$BaTiO_3$	d_{50} ~ 1.05 µm, spherical	Paraffin oil, mineral spirits, Stearin wax	Sucrose solution	31 vol%	Capillary suspension	0.15	10	0.12	Extrusion pressure: 480 kPa, Printed on porous alumina plate, Samples dried at RT for 5 days	[88]
PZT	d_{50} = 523 nm	Ethanol	Trisodium citrate, PVA, $PAA-NH_4$ or PAAS, Glycerin		Colloidal	0.6	8	0.3	Extrusion pressure: 0.2 MPa	[83]
$BaCO_3$, TiO_2		H_2O	PVA, PEG 400, Solsperse 20000	~ 75.1 wt%	Colloidal		5	0.5		[93]
PZT	APS = 0.5 µm	Deionized water	AG 165, Methylcellulose	52 vol%	Colloidal	0.26	8		Extrusion pressure: 0.3 MPa	[54]
PZT95/5	d_{50} = 1.25 µm, d_{max} = 4.50 µm	Deionized water	PVP		Colloidal	0.30			Samples dried at 60 °C for 24 h	[94]
PNZT	Bimodal size distribution of 1.8 and 4.5 µm	Terpineol	Polyenoic acid, Phosphate ester, Fatty acid, Fatty acid ester, Ethyl cellulose	35 vol%	Colloidal	8 mils				[75]
Li, Sb, and Ta-doped KNN	APS = 0.5 µm	Methyl methacrylate, Pentaerythritol three acrylate		56 wt%	Colloidal	0.25 – 0.40				[95]
$BaTiO_3$	500 nm	DMF	PVDF	25.85 –35.45 vol%	Colloidal	0.60	1	0.4	Printed on heat bed, Samples dried at 120 °C for 2 h	[86]
BST and β-TCP		Water	PVA		Colloidal	0.2	11 – 13		Extrusion pressure: 3.8 – 4 bar	[96]
BCTZ 50	d_{50} = 1 µm	Water	Dispex®AA4040, HPMC, PEI	41 vol%	Colloidal	0.25			Samples dried at RT for 24 h	[97]
PZT		Deionized water	Polyacrylate, Cellulose, HNO_3	32 vol%	Colloidal	0.41	5		Printing bed cooled below −25 °C, Freeze dried in vacuum chamber for 24 h	[98]
PZT	APS = 0.64 µm	Deionized water	PAA, Cellulose, NH_4OH and HNO_3	47 vol%	Colloidal	0.1 – 1	2 – 8	0.82D	Printed in oil bath, Sample dried at 30 % R.H at 23 °C	[56]
$BaTiO_3$		Distilled water	Na-PAA, Na-alginate, Glycerol	80 wt%	Colloidal	0.41			Extrusion pressure: 2–3 bar, Samples dried at RT for 4 h	[79]

[a] h is the strut hight and D is the nozzle diameter. [b] The nozzles were 24 mm long and had 6 mm diameter circular inlets which taper to elliptical outlet cross-sections of 580 µm x 580 µm (aspect ratio 1), 870 µm x 430 µm (aspect ratio 2), 750 µm x 250 µm (aspect ratio 3), and 1560 µm x 300 µm (aspect ratio 5). Tapered nozzles were used to reduce the printing pressure necessary to print continuous filaments. Nozzles with aspect ratios greater than 1 were custom made via stereolithography (3DSystems, State College, PA).

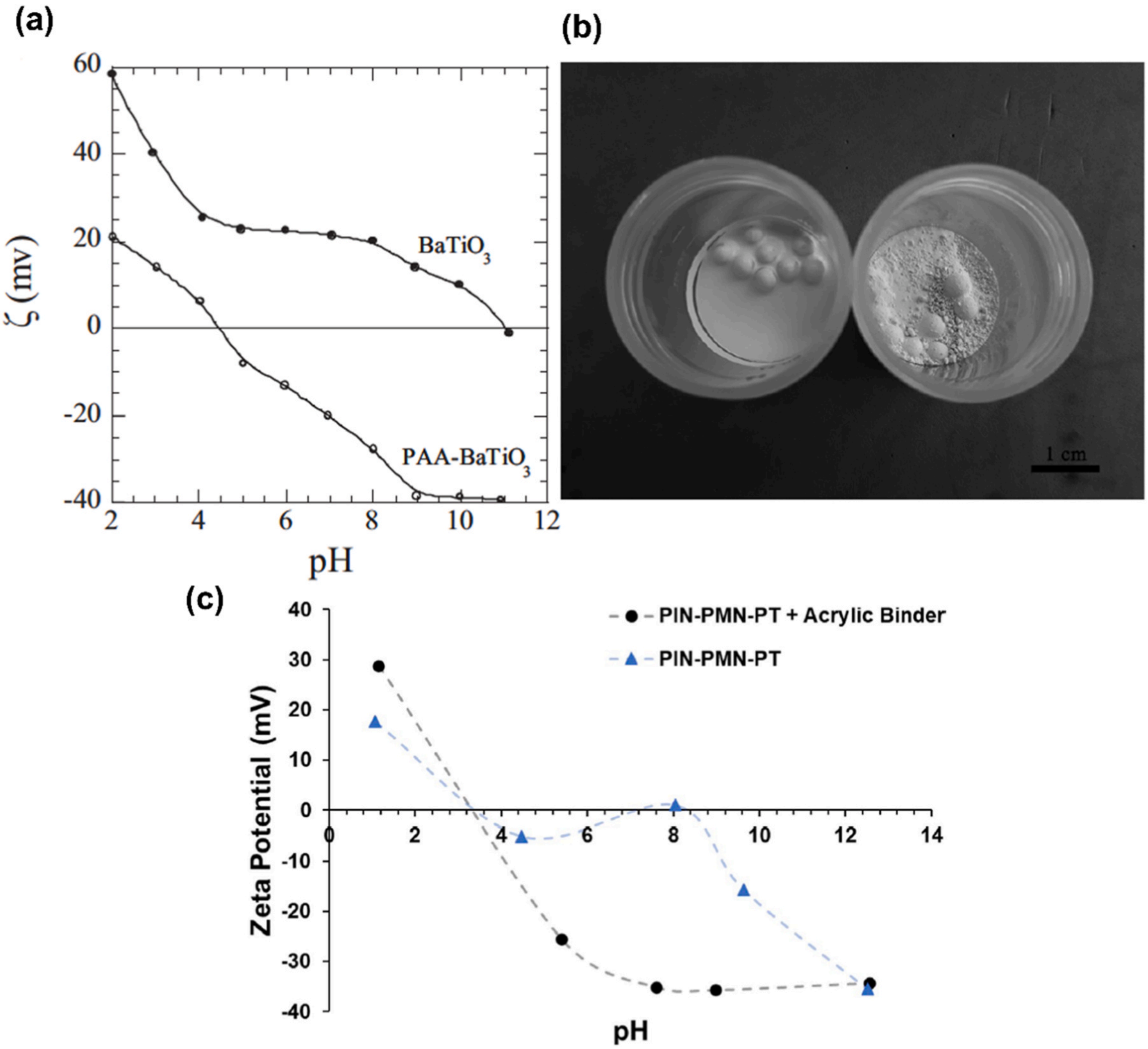

Fig. 2. Effect of the zeta potential and pH on the formulated ceramic ink. (a) Zeta potential variation of pure BT and PAA-coated BT as a function of different pH levels [49]. (b) The effect of surface treatment on the dispersibility of 40 vol% BCZT powders in the presence of 1.0 wt% dispersant made from the surface-treated powder (left) and the untreated powder (right) under the identical mixing conditions [51]. (c) Zeta potential as a function of pH for 0.08 vol% PIN-PMN-PT suspensions, with and without an acrylic binder [52].

Reproduced from Ref.: (a) [49], (b) [51], and (c) [52] with permission from John Wiley and Sons.

(Fig. 3(d)). With decreasing pH, the shape retention ability increased due to increasing viscosity, storage modulus and the yield stress, with the least deformation values being reported at a pH of 6.15 ($G'_{eq} = 150$ kPa, $\tau_y = 25$ Pa).

The pH of the ink has a significant impact on the surface charge of particles and the conformation of organic molecules. Consequently, depending on the interaction between the additives (surface modifier, dispersant, binder) and the ceramic powder, this may lead to a substantial deterioration of the properties such as increase/decrease in the viscosity, storage modulus and yield stress of the formulated ink, thereby affecting the shape retention capability of the ink. Regardless of the specific powder being used, it is important to determine the IEP and study the variation of the zeta potential, particularly for perovskite-structured powders that are susceptible to hydrolysis. The situation becomes further challenging when there is more than one IEP, as in the case of PIN-PMN-PT powders.

2.1.3. *Effect of salt solution*

In DIW, salt solutions have been sometimes used to induce gelation by cross-linking with the polymers used in the ink. Despite its effectiveness, this approach is no longer used by researchers because of post-processing challenges that include removal of residues from the salt solution after the printing.

Li *et al.* used two distinct salt solutions, each containing either a monovalent (NH_4^+) or divalent (Zn^{2+}) salt species, that facilitated the transition from fluid to gel with the desired viscoelastic response for a highly loaded BT suspension, as shown in Fig. 4(a) [49]. A noticeable discrepancy was observed in the elastic modulus, with a substantial increasing modulus by orders of magnitude in the presence of divalent ions as opposed to monovalent ions (Fig. 4(b)). Monovalent counterions such as NH_4^+ can only neutralize the negative charge of COO-groups of PAA; on the other hand, divalent counterions like Zn^{2+} have the ability to facilitate aggregation by means of “ion-bridging” interactions between charged PAA chains that are adsorbed on the BT nanoparticles. Such increase in elastic behaviour on additions of the ions (monovalent or divalent) can also be related to the inter-particle bonding using a power law scaling relation [57]:

$$y = k\left(\frac{\varnothing}{\varnothing_{gel}} - 1\right)^x \tag{2}$$

where y is the desired elastic property (such as yield stress or elastic modulus), k is a system specific constant, $\varnothing_{gel}$ is the minimum particle

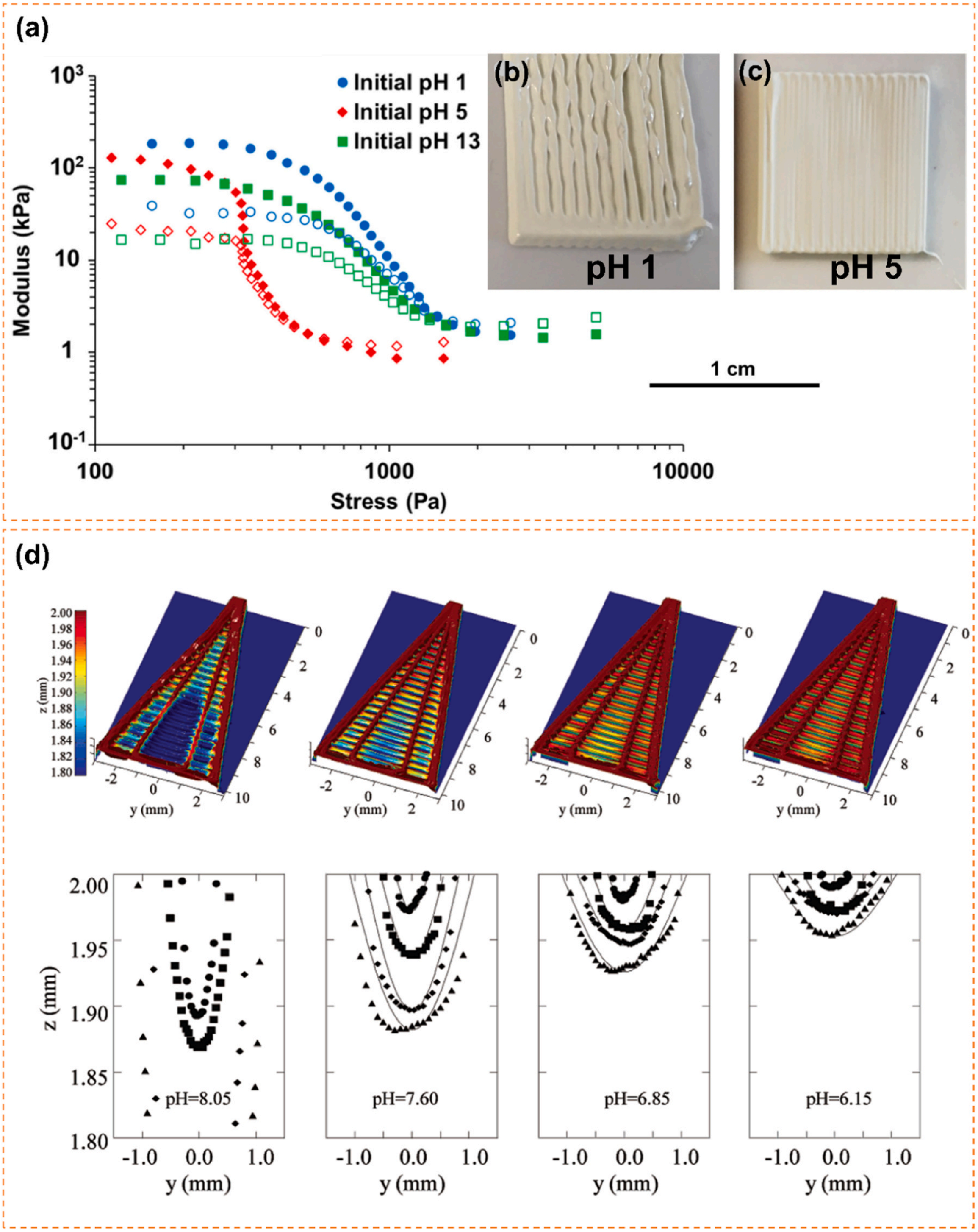

Fig. 3. Effect of the pH on the structural stability of the extruded ceramic ink. (a) Storage modulus (filled points) and loss modulus (hollow points) of 28 vol% PIN-PMN-PT pastes as a function of applied stress, formulated at various pH levels using a PAA binder system. Printing tests conducted with the same pastes prepared at (b) pH 1, and (c) pH 5 [52]. (d) Specific height profiles of test structures extruded from PZT colloidal gels for spans of approximately 3 mm (●), 5 mm (■), 7 mm (◆), and 9 mm (▲), at pH levels: 8.05, 7.60, 6.85, and 6.15. The colour scale indicates height between 1.8 and 2 mm [56].
Reproduced from Ref.: (a-c) [52], with permission from John Wiley and Sons. (d) [56], with permission from American Chemical Society.

loading necessary for gelation and $\varnothing$ is the solid volume fraction. The inter-particle interactions become more intense with increasing salt concentration, as a result $\varnothing_{gel}$ decreases (for a fixed $\varnothing$) resulting in increased elastic properties. Further, addition of divalent salt solutions ($[Zn^{2+}] = 0.06$ M) promotes the fluid to gel transformation with optimum elastic behaviour ($G > 10^4$ Pa) necessary for shape retention. Such concentration of Zn^{2+} ions help in the transformation of long-range van der Waals interactions to ion bridging effects, which in turn promotes stronger particle interaction leading to an increasing yield stress and elastic modulus of the ink. Nadkarni *et al.* observed similar results on addition of NaCl and $BaCl_2$ solution to APA-stabilized BT [50]. The magnitude of the rise in modulus was reported to be amplified in the presence of bivalent ions.

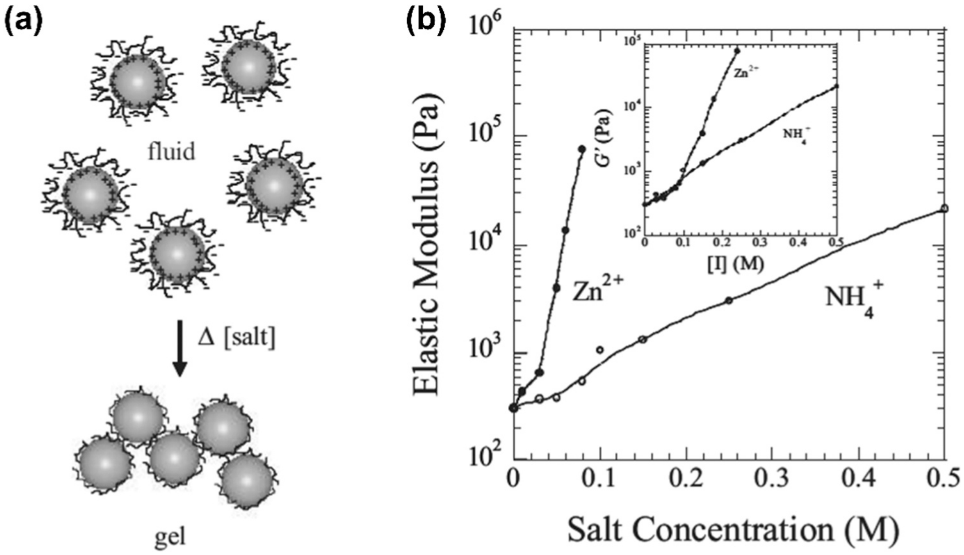

Fig. 4. Effect of the salt solution on the modulus. (a) Schematic illustration showing the transformation from fluid to gel state with the introduction of a salt solution. (b) Variation of the equilibrium elastic modulus for a 50 vol% BT ink, comparing the effects of adding monovalent vs. divalent salts [49].
Reproduced from Ref.: (a-b) [49], with permission from John Wiley and Sons.

2.1.4. Particle size, distribution and morphology

The viscoelastic behaviour of the ink is determined by the physical characteristics of the powder particles, which include their size, size distribution, shape and morphology. These characteristics play a significant role in determining the ink performance.

Several studies suggest that the particle size has a profound effect on the rheological properties of the prepared ink, which in turn affects the final density and the piezoelectric properties of the sintered components [58–61]. In this regard, Renteria *et al.* investigated the effect of various particle sizes of BT (100 nm, 300 nm, 500 nm) on the viscosity and the stress behaviour of the prepared ink using PVA in distilled water [58, 59]. Finer particles exhibited a greater initial viscosity at low shear rates, which subsequently decreased at high shear rates (Fig. 5(a-b)). This is a typical behaviour of pseudoplastic inks which exhibit shear thinning behaviour. As the size of particles decreases, there is an increasing total surface area of the particles that are dispersed and a corresponding reduction in the distance between the particles [62]. Reducing the inter-particle distance leads to an increase in both the frequency of particle contacts and the intensity of particle-particle interactions (mainly Van der Walls forces), resulting in high viscosity and yield stress [63]. At lower shear rates, ceramic particles in the ink have more opportunity to interact and create networks or structures within the solvent with other additives, obstructing the flow and thereby increasing viscosity. However, at higher shear rates, the interactions between the particles and the solvent or additives are disrupted, thereby reducing the viscosity. Conversely, the stress required to make the ink flow also decreases at higher shear. The viscosity difference between small and large particles is diminished at higher shear rates as particles are favourably rearranged with respect to the flow direction.

In addition to the particle size, particle size distribution (PSD) also plays an important role in dictating the rheological behaviour. For an ink formulation, finer powders are more favourable due to their enhanced sinterability. Conversely, coarser particles offer improved flowability but are more susceptible to sedimentation, which can result in unstable inks. Most of the researchers prefer having a narrow size or unimodal distribution of the ceramic particles as it ensures a uniform and consistent interaction with the solvent. On the other hand, bimodal distribution ensures good packing of the powder particles in the ink, as depicted in Fig. 5(c). Recent evidence suggests that using bimodal distribution of powders (replacing 100 nm by 400 nm of BT) helps in reducing the viscosity and the yield stress of the suspension, provided the volume content of the ceramic particles is kept constant (Fig. 5(d)) [61]. So, when the fine particles are replaced by the coarser ones, the inter-particle distance increases. As a result, there is more space for the finer particles to move around freely [64]. It is widely accepted that the maximum packing fraction of solids increase with increasing polydispersity [65]. In this context, some researchers have intentionally used bismuth molybdate ($Bi_2Mo_2O_9$) powders with a multi-modal particle size distribution [60].

Ceramic particles of various morphologies, such as sphere-like and platelet-like particles have been successfully used in preparing a printable ink [42]. In general, spherical particles are reported to exhibit greater flowability due to decreased inter-particle interactions and friction when flowing across each other. In contrast, platelet-like particles possess larger ellipsoids of rotation in contrast to spherical particles at a given constant volume, leading to increased inter-particle interactions [63,67,68]. Furthermore, these highly anisotropic particles tend to interlock owing to their irregular edges, thereby leading to agglomeration and high viscosity even at low solid loadings [67]. However, if the applied shear stress is capable of aligning the platelets in a single direction, the viscosity drops. Furthermore, using anisotropic templates leads to templated grain growth after sintering, which is reported to provide high piezoelectric properties along the growth direction.

Walton *et al.* studied the effect of the addition of BT (5 – 40 μm) platelets to a lead-based piezoceramic ink ($d_{50} = 0.28$ μm) [52]. It was discovered that, on adding the platelets, the modulus decreased and was further enhanced by increasing the amount from 0.3 vol% to 1.4 vol%. (Fig. 5(e)) This decrease can be attributed to the incorporation of large particles in a matrix constituted of fine powders. Once the dispersity index of the system changed from mono to poly, the viscosity and the modulus of the ink decreased. The modulus decreased gradually with applied shear stress in the ink containing templates, showing that the transition from solid-like to liquid-like behaviour is progressive throughout the range of applied shear stress. Additionally, the yield stress was almost constant (~1200 Pa) regardless of the volume fraction of the platelets, which was higher than the yield stress (~530 Pa) of the ink without the platelets. Anisotropic particles such as in the case of platelets tends to have particular directions in which they can align more easily when subjected to a shear stress, in contrast to the spherical particles which lack directionality. As a result, the presence of platelets increases the amount of stress required to overcome their resistance in

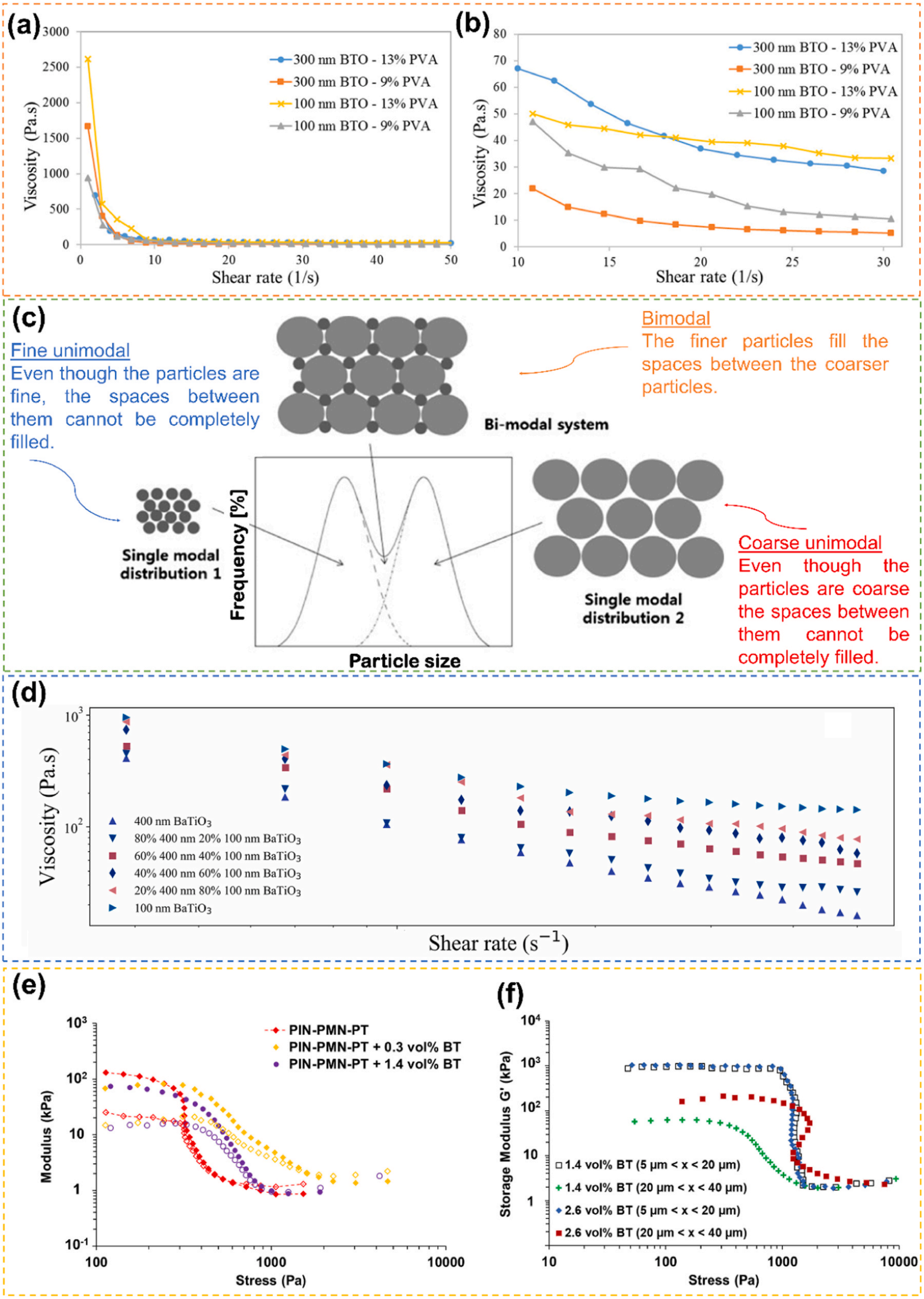

Fig. 5. Impact of particle size, shape and distribution on the rheological behavior. (a-b) Evolution of the viscosity as a function of particle size and binder content for BT inks [59]. (c) Schematic depiction of particle arrangements in unimodal and bimodal particle size distributions [66]. (d) Viscosity as a function of shear rate for monodispersed slurries and bimodal particle distributions with different BT particle size mixing ratios [61]. (e) Storage modulus (solid markers) and loss modulus (open markers) as a function of applied stress for 28 vol% PIN-PMN-PT ink at pH 5, comparing compositions with 0.3 vol% and 1.4 vol% of 2 – 40 µm anisotropic BT platelet particles [52]. (f) Storage modulus vs. applied stress for 28 vol% PIN-PMN-PT ink at pH 5 with varying amount and size fractions of BT platelets [52]. Reproduced from Ref.: (a-b) [59], with permission from IOP publishing. (c) [66], and (d) [61], with permission from Elsevier. (e-f) [52], with permission from John Wiley and Sons.

changing from a random orientation to a particular direction. This is the reason for the presence of a gradual decrease in the modulus as well as increased yield stress in case of an ink which contains platelets. While the volume fraction of the platelets remained constant (1.4 vol%), altering the size of the platelets from small (5 – 20 μm) to large (20 – 40 μm) resulted in a significant reduction in modulus and a slight increase in yield stress (Fig. 5(f)).

2.1.5. Effect of ceramic loading, binder, coagulant/dispersant concentration

Formulating an ink with high solid loadings (> 50 vol% or 80 wt%, please refer to Table 2) that display pseudoplastic and viscoelastic behaviour with a low concentration of additives is one of the main challenges in robocasting. The DIW technique is best suited for inks that have extremely high solid loadings for reasons such as high green

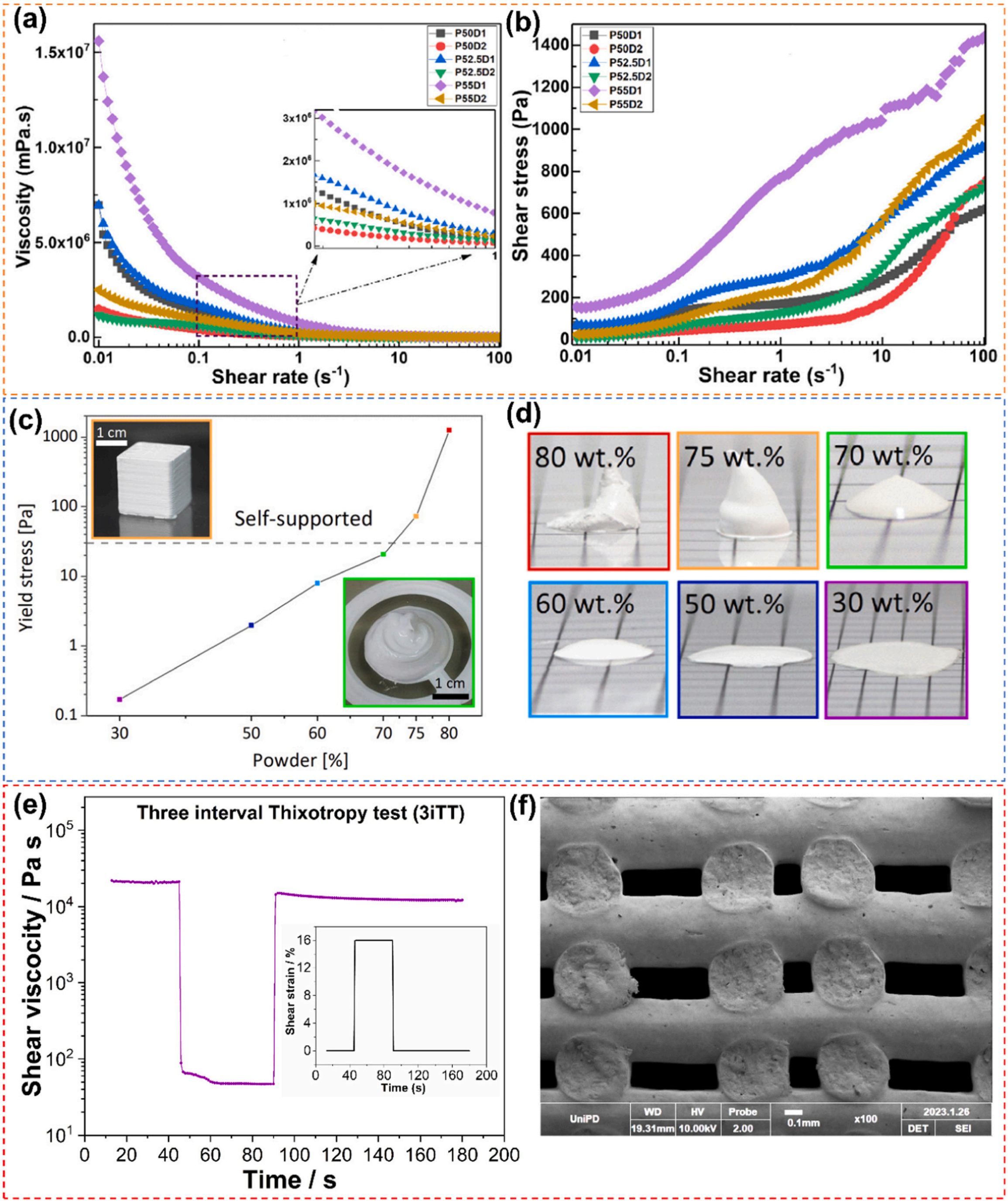

Fig. 6. Effect of ceramic loading on rheological properties and shape retention ability. (a) Viscosity, and (b) Shear stress vs. shear rate for PZT inks with varying solid loadings and dispersant concentrations [74]. (c) Yield stress of BT inks with different solid loadings, with insets illustrating the typical yield behaviour of printed objects using inks containing 70 wt% (lower inset) and 75 wt% (upper inset) ceramic particles [78]. (d) Photographs of various ink formulations shown in (c) exhibiting the shape retention capacity. The images correspond to the graph points in (c), with matching border colours on the pictures for easy reference [78]. (e) The three-interval thixotropy test (3iTT) for measuring the time-dependent recovery of viscosity. The inset depicts the change in shear strain over time [79]. (f) SEM image of the fracture surface of the sample, fabricated using the ink characterized by the 3iTT test shown in (e), highlighting suspended struts within the printed porous lattice [79].

Reproduced from Ref.: (a-b) [74], with permission from Elsevier. (c-d) [78], and (e-f) [79], with permission from John Wiley and Sons.

density of the printed component, minimal shrinkage/warping during the drying process, excellent mechanical properties, and high density following high-temperature sintering process.

Numerous studies have been conducted to study the impact of solid loadings on the rheological characteristics of an ink [52,69–75]. It is widely acknowledged that an increasing solid loading leads to an increasing viscosity, yield stress, flow stress and the modulus of the ink due to more inter-particle interaction. Fig. 6(a-b) depicts the variation of viscosity and shear stress with shear rate. This is a typical example of shear-thinning behaviour, where the viscosity of the material decreases as the shear rate increases, resulting in an increased shear stress. Often the flow curves are fitted according to the Herschel-Bulkley model with the following equation [76]:

$$\sigma = \sigma_y + k\gamma^n \tag{3}$$

where σ is the shear stress (Pa), σ_y is the yield stress of the ink, k is the consistency index, n is the flow index and γ is the applied shear rate (s^{-1}) on the ink. The most important feature to observe is that the ink should exhibit shear-thinning behaviour (when $0<n<1$), unlike shear-thickening ($n>1$) where the viscosity increases with shear rate, making it difficult to extrude through a nozzle. Such shear thickening behaviour has been reported while preparing BCZT ink (44 vol%) and hybrid sol-gel BT ink (40 vol%) [51,73]. This is due to a non-optimal powder dispersion or enhanced powder agglomeration with high solid loading. It is worth noting that the viscosity of the ink can also be influenced by the ageing process, mostly due to the spatial redistribution of the solvent in the ceramic paste [77].

Rosental *et al.* studied the rheological properties with varying amount of BT particles (30 – 80 wt%) [78]. The authors reported that with high loadings (> 75 wt%), the ink was not extrudable even with a nozzle diameter of 1.5 mm, as validated by the sharp increasing yield stress value showed in Fig. 6(c) [78]. Even though the inks with low solid loadings were extrudable, this did not guarantee that the printed parts were able to retain its shape (Fig. 6(d)). This leads to an important conclusion: *All printable inks are extrudable but not all extrudable inks are printable.* The ability of an extruded filament to retain its shape after the printing process is dictated by the yield stress, storage modulus and the elastic recovery of the ink, which depends on the solid loading.

It is important to note that the recovery time also determines the shape retention, space filling and the roughness of the external surfaces. In this context, Rowland *et al.* studied the effect of different solid loadings on the ink flowability behaviour [71]. Because of the lower water content in high solid loading ink, the ink dried up quickly indicating a short recovery time, leading to distinct noticeable interfaces as observed by optical microscope. On the other hand, an ink with low solid content had a better flowability owing to the slumping effect, leading to a better surface finish without any noticeable interfaces. Similarly, Walton *et al.* studied the effect of recovery time on the space filling behaviour of an ink with BT platelets [52]. The authors reported that the ink with the quick recovery time was not able to fill the space completely, thereby leaving behind residual porosity. Conversely, the ink with larger recovery time was able to completely fill the volume (Fig. 3(b-c)). Indeed, it is clear that the space filling behaviour is related to the recovery time of the ink. Nevertheless, in designs where geometrical porosity or intricate designs or overhanging are desired, the ink with quick recovery time would be better suited. The recovery time of the formulated ink can be easily quantified with the help of a three-interval thixotropy test [41,79]. The first interval mimics the ink is at rest, the second interval denotes the extrusion process where the viscosity decreases abruptly, and the third interval mimics the condition of the ink after being extruded. One can clearly observe from Fig. 6(e) that almost 90 % of the initial viscosity is achieved within 5 s, ensuring the shape retaining capacity of the overhanging filaments as depicted in Fig. 6(f).

The yield stress defines the resistance to flow of the ink under pressure. The higher the yield stress of the ink, the more pressure is required for extrusion. In general, the yield stress increases with solid loading [71,78]. An ink with moderate to high yield stress (higher solid loading) is often desired for printing, as it is capable of retaining the structure after extrusion. On the contrary, an ink with low yield stress (lower solid loading) exhibits less resistance to deformation and hence typically deforms/collapses under its own weight before the elastic recovery (Fig. 6(d)). Interestingly, the yield-stress of the ink can also be increased by heating the print bed, which promotes solvent evaporation from the ink and helps the ink to retain the extruded shape [71,80]. Renteria *et al.* intentionally aged the ceramic paste at low temperatures to re-activate the elastic properties of PVA, ensuring enhanced elastic response of the ink after being extruded [58]. A recent study by Li *et al.* reported that by using volatile components such as ethanol in the ink composition leads to rapid drying of the ink, leading to an increasing solid content thus enhancing the modulus/yield stress and the shape retention capacity [72]. Gadea *et al.* also emphasized that the yield stress is strongly related to the solid loading of the sol-gel ink [73]. The hybrid sol-gel BT ink showed relatively consistent yield stress values for solid loadings ranging from 30 to 35 vol%. However, the yield stress increased significantly when the solid loading was increased to 40 vol%.

The yield stress of the ink also plays a significant role in determining the maximum height of the printable object, which is given by [81]:

$$h \approx \frac{\sigma_{yield}}{\rho g} \tag{4}$$

where h is the maximum height of the printed object (mm), σ_{yield} is the yield stress (Pa), g is the acceleration due to gravity ($g = 9.81\ m\cdot s^{-2}$) and ρ is the density of the ink ($kg\cdot m^{-3}$). One can easily observe from Eq. 4 that inks with higher solid loadings possess higher yield stress, enabling fabrication of large components [73,78].

To facilitate, high solid loadings in the ink, it is necessary to have a homogeneous dispersion of the ceramic powder in the solvent. This is where dispersants play a important role in imparting stability (either through electrostatic, steric or electro steric mechanisms) to the ceramic particles, which otherwise would tend to flocculate or sediment. Hossain *et al.* carried out a thorough investigation to study the effect of dispersant content on the rheological property of a PZT ink [74]. The storage modulus and yield stress (in addition to the viscosity and the stress) as depicted in Fig. 7(a-b) decreased significantly when dispersant concentration increased from 1 to 2 wt%. This is due to the fact that the polymeric chains of the dispersant adhere more strongly to the surfaces of the particles, which reduces frictional and electrosteric forces and keeps the particles separated, thereby freeing the trapped solvent. However, increasing the dispersant concentration beyond the optimum value negatively affected the rheological properties. The prepared PZT ink slumped due to a comparatively low elastic modulus and yield stress. In addition, excess dispersant creates a disbalance of electroneutrality in the ink [82]. As a result, the attractive forces can dominate over the repulsive forces leading to agglomeration and nozzle clogging during the extrusion. Similar observations were made by Rowlands *et al.* [71]. The authors pointed out that using less than 0.5 wt% of dispersant led to agglomeration and nozzle clogging. A maximum of 1.5 wt% of dispersant was necessary to achieve a stable suspension with homogeneous dispersion of the ceramic particles. However, the dispersant should be carefully selected for a particular binder system. Liu *et al.* reported that *in situ* polymerization of PAA in presence of PVA led to the formation of a gel [83]. In this case, the gelation phenomenon was intensified leading to an increase in viscosity when the PAA concentration exceeded 1.75 wt%.

In contrast to dispersants, coagulants help to achieve the desired rheology by promoting particle agglomeration. Several studies reported the use of polyethyleneimine (PEI) as a coagulant [50,51,84]. The addition of PEI is reported to increase the viscosity and storage modulus by orders of magnitude [51]. Furthermore, the linear viscoelastic region (LVR) on adding PEI extends up to higher stress/strain values,

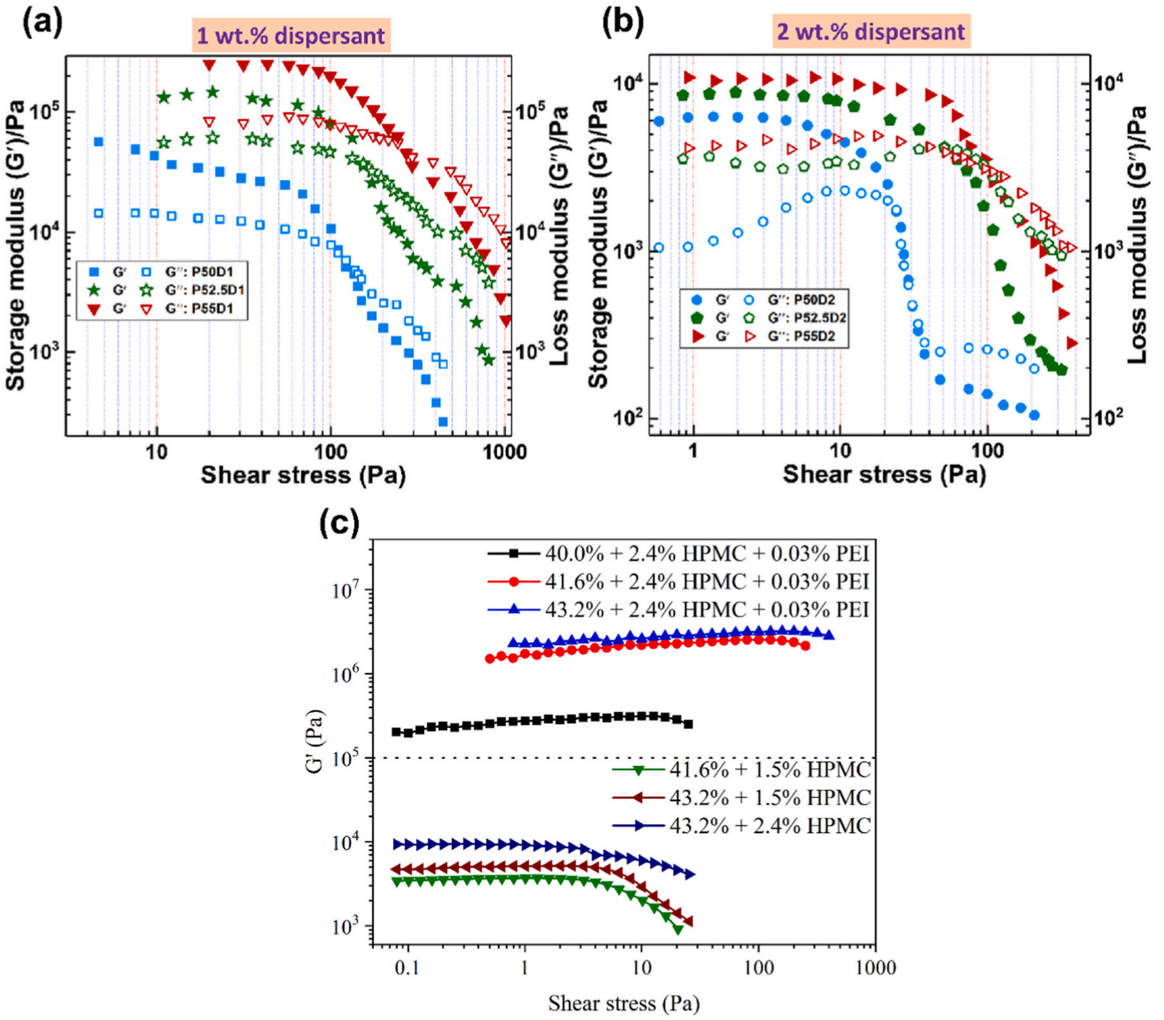

Fig. 7. Effect of dispersant, binder, and coagulant concentration on the rheological behaviour. (a-b) Rheological analysis of PZT inks, showing the relationship between storage modulus (G') and loss modulus (G'') with shear strain for inks with varying dispersant and solid loadings [74]. (c) Variation of elastic modulus (G′) with shear stress at different binder (HPMC) and coagulant (PEI) concentrations in BCZT pastes [51].
Reproduced from Ref.: (a-b) [74], with permission from Elsevier. (c) [51], with permission from John Wiley and Sons.

suggesting that the ink possesses higher elastic properties which are necessary for shape retention (Fig. 7(c)). The coagulation phenomenon can be explained by charge neutralization, which occurs when the positively charged secondary and tertiary amino groups in the PEI readily interact with the negatively charged functional groups in the dispersant (Dispex® A40). Nan *et al.* reported that the shape retention capacity of vertical free-standing pillars was enhanced by using 0.032 wt% PEI [84]. Although an excessive amount of PEI (0.068 wt%) improved the ability to form flocs, resulting in an increasing storage modulus, it also led to a reduction in electrostatic interactions between cationic-anionic couples due to multibody effects [84]. Furthermore, the concentration of PEI was maintained below the threshold required for monolayer formation, allowing it to function as a bridging flocculant. Such concentration keeps the PEI molecules more dispersed rather than completely encapsulating the ceramic particles providing more flexibility to interact with multiple particles or creating bridges/connections among the particles. Indeed, the steric hindrance (from the additives) will impose a restriction on the quantity of PEI chains capable of bridging. However, the probability of a PEI molecule forming complexes is expected to increase with the size of the PEI molecule. A similar interaction behaviour of PEI with APA-stabilized BT has also been reported elsewhere [50].

The binder used in formulating the ink also plays an important role in dictating the adhesion between the layers. In addition, it helps in binding the particles together so that the printed samples have enough strength to be handled during post processing. Liu *et al.* investigated the role of binder (PVA) concentration on the ink viscosity (keeping the solid content fixed at 86.21 wt% of PZT) and found that a binder concentration in the range of 6 – 12 wt% was suitable for easy extrusion and subsequent shape retention [85]. The viscosity was also reported to increase with the PVA concentration. As the amount of PVA increases, the hydrogen bonding among the PVA chains increases correspondingly, leading to an increasing viscosity. The ink with the highest amount of binder exhibited the least dimensional deviation. This is in good agreement with another study where PVA of 9 wt% and 13 wt% was successfully used in preparing BT inks [59]. Similar variation in the viscosity was also reported for BCZT inks prepared with different contents of hydroxypropyl methylcellulose (HPMC) binder [51]. Kim *et al.* reported phase separation and undesired flow rates during the printing process when the binder (PVDF) to solvent ratio (DMF) was maintained at 1:14 due to low viscosity of the paste on using excessive DMF [86]. On further increasing the ratio to 1:8.8, an ink with better rheology, controlled flow-rate and shape retention was achieved.

2.1.6. *Novel ink formulations: capillary suspension and sol-gel*

Significant progress has been made in the field of DIW, particularly with the introduction of unconventional ink formulations that differ from the traditional compositions. Some of these innovative formulations employ capillary and sol-gel based suspensions, offering a new perspective in the field of robocasting.

Unlike colloidal suspensions, where particle stability is determined by electrostatic repulsion or steric hindrance, the stability of particles in capillary suspensions (CapS) is maintained by the capillary forces arising by the addition of an immiscible secondary phase in the bulk phase [87]. Using CapS of BT, researchers in Germany successfully managed to fabricate log-pile structures with 150 μm nozzle diameter [88]. For the preparation of such inks, first a mixture of low viscosity paraffin oil, mineral spirits and stearin wax was heated up to 70°C with constant stirring and then homogenized using a high-speed mixer (2400 rpm). This constituted the bulk phase of the CapS ink. Subsequently, the addition of the secondary phase, i.e. aqueous sucrose solution led to the formation of capillary bridges between the particles with a coherent particle network spanning in the bulk phase. These capillary bridges are known to exist in two forms: pendular bridges, characterized by a contact angle $\theta_{SB} < 90^\circ$ and capillary bridges, characterized by a contact angle $\theta_{SB} > 90^\circ$. The contact angle θ_{SB} is defined as the angle between the secondary phase and the ceramic particles, when surrounded by the bulk phase [89]. In this case, θ_{SB} was calculated to be $31.6^\circ \pm 5.4^\circ$, which implies that the secondary phase was able to wet the ceramic particles, resulting in a stable suspension without any phase-separation. The secondary phase is believed to induce the transition from a fluid (low viscosity) to a highly elastic behaviour, necessary for shape retention. These suspensions are specifically designed for the fabrication of microstructurally porous ceramics. As a result, the ceramic loading was limited to only 31 vol%.

A recent study reported the use of a hybrid sol-gel ink containing BT particles [73]. The ink was prepared by mixing titanium isopropoxide (TTIP) and N-methyl diethanolamine (MDEA) in an argon-filled bottle and subsequently water and glycerol were added in drops. Finally, barium oxide (BaO) was added in stoichiometric concentrations to obtain a gel. In order to maintain the stoichiometry (Ba:Ti = 1:1), it was possible to only have a solid loading of 8 vol%. Such an ink is not suitable for robocasting as it lacks yield stress or shear thinning behaviour. Subsequently, commercial BT powder was added to the ink to increase the solid loading to 30 – 40 vol% and achieve suitable rheological parameters for printing.

One of the advantages of DIW is that it enables the use of a low amount of organic content, and it would be even more beneficial to eliminate the use of organics altogether, since they are one of the most challenging aspects in the thermal treatment (debinding) process. Rosental *et al.* proposed a solution by replacing the organic additives by a sol-gel precursor [78]. The sol-gel precursor was chosen in such a way that it yielded the same composition as the dispersed particles after the heat treatment. This precursor actually acted as a binder for the BT particles and was synthesized via a sol-gel technique using barium acetate and titanium isopropoxide (TTIP) as starting materials, with water and acetic acid as solvents.

2.1.7. Ink formulation steps

To guarantee that the ink formulation for DIW is appropriate for the printing process, it is essential to introduce the processing additives in the correct order, since an incorrect order of addition can significantly impact the quality of the final ink. At first, the dispersant is usually mixed well with the solvent before the ceramic powder is added. Subsequently, the binder, coagulant and other processing additivities are added to the system. Although some of the researchers prefer mixing the solvent and all of the processing additives before adding the ceramic powder, in any approach the additives should be added in the following sequence: dispersant → binder → humectant (solvent trap) → coagulant. To guarantee a homogeneous mixing, a mixing step should be performed after each component is added. One of the most efficient methods of mixing is adding the ceramic powder in batches and providing a gap of a few minutes between two successive mixing steps to avoid heat generation during the mixing process. This can lead to solvent evaporation or initiate some unwanted reaction among the additives. The ink is then transferred to a syringe and then defoamed to remove the entrapped air bubbles.

Instead of adding the dispersant to the solvent, the dispersant can also be mixed well with the powder using an agate mortar or a ball mill before adding it to the solvent. However, while preparing bigger batches, it can be difficult to maintain the homogeneity. Inhomogeneity can also arise due to use of certain additives such as PVA, which does not completely dissolve in deionized water at room temperature. In order to promote dissolution, a certain temperature with constant stirring is required to ensure homogeneous mixing of the binder. It might happen that some of the water evaporates during the process, thereby deviating from the target ink composition. A similar observation was made by Kim *et al.* while mixing PVDF in DMF solvent [86]. After the mixing process, an additional amount of DMF was added to maintain the ratio of the binder to solvent. Using such combination of solvent and binder, Wang *et al.* formulated a stable ink with nanoparticles just by stirring with a glass rod [69].

When formulating the ink composition, it is important to take into account that the amount of added dispersant, binder and coagulant is directly related to the ceramic powder content. The finer the ceramic particles, the more processing additives are required. On the contrary, the humectant (solvent trap) concentration depends on the overall liquid volume. This keeps the ink from drying out too quickly, which otherwise might lead to nozzle clogging.

It might also happen that the prepared ink cannot be completely used immediately after it has been prepared. In this situation, it is necessary to subject the ink to a secondary mixing process to counteract the effects of ageing. Otherwise, an undesirable increase in the viscosity of the ink may occur.

2.1.8. Printing parameters: optimization

The nozzle diameter, printing speed and extrusion pressure plays an important role in determining the quality of the printed component. Understanding the relation between the parameters not only ensures a smooth printing but also higher resolution in the printed component.

The nozzle diameter determines the resolution that is achievable during the printing. As a rule of thumb, the nozzle diameter should be at least 15 times the size of the largest particle size to ensure a smooth flow [40]. Particle agglomerates may compromise this simple rule. The minimum extrusion pressure required by the ink to flow out of the nozzle is governed by the equation [90]:

$$P_{\min} = \frac{4L\sigma_{yield}}{D} \tag{5}$$

where σ_{yield} is the yield stress of the ink, L is the length and D is the diameter of the nozzle. One can easily observe from the Eq. 5 that the value of $P_{\min}$ is strongly affected by the ink rheology (ceramic loading) and the nozzle diameter. It increases with increasing the ceramic loading or by decreasing the nozzle size. Hossain *et al.* carried out a thorough study and reported the variation of the minimum extrusion pressure with the nozzle size [74]. The authors reported that finer nozzle sizes certainly lead to a high resolution, but at the expense of really high extrusion pressure (Fig. 8(a)). On the other hand, using a large nozzle size reduces the printing accuracy. To balance these trade-offs, most of the publications to date, have used nozzle diameters larger than 400 μm (see Table 2), which provides a best compromise between the resolution achievable and the extrusion pressure employed.

Moreover, the extrusion width is also related to the extrusion pressure. It is quite evident from Fig. 8(b), that the strut width increases with increasing the extrusion pressure, while keeping the printing speed constant. Furthermore, as illustrated in Fig. 8(c), the extrusion pressure of the ink with a constant nozzle size is highly dependent on the printing

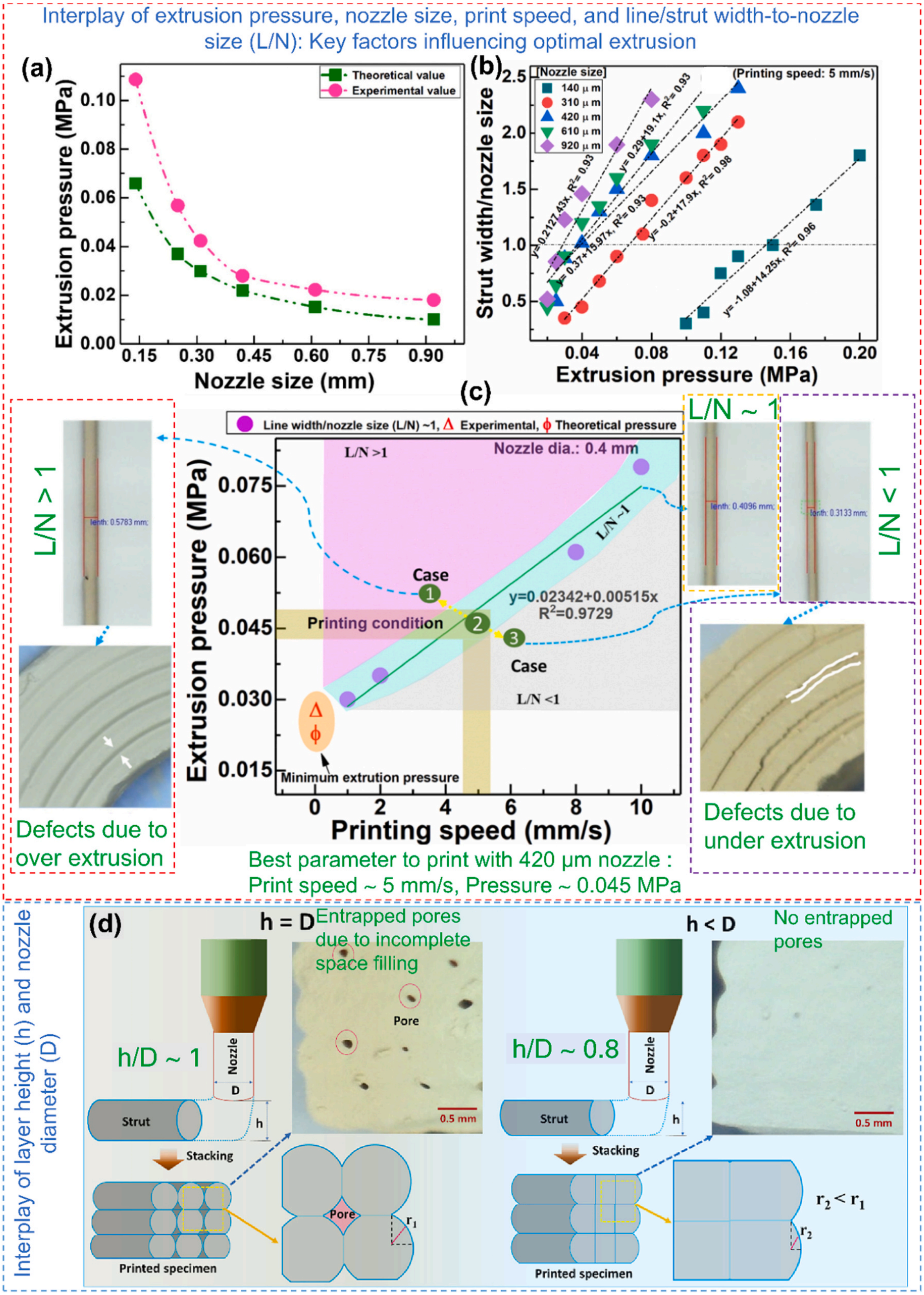

Fig. 8. Factors affecting the print quality. Printing dynamics [74]: (a) Variation in minimum extrusion pressure with nozzle diameter, (b) Effect of nozzle diameter and extrusion pressure on the L (line or strut width) / N (nozzle size) ratio, (c) Extrusion pressure as a function of printing speed for a constant strut width. The images (on the left and right) depict the possible defects that could arise die to under and over extrusion, (d) Factors contributing to inter-strut void formation and strategy for elimination of such entrapped void. This overall analysis was carried out with PZT inks with a solid content of 52.5 vol%.
Reproduced from Ref.: (a-d) [74], with permission from Elsevier.

speed. This indicates that a higher extrusion pressure is required to maintain a constant ratio between the diameter of the nozzle (D) and the width of the extrusion (L), with increasing printing speed. Ideally, a ratio of 1 ensures a defect-free deposition of the ink. On the contrary, deviations lead to defects, as shown in Fig. 8(c).

In addition, the height of the extrusion or the layer height influences the surface finish and the presence of inter-strut porosity. If the layer height is too low, the nozzle has to traverse through the already deposited layer, which leads to build up of material along the printing direction. On the contrary, higher layer height leads to misalignment and improper stacking of struts. This can lead to residual porosity entrapment. The effect of the layer height (H) on the formation of the inter-strut porosity has been shown in Fig. 8(d).

A lower H/D ratio (where, H is the layer height) is always preferred as it increases the curvature length (r) of the deposited strut, thereby minimizing the probability for generating inter-strut porosity. This defect is most prominent when printing dense structures, such as cylinders or bars. This problem could be minimized by using square nozzles instead of circular ones, which theoretically has the highest possible value of r [70]. However, it was discovered that the inter-strut pores were still present. This was due to the entrapment of oil during the movement of the nozzle in oil bath which prevents the ink from drying up at the nozzle leading to nozzle clogging. At the same time, it ensures a homogeneous drying rate after printing. Therefore, printing dense monoliths in oil is not a suitable option. To mitigate these issues, most of the authors, have used the layer height as 40 – 80 % of the nozzle diameter during printing (please refer to Table 2). This ensures better precision and minimizes the defects related to porosity entrapment.

The ability of particles with a high aspect ratio (e.g., platelets) to self-align along the extrusion path is a key feature of the direct ink writing process. The benefit of such alignment for piezoelectric ceramics lies is the exploitation of the texture-sensitive properties. The material after texturing exhibits enhanced piezoelectric properties along the oriented direction. Nevertheless, textured piezoelectric ceramics are still in the research and development stage, since it is quite difficult to manufacture piezoelectric platelets in bulk quantity. Walton *et al.* carried out a detailed investigation into the alignment process of BT templates in a PIN-PMN-PT matrix [91]. A unique aspect of this study was the implementation of a customized nozzle that incorporated a baffle wall to generate a lateral shear force in addition to the inherent shear effect of the nozzle (Fig. 9(a)). The authors found that the degree of alignment (measured by lotgering factor, explained more in Section 3.2) depends on the nozzle aspect ratio and the printing rate. An increase in both the factors are required to achieve the desired outcome (Fig. 9(b)). Additionally, the platelets were more aligned on the surface compared to the bulk as depicted in Fig. 9(c). In general, the shear rate experienced by the ink depends on the printing rate, according to [81]:

$$\dot{\gamma} \approx \frac{4S}{\pi r} \tag{6}$$

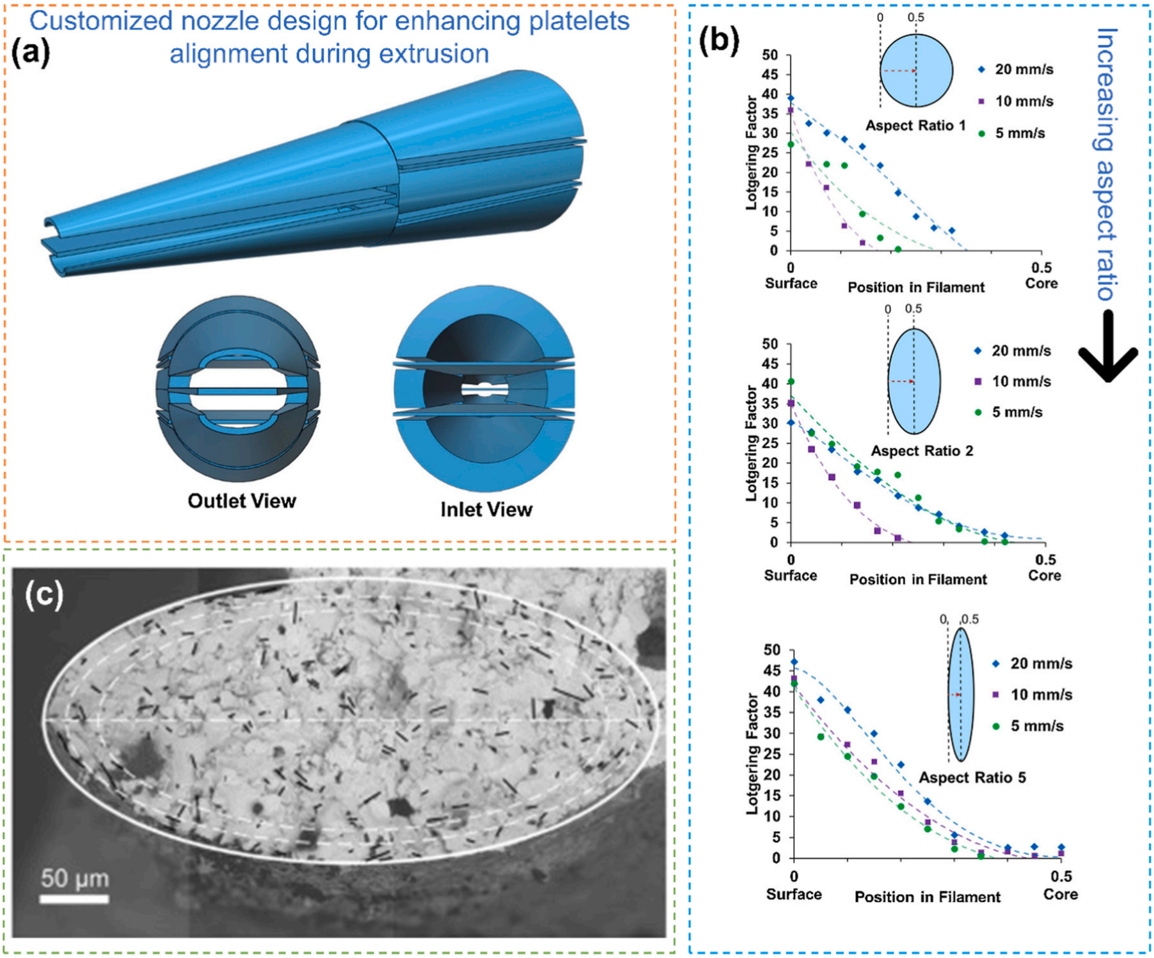

Fig. 9. Impact of nozzle design and printing speed on the alignment of template particles. (a) Schematic of the proposed baffled nozzle for direct writing, featuring an expanded side view, outlet view and inlet view, highlighting the addition of flat baffles within a standard tapered nozzle [91]. (b) Lotgering factor as a function of position (position/diameter) for filaments printed at different printing rates, with comparisons among nozzles of aspect ratios 1, 2, and 5 [91]. (c) The backscattered scanning electron (BSE) image of the sintered filament cross-section shows the alignment of the templates, visible in dark contrast [91].
Reproduced from Ref.: (a-c) [91], with permission from Elsevier.

where $\dot{\gamma}$ denotes the maximum printing shear rate experienced by ink during the extrusion, S denotes the printing speed (mm/s) and r denotes the inner diameter of the nozzle opening (mm). Eq. 6 suggests that using a finer nozzle and higher printing speed will generate more shear stress, thereby enhancing the alignment process more efficiently.

2.2. *Fused filament fabrication (FFF) / Fused deposition of ceramics (FDC)*

2.2.1. *Basics of the technology*

In a typical FFF process, the feedstock is composed of ceramic particles embedded in a thermoplastic binder in the form of composite filaments. The binder is usually heated to a molten state and then extruded onto the print bed through a fine nozzle. The slicing software controls the nozzle motion in the X-Y plane, whereas the print bed only moves in the Z direction.

To achieve a high density in the sintered stage, the composite filaments must contain a high loading of ceramic powder. However, this results in increased stiffness, brittleness, and reduced spooling efficiency, which may lead to frequent filament breakages during printing. It is therefore necessary to maintain some degree of flexibility in the filament, as well as low viscosity after melting, to ensure successful printing. In principle, the extrusion mechanism is similar to DIW, which uses a ceramic paste instead of a filament as a feedstock. Two major benefits of using DIW are energy savings, as there is no need to heat the paste for extrusion, and the ability to achieve higher solid loading due to the low organic content. However, the precise control of the rheological behaviour of the paste, which is crucial for the success or failure of the printing process, is not always easy to achieve. In the case of FFF, the ability of the extruded filaments to retain their shape is related to the thermoplastic nature of the binder. It solidifies immediately as it is deposited on the print bed. In such a scenario, FFF offers more shaping flexibility when compared to DIW especially where unsupported or overhangs or structures with numerous retractions are desired. The resolution of the printed components is often dictated by the nozzle diameter which is usually ≥ 400 μm (for ceramic-containing filaments, please refer to the Table 3). As a result, this often leads to an uneven surface finish of the components. The green samples can be post-processed to achieve a better surface finish through mechanical processing methods such as milling. In contrast, samples fabricated with DIW are typically more fragile and cannot withstand mechanical processing in the green stage.

The success of the printing process depends entirely on the rheological properties of the feedstock. The following sections will discuss in detail the important factors affecting the filament fabrication process.

2.2.2. *Choice of base binder*

One of the most important variables that significantly affects the FFF process is the formulation of the binder. In the FFF process, the term binder usually refers to a blend of various polymeric components. This usually consists of a base binder, tackifier, surfactant, wax and plasticizer [99]. Most importantly, the binder and the ceramic powders should be compatible with each other, otherwise it may lead to phase separation during the extrusion process.

In 1998, a team of researchers proposed a four-component binder system for fabricating composite filaments [99]. This binder system, termed ECG9, was extensively used in early studies for fabricating PZT filaments [100–103]. McNulty *et al.* successfully formulated an optimized binder composition with 100 parts of base binder, 20 parts of tackifier, 15 parts of wax and 5 parts of plasticizer to produce PZT filaments [99]. The flexibility of the binder was found to be mostly influenced by the tackifier rather than wax or plasticizer. On the other hand, addition of a tackifier to the base binder resulted in a considerable rise in viscosity and a drastic reduction in the strength. Bandyopadhyay *et al.* reported a similar binder composition to ECG9, but with 6 components [104].

In recent years, several commercial thermoplastic polymers such as acrylonitrile butadiene styrene (ABS), polyvinylidene fluoride (PVDF), polyvinyl alcohol (PVA), thermoplastic polyurethane (TPU), polylactic acid (PLA) and polycaprolactone (PCL) have been widely used as a base binder for incorporating piezoceramic powders [105–113]. Indeed, ABS is considered to be one of the most widely used binder matrices for filament fabrication [114]. This binder is characterized by a relatively low glass transition temperature (T_g) and excellent processing properties, that makes it suitable for the extrusion process. In addition, because of its amorphous nature, the shrinkage associated after the printing process is comparatively small, thereby maintaining a tight dimensional accuracy. In addition, PVDF is becoming increasingly recognized in the field of filament production because of its inherent piezoelectric characteristics [108,115]. The inherent nature of this property makes it a perfect option for further enhancing the properties of the 3D printed composite by using ceramic fillers such as BT (in this case, without sintering the filament after printing). Considering environmental concerns, there has been a recent trend towards the use of biodegradable polymers; PCL stands out to be a better choice concerning environmental challenges [111,113].

Researchers have more recently reported the use of ethyl vinyl acetate copolymer (EVA) as the backbone polymer for fabricating BT and PZT filaments [116,117]. This binder was modified slightly to replace with paraffin wax [118]. The use of a dual-binder system has gradually become important, as the low molecular weight of paraffin wax leads to low viscosity at the shaping conditions and the high-temperature backbone polymer provides sufficient green strength after the shaping and during the debinding process. In addition, paraffin wax usually has a lower melting point and decomposition temperature than the backbone polymer. This paves the path for chemically extracting the wax from the thermoplastic blend (better known as chemical debinding) before carrying out the thermal debinding.

2.2.3. *Effect of surfactant, plasticizer*

The use of a suitable surfactant ensures that the ceramic particles are homogenously dispersed in the binder matrix. The dispersion is usually accomplished via steric stabilization [119]. Inhomogeneity can lead to drastic changes in the rheological properties, resulting in a filament unsuitable for the FFF process.

McNulty *et al.* studied the adsorption behaviour of different surfactants, such as oleyl alcohol, stearyl alcohol, oleic acid and stearic acid on PZT-5H powder [120]. It was observed that under similar experimental conditions, adsorption of stearic acid was found to be highest with a value of 8.14 mg/m^2. While a small quantity of stearyl alcohol (0.811 mg/m^2) was adsorbed, the other surfactants did not adhere to the powder at all. This could be attributed to the limited solubility of the surfactant in toluene, which was used as a milling medium in this study. At similar concentrations of surfactants, stearic acid and stearyl alcohol reached the saturation point and started precipitating. These precipitates easily adsorb onto the powder surface due to electrostatic interactions. In contrast, oleyl alcohol and oleic acid do not reach the saturation point, therefore tend to remain in solution. Moreover, the presence of the COOH group enhances the functionality (better hydrogen-bonding and multiple bonding sites) of the stearic acid in comparison to the OH group in stearyl acid. This is the reason for preferential adsorption of stearic acid over stearyl alcohol. The adsorption process was found to approach saturation when the concentration of stearic acid in toluene reached 30 g/L. Allahverdi *et al.* reported that stearic acid outperforms all other surfactants used for bismuth titanate ($Bi_4Ti_3O_{12}$) powders and the saturation level was found to be 70 g/L [102]. Due to its superior adsorption capabilities, stearic acid has been widely studied as a surfactant [100,101,103,106,116–118,121–123].

Venkataraman *et al.* observed that the relative viscosity of a PZT-ECG 9 composite decreased on addition of surfactants such as KRTTS and

Table 3
Feedstock preparation and optimized printing parameters for fused filament fabrication.

Feedstock	Particle size and morphology	Binder	Additives	Ceramic loading	Printing parameters				Reference
					Nozzle temperature (°C)	Nozzle size (mm)	Layer height (mm)	Additional information	
PZT		ECG9		55 vol%	165 – 170			Build envelope temperature: 40 °C	[99]
PZT-5H	0.5 – 0.7 µm	ECG9	Stearic acid	52 – 60 vol%	145 – 160	0.355, 0.5	0.2 – 0.25		[121]
PZT-5H	0.5 – 0.7 µm	Proprietary binder		60 vol%	145	0.5			[130]
PZT	SSA = 2.58 m^2/g		Oleyl alcohol, Stearyl alcohol, Oleic acid, Stearic acid	55 vol%					[120]
PZT	1.2 µm	ECG9	Stearic acid	52.6 vol%	140	0.254, 0.381, 0.508		Filaments stored in controlled humidity	[100]
PZT		ECG2	Stearic acid	60 vol%		0.508	0.254		[122]
PZT	0.73 µm	ECG9	Stearic acid	52.6 vol%		0.508			[101]
BiT powder **BiT platelets**	0.5 – 1 µm	ECG9	Stearic acid, KD3, Solsperse 13940	48 – 50 vol% 5 wt%			0.250		[102]
PZT		ECG9	Stearic acid	52 – 60 vol%	140 – 150	0.25 – 0.50	0.025 – 0.25	Build envelope temperature: 20 – 40 °C	[103]
PZT—5H Spray dried		Proprietary from Strstasys		50 – 55 vol%	140 – 200	0.3		Print area temp: 30 °C – 40 °C	[104]
$BaTiO_3$	< 3 µm	ABS (in acetone)		0 – 70 wt%	230			Print bed: 110 °C	[127]
$BaTiO_3$		PVDF (in DMF)		3 – 15 wt%					[108]
$BaTiO_3$	Micro-particles	ABS (in acetone)	Octyl gallate, Dibutyl phthalate	32.7 – 33.2 vol%	210 – 225		0.1, 0.2		[105]
PZT	d_{50} = 1.1 µm	EVA, Paraffin wax	Stearic acid	60 vol%					[118]
$BaTiO_3$ **PZT**	2 µm 2.77 µm	EVA	Stearic acid	52 vol% 49 vol%	150 – 180	0.8	0.2	Print bed: 60 °C	[131]
$BaTiO_3$ **PZT**	2 µm 2.77 µm	EVA	Stearic acid	52 vol% 49 vol%	170	0.8	0.25	Print bed: 60 °C	[116]
$BaTiO_3$	3 µm	ABS	Stearic acid	10 – 50 vol%	230	0.3		Print bed: 110 °C	[106]
PZT	0.73 µm	ECG9	Stearic acid (in toluene)	52.6 vol%				Filaments stored at 50 % R.H	[129]
PZT	1.2 µm	ECG9	Stearic acid, KRTTS (both in toluene)	0 – 60 vol%					[124]
$SrTiO_3$	500 nm, spherical	ABS		67.89 wt%	240	0.4	0.1 – 0.3	Print bed: 110 °C, Speed: 80 mm/s	[107]
PZT	50 µm spherical granules crushed	Vestoplast V2103, Vestowax SH112, Indopol H—1900, Escorez 1304	Stearic acid (in toluene)	60 vol%	160	0.5, 1.0, 1.2		Speed: 10 – 100 mm/s	[123]
$BaSrTiO_3$	APS < 0.5 µm	ABS (in acetone)		0 –50.27 wt %	250	0.55	0.1	Print speed: 40 mm/s, Print bed: 100 °C	[126]
PZT	500 nm, spherical	TPU/carbon black		30 vol%	230	0.6	0.2	Speed: 20 mm/s, Filament dried at 60 °C for 1 day	[109]
$BaTiO_3$	< 2 µm	PCL (in dichloromethane)		25 vol%, 45 vol%, 65 vol %	130	0.4	0.2	Print bed: 30 °C, Speed: 30 mm/s	[111]
$BaTiO_3$, $CaTiO_3$, $Ba_{0.64}Sr_{0.36}TiO_3$	< 3 µm	ABS, PP		30 vol%		0.4	0.1		[132]
$BaTiO_3$		PLA		17.5 vol%					[110]
$BaTiO_3$, $SrTiO_3$, $Ba_{0.67}Sr_{0.33}TiO_3$	< 800 nm	ABS (in acetone)	Dibutyl phthalateoctyl gallate	15 – 30 vol%					[112]
$BaTiO_3$	d_{50} ~ 2 µm	PVA, PCL		24 – 54.5 vol %	210 – 230	0.3, 0.4	0.2	Speed:10 mm/s, Filament dried at 60 °C before use	[113]

(*continued on next page*)

Table 3 (*continued*)

Feedstock	Particle size and morphology	Binder	Additives	Ceramic loading	Printing parameters				Reference
					Nozzle temperature (°C)	Nozzle size (mm)	Layer height (mm)	Additional information	
PZT 5 H		Multi component binder		50 – 55 vol%	150 – 200	0.3		Build envelope temperature: 38 – 42 °C	[133]
$BaTiO_3$, CNT	700 nm	PVDF (in DMF)		6 – 75 wt%	220		0.34	Print speed: 5 mm/s, Print bed: 120 °C	[115]

stearic acid [124]. However, the one treated with stearic acid displayed the lowest relative viscosity. The mechanism behind the decrease in the viscosity was understood with the help of the Krieger-Dougherty model. The model is best described with the equation [125]:

$$\eta_r = \left(1 - \frac{\varnothing}{\varnothing_m}\right)^{-K_E \varnothing_m} \tag{7}$$

where, η_r is the relative viscosity, $\varnothing$ is the solid loading, $\varnothing_m$ is an empirical constant known as the maximum packing factor and K_E is an empirical constant called the generalized Einstein coefficient. One can observe from Eq. 7, that the viscosity decreases with increasing packing efficiency. The packing efficiency can be enhanced by the addition of surfactants by decreasing the inter-particle interactions. The greater value of $\varnothing_m = 0.73$ for the treated group, as opposed to 0.66 for the

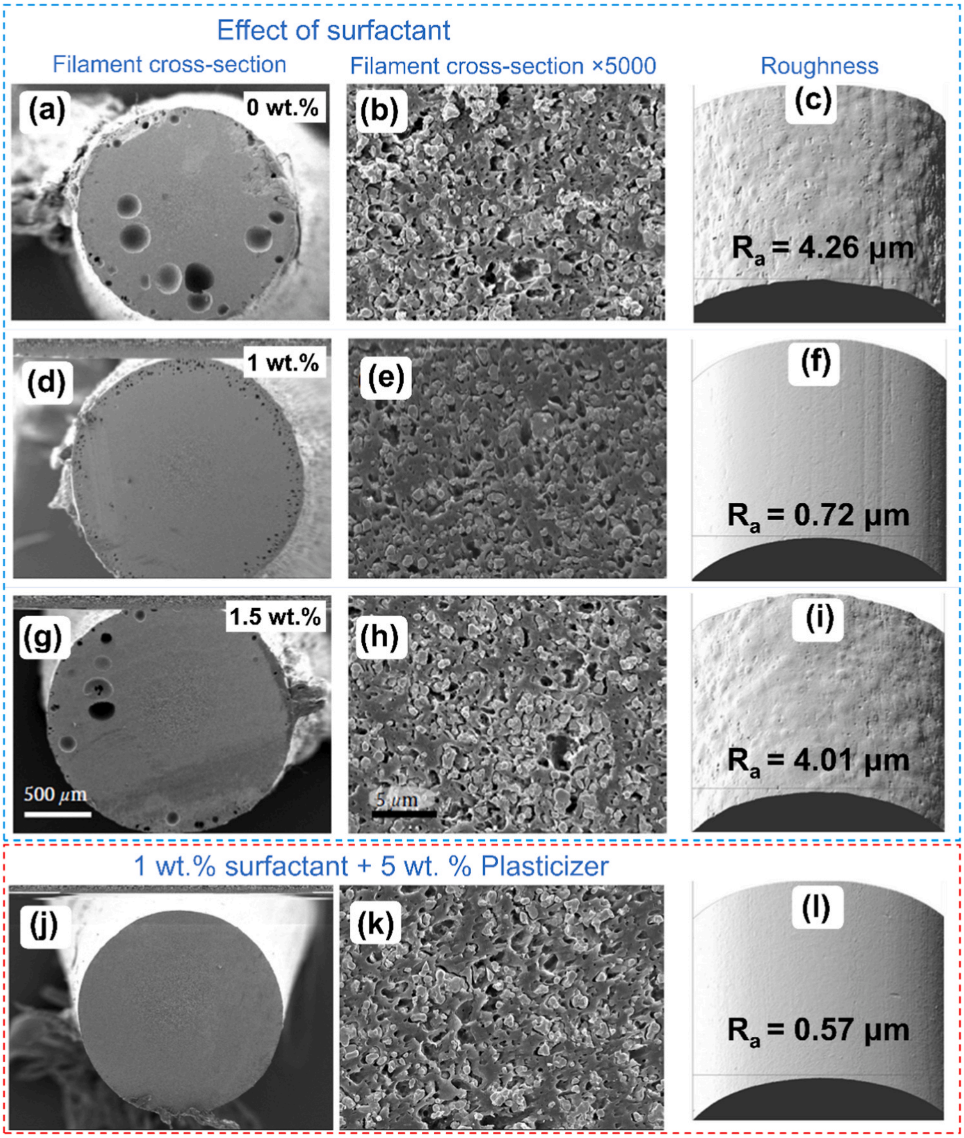

Fig. 10. Effect of the surfactant and plasticizer on the extruded filament. Overview scanning electron microscopy (SEM) images of the cross-section of 30 vol% BT/ acrylonitrile butadiene styrene (ABS) filaments with different amounts of surfactant (octyl gallate) [105]: (a-c) 0 wt%, (d-f) 1.0 wt%, (g-i) 1.5 wt%, and (j-l) with 1 wt% surfactant + 5 wt% of plasticizer (dibutyl phthalate), along with the corresponding optical images showing surface roughness.
(a-l) [105], Open access article distributed under the terms of the Creative Commons CC BY license.

untreated group, provided further evidence of better dispersion and packing. The empirical Einstein constant has a maximum value of 2.5 for equiaxed particles and this value can either increase if the particles are not equiaxed or decrease in case of slippage at the ceramic particle/polymer interface. The powder treated with stearic acid had a K_E value of 1.49 as opposed to a value of 2.5 for the untreated and treated with KRTTS, suggesting slippage at the interface. Although the exact reason behind such phenomenon was not clear, slippage may have resulted from the local presence of stearic acid in the polymer matrix, which may locally lower the viscosity. It also implies that stearic acid has also lubricating properties in addition to dispersing properties.

Wu *et al.* systematically studied the effect of different concentration of surfactant (octyl gallate) and plasticizer (dibutyl phthalate) on the extruded BT filament [105]. The addition of 1 wt% of the surfactant (octyl gallate) resulted in a reduction in porosity, as it enhanced the interaction between the ceramic particles and the polymer matrix (Fig. 10(d-e)). An excessive amount of surfactant results in the reappearance of porosity in the filament, as shown in Fig. 10(g-h), which is similar to the one reported in Fig. 10(a-b) without the use of any surfactant. However, there is still some residual porosity left in the filament even after using the optimized amount of surfactant. The residual porosity and the surface roughness can be further decreased using 5 wt% of plasticizers (dibutyl phthalate), as shown in Fig. 10(j-k). The plasticizer acts as lubricant enhancing the mobility of the polymer chains and occupying the free space. This effect is also realized in the form of decreased extrusion pressure. The coarse texture (or high roughness) of the filaments with insufficient or excess surfactant is a result of the aggregation of the powder, as demonstrated in Fig. 10(c, i) with high R_a values. With sufficient amount of surfactant (1 wt%), the R_a value decreased to 0.72 μm Fig. 10(f). Conversely, the filament with the optimum surfactant (1 wt%) and plasticizer (5 wt%) exhibited a smooth surface with a further decrease in the R_a value to 0.57 μm as depicted in Fig. 10(l). In addition, the flexibility of the filaments was measured by a two-point filament test device. The curvature of the bending filaments was noted just before the fracture, which revealed that the filament with 1 wt% of surfactant and 5 wt% of plasticizers had similar curvature of radius as the pure ABS filament (4.5 cm) before failure. The lower the curvature value at the fracture, the more flexible is the filament.

In a recent study, Goulas *et al.* reported the impact of not employing surfactant or plasticizer in the filament fabrication process employing $(Ba,Sr)TiO_3$ (BST) powder [126]. It was found that the printed composite exhibited agglomerated microstructure of the BST powder as shown in Fig. 11, which suggests that the ceramic fillers were not homogeneously distributed in the thermoplastic binder matrix. When submicron solid particles are dispersed into binder matrix without using the surfactant, they often form agglomerates due to strong electrostatic attraction. As a result, the ceramic loading in this experiment was limited to 50.25 wt% (15.26 vol%). Any composition exceeding this limit caused the filament to become brittle and challenging to extrude.

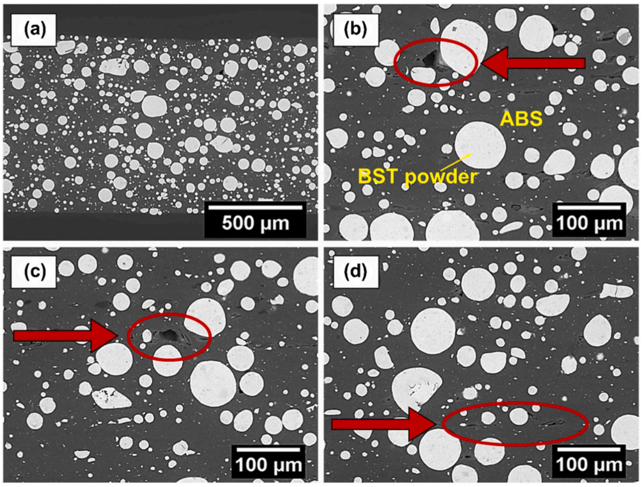

Fig. 11. Consequences of excluding surfactant and plasticizer. (a) Overview, and (b-d) Magnified SEM images of the cross-section of BST/ABS 3D-printed test samples at 50.27 wt% ceramic loadings (15.26 vol%). Arrows indicate defects that adversely affect the dielectric and physical properties of the samples [126].
Reproduced from Ref.: (a-d) [126], with permission from Elsevier.

2.2.4. *Effect of ceramic loading, flexibility*

Usually, a filament with high ceramic loading ($>$ 50 – 55 vol% or $>$ 70 wt%), refer to Table 3) is preferred to minimize the shrinkage, thereby reducing the probability of warping or cracking during the binder burn out process. Nevertheless, increasing the ceramic loading in the filaments induces brittleness (in other words, the compressive or elastic modulus also increases), which in turn causes filament fracture at the gears during the unspooling of the filaments or nozzle clogging during the extrusion.

According to Castles *et al.*, printing filaments with more than 70 wt% (29 vol%) of BT powder was impossible due to their excessive brittleness [127]. It is widely acknowledged that increasing the solid loadings in the filaments increases the viscosity, resulting in the filament being more fragile. Khatri *et al.* carried out a thorough characterization of the filaments with different weight fractions of BT [106]. The torque measurements obtained at the end of the kneading process indicated that the torque value increased with the ceramic content. However, when the temperature was increased to 210 °C, the torque value dropped, as reported for the filament containing 35 % by volume of the ceramic powder. Since viscosity is a temperature dependent property, it decreases with increasing temperature, resulting in reduced resistance to flow during the kneading process. In addition, the composites up to 35 vol% of BT, exhibited shear-thinning behaviour (Fig. 12(a)). Further increasing the ceramic content to 40 vol% lead to a brittle filament, with filament breakage at the gripping motors. The composite with 45 and 50 vol% of ceramics, exhibited a stick-slip phenomenon (Fig. 12(b)). Consequently, the filaments containing high ceramic loadings ($>$ 40 vol %) were challenging to extrude, resulting in substantial dimensional imperfections in the printed component. In a recent study, authors have reported that a maximum of 80 wt% of BT powder (45.8 vol%) could be incorporated in the thermoplastic matrix for a smooth printing and the shear thinning behaviour became more pronounced (n decreases from $\sim$0.61 to $\sim$0.34) with increase in the ceramic content [113]. The authors also reported an innovative way of measuring the elastic modulus and the maximum stress before buckling in compression mode to simulate similar conditions during FFF printing (Fig. 12(c-d)). The typical force-displacement curves reported in Fig. 12(e) suggest that with increasing ceramic loadings in the filament, the elastic modulus and the maximum stress before buckling increases. However, with lower solid loadings, the filament buckle and then deform plastically. In contrast, filaments with higher solid loadings exhibited a fracture as denoted by a sudden drop in the force values. The fracture behaviour of the filaments is clearly evidenced in Fig. 12(c-d). The filaments exhibited elastic modulus and critical stress before failure in the range of approximately 102 – 556 MPa and 3.5 – 9.6 MPa, respectively, with the highest values recorded for filaments with the highest ceramic loading and the lowest values for those with lower ceramic loading.

2.2.5. *Process maps to avoid buckling*

In the FFF process, the filament acts as a piston ensuring smooth extrusion during the printing process. This means that the filament should be able to generate and maintain the necessary pressure for facilitating the extrusion process. Failing to do so, results in buckling. The critical stress value required for buckling is denoted by [128]:

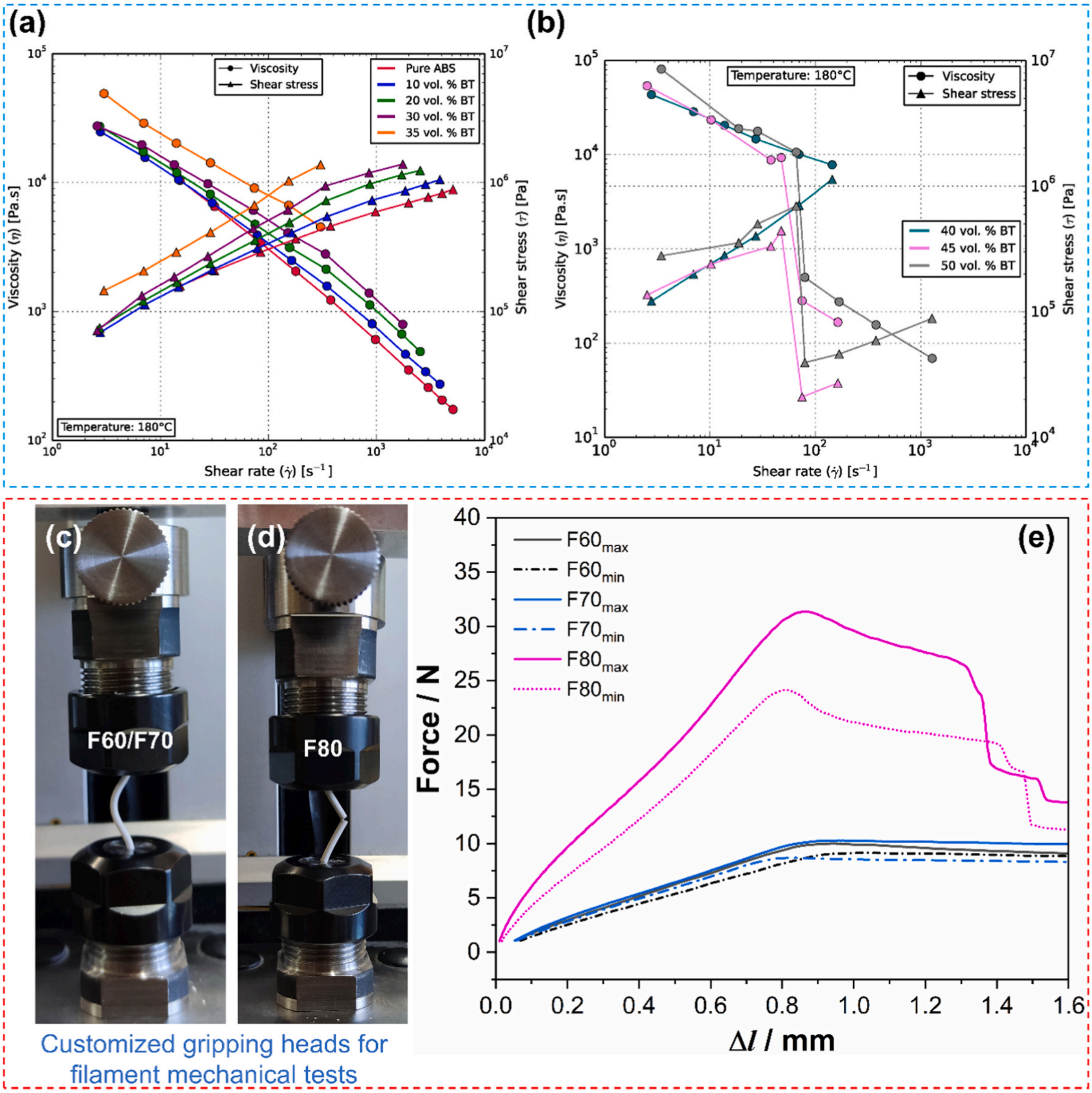

Fig. 12. Effect of the ceramic loading on the rheological and mechanical property of the filament. Rheological analysis of ABS-BT composites with varying solid loadings (a) suitable, and (b) unsuitable for printing. The 45 vol% and 50 vol% samples exhibit stick-slip-like behaviour [106]. Compression test setup for the composite filaments illustrating the buckling/fracture behaviour for filaments with: (c) 60 wt%, and 70 wt% of BT powder denoted as F60 and F70, respectively and (d) 80 wt% of powder, denoted as F80 [113]. (e) Typical force vs. displacement curves for the filaments carried out using the setup show in (c-d), with curves representing the maximum and minimum slopes for each filament type [113].

(a-b) [106], Open access article distributed under the terms of the Creative Commons CC BY license. Reproduced from Ref.: (c-e) [113], with permission from Elsevier.

$$\sigma_{cr} = \frac{\pi^2 E}{4\left(\frac{L}{R}\right)^2} \tag{8}$$

where σ_{cr} is the critical buckling stress, E is the compressive elastic modulus and L/R is the aspect ratio of the filament above liquefier, where the solid filament is heated and melted into a molten form before being extruded. It is quite evident from Eq. 8 that the critical stress required for buckling is directly proportional to the compressive elastic modulus of the filament. A filament with a higher ceramic loading tends to have a higher elastic modulus, thereby minimizing the risk of buckling. However, there needs to be a balance between the ceramic loading and the modulus, to ensure that the filament is flexible enough to be spooled/de-spooled. The ratio (L/R), also known as slenderness ratio, is a parameter specific to each printer. A printer with a direct drive is preferred over one with a Bowden tube, in order to minimize this ratio.

Venkataraman *et al.* developed a process map to predict conditions that might lead to buckling of the filament [100]. The map relies on two crucial factors: the pressure necessary for extrusion and the compressive elastic modulus of the filament. The pressure drop was found to increase with the flow rate and the aspect ratio of the nozzle. The extrusion process was simulated and the results indicated that the maximum pressure (90 %) drop takes place above the nozzle. This indicates that alterations to the nozzle geometry will have an impact on both the pressure drop and the buckling process. The conditions for buckling was determined by plotting P/E as a function of nozzle geometry and flow rate. In general, buckling should occur is the P/E value is greater than the P_{cr}/E value, as denoted by the shaded region above the horizontal straight line in Fig. 13. The process map suggests that the tendency to buckling increases with increasing flow rate and decreasing the nozzle diameter. Moreover, the aspect ratio of the nozzle plays an important role. One can easily observe that on increasing the L/D ratio from 2 to 5

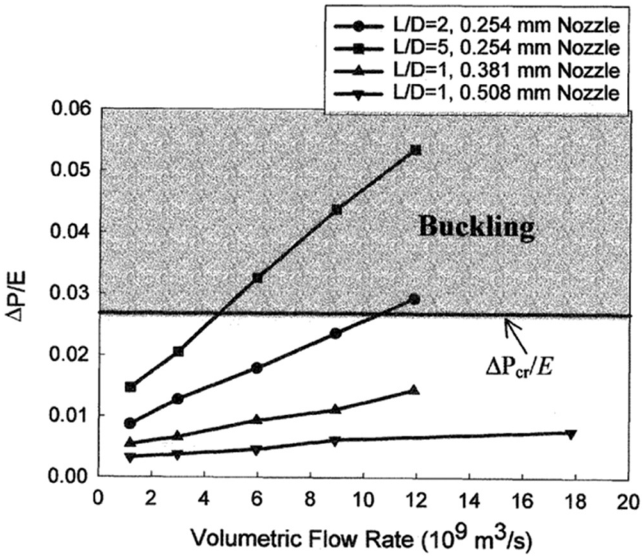

Fig. 13. Process map for predicting buckling in PZT ECG9 filament, illustrating the variation of the dimensionless quantity ΔP/E with fused deposition ceramic (FDC) nozzle diameter, aspect ratio and volumetric flow rate, measured at 140 °C. The dimensionless quantity represents the ratio of pressure drop (ΔP) to the elastic modulus (E) of the material, both measured in pascals (Pa) [100].

and keeping the nozzle diameter fixed at 0.254 mm, buckling occurs at relatively low volumetric flow rate. It is also clear that the buckling does not occur even at high flow rates with nozzle diameters of 0.508 mm and 0.381 mm. Such findings suggest that printing parameters must be carefully selected to ensure trouble-free printing when using finer nozzle sizes. These predictions have been further confirmed by carrying out independent extrusion measurements. It is important to note that this process map provides only a qualitative analysis, as it does consider the thermal effects or the rate dependence which might also affect the elastic modulus.

Venkataraman et al. proposed a new methodology to assess the filament buckling which was based on the ratio of compressive modulus (E) to the apparent viscosity (η_a) of the extruded filament [101]. The conditions derived for buckling can be written as [101]:

$$\frac{E}{\eta_a} < \frac{8Ql\left(\frac{L}{R}\right)^2}{\pi^3 r^4 k} \tag{9}$$

where Q is volumetric flow rate, R is the filament radius, L is the length between the extrusion mechanism and the printing head and l and r are length and radius of the nozzle respectively. One can easily observe from Eq. 9 that, for a particular printer configuration and flow rate, if the E/η_a value of the filament exceeds a critical threshold, it will buckle. In other words, the ratio has to be maximized to decrease the probability for buckling. It was reported that the critical value of E/η_a to avoid buckling is around 3–5 × 10^5 in a shear rate range of 100 – 200 s^{-1}. The authors claimed that this can serve only as a tool for selecting filaments based on the basic mechanical and rheological characterization of the filaments.

2.2.6. *Filament production process*

The first step in the filament fabrication process is the selection of the suitable binder. Thereafter, comes the powder coating step in which the ceramic particles are coated with the suitable surfactant. Now, there can be two different approaches for extruding the filaments: (i) solvent casting, and (ii) dry mixing.

In solvent casting, first the binder is completely dissolved in a solvent at a certain temperature with constant stirring to ensure homogeneous dispersion. The ceramic powder is then introduced to the binder solution and mixed well. This solution is now dispersed on a glass substrate/polytetrafluoroethylene (PTFE) plate and heated at a certain temperature to completely remove the solvent. This results into thin sheets of a polymer-ceramic composite, which can be further sliced down to small pieces for easy extrusion with the extruder.

In the dry mixing process, the binder is added to a shear mixer or torque rheometer where it is melted. To this molten binder, the ceramic powder is added in batches. This is basically done to de-agglomerate the powder and ensure a homogeneous mixing. The feedstock is then granulated into small pieces to be used as a feedstock for the final extrusion process. The granulates are fed to the extruder, where the second mixing happens and then extruded into filaments of desired diameter. In case the ceramic powder has not been coated before, the surfactant can also be added during the first extrusion.

It is important to note that, prior to the compounding process, the binders, additives and ceramic powder should be dried. Failure to do so might lead to rough/uneven surface of the extruded filaments due to moisture or residual solvent evaporation during the extrusion process [113]. Castles *et al.* reported that the composite mixture of ABS and BT particles was left in the oven at 70 °C for a week to ensure the complete removal of acetone, which was used as a solvent to dissolve the binder [127]. Residual acetone, if present, could have produced defects in form of bubbling on the extruded filaments.

It is also important to keep in mind the aging effects after the filament has been fabricated. Venkataraman *et al.* reported that the filaments tend to become more flexible with time, indicating that the modulus decreases with time. Such a phenomenon is undesirable for the printing process [129]. In addition, some of the most commonly used thermoplastic binders are hygroscopic in nature. In such a scenario, the filaments should be kept in a desiccator to prevent moisture absorption or dried in an oven before using it.

2.2.7. *Printing dynamics*

There are several important parameters that play a important role in determining the success or failure of the printing job. The printability of the filaments can be easily assessed by examining the external surface of the filaments after it passes through the feeder gears, as depicted in Fig. 14 [113]. In case of a printable filament, regular and distinct gear tooth marks can be observed (Fig. 14(a-b)). On the other hand, the non-printable filament exhibits irregular gear tooth marks with extensive surface grinding (Fig. 14(c-d)).

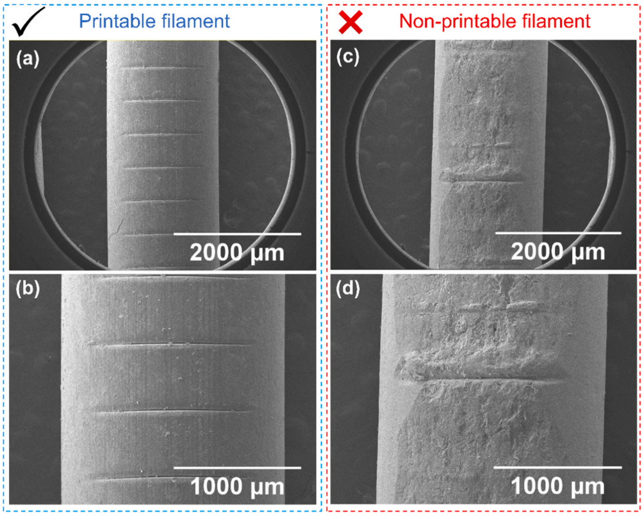

Fig. 14. Overview SEM images highlighting the clear difference between (a-b) a printable and (c-d) a non-printable filament. The images show in (b, d) are magnified version of (a, c) [113].
Reproduced from Ref.: (a-d) [113], with permission from Elsevier.

During the printing process, the nozzle is heated to a certain temperature (usually above the glass transition temperature (T_g) of thermoplastic binder) to provide a shear-thinning behaviour that allows the filament to get deposited on the print bed. Higher nozzle temperatures lead to better bonding between the layers. On the other hand, extremely high temperatures might lead to polymer decomposition. The threshold temperature can be easily assessed by performing a differential scanning calorimetry (DSC) analysis on the composite system.

In this regard, Goulas *et al.* analysed the DSC thermographs of a commercial filament with ABS matrix and strontium titanate ($SrTiO_3$) as ceramic filler in it [107]. The DSC analysis revealed two T_g at 68 °C and 105 °C and the thermal decomposition temperature at 285 °C. So, in this case the limiting extrusion temperature was 285 °C, beyond which the polymer starts to decompose. Accordingly, the nozzle temperature was chosen to be 240 °C. The print bed temperature is also important when adhesion to the print bed can be an issue. The bed temperature is suggested to be kept above T_g so that it forms a strong foundation for the 3D printed component. In cases where there is a strong affinity between the printed composite and a build plate, a tape can be used on the print bed for easy removal of the sample [116]. On the other hand, adhesive spray can also be used on the print bed to enhance the binding between the extruded filament and the print bed. The build chamber in the FFF printer can be sometimes heated to ensure that no thermal fluctuations would occur during the printing process.

The nozzle diameter determines the resolution of the printed component. A smaller orifice would enable deposition of thinner lines or layers, which can be particularly advantageous when printing intricate designs or small-scale objects. A better compromise between the resolution and the printability is achieved when printed using nozzles ≥ 400 μm as reported by several studies (refer to Table 3). However, there is a practical limit which is determined by the viscosity or the ceramic loading in the composite. Umarji *et al.* observed that by reducing the solid loadings from 60 vol% to 52.5 vol%, it was possible to employ a smaller nozzle size of 355 μm instead of 500 μm for fabricating tube actuators [121]. Bhandari *et al.* reported that filaments with lower ceramic content (60 – 70 wt%) could be printed with a 0.3 mm nozzle, although a higher temperature was required compared to using a 0.4 mm nozzle [113]. In contrast, filaments with 80 wt% of ceramic loading could not be extruded due to nozzle clogging. Increasing the nozzle temperature (viscosity decreases with temperature) can be an option which might help in easy extrusion. However, the limiting temperatures have to be kept in mind. As discussed in the Section 2.2.5, the probability of buckling and nozzle clogging also increases with decreasing nozzle diameter. In order to extrude through a fine nozzle, there has to be a compromise on the ceramic loading.

The thickness of each layer significantly affects the total time and expenses involved in fabricating the printed part. This is because a thicker layer will need less time to finish in contrast to a thin layer. In addition, it also determines the resolution along the z-axis and the aesthetics in terms of smooth or rough surface finishes. Goulas *et al.* discovered that a layer height of 200 μm is optimal for producing dense components with minimal porosity between the printed struts (Fig. 15 (c)), using commercially available filaments based on an ABS matrix containing stronium titanate ($SrTiO_3$) ceramics of high relative permittivity (ε_r) [107]. This is particularly important for dielectric measurements since the functional characteristics are negatively affected by the presence of porosity. The presence of air gaps (Fig. 15(a-b, d-e)) was observed as a consequence of deviations from the optimal layer height (100, 150, 250, 300). To address this issue, it is generally advisable to maintain the layer height between 30 % and 75 % of the nozzle diameter (refer to Table 3). This strategy facilitates a larger contact surface area between the filament and the print bed during extrusion, which enhances adhesion and lowers the likelihood of pore entrapment in subsequent layers.

The layer height is of utmost importance when it comes to aligning platelets for inducing templated grain development. Allahverdi *et al.* studied the degree of texturing using platelets in the fabricated bismuth titanate filament and the printed component, to find out the optimum deposition parameters [102]. The results indicate that platelet alignment on the filament surface was parallel to the direction of extrusion, while platelet orientation within the filament was predominantly random. This is similar to what has been observed during DIW of platelet-based inks (Fig. 9(b-c)). To optimize the alignment of the platelets, a printing layer height of 250 μm was used. Depositing thin layers instead of thick layers results in the application of a significantly higher shear stress acting on the platelets, forcing them to align along the printing direction.

It is important to note that circularity and filament diameter play a crucial role in the printing process. A circularity of 1 and the desired filament diameter are always preferred. Any deviation from these values can result in over- or under-extrusion, leading to defects in the printed sample.

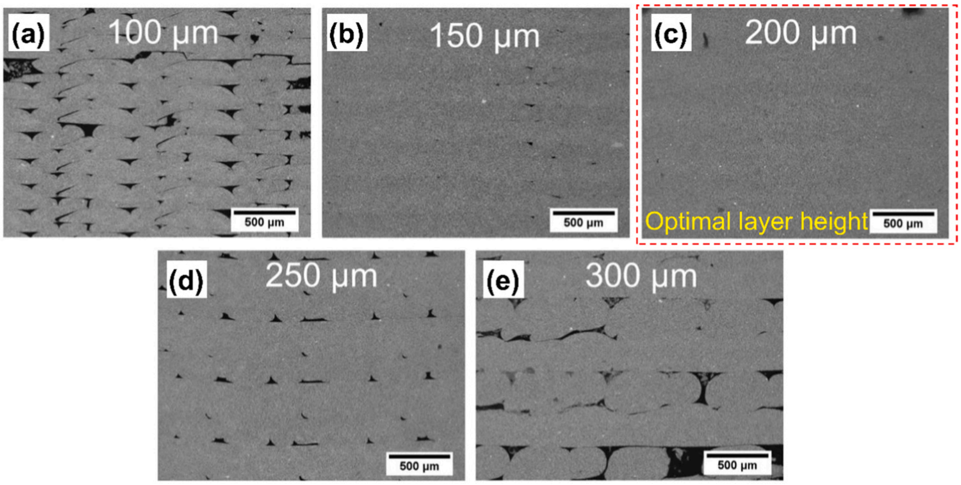

Fig. 15. Impact of layer height variation on the entrapped porosity. (a-e) Overview of SEM micrographs, depicting printing defects that occur at various layer thicknesses, ranging from 100 to 300 μm [107]. The optimal layer height has been marked in red dotted lines. (a-e) [107], Open access article distributed under the terms of the Creative Commons CC BY license.

(a-e) [107], Open access article distributed under the terms of the Creative Commons CC BY license.

2.3. Vat photopolymerization (VP)

2.3.1. Basics of the technology

Vat photopolymerization (VP) is an AM technique where a photocurable material in a vat is cured selectively by using a light source in the UV range. In the VP process, components are created layer-by-layer using stereolithography (SLA) or by projecting each complete layer using digital processing (DLP). This technique can be further classified according to the building direction of the fabricated component. In the top-down approach, the light source is positioned above the vat and the platform descends down to form the new layer. On the other hand, in the bottom-up approach, the light source is positioned below the vat and the platform ascends upward. A wiper blade is sometimes necessary to level the liquid surface before printing the subsequent layers, when using highly loaded ceramic slurries.

Among ceramic AM technologies, VP is known for its dimensional precision (mostly in the order of 10 – 50 μm, refer to Table 4), surface quality and ability to create intricate structures in miniature sizes. The success of printing using this technique heavily relies on the preparation of the slurry, which typically consists of a monomer or a mixture of different monomers, ceramic powder, dispersant, photo-initiators and photo-absorbers. In addition, it may also contain certain additives in form of diluents or pore-formers. Since ceramic particles are inert to light, polymerization only occurs in the organic monomer when exposed to light of certain frequency (usually 405 nm). So, the cross-linked monomers during the polymerization process uniformly surround the ceramic particles in each layer until the complete part is fabricated. The green components are then further processed by a high temperature treatment to completely remove the organics and obtain a high-density ceramic body.

There are certain requirements that need to be satisfied when using ceramic powders for such process. The ceramic suspension should have high solid loading ($>$ 50 vol%) along with low viscosity (3000 mPa·s). Higher solid loading lowers the possibility of generating defects during the binder burn out process, thereby leading to high densities and better mechanical properties. On the other hand, low viscosities ensure that the ink can be spread easily and uniformly. So, there has to be a balance in terms of ceramic loading in the suspensions and the viscosity. An additional problem is related to the density of the ceramic powders. High-density powders (such as those of most piezoceramics) tend to sediment within the slurry, leading to the formation of layers of inhomogeneous ceramic content and defects in the parts after sintering. Another important issue that concerns piezoceramic powders is their high refractive index (RI) when compared to the base resin, as shown in Fig. 16. The difference in the RI affects the curing depth (C_d) and the resolution of the final component, due to scattering phenomena. For example, Song *et al.* compared the curing depth of ceramic suspensions involving three different powders, i.e. PZT, Zirconia (ZrO_2) and Alumina (Al_2O_3) with 65 wt% of ceramic loading and found out that ceramic suspensions with PZT powders exhibited the least curing depth of 39 μm when exposed for 10 s [134]. In contrast, suspensions with ZrO_2 and Al_2O_3 exhibited curing depths of 82 μm and 340 μm, respectively.

Considering the challenges related to VP of ceramic suspensions involving high RI powders such as piezoceramics, this section will review the important parameters that one needs to consider for preparing a printable ceramic suspension.

2.3.2. Effect of monomer

The monomer is the key component in the ceramic suspension that gives most photocurable resins their characteristic properties. Usually, monomers based on acrylates and methacrylates are most widely used [136] as evident from monomers reported in Table 4. Such monomers are activated only by free radicals from the photo-initiator [137]. In order to improve the adhesion between layers in the green body, it is crucial for the ceramic suspension to exhibit sufficient curing ability (at least greater than the slicing thickness). The curing depth (C_d) of the photosensitive ceramic resin can be described by the equation [138]:

$$C_d = \frac{2d_{50}}{3\widetilde{Q}}\frac{{n_0}^2}{\Delta n^2}\ln\left(\frac{E_0}{E_c}\right) \tag{10}$$

where d_{50} is the average particle size of ceramic particles, $\widetilde{Q}$ is the scattering efficiency term, Δn^2 is the square of the difference between the ceramic refractive index (n_p) and medium refractive index (n_0) [$\Delta n^2 = \left(n_p - n_0\right)^2$], E_0 is the energy density and E_c is the critical energy density (the minimum energy density required for photopolymerization). One can clearly observe from Eq. 10 that the curing depth is directly proportional to the intrinsic RI of the monomer and inversely proportional to the difference in the RI between the monomer and the piezoceramic particles. This suggests that a small increase in RI of the monomer can significantly increase the curing depth. For example, the RI of BT/PZT powders ($n_p \approx 2.4$) is significantly higher than that of the most commonly used acrylate resins ($n_0 \approx 1.4 - 1.6$) as shown in Fig. 16. As a result, Δn^2 is higher for suspensions containing such powders. In contrast, Al_2O_3 with a RI of 1.7 will possess a lower Δn^2, hence denoting its strong curing ability.

To address this issue, Liu *et al.* compared the rheological and curing properties of 4 different monomers in a slurry containing 80 wt% of BT powders [139]. Among the monomers chosen for this investigation, acryloyl morpholine (ACMO) had the highest refractive index of 1.508, followed by polyethylene glycol diacrylate (PEGDA-1.466), 1,6-hexanediol diacrylate (HDDA-1.457) and tripropylene glycol diacrylate (TPGDA-1.450). The results indicate that the ACMO had the best curing capability among all the monomers used, followed by PEGDA (Fig. 17 (a)), while HDDA and TPGDA with almost similar values of RI exhibited poor curing characteristics. This can be clearly correlated to Eq. 10. The Δn and n_0 for suspension containing ACMO is the least, hence resulting in enhanced curing performance. In a recent study, authors prepared a photocurable resin 40 vol% of BT with different monomers (4-hydroxybutyl acrylate (HBA), PEGDA, HDDA, TMPTA) and reported that TMPTA exhibited better curing capability *(*Fig. 17(b)) [140]. This is related to the number of functional groups present in the monomer; TMPTA has 3 acrylic groups with most carbon-carbon double bond and the highest RI among the other monomers. For similar reasons, Ma et al. selected PPTTA along with a combination of other monomers due to its higher functionality of 4 and refractive index [141].

In addition, rheological properties of the monomers should also be considered. Liu *et al.* found that PEGDA, with an inherent viscosity of 30 – 70 cps at 25 °C, exhibited the highest viscosity and shear thickening behaviour at high shear rates [139]. High viscosity can drastically decrease the printing efficiency. On the other hand, the other monomers exhibited shear-thinning behaviour, which is desired for such a printing process (Fig. 17(c)). However, ACMO was chosen considering the curing depth and the viscosity. In another study, HDDA was found to be the best monomer, outperforming others like TMPTA with a higher functionality, primarily because the suspension with HDDA had the lowest viscosity, allowing for easier and faster levelling (Fig. 17(d)) [140]. Dufaud *et al.* studied the stereolithography of PZT components using a mixture of two different photo-sensitive resins using DuPont Somos 6100 and HDDA [142]. Despite its higher refractive index of 1.52, Somos 6100 exhibited relatively high viscosity. Therefore, a blend containing Somos 6100 and HDDA was used to enhance photopolymerization, most likely with the goal of optimizing the viscosity for improved handling and printing while retaining ideal optical properties.

In recent years, there has been a trend toward developing ceramic suspensions that use several monomers in specified ratios to achieve highest performance [139,140,142–152]. However, with the exception of a couple of studies [144,146,151], no one has truly specified the precise ratios and the reason behind such formulations to the scientific community. There might be several reasons for this, but the most significant ones could be:

Table 4
Feedstock preparation and optimized printing parameters for vat photopolymerization.

Feedstock	Particle size and morphology	Photocurable monomer	Additives	Ceramic loading	Printing parameters				Reference
					UV wavelength (nm)	Exposure time (s)	Layer height (µm)	Miscellaneous	
$BaTiO_3$	$d_{mean} = 1.27$ µm	HDDA	1-hydroxycyclohexyl phenyl ketone, Hypermer LP1, stearic acid, Triton X100, Zephrym 1000	0 – 55 vol%	350			Cured parts were dried for 24 h under UV light	[154]
PZT	$d_{50} = 5$ µm	Diacryl 101, HDDA, Somos 6100, Dupont, RPCure 200, RPC	DMPA, Phosphoric ester, Irgacure 651	40 – 83 wt%			10, 25		[142]
PZT-5H		Diacrylate	2-propanol	$\geq$ 40 vol %	260 – 550		20 – 40	Overnight drying at 50 °C	[176]
PMNT		HDDA, DPPHA	Triton X−114, Irgacure 784	40 vol%	628, 519, 462		50		[177]
PZT 5 H		HDODA, Diacrylate		38 – 40 vol%					[178]
$BaTiO_3$	100 nm	Photocurable resin SI500	Triton x−100	70 wt%					[179]
$BaTiO_3$	APS = 1 µm	Photocurable resin SI500	Phospholan PS−131, Triton x−100	25 vol%		1 – 16	20		[168]
KNN		Acrylamide monomer	Triton x−100,TPO	65 wt% (31.9 vol %)	405		20	Inert film of Polydimethylsiloxane (PDMS) was coated on the vat surface to reduce the separation force	[180]
$BaTiO_3$	500 nm			70 – 86 wt%					[181]
PZT−5A		HDDA	BYK−142, TPO	34.1 – 48.7 vol %	385				[164]
$BaTiO_3$	500 nm	HDDA, PEG(400)DA	BYK, TPO	40 vol%	405			Monomers in equal volume fraction	[146]
$BaTiO_3$	$d_{50} =$ 200 nm, 500 nm, 600 nm	PEGDA, HDDA	BYK, TPO	40 vol%			10		[147]
$BaTiO_3$	$d_{50} = 993$ nm	ACMO, PEG(400) DA, HDDA, TPGDA	Omnirad TPO, MEHQ, Triton x−100	65 – 82 wt%	405	10 – 180	30		[139]
PZT	1.5 µm	TMPTA	Triton X−100, TPO		405	10 – 60	20		[171]
PMMA	20 µm			5 – 35 wt %					
$BaTiO_3$	Micron, $d_{50} = 3.4$ µm, Submicron, $d_{50} = 1.02$ µm, Nanoscale, $d_{50} = 50 – 70$ nm	SG15 resin		70.1 wt % (30 vol %).	405	5 – 120	25, 50	Washed in absolute ethyl alcohol, Post curing 5 min in UV dryer	[159]
$BaTiO_3$	$d_{50} = 600$ nm	OPPEOA, HDDA, TPGDA, ETPTA	TPO, Solsperse 41000	30 – 40 vol%	405		25		[148]
PZT	$d_{50} = 0.452$ µm	PEGDA	BAPO, BYK−142,	80 wt%	385	10 – 100			[170]
$BaTiO_3$	$d_{50} = 136$ nm, 197 nm, 355 nm, 993 nm, 1486 nm	ACMO	Triton X−100, Acrylic block copolymer, TPO, MEHQ	80 wt%	405	10 – 30	30		[157]
BCZT	$d_{50} = 1.7$ µm	OPPEOA, HDDA, TPGDA, ETPTA	Solsperse 41000, TPO	40 vol%			25		[149]
$BaTiO_3$			DYSPERBYK−100	37.14 – 51.82 vol %	465		10		[182]
KNNLN-Er			BYK 9077, TPO	72 wt%					[183]
PZT	$d_{50} = 0.8$ µm	ETPTA, OPPEOA, TPGDA, HDDA	Solsperse 41000, TPO	40 vol%					[150]
Soluble starch				20 – 50 vol%					

(*continued on next page*)

Table 4 (*continued*)

Feedstock	Particle size and morphology	Photocurable monomer	Additives	Ceramic loading	Printing parameters				Reference
					UV wavelength (nm)	Exposure time (s)	Layer height (µm)	Miscellaneous	
PMN-PT	500 – 800 nm			77 wt%					[162]
BT templates	Length: 5 – 15 µm, Thickness: 0.5 – 1 µm			5 wt%					
$BaTiO_3$	APS = 100 nm	PEG(400)DA, HDDA	Triton X−100, TPO	62 – 77 wt%	405		40	Monomers mixed in same volume ratio	[151]
PZT	d_{50} = 0.452 µm	PEGDA	BAPO, BYK−142; PMMA	70 wt%	385	5 – 25			[174]
$BaTiO_3$	Fine, d_{50} = 149 nm, Coarse, d_{50} = 879 nm	ACMO	TPO, MEHQ, Triton X−100, UNIQ FLOW 6057, UNIQ FOAM 7032	80 wt%	405	10 – 90	30		[158]
PZT **Polystyrene**	d_{50} = 0.8 µm 3 µm, 8 µm, 16 µm	OPPEOA, HDDA, TPGDA, ETPTA	Solsperse 41000, TPO, PEG−200, PS		405		25		[152]
BCZT			Solsperse 41000, TPO	40 vol%			25		[184]
$BaTiO_3$	Micro powder, Nano powder	Acrylate-based photosensitive commercial resin	Triton X−100, TPO	20 – 50 wt%	405		25 – 100		[135]
$BaTiO_3$	600 nm	OPPEOA, TPGDA, HDDA, ETPTA	Solsperse 41000, TPO	40 vol%	405				[163]
BT platelets	Width: 5 – 20 µm, Thickness: 1 – 2 µm			5 mol%					
PZT **Polyethylene**	d_{50} = 0.8 µm	OPPEOA, HDDA, TPGDA, ETPTA	Solsperse 41000, TPO, PEG−200, Polyethylene	30 – 60 vol%	405				[172]
$BaTiO_3$	d_{50} = 200 nm	PUA, Acrylic ester, ACMO	DISPERBYK−111, TPO	65 – 80 wt%		5 – 35	20		[143]
KNN	d_{50} = 1.86 µm	HDDA, TMPTA	PEG200, Solsperse 41000, TPO	38 – 44 vol%	405		25	Monomers mixed in the mass ratio 5:4	[144]
$BaTiO_3$-$xBaSnO_3$	1.99 – 3.4 µm	OPPEOA, HDDA, TPGDA, ETPTA	TPO, Solsperse 41000	40 vol%			25		[167]
PZT	d_{50} = 3 µm	SI500		65 wt%		10	20		[134]
$BaTiO_3$		SI500		50 – 70 wt%	405	37	30		[185]
Barium acetate, titanium (IV) isopropoxide, acetic acid, acrylic acid		Ethoxylated trimethylolpropane triacrylate	TPO, Sudan Orange G		385	2	200	Samples washed with isoproponol	[175]
PZT 5 H		HDDA, PEG, Polyurethane acrylate U600, Capryl alcohol		78 – 89 wt%		10	20		[186]
$BaTiO_3$	<1 µm	Yellow dental clear	DISPERBYK−100	10 – 55 vol%	465		100		[187]
PZT855		PEGDA	Irg819	15 – 45 vol%			15		[188]
PZT **Polystyrene**	APS = 3 µm	HDDA, OPPEOA, ETPTA, TPGDA	Solsperse 41000, PEG−200, TPO				25		[145]
$BaTiO_3$	d_{50} = 500 nm	HBA, PEGDA, HDDA, TMPTA	TPO, KOS110	40 vol%	405		10, 80		[140]
PZT	d_{50} = 0.452 µm	PEDGA	BAPO, DISPERBYK−142	70 wt%	405	10	10		[189]
PMMA	d_{50} = 5.86 µm								
$BaTiO_3$	500 nm			75 – 85 wt%	405	9 – 27	30		[190]
Sm-PMN-PT	APS = 0.6 µm, 1.5 µm, 2.5 µm	HDDA, ACMO, OPPEA, PPTTA	PPG, POE, TPO, DISPERBYK−180	40 vol%	405	8, 30	25		[141]
BCZT		HDDA	TPO, DISPERBYK−110	45 – 55 vol%			25		[165]

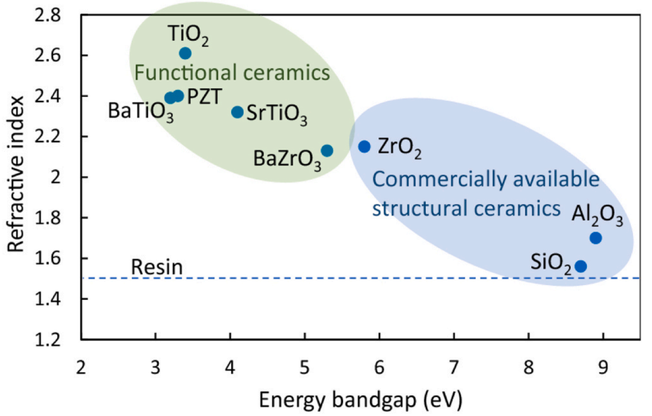

Fig. 16. Correlation between the energy bandgap and refractive index for different ceramic materials. The materials highlighted in green are of particular interest. The dashed line indicates the standard refractive index for a typical commercial resin [135]. [135], Open access article distributed under the terms of the Creative Commons CC BY license.

(i) increasing the functionality to reduce the exposure time or the radiation energy required for curing,
(ii) decreasing the viscosity,
(iii) decreasing Δn by increasing the RI of the photocurable resin

Polyfunctional monomers such as dipentaerythritol penta/hexa-acrylate (DPPHA), or ethoxylated trimethylolpropane triacrylate (ETPTA) have multiple cross-linking sites when compared to HDDA or PEGDA which possess only two active cross-linking sites [153]. Such multiple-cross linking sites enable to form extensive and interconnected polymer networks, leading to enhanced green strength. Monomers such as HDDA can be used as a diluent because of their relatively low viscosity. Monomers with considerably higher RI, such as ACMO and oligo (propylene glycol) ethoxy triacrylate (OPPEOA), decrease the Δn of the overall ceramic suspension and this leads to a higher curing depth.

2.3.3. *Effect of particle size*

The particle size has a strong influence on the curing depth and the viscosity of the formulated suspension. It is quite evident from Eq. 10, that the curing depth increases with d_{50}. By maintaining a constant volume of solid particles, replacing fine particles with coarse particles reduces the scattering centres, leading to an increasing curing depth and a reduction in the over curing width. In this context, Jang *et al.* measured the reflectance of BT particles of two different sizes ($d_{mean} = 1.27$ μm and

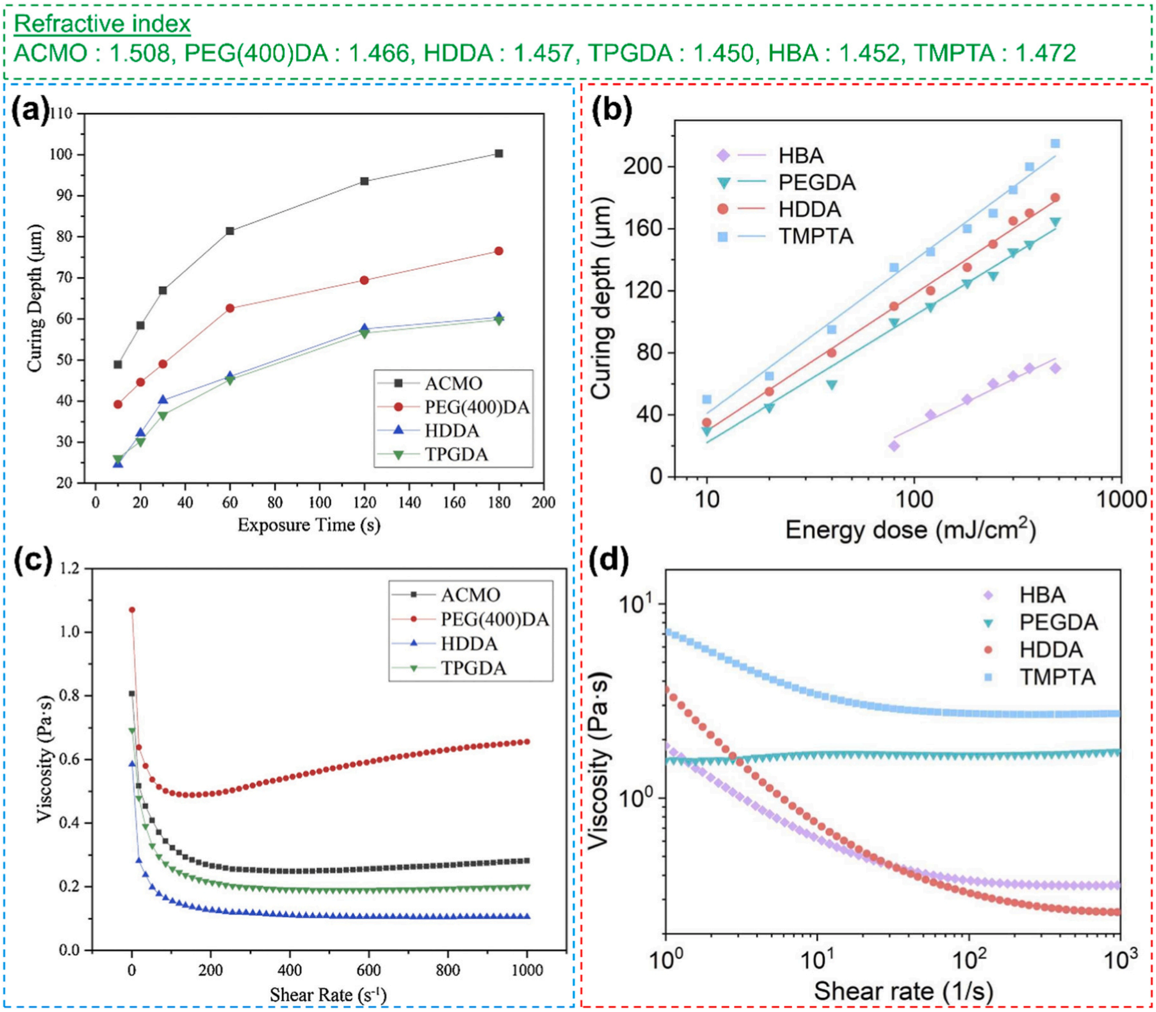

Fig. 17. Effect of the functionality and viscosity of different monomers for choosing the optimal one for the printing process. Curing and rheological properties of formulated with different monomers: Variation in curing depth as function of (a) Exposure time [139], and (b) Energy dose [140]. (c-d) Variation of viscosity with shear rate [139,140].
Reproduced from Ref.: (a, c) [139], and (b, d) [140] with permission from Elsevier

2.09 μm) in HDDA suspensions at varying solid loadings (10 vol% and 30 vol%) and reported that suspension with higher ceramic content and finer particle size exhibited increased reflectance due a large scattering centres, as shown in Fig. 18(a) [154]. Further, the suspensions with larger particle sizes exhibited a greater curing depth compared to suspensions with smaller particle sizes [141]. This was additionally corroborated by simulations conducted by Qin *et al.*, which predicted that finer particles would have greater scattering angles and lower penetration depths [155]. Conversely, fine particles can result in weak interfaces between layers, which becomes more pronounced after debinding and sintering [141].

Chen *et al.* compared the rheological and curing characteristics of BT suspensions (40 vol%) prepared with three different particles sizes (d_{50}) of 200, 500 and 600 nm [147]. The study revealed that the suspension containing coarse powder had the lowest viscosity, which is advantageous in terms of self-levelling and recoating during the printing process. The suspensions with finer particles exhibited increased viscosity, due to high van der Waals forces causing them to strongly attract and clump together resulting in agglomeration (Fig. 18(b)). Nevertheless, all of the suspensions exhibited shear-thinning behaviour with viscosities well below 3000 mPa·s. This value is usually considered as an upper limit for a printable resin using conventional equipment [156]. Furthermore, the curing depth was analysed for all the suspensions and fitted according to Jacob's equation [136]:

$$C_d = \quad D_p \ln\left(\frac{E_0}{E_c}\right); D_p = \quad \frac{2d}{3\varnothing Q} \tag{11}$$

where D_p is the attenuation length, d is the average particle size, $\varnothing$ is the volume fraction of solids and $\widetilde{Q}$ is the scattering efficiency. It was found that the curing depth increased with the applied energy dose (Fig. 18

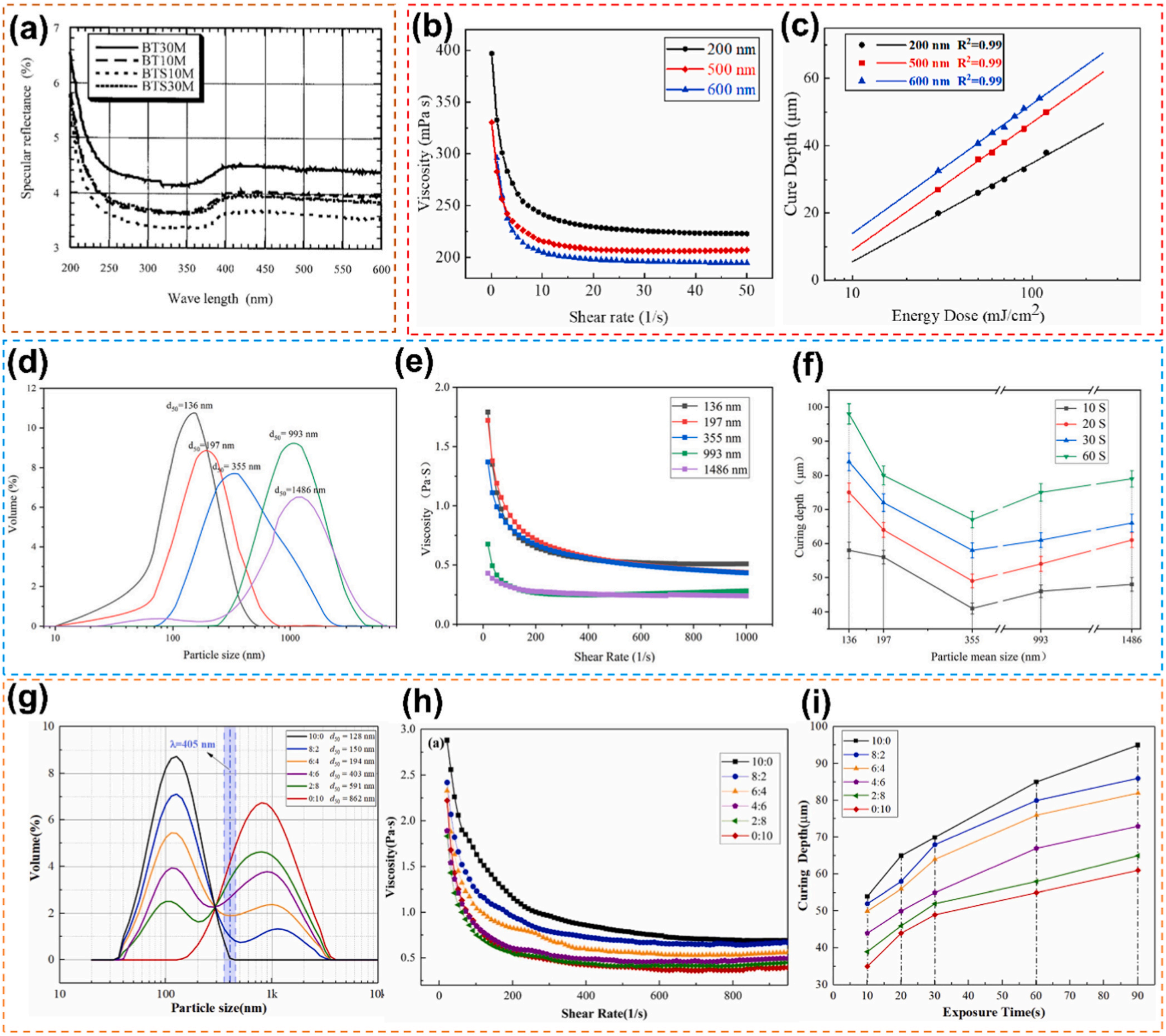

Fig. 18. Effect of the particle size and distribution on the viscosity and the curing behaviour. (a) Specular reflectance spectra of uncured BT-HDDA suspensions with mean particle sizes of 1.27 μm (denoted by BT) and 2.09 μm (denoted by BTS), with 10 vol% and 30 vol% ceramic powder [154]. (b) Viscosity as a function of shear rate, and (c) Dependence of curing depth and energy for different BT particle sizes [147]. (d) Particle size distribution, (e) Variation of viscosity, and (f) Curing properties of slurries containing ceramic powders with mean particle sizes of 136 nm, 197 nm, 355 nm, 993 nm, and 1486 nm [157]. (g) Particle size distribution, (h) Evolution of viscosity, and (i) Curing depth of BT ceramics in slurries at different particle size mass ratios [158].
Reproduced from Ref.: (a) [154], and (d-e) [157], with permission from John Wiley and Sons. (b-c) [147], and (f-h) [158], with permission from Elsevier.

(c)), which in accordance with Eq. 11. As a rule of thumb, the applied energy dose should be selected so that the cured thickness is at least double the slicing thickness to ensure better bonding between the layers.

Additionally, other investigations have also shown a similar relationship between viscosity and particle size [135,157,158]. In a recent study Liu *et al.* formulated inks with varying particle sizes (Fig. 18(d)), showing that the viscosity of 80 wt% BT decreased as the particle size increased to approximately 1 μm [157]. Further increasing the particle size to around 1.5 μm, the viscosity values almost saturated, indicating that particle size beyond this threshold value has no influence on the viscosity (Fig. 18(e)). Further, the relation between the curing depth and particle size was investigated for different exposure times. The results revealed that the curing depth increased with the exposure time. From Eq. 12, it can be observed that the curing depth is dependent on the median particle size and the scattering efficiency ($\widetilde{Q}$), which is related to the particle spacing S (nm) and the UV wavelength λ (nm) using the equation [138]:

$$\widetilde{Q} \propto \frac{S}{\lambda} \tag{12}$$

The results were quite surprising. With increasing particle size, the curing depth first decreased and then increased (Fig. 18(f)). However, one would expect that the curing depth should increase with increasing particle size. This is only valid for suspensions with relatively low solid loadings [156]. For highly concentrated ceramic slurries, the curing depth is strongly affected by the ratio of the inter-particle distance to the wavelength of light used for curing. When the particle size is smaller than the wavelength, typically $\lambda = 405$ nm, the particles will tend to agglomerate due to strong inter-particle forces. This suggests that the value of $\widetilde{Q}$ decreases further with decreasing particle size and is inversely related to the curing depth. In other words, $\widetilde{Q}$ increases with increasing particle size and the curing depth decreases. On the other hand, when the particle size is greater than 405 nm, the tendency to agglomeration decreases. Hence the inter-particle spacing increases and the particle characteristics become dominant compared to scattering. As a result, the curing depth increases. However, despite the fact that the curing depth improves as the particle size exceeds 405 nm, it does not exceed the curing depth achieved with smaller particles under identical exposure duration. For instance, the curing depth for suspensions containing 1.5 μm particles was 80 μm, whereas that with 136 nm particles was 100 μm, with both suspensions being exposed for 60 s.

Liu *et al.* prepared ceramic suspensions by incorporating two distinct BT powders with average particle sizes (d_{50}) of 149 and 879 nm in different ratios (Fig. 18(g)), respectively, at a ceramic loading of 80 wt% [158]. The curing depth (and viscosity) was strongly related to the particle size; both of them decreased with increasing amount of coarser particles (Fig. 18(h-i)). This is due to the fact that when the weight proportion of the coarser particles increased, the proportion of particles with sizes near the UV wavelength also increased, as marked in Fig. 18(g). Consequently, this leads to an increase in scattering and a reduction in the curing depth. The closer the particle size is to the UV wavelength, the greater the scattering.

Sotov *et al.* prepared ceramic suspensions with 70.1 wt% of BT using different particle sizes (micron-sized = 3.4 μm, sub-micron = 1.02 μm, nano-sized = 50 – 70 nm) [159]. The viscosity of the suspensions with micron and sub-micron sized particles were well within the widely accepted value of 3000 mPa·s. In contrast, the suspension with nano-particles possessed extremely high viscosity values. Due to the high viscosity, recoating of the slurry using the scraper blade resulted in an uneven surface. As a result, such suspensions were ruled out for further use. Moreover, the suspensions prepared with micron-sized particles ($d_{10} = 0.1$ μm, $d_{50} = 3.4$ μm, $d_{90} = 25.4$ μm) resulted in delamination of the printed samples. This was attributed to the presence of larger particles which lead to weak adhesion of the layers. The suspensions with sub-micron sized particles were the best in terms of printing accuracy.

2.3.4. Platelets orientation

Generally, textured piezoceramics exhibit better properties when compared to the non-textured counterparts and are obtained by a process called templated grain growth. It is to be noted that platelet alignment and induced grain-growth by thermal treatment are the two important factors that determine the final texture. However, the main concern here is the alignment of these platelets during the printing process.

The platelet alignment during the printing is a crucial step that influences the final degree of texture. Such texturing can be only obtained with printers that employ a doctor blade to level-off the slurry after each layer has been printed. The doctor blade aligns the platelets by exerting sufficient shear forces. The extent to which texturing can be achieved in the green bodies depends on the ratio of the pressure-driven forces to the slurry-driven force and it can be written as [160,161]:

$$\Pi = \frac{\Delta P H^2}{2\mu t_{blade} U} = \frac{pressure - driven\ forces}{slurry - driven\ forces} \tag{13}$$

$$\Delta P = \rho_{slurry} g H_{slurry} \tag{14}$$

where ΔP is the pressure exerted by the slurry head, H is the blade gap, μ is the slurry viscosity, t_{blade} is the thickness of the doctor blade, U is the carrier velocity, ρ_{slurry} is the density of the slurry, H_{slurry} is the height of slurry. A lower value of this ratio (Π) yields a better alignment. One can clearly observe from Eq. 13, that the alignment is completely dependent on the printing parameters, provided that the platelets concentration is sufficient.

Zhang *et al.* prepared ceramic suspensions using PMN-PT ceramics with 5 wt% of (001)-BT platelets to provide sufficient evidence that stereolithography is similar to the tape casting process, but with more benefits associated [162]. In order to minimize the ratio as mentioned in Eq. 13, a ceramic loading of 77 wt% with a blade gap of 30 μm was chosen as the best parameter. The platelet alignment in the polymer-ceramic matrix was confirmed by cross-sectional SEM observations which revealed an average deviation angle of 11.77°.

In a more recent study, Du *et al.* employed different amounts of <001> oriented BT platelets in a BT slurry with solid loadings of 40 vol %. 5 mol% of platelets were chosen as the optimal concentration [163]. Further increasing platelet concentration hindered the parallel alignment of the platelets. The height of the scraper blade was determined to be 100 – 125 μm. Increasing the height of the scraper blade subsequently decreased the shear forces acting on the platelets. It is important to mention here that the optimized concentration was decided after analysing the X-ray diffraction (XRD) pattern of the sintered components produced with different processing parameters.

2.3.5. Effect of ceramic loading

Higher ceramic loadings in the slurry ensures better properties in terms of better density, minimized residual porosity and reduced defects after the binder burn out and sintering process. In general, the viscosities of ceramic suspensions increase with increasing ceramic loading and their shear-thinning behaviour becomes more pronounced, as evidenced by numerous studies [135,142,144,159,164,165].

In a recent study, Stefan *et al.* characterized the rheology of slurries with different ceramic content of BT. Up to solid loadings of 40 vol%, the viscosities remained unaffected by the shear rates (Fig. 19(a)), suggesting a strong Newtonian behaviour ($n = 1$) [135]. This was further confirmed by determining the power law parameter (n), which resulted in the range of 0.95 – 1.08, which is close to 1. With further increasing the solid loading to 45 vol%, the viscosity drastically increased by around two folds and displayed a strong shear thinning behaviour. However, since the viscosity of all the prepared ceramic suspensions were well below the standard value of 3000 mPa·s [156], it was

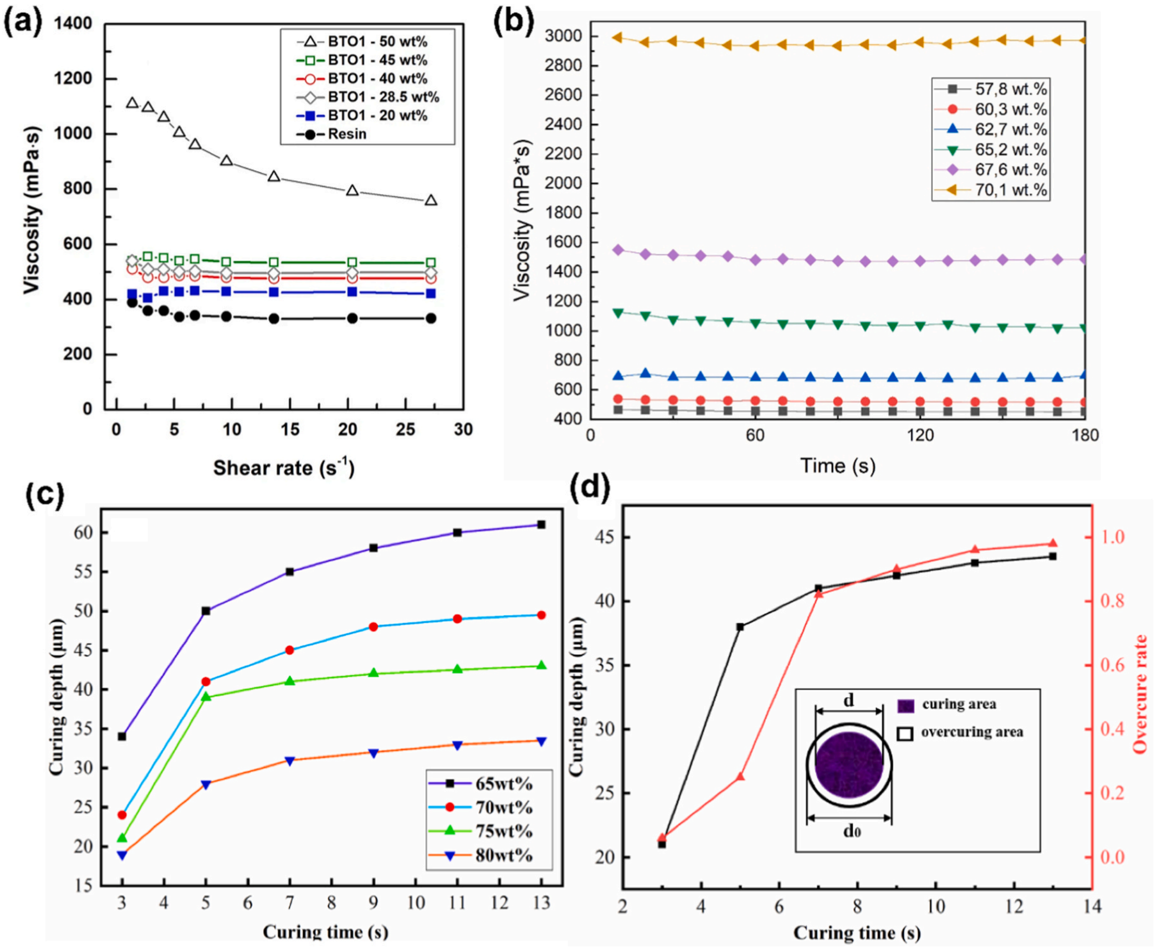

Fig. 19. Effect of the ceramic loading on the viscosity and curing depth. (a) Viscosity as a function of shear rate for ceramic resins containing different weight fractions of BT powder [135]. (b) Evolution of the ink viscosity with different BT solid loadings over varying measurement times, exhibiting the stability [159]. (c) Variation of the curing depth as a function of the curing time for varying ceramic loadings [143]. (d) Curing depth and over-curing rate as a function of curing time for a ceramic loading of 75 wt% [143].
(a) [135], (c-d) [143] Open access article distributed under the terms of the Creative Commons CC BY license. Reproduced from Ref.: (b) [159], with permission from Elsevier.

considered suitable for printing.

In addition to the viscosity, the stability of the slurry is important which needs to be taken care of. In an ideal situation, the viscosity should remain constant as a function of time. This is in good agreement with the results reported by Sotov *et al.* (Fig. 19(b)) [159]. This means that the ceramic particles are well dispersed and there is no sedimentation in the prepared ink. However, the results reported in Fig. 19(b) describe the stability only for a short period of time. For low-cost printers, a scraper blade may not be present and, in that case, it is advisable to assess the stability of the slurry over an extended duration of time.

As indicated by Eq. 11, the curing depth is inversely proportional to the volumetric ceramic content in the suspension. The greater the ceramic content, the more the particles act as scattering centres for light. This was also demonstrated by reflectance measurements conducted by Jang *et al.* on suspensions containing 10 vol% and 30 vol% of piezoceramic particles (Fig. 18(a)) [154]. Conversely, slurries with extremely low ceramic content exhibit an increase in curing depth. However, this comes at the expense of post-processing complexities, such as high shrinkage and cracking after the thermal treatment. Note that the scattering causes the UV radiation to propagate in a different direction. This results in an increasing curing width perpendicular to the incident light and in an decrease in the curing depth in the direction of the incident light [166]. The best compromise is to optimize the balance between ceramic content and the curing time in order to reduce the over-curing width. It is important to note that the curing depth determines the vertical resolution, while the curing width determines the lateral resolution. Moreover, the additions of dopants significantly affect the physical properties of the ceramic powders such as the RI and density [167]. So, it is necessary to understand the curing behaviour of such doped powders for reliable printing.

In this context, Zhang *et al.* investigated the curing depth and over-curing rate as a function of ceramic loading and exposure time [143]. It was found that curing depth increased with exposure time and with prolonged exposure the over-curing width also increased (Fig. 19(c-d)). The best compromise was achieved by using solid loadings of 75 wt% with a curing time of 5 s. This resulted in the desired curing depth with decreased width of over-curing. Similar reports on the effect of curing depth by varying the ceramic loadings has been reported elsewhere [135,144,168].

2.3.6. *Effect of dispersant concentration*

Dispersants are often used for several reasons, including the stabilization of ceramic suspensions, breaking up of agglomerates and the prevention of sedimentation. In general, the amount of dispersant should be proportional to the surface area of the ceramic powders. This is because adsorption is a surface effect. However, the concentration should be adjusted when the volumetric fractions of ceramic powder increases.

In this regard, Wang *et al.* thoroughly investigated the viscosity of 15 vol% BT with concentration of dispersant ranging from 0.3 wt% to 8 wt% [146]. The optimal dispersant concentration was reported to be 1 wt% (Fig. 20(a)). There usually exists an optimum concentration of the dispersant that leads to the lowest viscosity. Inadequate amount of dispersant may result in insufficient covering of particle surfaces, hence leading to agglomeration and high viscosity. On the contrary, excess dispersant is reported to degrade the rheological characteristics of the suspension. The excess dispersant moves freely inside the slurry and leads to depletion flocculation, a condition in which the inter-particle distance decreases, thereby enhancing the agglomeration and viscosity of the suspension. Several researchers have optimized the dispersant concentration by carefully observing the variation of viscosity at higher shear rates ($\geq$40 s^{-1}) [144,149,169].

Kim *et al.* reported a detailed investigation on the influence of dispersant concentration (1 wt%, 2 wt%, 3 wt%) on the rheological behaviour and the curing properties of a PZT suspension [170]. Initially, Fourier transform infrared spectroscopy (FTIR) analysis revealed that the optimum dispersant concentration was either 2 wt% or 3 wt% based on the degree of adsorption of the dispersant to the ceramic particles. The flow curves revealed that the suspension with 2 wt% of dispersants had the least viscosity with strongest shear-thinning behaviour ($n = 0.19217$ compared to 0.46280 for 3 wt%. and 0.82873 for 1 wt%) (Fig. 20(b)). Further, the dispersion stability of the suspension was measured by a dispersion stability analyser. Since sedimentation is most favoured for the particles in the upper part of the size scale, this region was considered for the stability measurements. The backscattering intensity as a function of time (72 h) decreased for all suspensions, indicating that some sort of sedimentation occurred (Fig. 20(c)). The suspensions with 1 and 3 wt% of dispersant exhibited almost similar backscattered intensity (≈ -46), with the latter exhibiting a non-linear/abrupt decrease. In contrast, the suspension with 1 wt% of dispersant exhibited a value of −35. This lower value indicates that the sedimentation rate was lower when compared to the others. The dispersion stability was further quantified using the Turbiscan stability index (TSI). These results emphasize that the suspension with 2 wt% of dispersant was the best overall choice.

In further experiments, the curing ability was measured using a photo-calorimetry and the results revealed that the suspension with 2 wt % dispersant exhibited the highest polymerization rate of 0.085 s^{-1} and a maximum conversion of 43 % among all suspensions (Fig. 20(d)). In order to analyse the effect of the dispersant on the curing depth, a circle of 1000 μm was used as a reference. The curing depth increased with applied energy. However, no correlation between dispersant concentration and curing depth could be identified at this time. This can be due to differently dispersed or flocculated states of the powder. The surface of the printed circles was investigated with the help of SEM (Fig. 20(e)) and the suspension with 2 wt% of dispersants had the smallest average particle size of 352 nm. In comparison, for the suspensions containing 1 and 3 wt% dispersants the smallest average particle size was 675 and 553 nm, respectively. This variation in the average particle size has a considerable impact on the surface roughness of the printed component. The samples were quantified by two roughness parameters namely, R_a and S_a. Both parameters exhibited similar trends, even though some difference existed in the numerical value. The most significant outcome was that the solution containing 2 wt% of dispersants, regardless of the curing parameters, showed the lowest levels of R_a and S_a, corresponding to a better surface finish. By correlating both the curing depth and the surface roughness, a revised curing depth parameter ($C_d{}'$) was plotted (Fig. 20(f)). The findings indicate that suspensions containing 2 wt% and 3 wt% of dispersants were suitable for achieving a high curing depth, hence enhancing inter-layer adhesion. The revised curing depth curve was fitted with the Jacobs equation (Eq. 11), in order to calculate D_p and E_c. Interestingly, the suspension with 2 wt% of dispersants had the lowest D_p and E_c values. The decrease in the depth of curing may be related to the comparable values of the wavelength of UV radiation used for curing (385 nm) and the particle size (352 nm) of the suspension with 2 wt% of dispersants. The scattering effect is prominent at such conditions and can decrease the curing depth drastically. However, having the smallest E_c is desirable as it suppresses the scattering and leads to a high printing accuracy, with decreased value of over-curing width. Finally, the over-curing width measurements pointed out that the suspension with 2 wt% of dispersants showed the lowest value (Fig. 20(g)).

2.3.7. Effect of photo-initiator (PI) concentration

Low molecular weight organic photo-initiators are sensitive to the UV light and produce free radicals that can attack the functional sites of the photocurable resins or monomers. Most of the acrylate monomers are activated using free radical photo-initiators (PI). The amount of PI used should be in proportion to the total amount of monomer used in the formulation. For the best curing properties, an optimum amount of PI is desired; deviation from this amount leads to degradation in the curing ability.

The inherent curing ability of the ceramic suspension is dictated by the amount of PI present in the suspension. Liu *et al.* investigated the effect of using different PI concentrations (TPO: 1 wt%, 2 wt%, 3 wt%, 4 wt%, 5 wt%) on the curing depth of suspensions containing 40 vol% of BT [148]. An energy dose of 160 mJ/cm^2 was chosen since the curing depth (50 μm) was at least double the slicing thickness (25 μm). Initially, the curing depth increased with the TPO concentration up to 3 wt%. However, beyond such optimum concentration, the cured depth decreased (Fig. 21(a-b)). This is in good agreement with a recent study [167]. The TPO absorbs the incident UV light and generates free radicals. The higher the concentration of TPO, the more radicals are generated, thereby increasing the curing depth until the optimum concentration is reached. On further increasing the concentration, the freely moving TPO in the slurry can absorb the UV radiation, generating more free radicals that can lead to a chain termination reaction between the free radical and the acrylate monomer, or decrease the reactivity by recombination of the free radicals. As a result, a decrease in the curing depth was observed on using excessive PI.

Almost similar observations were reported by He *et al.* for a 40 vol% BCZT suspension [149]. However, beyond the optimum concentration of TPO (3 wt%), the curing depth did not exhibit any dependency on the TPO content (Fig. 21(c)). The variation of the curing depth with the applied energy dose was plotted to understand the D_p and E_c (Fig. 21(d)). The slope of the curves is essentially identical, suggesting that the photo-initiator concentration has little impact on the attenuation length, D_p. However, with the increasing concentration of TPO, E_c decreased from 5.58 to 5.10 mJ/cm^2, suggesting a lower energy dose is required to initiate polymerization. Finally, a TPO content of 3 wt% with an energy dose of 40 mJ/cm^2 were chosen as the optimum values for a layer thickness of 25 μm. In a recent study, Pan *et al.* reported that the optimum TPO concentration for a suspension containing 42 vol% of KNN was 1.5 wt% with an exposure energy of 29 mJ/cm^2 for fabricating samples with a layer thickness of 25 μm [144]. In conclusion, high PI concentration can lead to an increasing over-curing width and low printing accuracy.

2.3.8. Effect of using additives with low RI

It is clear that ceramic suspensions containing piezoceramic powders suffer from low curing depth and severe scattering because of the higher refractive index (RI) of the particles with respect to that of the most commonly used acrylate monomers. One effective way to solve this issue is the addition of materials with low RI and high UV absorptivity to the suspensions. Replacing the piezoceramic powder by materials such as polystyrene (PS), polyethylene (PE), polymethyl methacrylate (PMMA) and soluble starch (SS) will decrease Δn^2 in Eq. 10, leading to enhanced

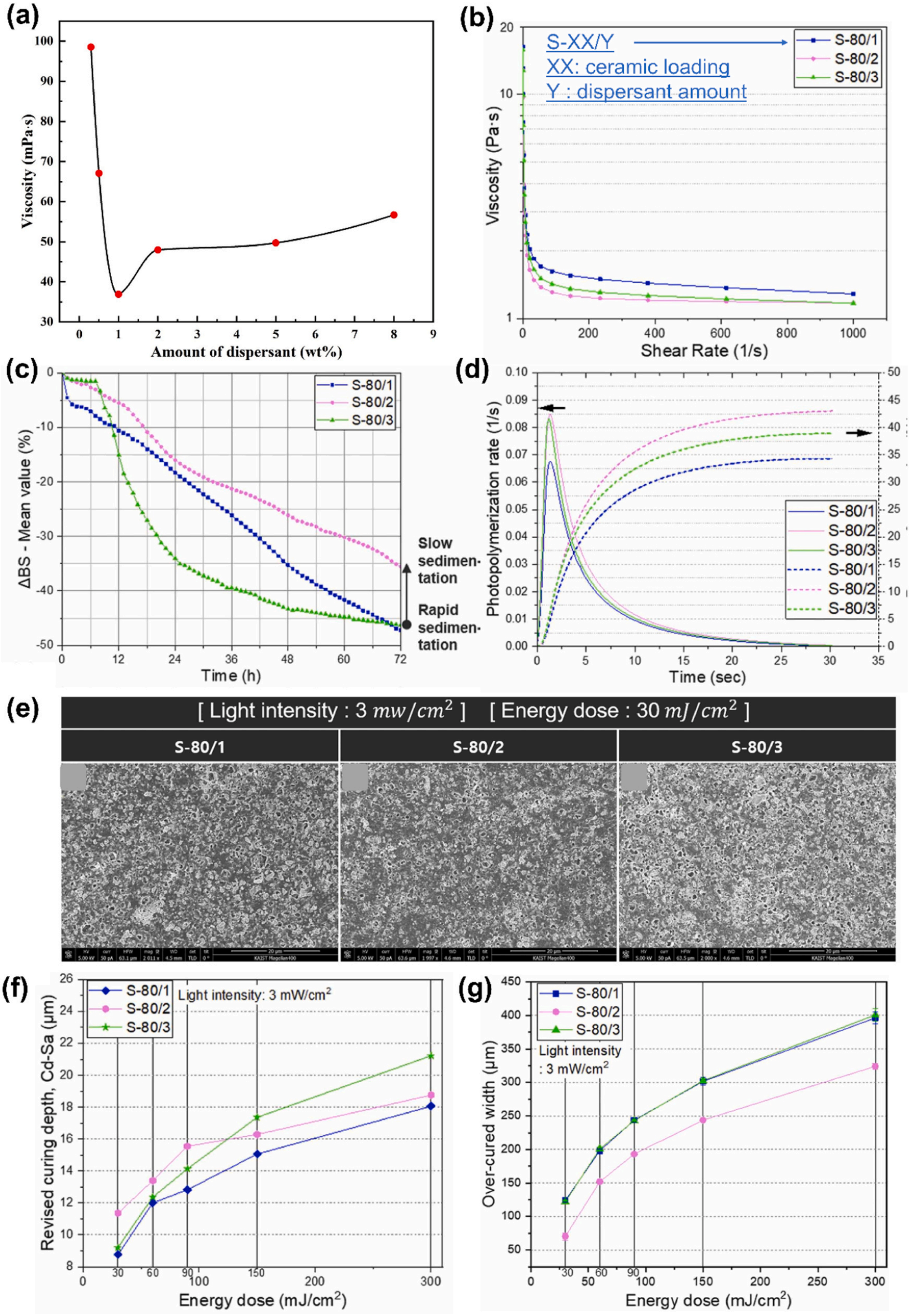

Fig. 20. Influence of the amount of dispersant on the rheological properties and curing behaviour. (a) Variation of the apparent viscosity of ceramic suspensions with the dispersant concentration at a shear rate of 46.5 s^{-1} [146]. In-depth analysis of different amount of dispersant concentration in 80 wt% ceramic loaded ink [170]: (b) Rheological behaviour of ceramic suspensions with varying dispersant concentrations. The number (1, 2, 3) denotes the amount of dispersant in wt%. (c) Sedimentation properties of ceramic suspensions measured over different time periods. (d) Curing characteristics of ceramic suspensions, including conversion profiles and photopolymerization rates for different formulations under a reference light intensity. (e) SEM images showing the surface morphology of components produced at a light intensity of 3 mW/cm² and an energy dose of 30 mJ/cm². (f) Revised curing depth ($C_d - S_a$) as a function of energy dose. (g) Over-curing width of the cured suspensions with varying energy dose.

Reproduced from Ref.: (a) [146], and (b-g) [170], with permission from Elsevier.

curing depth. In contrast, a considerable amount of porosity prevails after the thermal treatment. This potentially decreases the piezoelectric characteristics of the sintered ceramic.

In this context, Hu *et al.* combined micro-stereolithography (μSL) with the burnable plastic sphere (BURPS) technique to fabricate porous PZT ceramics [171]. Spherical PMMA particles with an average size of 20 μm were mixed in different weight fractions (5–35 wt%). The addition of the PMMA particles was found to increase the curing depth C_d (Fig. 22(a)). Similar variations of curing depths as a function PE content were also reported by Liu *et al.* (Fig. 22(b)) [172]. The authors also revealed that when the PE content was high (60 vol%), it can induce an inhomogeneous distribution of the PE particles due to increased viscosity. Therefore, an optimum concentration of these materials has to be used to have a balance between the density, porosity and piezoelectric properties.

Liu *et al.* studied the effect of incorporation of SS (20 – 50 vol%) to a ceramic suspension containing 40 vol% of PZT powders [150]. The authors reported that it was impossible to print without the use of the starch and that its addition significantly increased the curing depth and the printing accuracy. However, the inclusion of the starch granules led to an irregular and uneven surface finish due to the presence of larger particles. From the cross-sectional SEM image as shown in Fig. 22(c-f), the individual layers after printing can be easily identifiable when the starch content was at a volume fraction of just 20 %. With a subsequent increasing starch concentration, the inter-layer bonding increased. This indicates the positive outcome of the addition of the starch, however at the cost of the density and functional properties (as discussed later in Section 3.2).

Liu *et al.* reported the effect of using various PS particles (3 μm, 8 μm, 16 μm) in a photocurable resin with PZT powder [173]. The curing depth was found to be in proportion to the polystyrene particle size. This is because of their relatively low RI and higher particle size compared to PZT ($d_{50} = 0.8$ μm). The surface morphology and the cross-section of the printed samples exhibited some noticeable features. The roughness increased with the particle size of the PS. The cross-section of the printed samples with PS particles of 16 μm exhibited delamination and cracks, probably due to inhomogeneous mixing (Fig. 22(h)). The sample produced using finer PS particles had a homogeneous distribution of the PS particles, with better inter-layer bonding (Fig. 22(g)). A similar conclusion was also reported elsewhere [145].

For ceramic suspensions containing both pore-forming agents and ceramic particles, the scattering behaviour should also be affected by the particle size and distribution of the ceramic particles (CPs) or PFAs (Pore Forming Agents) and difference in dimensions of the PFAs and CPs. In this regard, Kim *et al.* investigated the rheological and photocurable characteristics of a 70 wt% PZT ($d_{50} = 0.452$ μm) suspension containing 3.5 wt% of PMMA ($d_{50} = 5.86$ μm) [174]. Three ceramic suspensions were prepared by using distinct ball milling procedures, resulting in variations in the size of ceramic particles (fine, coarse, medium), as reported in Fig. 23(a). In general, the viscosity of a suspension increases

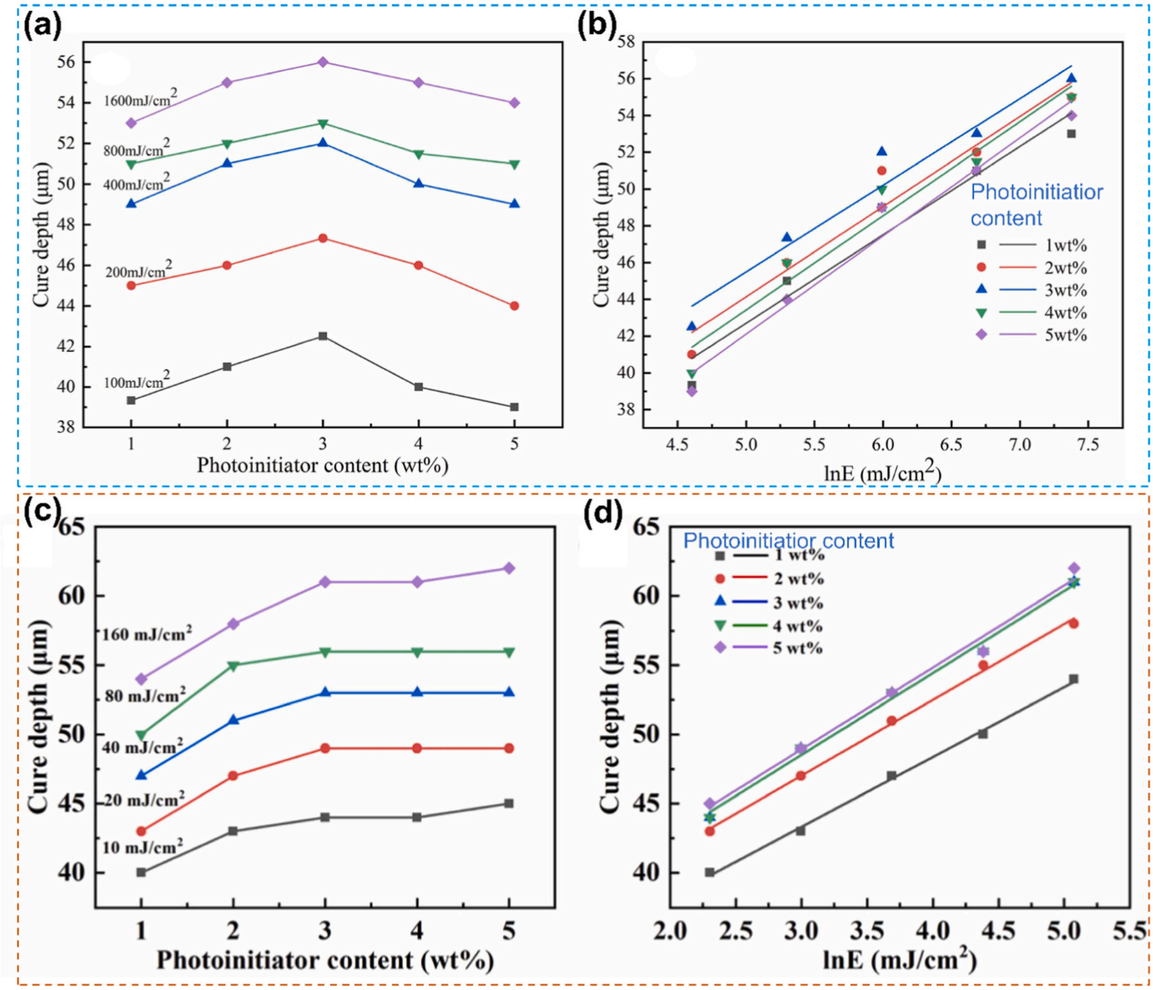

Fig. 21. Effect of the photo initiator concentration on the curing properties. Variation of the curing depth as a function of the (a, c) photo initiator content and (b, d) applied energy dose [148] [149].
Reproduced from Ref.: (a-b) [148], and (c-d) [149], with permission from Elsevier.

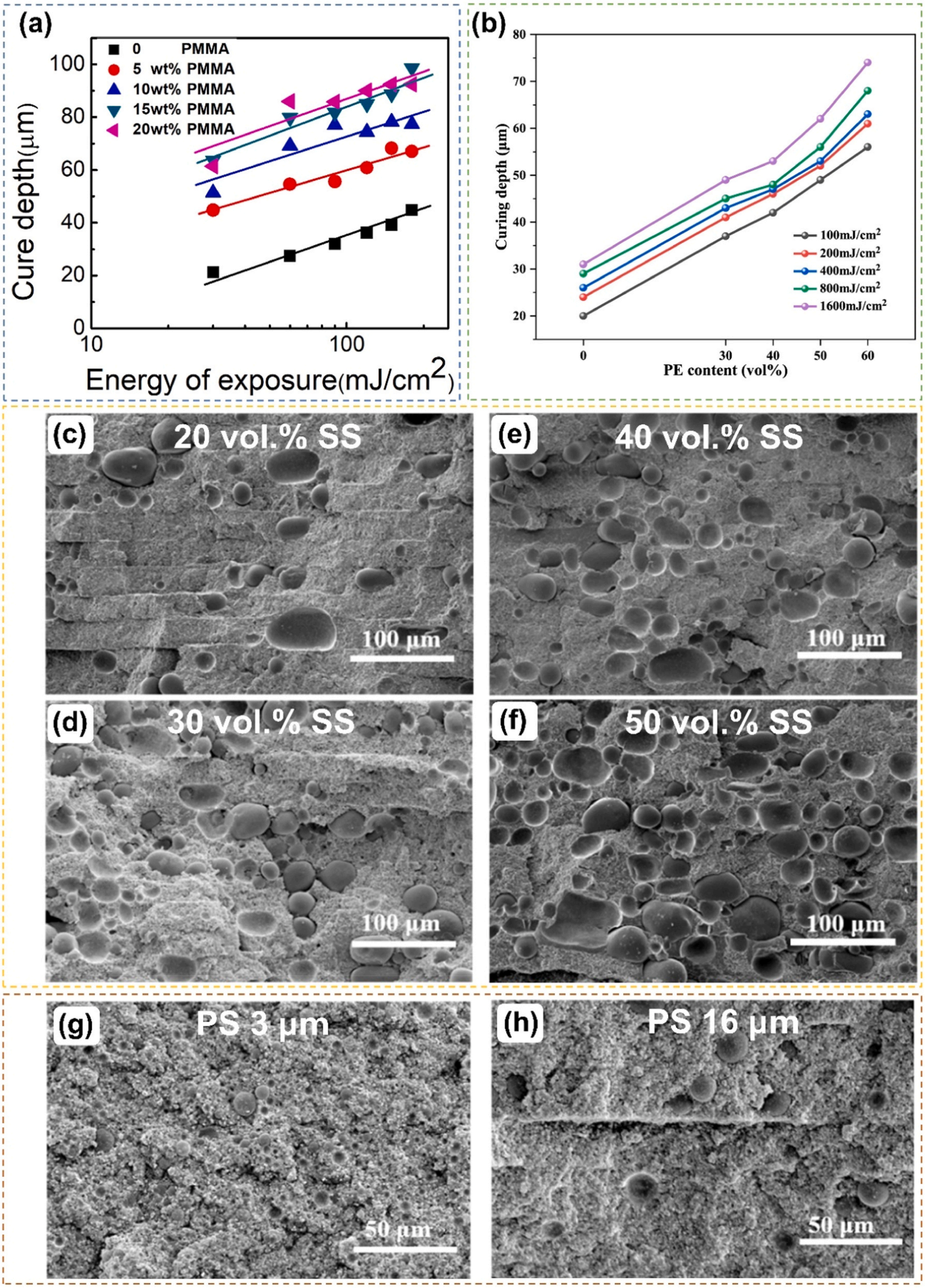

Fig. 22. Effect of the pore forming additives (PFAs) on the curing behaviour. (a) Curing depth as a function of energy dose with varying concentrations of PMMA (Polymethyl Methacrylate) [171]. (b) Curing depth variation as a function of PE content (Polyethylene) content and applied energy dose [172]. Cross-sectional SEM micrographs of PZT green parts with different (c-f) amount of soluble starch (SS) content [150], and (g-h) PS (polystyrene) particle size [173].
Reproduced from Ref.: (a) [171], (b) [172], (c-f) [150], and (g-h) [173], with permission from Elsevier.

with a decrease in the particle size. This is valid for a monomodal particle size distribution. In this case, the ceramic suspensions were bi-modal because of the size difference between the CPs and PFAs. Therefore, the suspension exhibited quite unusual viscosity dependence with the shear rate (Fig. 23(b)). The viscosity increased with an increasing ceramic particle size. In the case of fine CPs, the particles can easily fit into the voids generated by the packing of the PFAs and as a result the liquid resin can escape easily from those voids resulting in an increased amount of mobile resin and enhancing the flow behaviour. As the size of the CPs increase, it can no longer get into the voids and the liquid resin is trapped in those voids. Hence, the viscosity increases as the size of the CPs approaches the size of the PFAs. The curing behaviours of the suspensions were in good agreement with the previously reported literature. C_d increases with increasing particle size, the energy

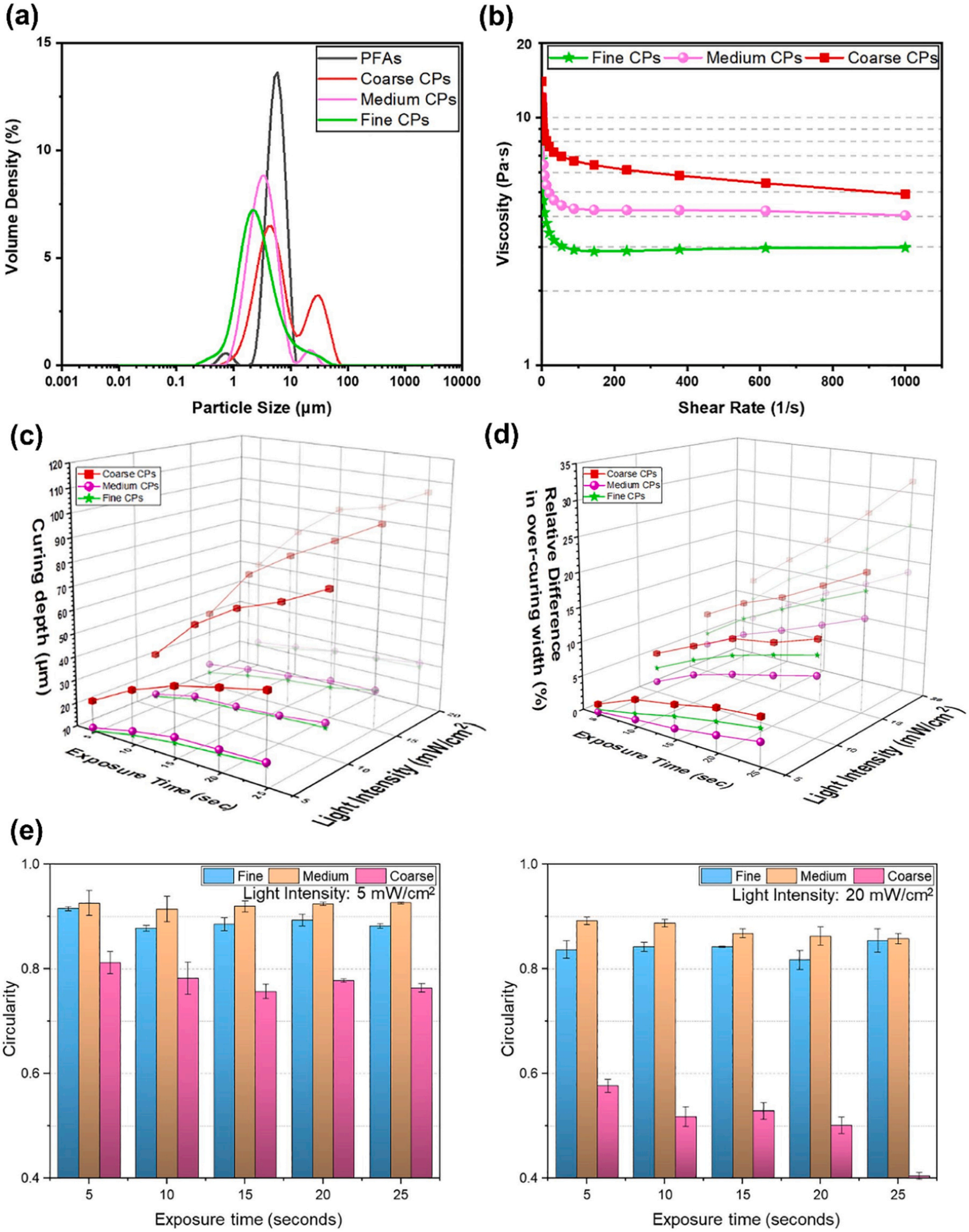

Fig. 23. Effect of the different ceramic particles (fine, coarse, and medium) in combination with PFAs leading to distinct particle size distributions and its impact on the rheological and curing ability [174]: (a) Particle size distribution for both ceramic particles (CPs) and pore-forming agents (PFAs), (b) Rheological properties of the suspension, (c) Curing depth (C_d) and (d) Over-curing width measurements, plotted against process parameters such as light intensity and exposure time, and (e) Analysis of circularity from laser confocal microscope images under different conditions of different light intensities.
Reproduced from Ref.: (a-e) [174], with permission from Elsevier.

dosage and the exposure time (Fig. 23(c)).

Furthermore, the scattering phenomenon induced by the ceramic particles is always reflected in the form of over-curing width. This was visualized by printing a circular pattern with all the ceramic suspensions at different intensities and exposure times. The suspension with the fine and medium sized ceramic particles exhibited uniform and isotropic solidification around the periphery. In contrast, the suspension with the coarse particles showed uneven and anisotropic solidification with irregular protrusions. These topological differences point to a difference in the light field distribution with particle size. Simulations performed by Qian *et al.* revealed that the over-curing width increases with the particle size [155]. However, in this study the observed trend was somewhat different and according to the following order: Coarse > Fine > Medium (Fig. 23(d)). For the fine and medium sized particles, the authors tried to correlate the observed trend for over-curing with the scattering efficiency $\widetilde{Q}$ (Eq. 12), however, no justification was found for the coarse particles. It was also reported that the over-curing width increased with increasing exposure time and energy. Further, circularity measurements were carried out to quantify the deviation. Suspensions with fine and coarse particles exhibited better circularity than the coarse ones (Fig. 23(e)). However, with increasing light intensity, the circularity values decreased. The surface roughness measurements revealed that the suspension with the coarse ceramic particles exhibited the roughest surface due to non-uniform packing density. Finally, it was reported that the interfacial properties between the PFAs and the CPs can be tailored easily by varying the particle size and the process parameters. The formation of a ceramic-polymer matrix with well-incorporated PFAs was achieved by using fine ceramic particles with a higher intensity of UV radiation. On the other hand, de-adhesion of PFAs from ceramic-polymer matrix and aggregation of the PFAs were observed for medium and coarse CPs respectively. The authors postulate that the reduced inter-particle distance between the fine CPs and PFAs makes the scattering process complicated, resulting in a strong adhesion force between the particles.

2.3.9. Novel ink formulations based on the sol-gel process

One of the most recent novel developments in feedstock formulation involves using the sol-gel technique to create UV-curable and particle-free compositions, as a possible alternative to traditional particle-based slurries. This means there are no particles suspended in the formulated system, which can reduce the scattering effects to a large extent and help in achieving a better resolution.

In this context, Rosental *et al.* developed a sol-gel formulation by employing the following steps [175]: an appropriate amount of barium acetate was dissolved in a solution composed of acetic acid and double-distilled water in a polyethylene terephthalate (PET) vial at 65 °C. Thereafter, this solution was cooled down to room temperature (RT) and poured in another PET vial containing appropriate amount of TTIP solution (TTIP + acetic acid) followed by vigorous stirring and sonication. After a few minutes, acrylic acid was added. In addition, acrylate monomer and the photo-initiator were introduced, followed by sonication. Sudan orange powder was used to control the penetration depth of the radiation. The authors also reported that the formulated ink exhibited no difference when printed using layer heights of 30 μm and 200 μm, with an exposure time set to 2 s. This is quite remarkable and is only possible because the ink contains no ceramic particles, thereby avoiding scattering. In contrast, inks containing piezoceramic particles typically require a longer exposure time, greater than 10 s, for layer thicknesses in the range of 10–50 μm (Table 4).

2.3.10. Steps to prepare the feedstock

The first step in the feedstock preparation process is the selection of the best monomer on the basis of the curing capacity and the viscosity. In situations when more than one monomer is being used, it is important to thoroughly combine them. Then the diluent, dispersant and photo-initiator can be added to the prepared monomer system. One can also modify the as-received powders with a dispersant and then use it as a feedstock. The ceramic powder should be added in steps so that there is homogeneous mixing. After each step, the composite system has to be mixed well with the help of a planetary mill. To further homogenize and break the agglomerates, often a ball-milling step is employed. The duration and speed of the milling process depends on the nature of the agglomerates: hard or soft. After the addition of the photo-initiator, one needs to carefully handle the suspension: it should not be exposed to light. To avoid unwanted photo-chemical reactions, the photo-initiator can also be added after the ball milling step. In that case, the amount needs to be adjusted accordingly, as there is always some mass loss after the ball milling step during the feedstock transfer from the ball milling container to the vat.

2.4. Binder Jetting (BJ)

2.4.1. Basics of the technology

Binder jetting is an AM process in which a binder is selectively deposited using an inkjet print head on the powder-bed, in a layer-by-layer fashion. The green-part is taken out from the powder-bed and then de-powdered and is then cured, debinded and sintered to obtain the final product. The binder jetting process is well-known for its high volumetric output, thereby making it suitable for large scale productions. However, the need to use flowable coarse particles to generate the powder bed and the limited resolution of the technology (of the order of a few hundred microns) all contribute to a significant reduction in the density and the piezoelectric response of the printed parts decreases drastically.

The resolution of the printed components is dictated by the particle size, shape and size distribution. Despite the layer height ranging from 15 to 135 μm, as reported in Table 5, the resulting samples often exhibit low resolution due to factors such as binder spreading, limited powder packing density, and insufficient precision in the binder deposition process. A higher packing bed density is desired for high green and sintered density of the printed components. Binder selection and quantity (binder saturation) is another important parameter that greatly affects the printing process.

2.4.2. Particle shape, size and distribution

The properties that are mostly affected by the powder characteristics are the flowability, green density, powder-bed packing density and the sinterability as well as the residual porosity of the printed components. Bigger particles are often desired because of their increased flowability. In contrast, finer particles exhibit better sintering and functional properties. Spherical particles are preferred because they have fewer contact points and hence provide less resistance to flow, enabling the deposition of defect-free powder layers. In addition, a multi-modal particle size is often desired for better packing density as the smaller particles can fill in the void generated by the packing of the coarser particles.

Mariani *et al.* reported the Hausner ratio (H) of synthesized KNN powders to be 1.78 ± 0.1, which was higher than the threshold value of 1.2 for powders with high flowability [191]. This higher value was correlated to the low density and irregular shape of the particles, along with the hygroscopic nature due to the presence of fine particles (d_{50} = 310 nm) and the formation of agglomerates due to high inter-particle-forces among the fine particles. In contrast, Sufiiarov *et al.* synthesized spherical BCZT powders (d_{10} = 10.3 μm, d_{50} = 31.8 μm, d_{90} = 100.4 μm) by combining partial sintering of the initial powders followed by plasma spheroidization [192]. Hall funnel flowability index tests indicated a value of 50s/50g with an apparent density of 2.49 g/cm^3. The relative density after sintering reached more than 90 % in this case. On the other hand, the relative density values were comparatively low (~40 – 60 %) when a non-optimized feedstock was used.

Several investigations have used commercial powders, which may be unimodal or poly-modal in size, with sphere-like or irregular

Table 5
Feedstock preparation and optimized printing parameters for binder jetting.

Feedstock	Particle size and morphology	Additives	Binder fluid	Binder saturation (%)	Printing parameters			Reference
					Feed to build ratio	Layer height (µm)	Miscellaneous	
$BaTiO_3$	1 µm powder particles with agglomerates of 10 µm			60, 75, 100 and 120	2:1	15, 30	Binder cured at 195 °C	[196]
$BaTiO_3$ **Hydroxyapatite**	$d_{50} < 3$ µm $d_{50} \sim 40$ µm Spray-dried	PEMA	SOLUPOR, Hexane−1-ol, 2-ethylhexyl acetate, Hexyl acetate				Samples stored in drying cabinet 40 °C for 24 h	[197]
$BaTiO_3$	0.85 – 1.45 µm			60, 75, 120	2:1	30		[195]
KNN	$d_{10} = 0.15$ µm, $d_{50} = 0.31$ µm, $d_{90} = 4.69$ µm		AquaFuse®	75, 90, 120		50	Powder bed cured at 180 °C for 6 h in air	[191]
$BaTiO_3$	Micron multi-modal, $d_{10} = 0.1$ µm, $d_{50} = 3.4$ µm, $d_{90} = 25.4$ µm	CL001 cleaner	ExOne BS004	40 – 140 (steps of 20)		100	A lot of parameters has been disclosed, Cured at 180 °C for 3 h	[194]
	Submicron uni-modal, $d_{10} = 0.6$ µm, $d_{50} = 1.1$ µm, $d_{90} = 2.1$ µm			50 – 200 (steps of 50)		35		
$BaTiO_3$	Non-spherical, $d_{10} = 0.67$ µm, $d_{50} = 2.04$ µm, $d_{50} = 4.30$ µm		AquaFuse®consisting of water, 10 – 30 % ethylene glycol, 10 – 30 % 2-butoxyethanol	175		15	Target bed temperature 40 °C, Cured at 200 °C for 10 h.	[198]
BCZT	Spherical, $d_{10} = 10.3$ µm, $d_{50} = 31.8$ µm, $d_{90} = 100.4$ µm			80		100		[192]
PZT-N	$d_{10} = 0.2$ µm, $d_{50} = 1.6$ µm, $d_{90} = 5.0$ µm,		AquaFuse®consisting of water, 10 – 30 % ethylene glycol, 10 – 30 % 2-butoxyethanol	75, 90, 105		50	Curing at 180 °C for 6 h	[199]
$BaTiO_3$	Max 45 µm		BS004 solvent, CL001 cleaner	100	1.75	135	Curing at 200 °C for 2 h	[200]

morphology, which is not an ideal scenario for creating a powder bed for the binder jetting process. In order to achieve spherical powders, additional experimental steps such as spray-drying are often required. However, these techniques may not be feasible for all researchers due to limitations in equipment or resources.

2.4.3. *Binder saturation*

The interaction between the binder and the ceramic powder is essential to achieve high accuracy printing and better green mechanical strength. The term binder saturation refers to the amount of binder dispensed as a function of powder-bed porosity. A value of 100 % binder saturation means all the empty voids have been filled by the binder.

Chavez *et al.* reported that with increasing the binder saturation content, the relative green density showed an upward trend [193]. This could be due to the incorporation of the binder in the powder bed pores and re-arrangement of particles with better packing density induced by the spreading action of the roller. However, an excessive amount of binder can limit the density of the green parts, as shown in Fig. 24. In another study, Sufiiarov *et al.* optimized the binder saturation content by evaluating the deviation of the printed object from the CAD model [194]. It is important to note that at extremely low levels of binder saturation, green bodies are not strong enough to prevent delamination during either the curing, debinding and sintering processes. On the other hand, high saturation of the binder yields distorted parts.

2.4.4. *Printing dynamics*

The printing parameters determine the resolution of the printed parts to a great extent. Apart from the powder characteristics and binder saturation, the parameters that influence the printing accuracy are the layer height and the feed-to-build ratio.

The resolution in the z-direction is dictated by the layer height but is strongly dependent on the particle size of the initial feedstock. For instance, a layer thickness of 100 µm was chosen for a coarse barium titanate powder (d_{10} = 0.1 µm, d_{50} = 3.4 µm, d_{90} = 25.4 µm). Conversely, a layer height of 35 µm was chosen for the finer feedstock (d_{10} = 0.6 µm, d_{50} = 1.1 µm, d_{90} = 2.1 µm) [194]. In general, for finer powders the minimum layer height should be at least thrice the diameter of the maximum particle size. This ratio can be decreased to one if the particles are spherical agglomerates. Nevertheless, the layer height obviously cannot be less than the particle size to avoid the formation of macroscopic defects when depositing the powders.

Fig. 24. Effect of binder saturation on the green body density and final sintered density of binder jet (BJ) printed BT ceramics [193]. [193], Open access article distributed under the terms of the Creative Commons CC BY license.

The feed-to-build ratio parameter controls the amount of powder transferred from the feeder to be utilized in the printing process. This helps in achieving a better powder packing ratio by depositing more powder on the printing site. Gaytan *et al.* reported a ratio of 2:1 [195]. This means that two layers of powder from the feed were used to fabricate one layer of the 3D printed object. Lowering this ratio was found to affect the surface finish of the powder bed.

There are several other parameters such as the roller speed, vibration frequency of the powder feeder, recoating speed, drying temperature, drying time, etc. that can affect the process. However, as shown in Table 5, there is very limited literature available, and the effects of other unexplored parameters on the printing process have not yet been thoroughly investigated.

2.5. Selective laser sintering (SLS)

2.5.1. Basics of the technology

This process works similarly to the BJ technique. However, in this method, a high-powered laser is utilized to bond the ceramic particles, instead of a binder. The SLS process for processing ceramic components can be classified as: direct or indirect, depending on the starting feedstock [201]. If the initial feedstock has only ceramic particles, it is referred to as direct SLS. Conversely, if the ceramic powders are mixed with a polymer or binder with it, it is referred to as indirect SLS. In direct SLS, obtaining crack-free parts is challenging considering the poor resistance to thermal shock of ceramics. Furthermore, the short interaction time between the laser and ceramic powder limits the diffusion process, leading to a reduced density. In order to overcome these challenges, often binders are employed along with the powder, resulting in a polymer-ceramic composite after the printing process [202–204]. The presence of polymers or binders significantly reduces the required laser energy, as it is the polymer or binder that needs to be consolidated.

The technology is hardly suitable for use with ceramic powders, because of the high thermal gradients produced during 3D-printing, leading to defects or fractures in the sample. To mitigate thermal gradients that can cause internal stresses, leading to cracks or defects, a laser preheating or preheating at a certain temperature is often used before the SLS process [205,206]. In addition, the SLS equipment is expensive, using powerful infrared lasers. A strong advantage of this approach, however, lies in the possibility of obtaining already sintered parts that do not require a following high temperature heating step for consolidation. That means the processing parameters are directly linked to the sintered density of the ceramic, especially when the goal is to obtain pure ceramics, as is the case in this review paper.

The powder-bed requirements are similar to the ones of the binder jetting process. The most important parameters influencing the printing process include the powder size, laser power (W), scan speed (mm/s), beam diameter (μm or mm) and the powder feed ratio (g/min).

2.5.2. Process variables

The heating efficiency of the laser in irradiating the ceramic particles is strongly dependent on the absorption efficiency at the laser wavelength. In order to study the effect of particle size, Basile *et al.* studied the effect of the single line scan on various powder fractions consisting of nano and micro powders by using a laser power of 22.8 W and scan speeds of 100, 500, 1000 and 1500 mm/s with laser energy densities respectively of 5.1, 1.0, 0.1 and 0.3 J/mm^2 [207]. The authors reported that with decrease in the scan speed, the laser energy density increases leading to an overall increase in width of the heat affected zone (Fig. 25 (a)). In addition, the width of the heat affected zone goes through a maximum on using a ratio of 70 % nanometric and 30 % micro powders for any given laser energy density. In any case, the addition of nanometric powders improves the heat absorbing capacity of the powder mix. The same authors reported the effect of the scan speed. A low scan speed (80 mm/s) lead to a highly dense microstructure with severe cracks (Fig. 25(b, d)). Conversely, with a higher scanning speed (600 mm/s) the severity of the cracks was supressed however, the surface was characterized by a wave-like pattern (Fig. 25(c, e)). Nevertheless, such densification operates only in the top 5 – 10 μm.

Yu *et al.* reported that the scan speed needs to be adjusted accordingly to the laser power [208]. For instance, when the laser power was 9.7 W, the scan speed was varied from 22 – 65 mm/s. The moment the laser power was increased to 20.7 W, the scan speed was varied from 108 – 161 mm/s.

Gureev *et al.* reported the sintering depth varied with the laser power and the scanning speed [211]. At lower laser power, the sintered thickness was limited. However, with increasing power and decreasing speed, the sintered thickness increased which was accompanied by the laser-induced deformations (Fig. 25(f)). Since the laser power is directly related to the temperature generated, deviations from the optimized laser power can lead to defects. For instance, Zhang *et al.* reported that after the preheating procedure with a power of 2.5 W/mm^2 and a scanning rate of 60 mm/min, the surface of the sample was still completely flat [205]. However, on further increasing the power for the SLS process, the sample presented some defects in the form of V-shaped grooves, cracks, and melted powder agglomerates on the surface. The authors also reported that the densification was quite inhomogeneous: the top 500 μm exhibited dense layers >97 %, with the density decreasing to almost 76 % at a depth of 900 μm (Fig. 25(g)). Such improvement in the top 500 μm was related to the laser preheating step.

The density has been also reported to increase with the power and the irradiation time: increase in either of the factors leads to increase in the density. However, excessive power can also lead to the melting of nanometric BT powder [209]. In another study, the authors observed that increasing the power while decreasing the scan speed and powder feed rate resulted in higher laser energy input. This caused burning and evaporation of PZT, leading to non-uniformity in the printing process

Table 6
Feedstock preparation, optimized printing parameters, densification and functional properties for samples fabricated with selective laser sintering.

Feedstock	Particle size	Laser, Wavelength	Power$_{max}$ (W)	Printing parameters			Density (%)	Additional information	Reference
				Power density / power	Scan speed (mm/s)	Beam diameter			
BaTiO$_3$	50 – 70 nm	CO$_2$, 10.64 μm	40 W	3.5 – 3.7 W/mm^2	0.5	2.5 mm	98.7	Preheating: 2.5 W/mm^{2}with 60 mm/min, Difference in density in the top surface and bulk, $\varepsilon_r = 200 – 1800$	[205]
PZT		Nd:YAG	16 W	11 – 14.5 W	15 – 30	50 μm	1.65 – 2.00 g/cc		[211]
PZT		Nd:YAG	20 W	9.7 – 20.7 W	22 – 213	50 μm	2.1 – 4.1 g/sm^3		[208]
BaTiO$_3$	d_{50}= 0.44 μm, d_{50}= 50 nm	Nd:YVO$_4$, 1064 nm	22.8 W	Studied the effect of these parameters on the resulting samples				Coarse and fine powders used	[207]
PZT	1 μm	Nd:YAG	4 kW	150 – 300 W	5 – 15			Powder feed rate 1.3 g/min, ε_r = 430, tanδ < 5 %	[210]
BaTiO$_3$		CO$_2$		5 – 8 W/mm^2		3.5 ± 0.5 mm	~ 92 – 98	Preheated upto 400 °C, Holding time during laser irradiation: 5 – 30 min	[209]
BiT		CO$_2$		10 – 30 W		4 ± 0.5 mm	98	Preheated upto 350 °C, $(P_r) = 6.5$ μC/cm^2	[206]

[210]. Unfortunately, there have been very limited studies concerning SLS of piezoceramics, hence, the parameters affecting the printing process could not be addressed further .

3. Post-fabrication processing

The post-processing steps adopted for printed samples are determined by the specific AM processes used, whether they are classified as

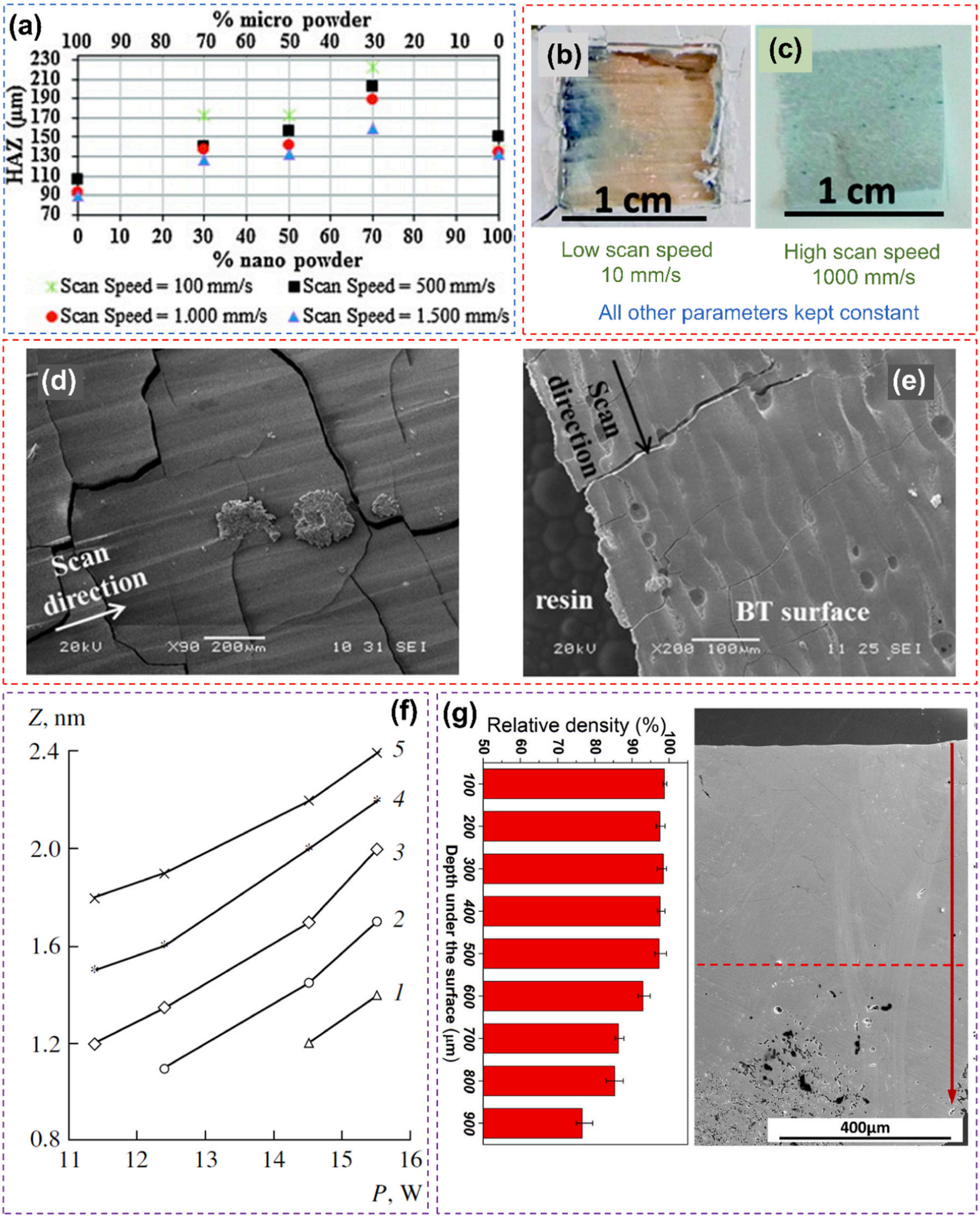

Fig. 25. Effect of the powder size, laser power and scan speed on the sintering depth and microstructure. (a) Variation of the heat affected zones (HAZ) as a function of the BT particle size and scan speed [207]. (b-c) Optical images, and (d-e) SEM images of BT samples sintered at different scanning speeds [207]. (f) Sintered layer thickness as a function of the laser power and scanning speed for PZT. The different speeds used are described as follows: (1) 60 mm/s (2) 30 mm/s (3) 20 mm/s (4) 15 mm/s (5) 12 mm/s [211]. (g) Inhomogeneity in the microstructure along the cross-section of the SLSed BT. The graph reveals the density variation with the depth from the surface [205].
Reproduced from Ref.: (a-e) [207], with permission from Elsevier. (f) [211], with permission from Springer Nature. (g) [205], with permission from John Wiley and Sons.

direct or indirect [33]. In direct AM methods, the material is selectively deposited only along the specified printing path to obtain the final form. Material extrusion-based techniques, such as DIW and FFF, fall under this category, hence no post-processing as such is required. However, DIW-fabricated samples are often subjected to controlled humidity conditions to guarantee uniform drying and to prevent any distortion or flaws that may arise during this process, particularly when the powder particles are fine and high solid loadings cannot be achieved.

In contrast, indirect AM methods often include the incorporation of the printed material inside a powder or resin bed, which must be subsequently cleaned or removed in order to obtain the finished product. This category of AM technologies includes VP, BJ and SLS. In VP, the printed green models are often cleaned in organic solvents (sometimes using ultra-sonic cleaning as well), such as alcohol or acetone, to remove uncured ceramic suspensions before drying at room temperature. Whereas, in BJ, the deposited binder is usually cured using heat to strengthen the green part before the de-powdering process.

Special care has to be taken for samples fabricated with novel feedstocks such as the ones mentioned in Section 2.1.6 and Section 2.3.9. For example, samples fabricated with capillary suspensions were printed on porous alumina plates (to remove some of the organic components by the action of capillary forces) and kept at ambient conditions for 5 days before thermal debinding [88]. Feedstocks based on sol-gel precursors are often subjected to an aging period before further processing [175].

3.1. Debinding

The main goal of the debinding procedure is to remove the binder used in the shaping process. The debinding process is heavily dependent on the type of binders that is used and can be classified into one of the following types: chemical (dissolving in a solvent), catalytic (using a catalytic acid vapour), wick (using capillary forces) or thermal (using a heat treatment) [212].

Chemical debinding is specifically employed when the binder system consists of a combination of two or more thermoplastic binders. One of the components, usually a low molecular weight polymer, is selectively dissolved in a solvent, that creates interconnected open porosity for the easy removal of the left-over binder during the thermal debinding process. The other components ensure that the green part is able to retain its shape during or after the debinding. This process is complex and requires careful attention since it involves the phenomena of dissolution and diffusion, which depends on the temperature, time and the powder characteristics. In a recent study, authors fabricated BT filaments with a blend of polyvinyl alcohol (PVA) and polycaprolactone (PCL) and partially removed the PCL by dissolving it in toluene at room temperature [113]. This partial removal of the binder helps in creating an interconnected open porosity, facilitating the subsequent binder removal during the thermal debinding step. Further, the removal of the PCL was confirmed by TGA and FTIR measurements. Poorly optimized chemical debinding processes, including solvent selection and parameters, may result in sample defects such as delamination or swelling. In contrast, catalytic debinding utilizes acid vapor to selectively remove one component of the binder system and is considered a faster debinding process compared to other methods.

The thermal debinding process is recognized as the most time-consuming and energy intensive in the entire fabrication procedure. Typically, slow heating rates are employed to ensure the complete removal of the binder and gradual, smooth decomposition of all organics. The heating rate during the thermal treatment process is found to affect the structural integrity of the printed structure and the densification process [143]. A rapid heating rate of 8°C/min was reported to induce deformation and cracking in the printed structure, thereby leading to decreased density (Fig. 26(a-b)).

More recently, Kim *et al.* provided a detailed insight on the effect of the heating rate during the debinding step in order to preserve the porosity obtained after burning out of PMMA [189]. Three different heating rates (0.5 °C/min, 1 °C/min, and 2 °C/min) were chosen in vacuum for debinding. The authors observed that the least shrinkage and highest density (Fig. 26(c-d)) was observed with a debinding rate of 1 °C/min and correlated with the decomposition behaviour of the organic matter in inert environment. The EDS analysis revealed that the sample debinded at 1 °C/min sample had the lowest carbon content, followed by 0.5 °C/min and 2 °C/min. This is because the heating rate during vacuum debinding affects how quickly the decomposition products move from inside the sample to the surface. At a lower heating rate (0.5 °C/min), the gas generated form the pyrolysis of the organic matter builds up inside because it cannot escape fast enough, but the longer heating time helps some carbon on the surface evaporate. In contrast, at a higher heating rate (2.0 °C/min), a film forms on the surface due to quick binder flow, but there is not enough time for carbon to evaporate, leading to more carbon residue. This conclusion was further supported by the roughness measurements, which showed a similar trend to the carbon content levels suggesting the roughness was affected by the residual carbon (Fig. 26(e)). Most importantly, the optimal debinding rate ensured that the pore size distribution matches well with the particle size distribution of the PMMA particles after sintering.

During the DIW process, the solvent (typically deionized water, as reported in Table 2) evaporates from the sample after printing, leaving behind a small amount of organics that can be thermally removed. Since the amount of organics remaining is minimal (similar to binder jetting), the thermal debinding process is relatively straightforward. This is also applicable for samples fabricated using binder jetting technology. Most of the studies have reported a debinding rate of 1 – 5 °C/min (Table 8), which is often accompanied with a certain dwell time at temperatures where complete decomposition of the binder or additives is anticipated. These temperatures are usually determined by performing TGA analysis on the prepared feedstock.

The debinding scenario is similar for the samples fabricated with VP technique. Thermoset polymers undergo irreversible cross-linking during the curing process, making them resistant to all methods of debinding except thermal treatment. As opposed to DIW, the monomer that serves as the solvent in this case does not evaporate. As a result, the process of thermal debinding is challenging and requires special attention while designing the debinding schedule. The thermal debinding process is slow and can last up to a few days with a debinding rate limited to a maximum of 1 °C/min (Table 10). It is important to keep in mind that researchers often prefer to carry out the thermal debinding process in an inert atmosphere, either argon (Ar), nitrogen (N_2) or vacuum (Table 10). The binder decomposition behaviour is strongly influenced by the debinding atmosphere [213]. Organic compounds undergo vigorous exothermic reactions due to oxidative decomposition in the presence of air, which may result in the formation of defects such as cracks or delamination (Fig. 27(a)). Such defects have been reported by several authors [159,165]. On the other hand, the exothermic behaviour is significantly inhibited in inert atmospheres due to the absence of oxygen and the decomposition proceeds through the disruption of the chemical bonds by heat absorption [214]. As a result, a certain amount of carbon remains in the sample leading to a black colour (Fig. 27(b)), which is subsequently eliminated by a second debinding process in the presence of air (Fig. 27(d)). Certain additives such as polyethylene (PE) swells when heated in argon, thus making the process complicated [172]. In such a scenario, debinding in argon is not recommended. The best way to design a debinding schedule is to perform a TGA analysis and using this data to plot the DTG (or DSC to observe the endothermic or exothermic peak) to see the peaks where the most intense mass loss occurs (Fig. 27(c)). To ensure the integrity of the printed structure during the binder removal process, it is important to employ a slow heating rate and/or dwell time in regions where strong decomposition occurs so as to facilitate gradual and smooth removal of organics. Sometimes, low-temperature volatile additives are employed to generate a network of transient porosity that facilitates the removal of

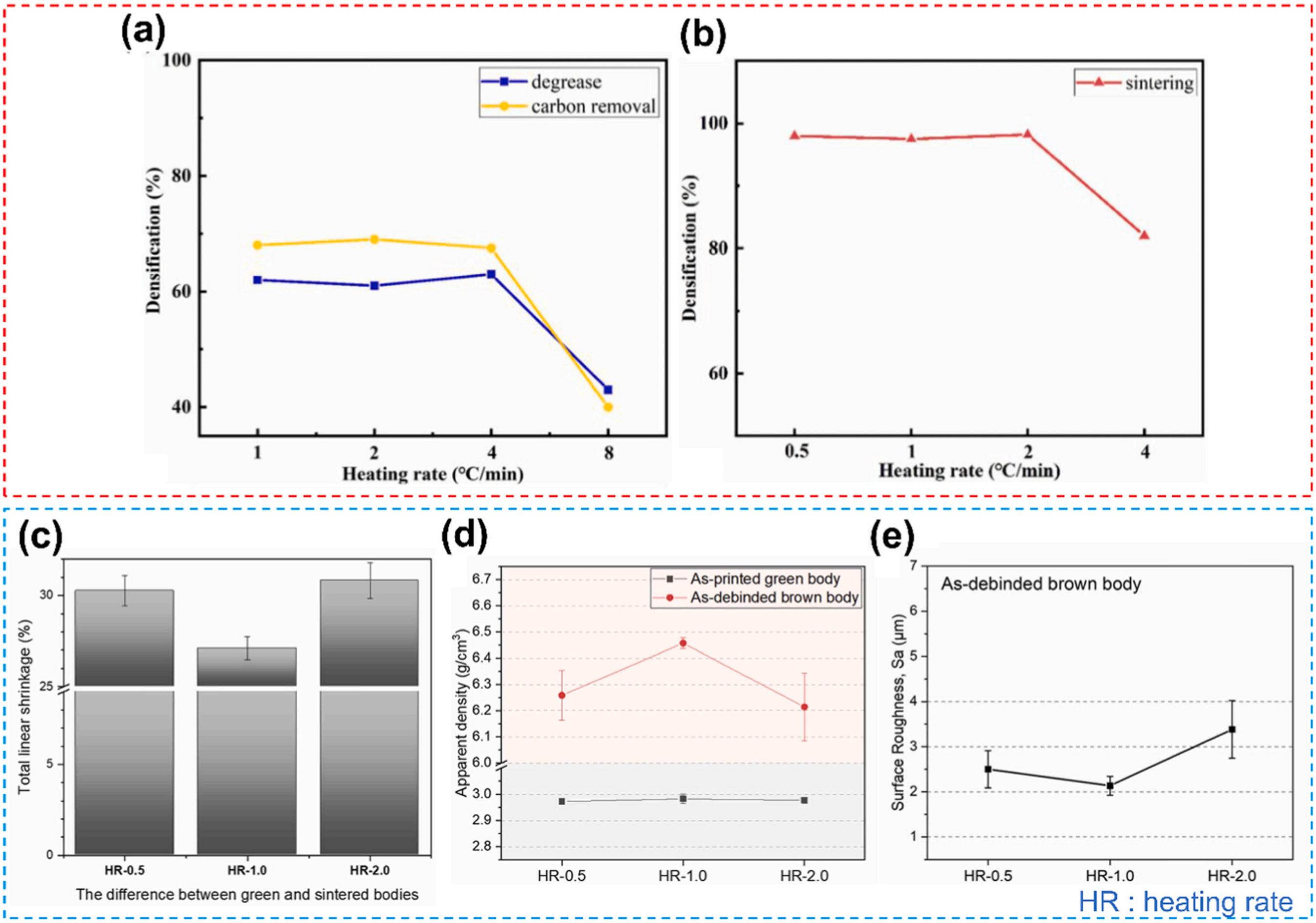

Fig. 26. Effect of the heating rate on different physical properties of the debinded and sintered samples. Densification after (a) debinding, and (b) sintering with different heating rates for BT ceramics fabricated with VP [143]. The variation of the (c) linear shrinkage, (d) density, (e) surface roughness as a function of different heating rates for PZT ceramics fabricated with VP [189].
Reproduced from Ref.: (a-b) [143], Open access article distributed under the terms of the Creative Commons CC BY license, (c-e) [189], with permission from Elsevier.

the decomposition gases generated by the decomposition of the organics at higher temperature.

The debinding cycle shown in Fig. 27(d) has been designed according to the TGA/DTG/DSC plot in Fig. 27(c) and a similar approach to design the debinding schedule has been reported by numerous studies, as evidenced in Table 8 – 10. The binder decomposes in the range of 350 – 550 °C with the intense mass loss happening at around 420 °C (also evidenced by exothermic peak in DSC). The debinding process was carefully designed to gradually increase the temperature in steps, with hold time at certain temperatures (200 °C, 300 °C, 400 °C, 450 °C, 500 °C, and 600 °C for 1 h). This ensures homogeneous heat distribution within the samples, prevents stress development and allows for complete binder decomposition. Subsequently, any residual binder is removed by a second heat treatment in air. In general, this idea of designing the debinding cycle can be applied to samples produced using any other AM technique.

The effect of the binder content on the debinding process can be clearly visualized from Fig. 27(d-e). Samples with a limited amount of organics, such as those fabricated using DIW, can be processed using high heating rates. On the other hand, samples fabricated with VP, usually possess a high amount of binder (~ 18 wt% as shown in Fig. 27 (c)) and therefore the debinding rate is slow, making this an energy-intensive process. To increase the energy efficiency of the thermal treatment process, it is necessary to create novel feedstock formulations with low binder content and high ceramic loading.

Similar to VP technique, FFF also requires careful designing of the debinding cycle, because of the high-volume fraction of the binder (typically 40–50 vol%) used in the production of a printable filament. Most of the studies have reported a heating rate in the range of 0.2 – 1 °C/min (Table 9). In a recent study, wick debinding has been successfully used to remove low molecular weight organic wax (paraffin wax) [118]. In this process, the green part is embedded inside a highly porous powder bed which is subsequently heated to a desired temperature. The low molecular weight organic wax begins to melt as the temperature rises and the capillary forces arising from the pores extract the melted wax out of the sample. The final temperature and hold time are important parameters that need to be carefully adjusted. The authors reported that the best results were achieved at isothermal conditions of 200 °C (for 60 h) with a slow heating rate of 0.2 °C/min. Thereafter, the samples could be sintered with a high heating rate of 10 K/min. A recent study reported that the binder decomposition temperature decreases with the increase in the ceramic loadings in the filament [113]. This can be associated with the catalytic effect at the surface of the used ceramic powder [215]. This effect is reported to be more prominent in air when compared to inert atmospheres.

3.2. *Sintering and functional properties*

In general, after the thermal debinding step, the samples are highly fragile and an additional heat treatment at elevated temperatures below

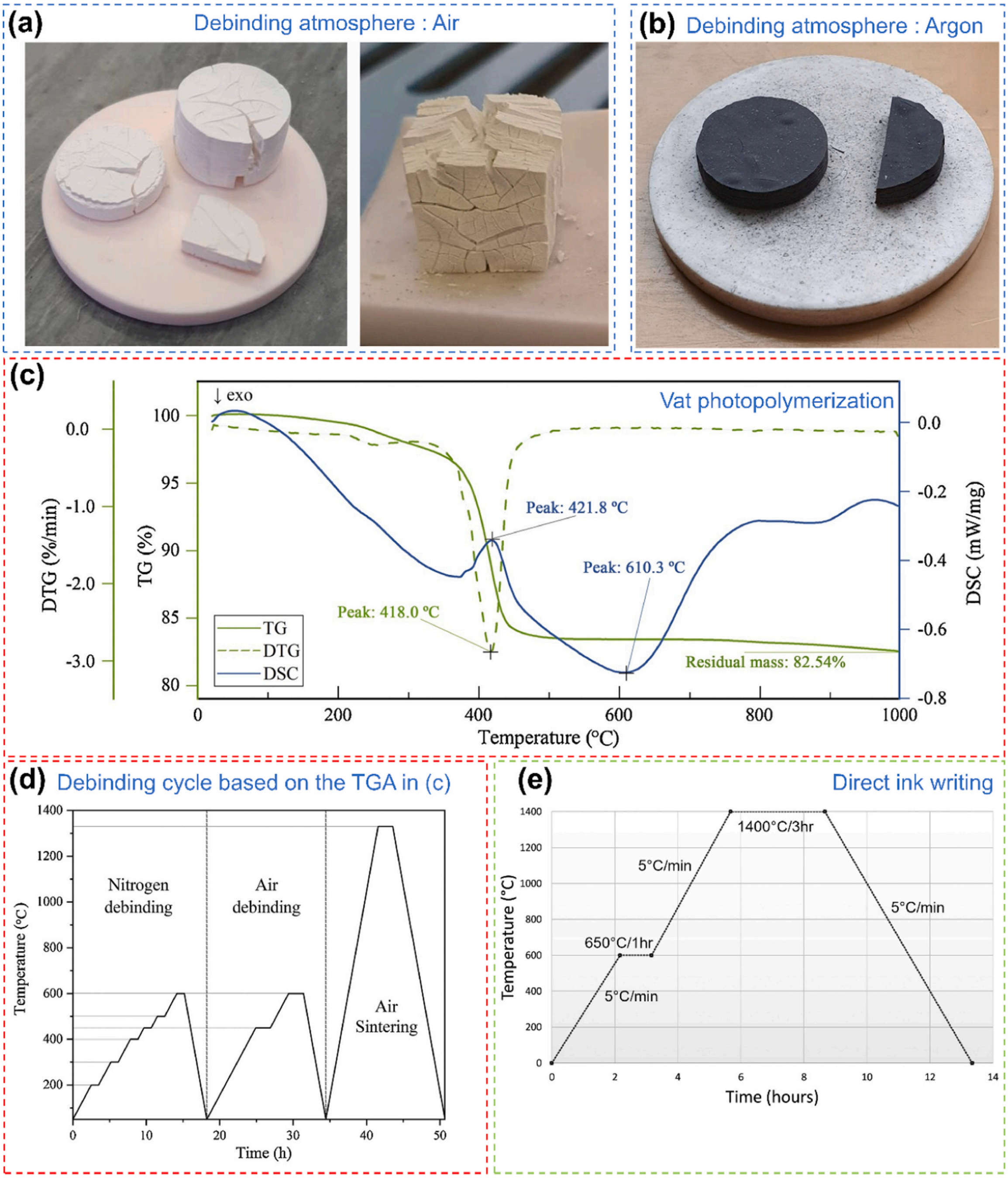

Fig. 27. Comparison of the sample cracking in different atmospheres, accompanied by TGA and corresponding debinding cycles to ensure a defect free sample. (a) Cracks observed in samples during the debinding process in atmospheric air, and (c) Crack free samples when processed in a vacuum, with the black coloration indicating residual carbon content in BT ceramics [159]. (d) TG-DSC analysis of a green body conducted under a nitrogen atmosphere, and (e) the corresponding debinding and sintering process used to sinter the debinded samples [139]. (f) Debinding and sintering profile for samples produced via DIW [86].
Reproduced from Ref.: (a-c) [159], and (d-e) [139], with permission from Elsevier. (f) [86], with permission from John Wiley and Sons.

the melting point (known as sintering) is necessary to achieve high density and desired properties. The desired sintering temperature can be found out by performing a dilatometry test on the powder pressed disc or the printed sample (similar dimension to disc, with flat opposite sides). Kindly note that the dielectric and piezoelectric/ferroelectric measurements are usually carried out on regular-geometry (specially disc shaped samples), as usually required by the equipment.

The most crucial factors that affect the sintering process are the temperature, atmosphere composition, heating rate and the hold time. These variables are crucial in the development of the microstructure, which directly affects the electrical properties, as will be discussed later.

For sintering, alumina crucibles are typically used as a substrate for BT [116] as well as for most of other ceramic materials. The contact area between the sample and the crucible can lead to some unwanted reactions, thus modifying the stoichiometry of the sample. Traces of barium aluminate ($BaO•Al_2O_3$) based compositions are formed in a temperature range between 800 °C and 1400 °C [216]. The sintering of BT takes place at temperatures within this temperature range. To avoid this unwanted reaction with the samples, a platinum wire coil or platinum foil can be used to prevent contact between the sample and the crucible [176]. In the case of compositions containing volatile elements such Pb or K, samples are sintered in a closed alumina crucible using a powder bed from the same material as the sample to minimise the loss of material and stoichiometry due to volatilization [54,72,74,75,77,83,94,98,104,116,118,121–123,131,133,177].

The relative density of the sintered samples increases with the sintering temperature [73,74,78,86,144]. Further, no further densification occurs by increasing the temperature beyond the temperature where the densification reaches its maximum (also known as over-sintering). In fact, it may even result in a slight decrease in density [51,60,144,149,159,175]. This can be related to the formation of additional porosity due to over-sintering [149]. For instance, Hossain *et al.* reported that, for PZT, a maximum relative density of 97.5 % was achieved at a sintering temperature of 1200 °C. The density decreased slightly on further increasing the sintering temperature to 1300°C (Fig. 28(a)), probably due to loss of volatile PbO in PZT ceramics at such elevated temperatures [74]. This suggests that compositions such as KNN, PMN-PT etc., containing volatile components must be handled with caution during sintering. A similar trend was observed for BCZT. The relative density decreases from 95.88 % to 95.20 % on increasing the temperature to 1525 °C from 1500 °C due to over-sintering (Fig. 28(b)) [149].

Further, the increase in density is also manifested in the form of shrinkage due to decreasing volume of the porosity. In general, owing to the layer by layer build up process, the shrinkage in the z-direction (or, axial) is always higher than the shrinkage in x and y directions (or, radial) [77,144,148–150,152,168,169,172,177,180,183,184,186]. It is to be noted that the shrinkage (in both directions) decreases when the sample is over-sintered (Fig. 28(c)) [144]. However, surprisingly, some of the studies reported that the converse (shrinkage in x and y higher than in z) is also true [113,139,175,189]. Shrinkage decreases with ceramic loading (Fig. 28(d)) [113,148] and thereafter increases after the optimum loading [139]. An almost similar shrinkage in both directions has also been reported [159].

A recent study reported differences in shrinkage after sintering between dense objects and porous structures, such as TPMS, even though the samples were printed with the same composition [141]. Therefore, to accurately calculate shrinkage in different directions after sintering, it is recommended to print the desired geometry, measure the shrinkage, and then either scale up or scale down according to the desired dimensions.

Along with the density, the grain size also increases with the sintering temperature due to enhanced mass diffusion at elevated temperatures (Fig. 29(a-f)) [73,78,79,83,86,95,113,140,144,184]. In addition to the sintering temperature, dwell or hold times are an important variable affecting the densification process. This can serve various purposes, e.g., an optimized dwell time enhances the particle rearrangement and diffusion rates, thereby ensuring a dense microstructure. Moreover, the dwell time ensures homogeneous temperature distributions, reduces thermal gradients and uneven sintering. In this context, Wei *et al.* studied the effect of different dwell times (2 h, 5 h,

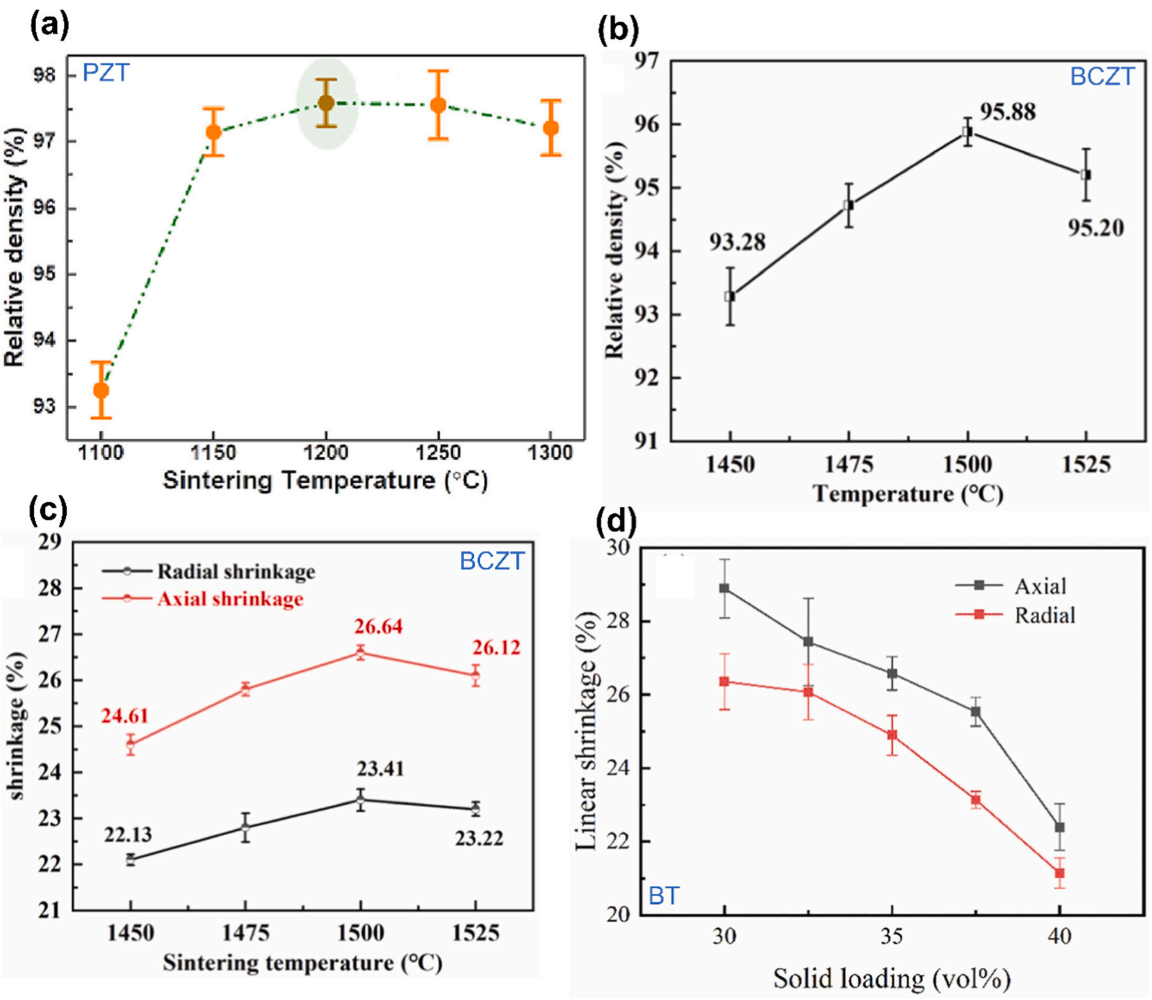

Fig. 28. Effect of sintering temperature and ceramic loadings on the density and shrinkage. (a) Variation in relative density of PZT ceramics as a function of sintering temperature [74]. (b) Linear shrinkage, and (c) Relative density of BCZT ceramics subjected to various sintering temperatures [149]. (d) Linear shrinkage measurements for sintered BT ceramics with varying solid loadings [148].
Reproduced from Ref.: (a) [74], (b-c) [149], and (d) [148], with permission from Elsevier.

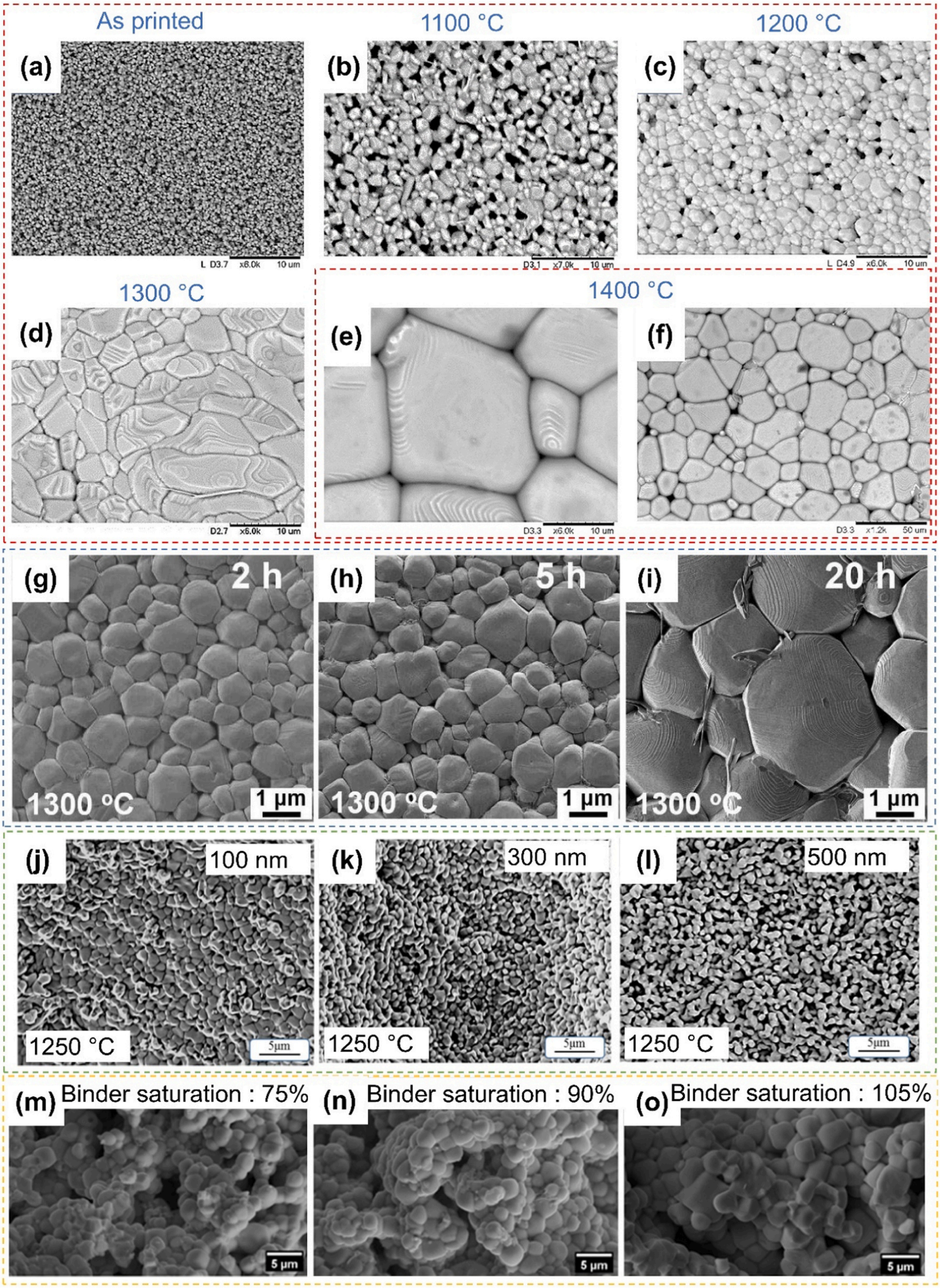

Fig. 29. Various parameters that affect the sintering density and microstructure. SEM images depicting the microstructures of samples at various stages: (a) as-printed, and (b-f) sintered at different temperatures [86]. (g-i) SEM micrographs of BT ceramics sintered at 1300°C for different holding times [93]. (j-l) Particle size effect on the microstructure of BT ceramics sintered at same temperature [58]. (m-o) SEM microstructures of binder jetted Nb-doped PZT ceramics sintered at 1250°C with varying binder saturations [199].
Reproduced from Ref.: (a-f) [86], with permission from John Wiley and Sons. (g-i) [93], with permission from Elsevier. (j-l) [58], with permission from IOP Publishing.(m-o) [199], Open access article distributed under the terms of the Creative Commons CC BY license.

and 20 h) at 1300 °C on the densification process and microstructural evolution of BT ceramics [93]. Experimental results pointed out that the relative density increased with the holding time due to the elimination of the pores [183]. However, with prolonged holding time of 20 h, grain growth takes place, with grain sizes reaching almost 2 – 3 μm (Fig. 29 (g-i)). The phenomenon of abnormal grain growth observed in BT ceramics is observed after a certain threshold temperature (usually around 1325 °C), where a liquid eutectic phase is formed and thereafter grains may grow abnormally due to Ostwald ripening [113].

The initial particle size is reported to have a profound effect on the densification behaviour of the sintered sample [58]. Often, mechanical milling is employed to break up agglomerates and/or decrease the particle size in the starting feedstock. Finer particles are reported to have better sintering behaviour owing to their large surface area or more increased particle-to-particle contact [147,157]. This has been validated by the findings of Renteria *et al.* [58]. The authors reported that the relative density of the sintered samples increased to almost 85 % from 68 % on changing the initial particle size of 500 nm down to 100 nm. The sample with finer particles exhibited a dense microstructure with slightly bigger grains (due to grain growth) even when sintered under the same conditions. On the contrary, the sample with coarser particles (500 nm) exhibited a significant amount of open porosity with the grain size remaining similar to the initial particle size (Fig. 29(j-l)). This means the thermal activation energy (here, it is the sintering temperature) required to initiate the mass transport phenomenon is higher for coarser particles than for finer particles. Similar results have also been verified for samples fabricated using VP [147].

In contrast to the microstructures shown in Fig. 29(a-f) typically for extrusion-based techniques, the microstructures that are produced by binder-jetted samples are highly porous as depicted in Fig. 29(m-o). Even though the densification increases with the binder saturation value, it still does not reach the levels produced by extrusion or vat photopolymerization. When examining the densification values in Tables 8, 9, 10 and 11, this aspect appears to be clearer.

In general, it is challenging to prepare a feedstock with fine particles. A compromise can be achieved by using particles with a bimodal distribution. In general, inclusion of smaller particles in coarser particles serves to enhance the packing density and consequently the green density of the printed component. In this regard, Renteria *et al.* investigated the effect of bimodal particles (100 and 400 nm) on the packing density and the densification behaviour [61]. The packing density was maximized at 55.8 vol% of large (400 nm) powder particles. It was observed that the densification behaviour is strongly affected by the volume fraction of the fine particles. Surprisingly, the decreasing density was not linear with the increasing coarser fraction. An inflection at 50–50 vol% was observed, suggesting that the final density might be affected by the dominant powder fraction in the sample.

Several studies have demonstrated that density increases with higher solid concentration (as shown in Fig. 30(a)) [148,151,164,169,186]. However, beyond a certain threshold, density may begin to decrease. Possible factors contributing to this include: excessive use of dispersants to lower viscosity [181], limitations in the recoating ability of the scraper blade during printing [139], insufficient curing due to excessive loadings resulting in poor bonding force between layers [151,186], and nozzle clogging leading to uneven flow rates [77]. The addition of low RI materials, generally termed as pore forming agents (PFAs) as discussed in Section 2.3.8, compromises the density to a certain extent after sintering. The porosity increases with increasing amount and size of the PFAs [145,150,152,171,172] and, subsequently, the shrinkage also increases (Fig. 30(b-d)). The inset SEM images in Fig. 30(d) illustrate the difference in microstructure, where an increase in the amount of PFAs results in higher porosity. The quantity of binder utilized in formulating the ink for DIW or in jetting onto the powder bed for BJ also plays a role in determining the final density of the sintered component [85,193]. Deviation from the optimum value led to the formation of large circular pits or residual porosity from the binder burn out. It is worth mentioning that the sintered microstructure is highly sensitive to the ceramic loadings [181,186]. The grain size increases with the ceramic loading and this can be attributed to the decreasing amount of defects in form of porosity (Fig. 30(e)). Porosity exert a dragging force to grain boundary motion hindering the grain growth and densification during sintering [217].

It is important to note that the reported density of the samples that are produced using 3D printing is always lower than the density of samples that are powder-pressed [80,113,122,123,146,151,168,179,186]. This is mostly because of the residual porosity generated from the binder-burn out process, as depicted in Fig. 31. Additionally, as observed from Tables 8, 9, 10, and 11, nearly full densification is completely missing in the reported density values. A recent study has further evidenced this fact by carrying out mercury porosimetry analysis on a powder pressed and printed sample. It was found that pore size in the range of 0.1 – 5 μm was attributed to the residual porosity after the binder burn out process as this size fraction of porosity was completely missing in the powder pressed sample [113]. In addition, the presence of printing defects cannot be ignored completely. For samples fabricated using FFF, VP, and DIW, the difference in values between the achieved density and full densification (100 %) is comparatively small (Tables 8, 9, and 10). However, this difference increases significantly for samples fabricated using BJ, where the achieved density is significantly lower (Table 11). This disparity is primarily due to the higher levels of residual porosity mostly generated from the powder-bed packing, which hinders the densification process. Consequently, the piezoelectric performance of the printed components is typically inferior to conventionally powder-pressed samples.

The density of the sintered piezoceramics is strongly affected by the sintering atmosphere as well. In a recent study, authors have utilized innovative sintering processes such as ultra-fast high temperature sintering (UHS), pressure-less spark plasma sintering (P-SPS) and fast firing (FF) to achieve rapid debinding and sintering of the BT components fabricated using DIW [79]. The experiments were carried out in inert atmosphere for UHS (Ar/N_2) and P-SPS (Ar) to prevent the oxidation of the graphite felt or the die at such high temperatures. On the other hand, fast firing experiments were conducted in ambient conditions. The samples were able to resist the rapid heating and cooling rates, without any noticeable defects in the samples. However, the densification was restricted to around 70 – 78 % for samples sintered using UHS and P-SPS (Fig. 32(a-b)). On the contrary, samples sintered using FF exhibited high densities of up to 95 % (Fig. 32(b)). The authors reported that the phase transition from tetragonal to hexagonal, while sintering in inert atmospheres (Fig. 32(c-e)), adversely affects densification by enhancing the pore-grain boundary separation and anisotropic coarsening (formation of elongated grains) as shown in Fig. 32(h-i, k-l, n-o). Such elongated grains are typical for the hexagonal phase. Additionally, the samples exhibited dark coloration which was correlated to the reduction of the oxide in such low p(O_2) conditions. Similar observation was made for BT ceramics sintered using SLS [205]. In contrast, when sintered in air, the tetragonal phase was retained with dense microstructure and equiaxed grains (Fig. 32(f, p-r)). The tetragonal phase was also retained at lower UHS currents (20 A) and P-SPS temperature (1300 °C), however no densification was observed as the thermal activation energy for mass diffusion was insufficient as evidenced in Fig. 32(g, j, m).

A similar phase transformation has been reported for samples sintered using SLS [205,207]. Such phase transition is reported to occur at 1460 °C in air. However, when sintering in H_2 atmosphere, the phase transition temperature decreases to 1360 °C which can be related to the formation of oxygen vacancies and Ti^{3+} which stabilizes the high temperature hexagonal phase at room temperature [218,219]. In addition, the very high cooling rates achieved in SLS (similar to UHS) can be one of the most probable mechanisms that helps in retaining the meta-stable phase at room temperature [206,207,210]. The high cooling rates achieved during such process helps in retaining a fine very microstructure, which otherwise would have been difficult to achieve [210]. Similar to

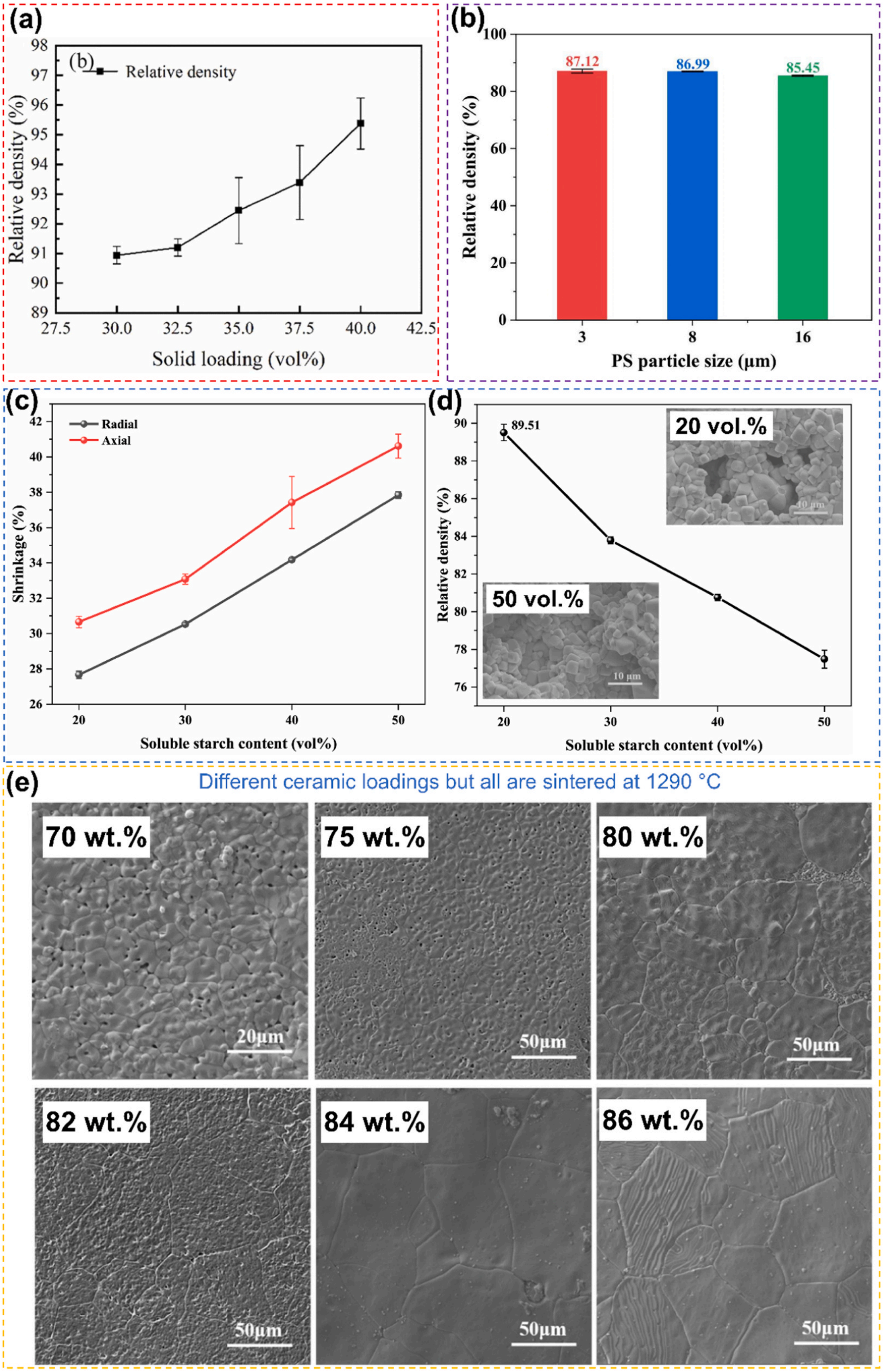

Fig. 30. Effect of the ceramic loadings and PFAs on the density, shrinkage and microstructure of the sintered ceramic. (a) Relative density measurements of sintered BT ceramics with varying solid loadings [148]. (b) Relative density as a function of different PS particle sizes [152]. (c) Shrinkage, and (d) Relative density of PZT piezoceramics as a function of different amount of soluble starch content. The insert in (d) shows the SEM images after sintering with different amount of SS [150]. (e) SEM micrographs as a function of different ceramic loadings sintered at same temperature [181].
Reproduced from Ref.: (a) [148], (b) [152], and (c-d) [150], with permission from Elsevier. (e) [181], Open access article distributed under the terms of the Creative Commons CC BY license.

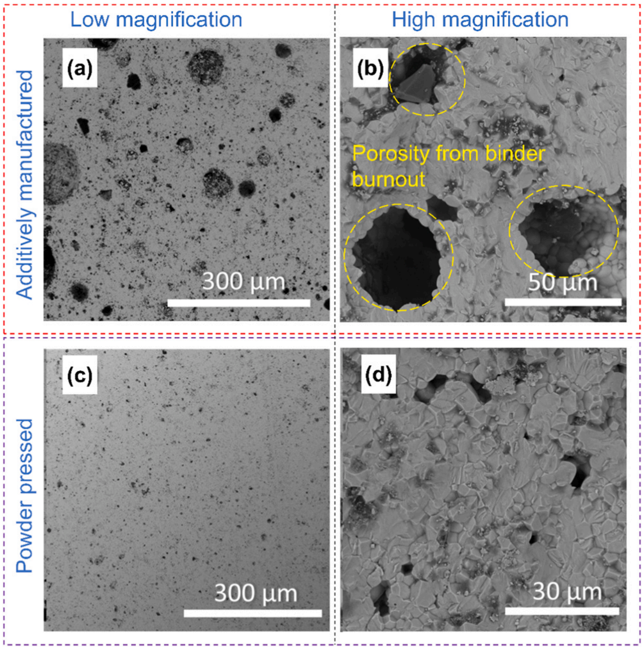

Fig. 31. SEM micrographs of sintered PZT ceramics exhibiting the difference between the (a-b) 3D printed sample and (c-d) a powder pressed sample [77]. Reproduced from Ref.: (a-d) [77], with permission from Elsevier.

the UHS process, the temperature control during the SLS process is very challenging. Usually, the laser spot follows a Gaussian distribution of energy with the maximum being achieved at the centre of the spot [205]. Thus, it is quite challenging to maintain the same temperature at each scanning spot on the powder bed, which then leads to inhomogeneity.

Since most of these piezoelectric materials have a crystalline structure, XRD is the most widely used method to study the structure and phases. As an alternative, Raman analysis is sometimes carried out for determining the developed phases as well [113,151,186].

With XRD, the lattice parameters are accessible and a unit cell distortion can be calculated. The unit cell distortion describes the distortion from the paraelectric cubic phase. The spontaneous polarisation in ferroelectric phases is oriented along the direction of the unit cell distortion, which is the $[001]_{pc}$ direction in tetragonal symmetry, the $[110]_{pc}$ direction in orthorhombic symmetry, the $[111]_{pc}$ direction in rhombohedral symmetry or more complex directions in monoclinic symmetry [220]. The subscript “pc” refers to the pseudocubic undistorted perovskite unit cell. The unit cell distortion increases with increasing lattice parameters towards the direction of the spontaneous polarisation [113,147]. The intrinsic piezoelectric effect has a direct proportional relationship to the unit cell distortion. In ferroelectric ceramics with tetragonal symmetry, the unit cell distortion is referred to as tetragonality and is defined as the c/a ratio, which is the ratio of the long c-axis (c) to the short a-axis (a) of the crystal structure.

The tetragonality is reported to increase with the sintering temperature as depicted in Fig. 33(a) [86,113,149]. This increase is evidenced by the enhanced 200 reflection splitting to 200_T and 002_T in XRD patterns, indicating a greater degree of unit cell distortion after the phase transformation from cubic to tetragonal symmetry, i.e., for Cu K_α radiation these reflections are located around of $2\theta = 45$ °. This is also evidenced by high c/a ratio (also denoted by η_T) for the sample sintered at 1350 °C with bigger grains (> 20 µm) (Fig. 33(b)).

The initial particle size also affects the tetragonality of ferroelectric ceramics. Fine powders require less energy and hence are expected to exhibit higher tetragonality when compared to coarse powders processed in the same conditions [58,59,61,158]. This can be related to the final grain size of the sintered ceramic. For instance, Reneteria *et al.* reported that the samples fabricated with 100 nm particles exhibited a grain size of approximately 1.18 µm after sintering [58]. On the other hand, the 300 nm and 500 nm particles exhibited a grain size of approximately 871 nm and 757 nm, respectively. It should be noted that the sintering temperature was similar for all particle sizes. However, the sample processed from 100 nm particles showed the highest 200 reflection splitting. In an another study, authors have used different sintering temperatures for different particles sizes; 1300 °C for 200 nm and 1330 °C for 600 nm particles sizes [147]. The sample processed from 600 nm particle sizes and a final grain size of 875 nm exhibited higher reflection splitting (Fig. 33(c)). It is widely accepted that the tetragonality decreases on reducing the grain size of the sintered ceramic. This is due to increased internal stresses generated by the high volume of grain boundaries and domain walls [15,16,221]. Smaller grains have a higher domain wall density, leading to higher internal stresses that hinder the crystal lattice distortion, lowering the c/a ratio. In contrast, larger grains, with lower domain wall density and lower stresses, maintain higher tetragonality (high c/a ratio). Since a higher ceramic loading results in a microstructure with less porosity and larger grains, it will also result in a higher tetragonality [164,181].

Polycrystalline ceramics are considered to consist of a microstructure of randomly oriented grains. However, if there is a preferential orientation, it can be detected and quantified by XRD analysis. This anisotropy of the distribution of crystallographic directions is called texture. XRD patterns are used to evaluate or understand the degree of texturing. For instance, Lorenz *et al.* investigated the diffraction patterns of sintered BT, measured parallel and perpendicular with respect to the extrusion direction in reflection geometry at the surface (Fig. 33(d)) [70]. The authors reported that the variation in the reflection intensities along different directions is due to the preferential particle alignment along the extrusion direction during the printing process. In general, the Lotgering factor (F) is often used to quantify the degree of texturing [91,102,162,163] and it can be calculated using Eq. 15 [222]:

$$F = \frac{(I - I_0)}{(1 - I_0)} \tag{15}$$

where, I_0 is the reflection intensity of a sample with random orientation and I the reflection intensity of a textured sample. The Lotgering factor is calculated with the intensities of characteristic reflections for the respective symmetry. Walton *et al.* reported that the Lotgering factor F declines on advancing from the surface ($F \sim 40$) of a filament to ($F \sim 0$) at the centre of a filament, as also depicted in the microstructure in (Fig. 9(c)) [91]. This is in accordance with the torque simulation findings carried out on the filaments. Highest torque is experienced on the surface, while least in the core. A low Lotgering factor of 0.46 was reported in case of additively manufactured bismuth titanate [102]. The authors reported that the initial matrix particles were quite coarse (0.5 – 1 µm), which led to a sluggish grain growth. Another probable reason could be the lack of alignment of the templates during the extrusion process itself. In a recent study, the authors have shown that the degree of texturing increases (from 94.3 % to 97.4 %) with sintering temperature (increasing from 1250 °C to 1300 °C) due to templated grain growth of the used seed platelets (Fig. 33(e)) [163]. However, as the temperature increases above a certain temperature, grain growth of the matrix grains occurs without any distinct texture, resulting in an overall reduced texturing.

Often, researchers use sintering aids to lower the sintering temperature by forming a liquid phase. The mass transport and diffusion phenomena are reported to be higher in the presence of a liquid phase due to increased atomic mobility compared to solid-state sintering. In addition, the residual porosity left after binder burn out often limits the degree of texturing as well. Copper oxide (CuO) is one of the most widely used sintering aids reported in the literature [163,184]. He *et al.* reported that the density and the grain size increased with increasing CuO content up to 1.5 mol.% (Fig. 34(b-c)) [184]. Excess CuO (2 mol.%) resulted in a

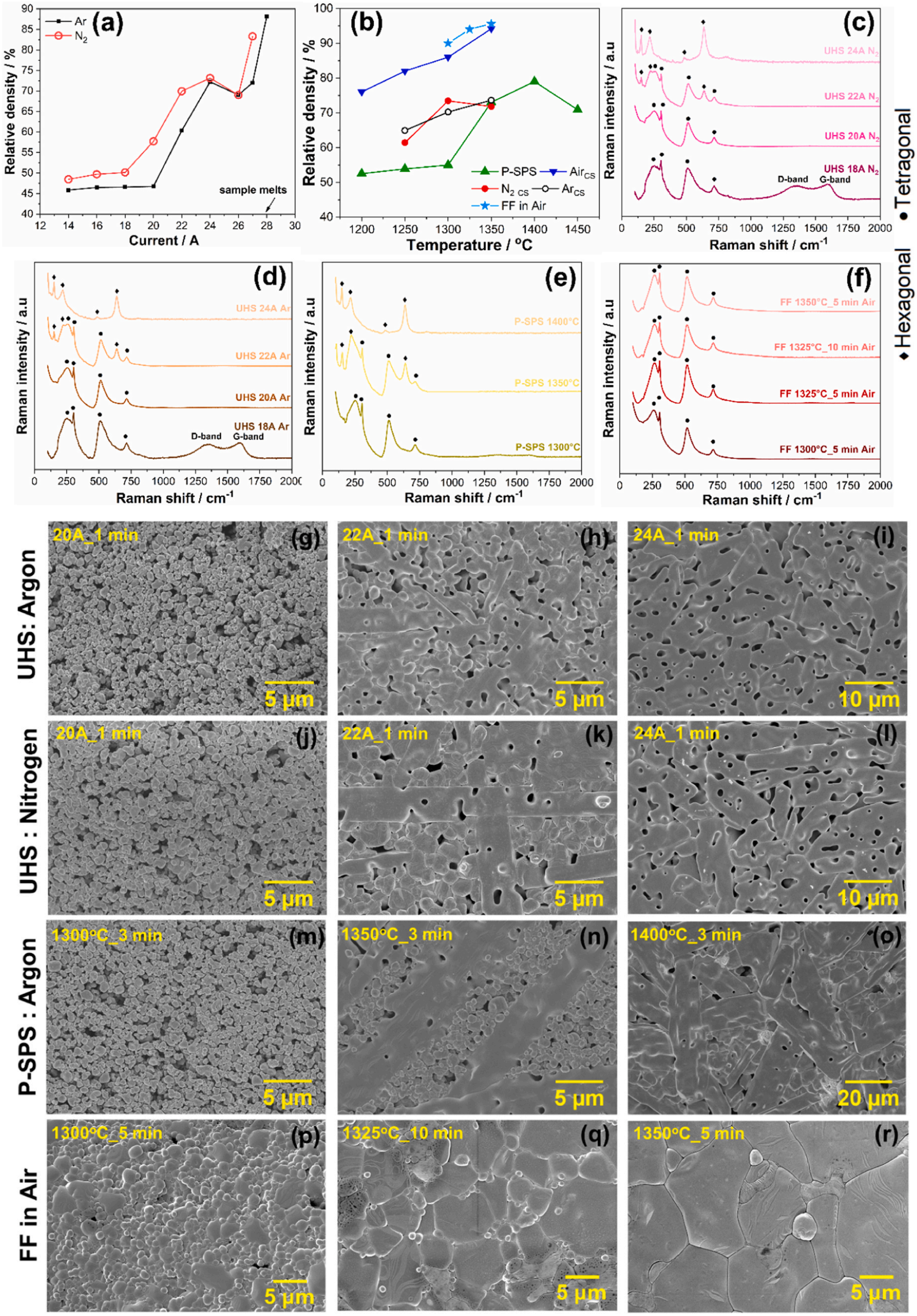

Fig. 32. Effect of the sintering atmosphere on the phase evolution and microstructure of sintered BT ceramics. Variation of the density as (a) a function of the applied current in UHS, and (b) a function of temperature, different hold time, and atmosphere in FF and P-SPS [113]. Raman and SEM analysis of the samples sintered using (c-d, g-l) UHS in different atmospheres, (e, m-o) P-SPS, and (f, p-r) FF [113].
Reproduced from Ref.: (a-r) [113], with permission from John Wiley and Sons.

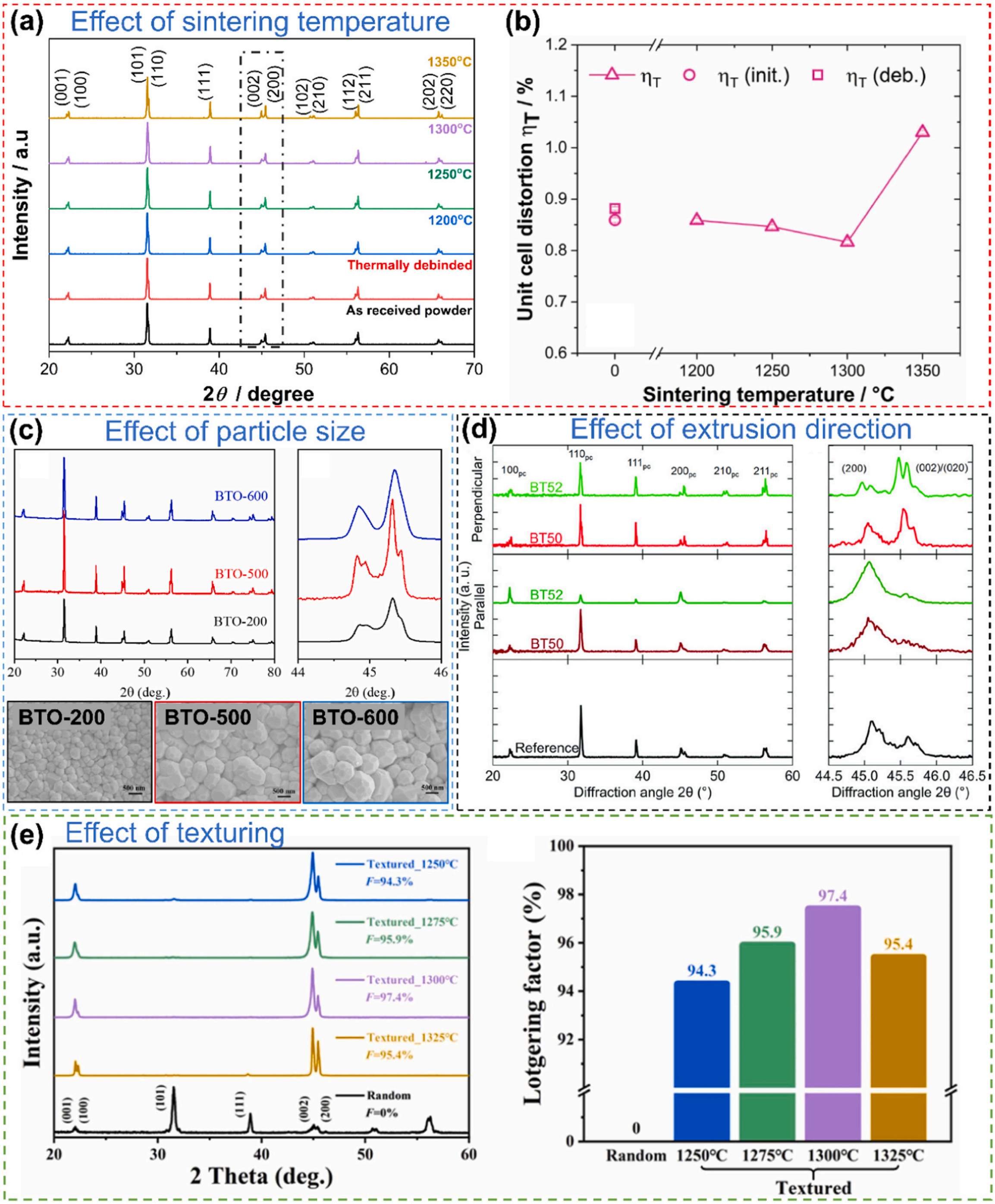

Fig. 33. Effect of sintering temperature, initial particle size, extrusion direction, and alignment on the XRD. XRD patterns of: (a) Sintered BT samples at various temperatures. The reflection at 45° has been marked with black colour and the corresponding unit cell distortion is shown in (b) [113], (c) Sintered BT ceramics with three different particle sizes; corresponding SEM images illustrating the diffraction patterns are provided below [147], and (d) Sintered BT samples measured in parallel and perpendicular to the extrusion direction [70]. (e) XRD patterns, and (f) Lotgering factor (F) values for both randomly oriented and textured BT ceramics sintered at different temperatures [163].
Reproduced from Ref.: (a-b) [113], (c) [147], and (e-f) [163], with permission from Elsevier. (d) [70], Open access article distributed under the terms of the Creative Commons CC BY license.

decrease in density as well as shrinkage (Fig. 34(a)) with precipitation of impurity phases (evidenced by XRD) and abnormal grain growth (Fig. 34(d)). The addition of CuO resulted in a shift of the reflection positions to lower 2θ angles [184] due to the larger ionic radius of Cu^{2+} compared to Ti^{4+} and Zr^{4+}, leading to lattice expansion. A similar reflection shift has been observed for substituting Ti^{4+} with Sn^{4+} in BT ceramics [167]. The decrease of the 200 reflection splitting (at $2\theta = 45°$) with increasing Sn^{4+} content, indicated the transformation of tetragonal to cubic symmetry.

In a recent study, authors have employed a mixture of copper oxide (CuO) and bismuth oxide (Bi_2O_3) as a sintering aid to induce liquid phase sintering [162]. It was found that the addition of the sintering aid increases the density (from 91 % to 93 %) and the Lotgering factor to about 58 %. In contrast, the Lotgering factor was only 2 % when only

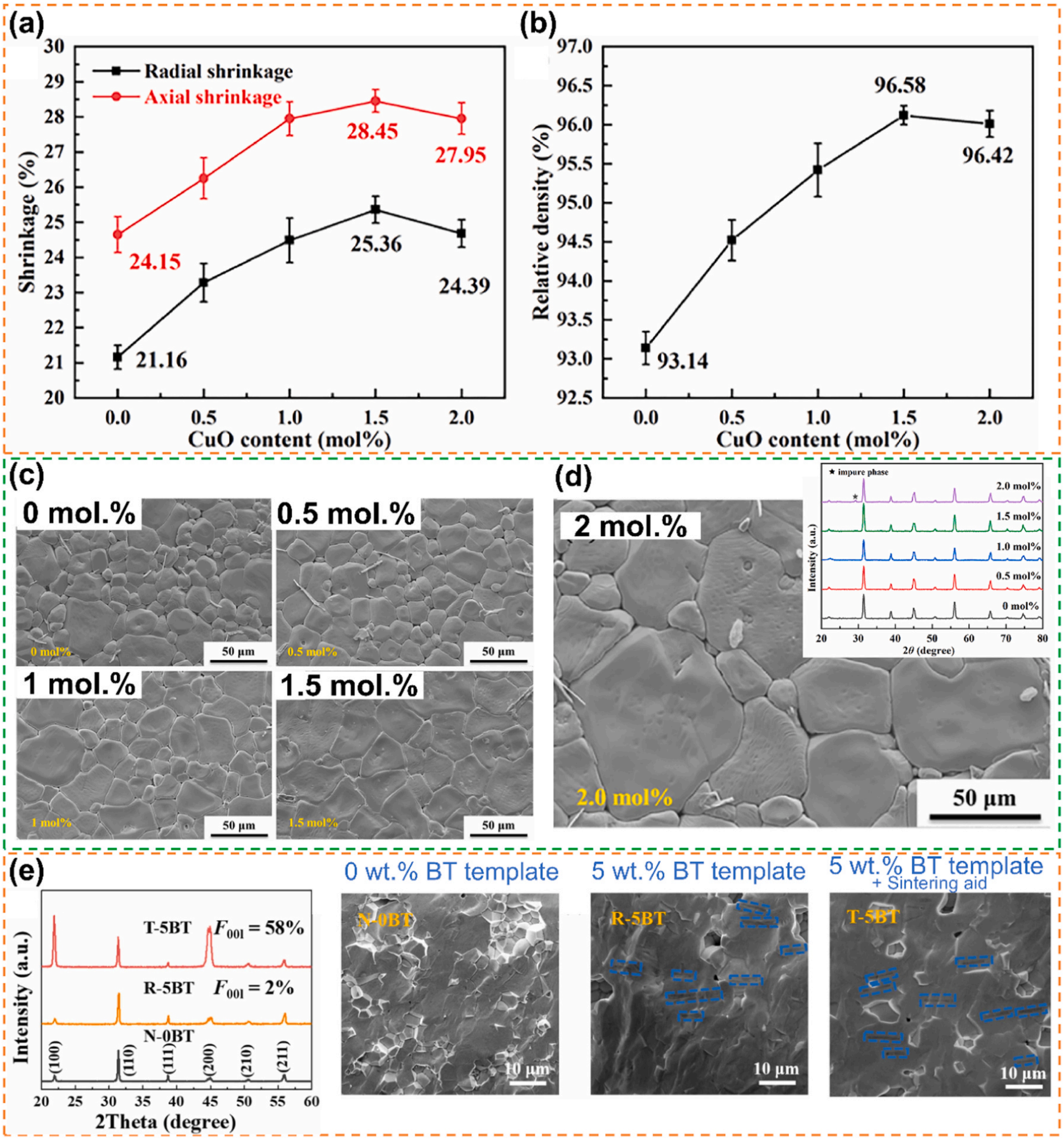

Fig. 34. Effect of sintering aid during sintering (a) Variation of shrinkage, and (b) Relative density of BCZT ceramics doped with varying amount of CuO. The corresponding microstructures are depicted in (c) [184]. (d) Abnormal grain growth with an excessive CuO content of 2 mol.% and the precipitation of unwanted secondary phases, as shown in the inset XRD pattern [184]. (e) XRD patterns of PMN-PT ceramics with BT templates and sintering aid, along with their corresponding SEM images [162].
Reproduced from Ref.: (a-d) [184], and (e) [162], with permission from Elsevier.

5 wt% of BT platelets were used without the sintering aid (Fig. 34(e)).

Usually, the permittivity (ε_r), which denotes the ability to store electrical energy, is measured as a function of frequency or temperature and shows maxima at phase transformation temperatures [86,139,146,147,150,158,168,171,172,180]. Above RT for BT ceramics ε_r decreases with temperature (up to 75 °C) which is correlated to the orthorhombic-to-tetragonal phase transformation [70]. Similar phase transformation temperatures have been reported for several other compositions [80,149,180,184]. Some compositions even show two intermediate phase transformation temperatures as reported for Sn-doped BT [167]. With a further increase in temperature up to the Curie temperature (T_c) the ε_r increases and shows a maximum at T_c [146,147,169,180]. A similar temperature dependence behaviour is exhibited by d_{33} or the piezoelectric coefficient. However, at T_c (Tetragonal to cubic phase transformation), the value decreases sharply to almost zero, denoting that the material no longer exhibits piezoelectric properties. Therefore, higher Curie temperatures are desired, so that the material can retain its piezoelectric properties at higher temperatures. For instance, the T_c of PZT (220 °C) [94] and KNN (230 °C) [180] are much higher than those of BT (130 °C) [70] and BCZT (86 – 88 °C) [51]. This suggests that PZT and KNN are better candidates when high temperature applications are necessary.

The T_c is a material specific property and is highy sensitive to various factors such as interfacial strain, defect density and internal stresses, all of which which depend on the microstructural features of the sintered ceramics. For BCZT ceramics, T_c decreases slightly with increasing sintering temperature or grain size. This is in good agreement with the fact that T_c varies inversely with grain size [51,223]. Conversely, an increase in the ceramic loadings (the grain size also increases) in the ink leads to an increase in T_c [151,224]. The authors reported that the increase is attributed to the growth of the domains with increasing grain size, while small grain sizes in the range of nanometres can increase T_c [146,147]. The fine grain size at nanometer level contributes to the improvement of T_c due to increased grain boundary effects, stress and surface-to-volume ratio. Additionally, the presence of residual porosity after the debinding, as well as the use of pore-forming agents increases the phase transformation temperatures [80,145,150,172,173]. This can be attributed to the stress relaxation near the porosity [225]. Interestingly, the effect of texturing on T_c is complex and reported to result in both decrease and increase. In a recent study, where BT platelets were used in a PMN-PT matrix, T_c decreased after texturing due to the heterogeneous interface effects leading to interfacial stress between the platelets and the matrix [162]. In contrast, when both the matrix and platelets are of the same composition, T_c is reported to increase after texturing because of the decreased grain boundary effects and aligned grain growth [163]. In a recent study, authors reported that T_c of BT ceramics decreases with increasing Sn^{4+} doping concentration *(*as shown later in Fig. 41(a-b)) [167]. This is related to the distortion in the lattice by substitution of Ti^{4+} by Sn^{4+}.

Permittivity (ε_r) measurements are often accompanied by dielectric loss (tanδ) measurements. Dielectric loss represents the energy lost in ferroelectric domains when they move in response to an applied electric field. The tanδ value increases with the frequency [146,147,150,171,180]. This is due to the fact that higher frequencies cause dipoles to reorient themselves more frequently, which can lead to a greater loss of energy. Additionally, sintered piezoceramics with low density and high porosity exhibit increased loss [85]. The presence of porosity leads to more interfaces, scattering of charges and disruption of uniformity, all of which contribute to tanδ. The dielectric loss also exhibits a sharp rise at T_c [51,94]. The phase change could potentially result in frictions between the ferroelectric domains, leading to enhanced tanδ [226]. Beyond the T_c, tanδ continues to rise, indicating that the material's ability to store and dissipate electrical energy changes as it moves away from its phase transformation point [151].

When considering the dielectric and piezoelectric response of the sintered samples, several parameters must be considered. In our investigation, we have identified the key parameters that significantly influence the electrical response of the material. Before proceeding further, let us provide a brief overview of the related piezoelectric or ferroelectric behaviour, which will be often used in the subsequent discussions.

a. *Piezoelectric coefficient or d_{33}:* This value quantifies the electrical displacement generated per unit of the applied mechanical stress along the same direction of the electrical field. Higher d_{33} implies more efficient conversion of mechanical to electrical energy.
b. *Remanent polarization or P_r:* This value dictates the ability of the material to retain polarization in the absence of an electrical field. Polarization in this text refers to the alignment of the dipoles. Usually, the dipoles are randomly oriented in the absence of an electrical field. On applying an electric field, the dipoles are oriented in the direction of the applied field.
c. *Strain or S*: Strain represents the relative change in the dimension of the material when subjected to an external electrical field.
d. *Piezoelectric voltage coefficient or g_{33}*: This value quantifies the electric field (or voltage) generated in the same direction as the applied stress.
e. *Figure of merit (FOM)*: This a measure of overall efficiency of a particular device. It takes into account different piezoelectric coefficients, permittivity and mechanical quality factors.

(i) Effect of initial particle size

The particle size of powders plays a crucial role in determining their functional properties, particularly in piezoelectric and dielectric ceramics. At identical sintering temperatures, a powder with fine particles exhibits high sinterability, leading to grain growth and a dense microstructure easily. This is because fine particles have a larger surface area to volume ratio, which enhances the mass diffusion promoting the sinterability and grain growth. Conversely, a powder with coarser particles shows limited grain growth with residual porosity due to incomplete sintering. Hence, finer particles should exhibit superior properties compared to coarser particles (Fig. 35(a-b)) [58,59]. In a recent study, authors employed different sintering temperature for different particle size of the initial powder [147,194]. For instance, a temperature of 1300 °C, 1320 °C, and 1330 °C was selected for powder of 200 nm, 500 nm, and 600 nm in size. The best properties were achieved for 600 nm powder as the grain size after sintering was around 875 nm [147]. According to Ma *et al.*, optimal functional properties were observed with a particle size of 1.5 μm, while finer particles (0.6 μm) caused micro-cracks in the sample, due to weak inter-layer adhesion [141]. Increasing the particle size to 1.5 μm led to a decrease in density, which negatively impacted the dielectric/piezoelectric properties.

The situation becomes complex with a multi-modal particle size distribution. For instance, properties in a bi-modal particle size distribution decreased with increasing volume fraction of the coarser particles [61]. However, piezoelectric characteristics peaked at equal fractions of particles of 100 nm and 400 nm (Fig. 35(c-d)). This can be attributed to better densification behaviour and optimal grain size (1.46 ± 0.277 μm). Several studies reported that better properties are achieved when the average grain size after sintering is close to 1 μm [16,147,158]. In order to achieve a grain size of around 1 μm, the authors employed appropriate ratio (2:8) of fine and coarse powders [158].

To understand the peak value of properties, it is essential to consider the size of the domains and the configuration of the domain walls. In ferroelectric materials like BT, domains are regions where the electric polarization is uniformly aligned in a particular direction. These domains are separated by domain walls, which are boundaries where the polarization direction changes. Typically, the tetragonal phase of BT consists of two types of domains: anti-parallel 180° domains and perpendicular 90° domains [227]. In coarser grains (>10 μm), both types of domains are present as coarser grains provide more space to accommodate multiple domain configurations. Conversely, only 90° domain walls are dominant when the grain sizes are <10 μm. When the grain sizes are around 1 μm, the width of the 90° domains decreases [228]. Smaller grain sizes lead to smaller domains with higher domain wall densities, thereby increasing sensitivity to applied external fields or stress. However, well below 1 μm the domain wall mobility decreases significantly, resulting in lower properties [15,16,229].

BT ceramics exhibit optimal dielectric and piezoelectric properties at an average grain size of approximately 1 μm and a stoichiometric Ba/Ti ratio of 1 [229]. At this grain size range, the density and mobility of domain walls are maximized, enhancing the material's response to electric fields. This grain size range also minimizes the adverse effects of grain boundaries, which can pin domain walls and reduce their mobility in smaller grains. Maintaining a precise Ba/Ti ratio is equally crucial. A stoichiometric Ba/Ti ratio ensures minimal defects and secondary phases, which can degrade the material's properties. Ba deficiency ($Ba/Ti < 1$) leads to the formation of titanium-rich phases and oxygen vacancies, which pin domain walls and reduce the permittivity. Conversely, Ba excess ($Ba/Ti > 1$) introduces barium-rich phases and localized stresses, negatively impacting the dielectric and piezoelectric properties. It is worth noting that while an average grain size around 1 μm often results in high properties, it is not a straightforward conclusion. For instance, Sufiiarov *et al.* reported that the best properties are achieved when the grain size of the sintered BT ceramic is 10 – 50 μm [194]. The functional properties of BT ceramics are quite complex and depend on various factors, such as grain size, grain boundaries, domain walls, stoichiometry, defect chemistry and porosity.

(ii) Effect of ceramic loadings and binder concentration

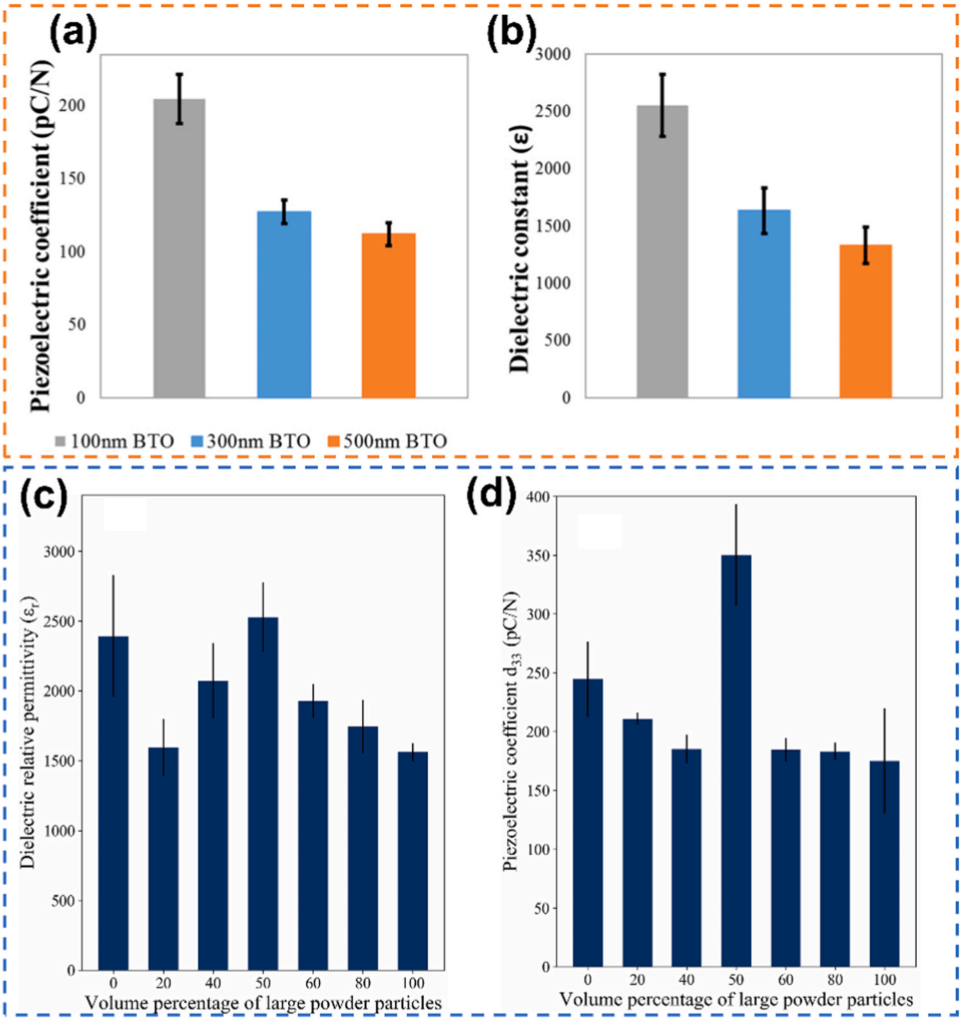

Fig. 35. Effect of particle size on the piezoelectric/dielectric properties. Variation of: (a) Piezoelectric coefficient, and (b) Dielectric constant as function of different unimodal particle size [58]. (c) Dielectric permittivity, and (d) Piezoelectric coefficient as a function of bimodal particle size, with different ratios of fine and coarse particles [61].
Reproduced from Ref.: (a-b) [58], with permission from IOP Publishing. (c-d) [61], with permission from Elsevier.

The electrical properties of functional ceramics are strongly influenced by the ceramic loading in the ink. As the ceramic loading increases, the amount of binder decreases, leading to improved densification and reduced porosity. Lorenz *et al.* reported that the dielectric and piezoelectric response of the sintered ceramic increased on increasing ceramic loading from 50 to 52 vol%. The samples fabricated with 52 vol% exhibited higher piezoelectric coefficient and relative permittivity values, as illustrated in in Fig. 36(a-b) [69]. However, this improvement works just up to a certain threshold. For instance, Cheng *et al.* used different amounts of BT (70 wt%, 75 wt%, 80 wt%, 82 wt%, 84 wt%, 86 wt%) and found that the piezoelectric (96 – 133 pC/N) and ferroelectric response increases to 80 wt% of ceramic loading, but slightly decreased beyond this point as evidenced by the P/E hystereses in Fig. 36(c) [194]. A similar variation in the properties has been reported by several authors [127,137]. In general, the polarization value also increases with the applied electric field as shown in Fig. 36(d), since the polarization is proportional to the electric field.

It has been reported that beyond an optimal point, further increase in ceramic loading can lead to higher viscosity, resulting in processing difficulties and defects that can negatively impact the properties [61, 114,121,145]. Therefore, maintaining an optimal balance between ceramic loading and binder content is crucial for achieving superior electromechanical performance.

In a recent study, authors explicitly reported the effect of different amount of binder on the electrical properties. For this, the binder concentration was varied from 6 – 12 wt% (in steps of 2 wt%). It was found that with 10 wt% binder, the grain growth was optimal, the particle size was uniform, and there were fewer defects, leading to a maximum in the dielectric and piezoelectric response (Fig. 36(e-f)) [84]. The authors also correlated this behaviour with the shape of the ferroelectric domains. For ceramics containing up to 6 wt% binder, the sintered ceramics exhibited a reversible 90° domain configuration. However, with higher binder concentrations, the grain size increased, leading to the appearance of irreversible 180° domain configurations. At a binder concentration of 12 wt%, the ceramics contained only irreversible domains. A similar effect has been reported for samples with different binder saturation (75 %, 90 %, and 120 %) values [162]. Maximum d_{33} value was reported for the sample fabricated with binder saturation of 90 % *(*Fig. 36(g)). The use of excessive binder might generate a local overpressure on the powder bed, resulting in the movement of particles away from each other. This can potentially hinder densification during sintering, resulting in decreased piezoelectric properties.

(iii) **Effect of sintering temperature, hold time and cooling rate**

The sintering temperature and holding time significantly impact the

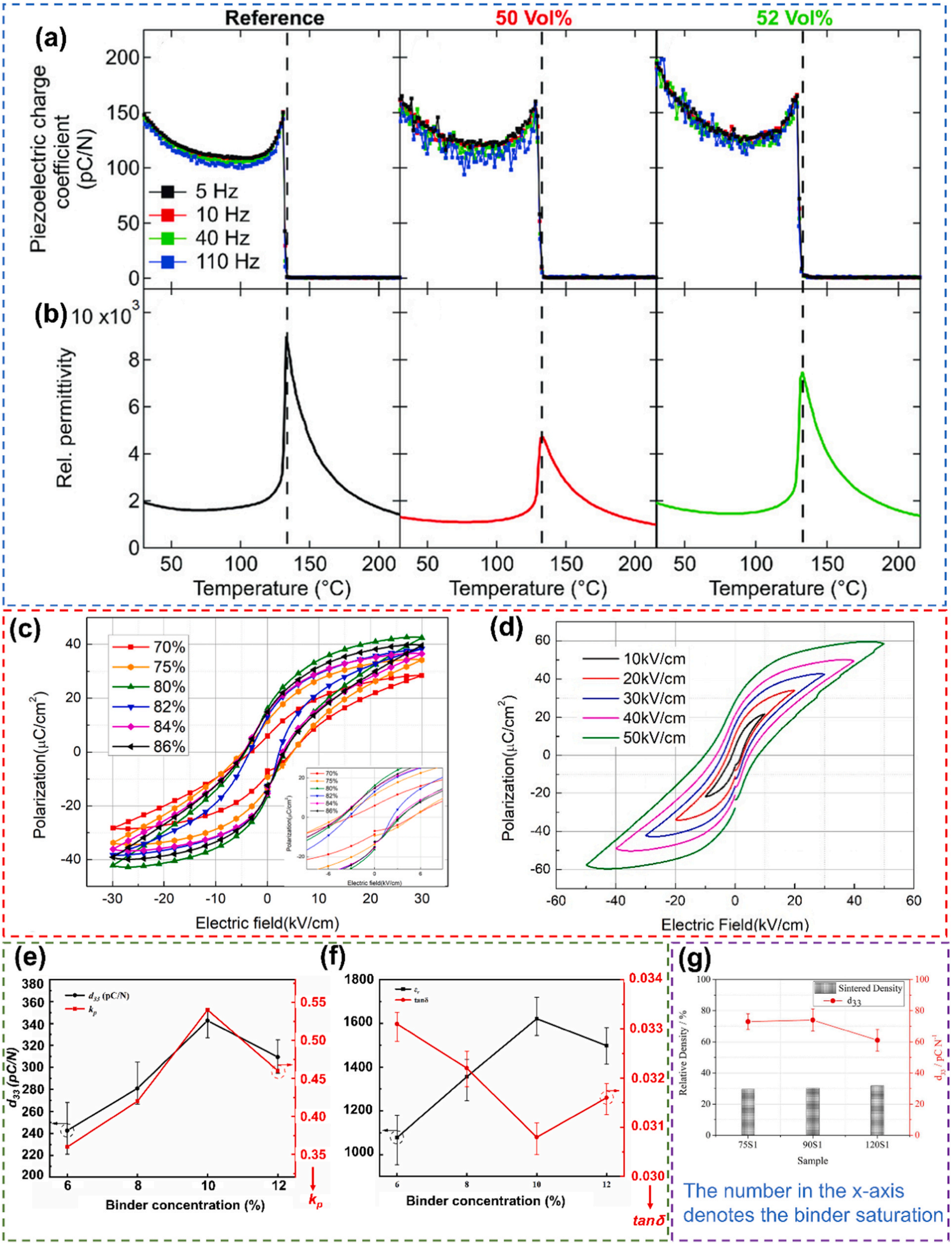

Fig. 36. Effect of the ceramic loading and binder concentration on the electrical properties. (a) Piezoelectric charge coefficient, and (b) Relative permittivity as a function of temperature for BT samples fabricated with varying amount of ceramic loadings [70]. (c) Polarization-electric field (P-E) hysteresis loops of sintered ceramics with different BT concentration (inset shows the magnified image highlighting the remanent polarization). The corresponding P/E loops for 80 wt% BT with different electric fields are shown in (d) [224]. The effect of the binder (PVA) content on the (e) Permittivity and dielectric loss, and (f) Piezoelectric coefficient of PZT ceramics [85]. (g) Variation of the piezoelectric coefficient as a function of the binder saturation value for binder jetted KNN samples [191].

(a-b) [70], (c) [224], Open access article distributed under the terms of the Creative Commons CC BY license. Reproduced from Ref.: (d-e) [85], and (f) [191], with permission from Elsevier.

microstructural and electromechanical properties. As the sintering temperature increases, the mechanisms of mass diffusion in the material are enhanced. The phenomena of densification and grain growth occur more rapidly. If the parameters are adjusted to obtain a dense microstructure, with desirable grain sizes, no defects and no porosity, this will result in a better dielectric and piezoelectric response from the material (Fig. 37(a-c)) [51,86,149]. Higher temperatures and appropriate holding times facilitate better sinterability, leading to larger, more uniform grains and reduced porosity, which enhance domain wall mobility and overall material response. However, beyond an optimal sintering temperature and holding time, properties begin to decline (Fig. 37(a-c)) [149,183,198]. This decline is attributed to over-sintering, which causes excessive grain growth, grain coarsening and the potential formation of secondary phases that disrupt the uniformity and stability of the material. Excessive grain growth can lead to decreased density and create undesirable internal stresses, ultimately reducing the dielectric and piezoelectric properties. Thus, while increasing the sintering temperature and optimizing holding time initially enhances the properties by improving microstructural characteristics, surpassing the optimal point results in a degradation of these properties due to the adverse effects of over-sintering. Moreover, to avoid the large grain size that could reduce the piezoelectric properties, a recent study with 3D printed BT used a step cooling profile, resulting in an average grain size around 1 μm with d_{33} value reaching 420 pC/N (Fig. 37(d)) [93]. However, the d_{33} value increased from 290 to 360 pC/N on increasing the dwelling time from 2 to 20 h resulting in a grain size up to 2 – 3 μm, which is less than the value obtained using the step cooling process (see Fig. 29(g-i) for the microstructure).

(iv) **Effect of texturing**

Texturing has a significant impact on the properties of piezoelectric ceramics by aligning the grains in a preferred crystallographic orientation. This alignment significantly increases the piezoelectric coefficients of ceramics.

For instance, Zheng *et al.* reported that in PMN-PT ceramics, textured via BT platelets, d_{33} was approximately 60 % higher compared to non-textured ceramics [162]. Additionally, texturing affects other properties as well. The remanent polarization (P_r) decreases from 25.5 μC/cm^2 for non-textured samples to 19.5 μC/cm^2 for textured samples (Fig. 38(a)). The maximum ε_r at T_c decreases from approximately 22,100 in non-textured ceramics to around 18,500 in textured ceramics (Fig. 38(b)). This decrease in ε_r in textured ceramics is primarily associated with the lower dielectric ε_r of BT platelets at T_c compared to the matrix. However, at room temperature, the ε_r is higher for the textured samples which can be related to the enhanced extrinsic contributions at low temperatures (Fig. 38(b)). Extrinsic contributions such as domain reorientations play a more significant role at lower temperatures, when the unit cell distortion is larger. Furthermore, the maximum unipolar strain (S_{max}) at 25 kV/cm is 0.20 %, which is about 1.4 times that of the non-textured sample (Fig. 38(c)). Similar results were reported by Walton *et al.*, who observed a substantial improvement in strain and piezoelectric coefficient values that became more pronounced with increasing aspect ratio of the extrusion nozzle [91]. This significant enhancement in strain is another proof to the improved performance of textured ceramics.

Similarly, Du *et al.* reported a larger piezoelectric coefficient (d_{33} = 275 pC/N) in printed textured BT ceramics compared to non-textured BT ceramics (d_{33} = 172 pC/N) [163]. This improvement in the piezoelectric properties is accompanied by a significant enhancement in remanent polarization (P_r) values, with non-textured and textured samples showing approximately 6.15 μC/cm^2 and 14.88 μC/cm^2, respectively

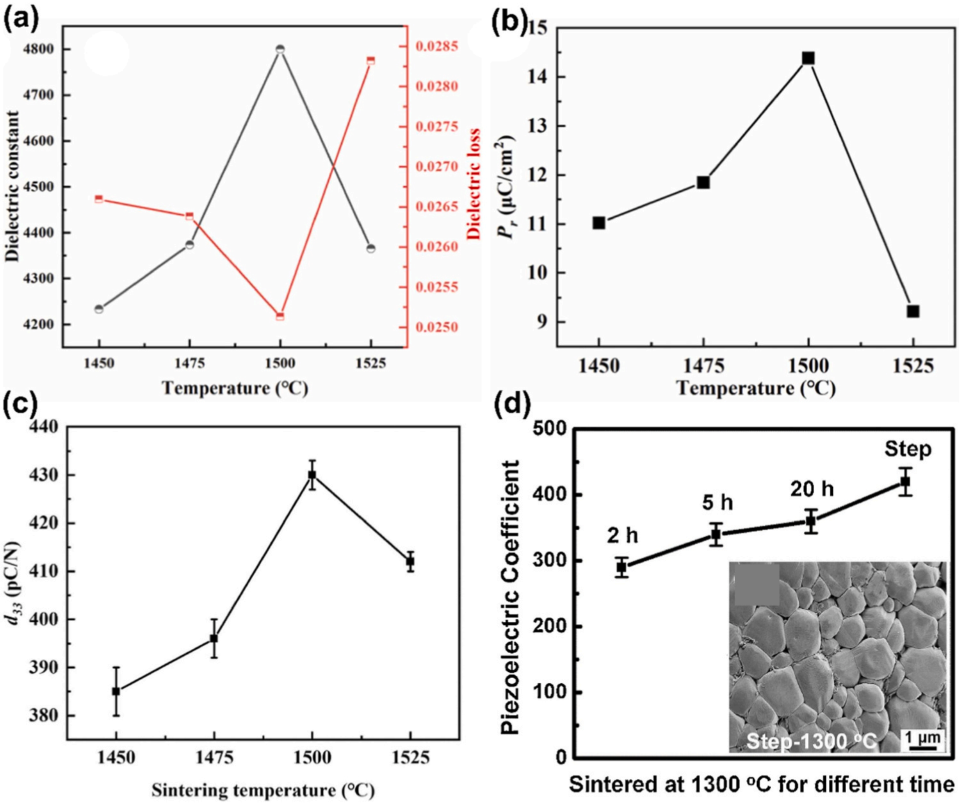

Fig. 37. Effect of the sintering temperature, hold time or cooling time on the electrical properties. Variation of the (a) Permittivity and dielectric loss, (b) Remanent polarization, and (c) d_{33} as a function of sintering temperature for sintered BCZT ceramics [149]. (d) Impact of dwelling time and step cooling process on the piezoelectric coefficient of sintered BT ceramics [93]. The inset shows the micrograph for the step cooled sample.
Reproduced from Ref.: (a-b) [149], and (c-d) [93], with permission from Elsevier.

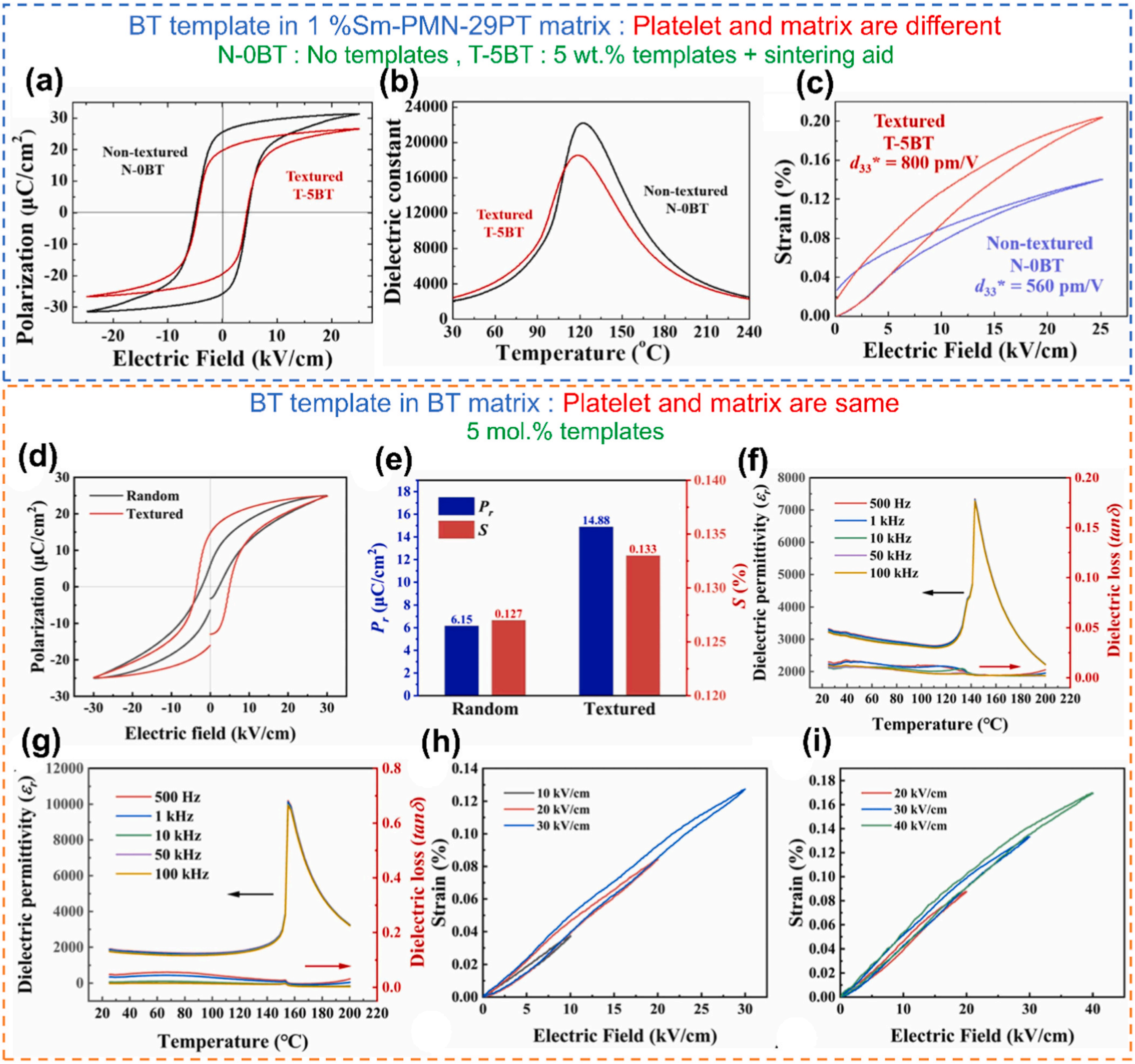

Fig. 38. Texturing effect on different electrical properties. Effect of texturing on [162]: (a) Polarization-electric field (P-E) hysteresis loops, (b) Temperature dependent permittivity at 1 kHz, and (c) The unipolar strain by using BT platelets in a PMN-PT matrix. Effect of texturing using BT platelets in a BT matrix [163]: (d) Polarization-electric field (P-E) hysteresis loops, (e) Comparison of the remanent polarization and strain at an electric field of 30 kV/cm, and Dielectric permittivity, dielectric loss, and strain of (f, h) Random, and (g, i) Textured BT ceramics sintered at 1300 °C.
Reproduced from Ref.: (a-c) [162], and (d-i) [163], with permission from Elsevier.

(Fig. 38(d-e)). The enhanced P_r is attributed to the more effective alignment of dipoles in the <001>-textured BT ceramics under a high direct current electric field. Furthermore, at 1 kHz and 25 °C, the textured samples exhibit a smaller permittivity (~1867) compared to the random samples (3303) (Fig. 38(f-g)). The dielectric loss increases in the textured sample. When subjected to an electric field of 40 kV/cm, the strain value exhibits a maximum of 0.17 % for the textured one (Fig. 38 (i)). In contrast, the random oriented samples are broken with such high field (Fig. 38(h)). Buessen *et al.*, developed an internal stress model that correlates the permittivity and the 90° domain configurations [230]. At room temperature, a BT single crystals show strong anisotropy in the permittivity with highest values along the a axes [231,232]. In polycrystalline BT, the permittivity may reach even higher values due to complex domain configurations and phase transformations, which allow more directions for the reorientation of the spontaneous polarization and stress distributions [16]. Using large plate-shaped particles to texture the material may have a positive effect on the piezoelectric constant. However, the permittivity might be reduced due to limited possibilities for the polarization orientations.

The reason for the larger piezoelectric coefficients is that texturing aligns the domains more uniformly towards the external loading direction. This alignment optimizes the contribution of each domain to the overall piezoelectric response, significantly increasing the piezoelectric coefficients. In addition to enhancing piezoelectric properties, texturing reduces grain boundary scattering and ensures a more uniform stress distribution across the material. The uniform domain alignment facilitates the material's ability to undergo larger deformations when an electric field is applied, resulting in high strain. Additionally, the alignment enhances the material's ability to retain polarization after the removal of the external electric field, leading to a higher P_r. This not only improves the mechanical stability of the ceramics but also contributes to their overall performance and reliability in various applications.

(v) Effect of sintering additives or dopants

The main purpose of adding sintering additives or dopants is to enhance the functional properties. As discussed before, Copper oxide (CuO) is one of the most widely used sintering aid to improve the densification behaviour of the ceramics by forming a transient CuO-BaO liquid phase and facilitating liquid-phase sintering [184]. The electrical properties of the CuO-doped ceramics increase up to a certain concentration because of the increase in the density and grain size (Fig. 39(a-c), please refer to Fig. 34(c-d) for the corresponding microstructures). The grain growth facilitates the movement of domain walls during the polarization process, while the increase in density leads to a more even distribution of electric fields and enhanced polarization efficiency. Further increasing the concentration, the porosity reappears in the samples (or the density decreases) that deteriorates the ferroelectric response.

In a recent study, authors have introduced Sn^{4+} to substitute Ti^{4+} at B-sites in BT ceramics [167]. With increasing Sn^{4+} content (up to 13 mol.%), the room temperature ε_r increases. This is due to fact that the ceramics with higher Sn^{4+} content (11, 13 mol.%) exhibited fine grains of about 1 – 5 μm. On the other hand, the grain sizes were in the order of 4 – 10 μm for Sn^{4+} content of 2 and 6 mol.%. The ferroelectric properties of such doped ceramics decrease with the increasing Sn^{4+} content, as evidenced by the thinning of the P-E loops (Fig. 40(c-d)). The P_r decreases significantly from 11.92 μC/cm² to 1.11 μC/cm². This can be attributed to the fact that since $BaSnO_3$ is non-ferroelectric, increasing the amount of Sn gradually changes the behaviour of a normal ferroelectric to a diffuse ferroelectric as depicted from the dielectric behaviour (Fig. 40(a-b)). The piezoelectric coefficient values increased up to 6 mol.% of Sn^{4+} because of bigger grains and enhanced density and thereafter decreased for higher concentration due to small grain size and reduced density as a result of insufficient sintering (as the Sn content increases, the sintering temperature increases correspondingly).

(vi) Effect of pore forming additives

The addition of pore-forming additives such as PMMA, PE, PS, SS, etc. has a detrimental effect on the piezoelectric and ferroelectric characteristics, as it results in the formation of residual porosity that remains even after the additives are removed during the subsequent debinding and sintering process [145,150,171–173].

With increasing amount of the PFAs, the ε_r and piezoelectric coefficient decreases because of the reduced sintered density (Fig. 41(a-b)) [150,171,172]. The ferroelectric behaviour exhibits a similar response (Fig. 41(c)). The presence of residual porosity after debinding results in an increase of the unpolarized region (pores) in the sintered ceramics (or in other words, decreasing the active area for polarization). The higher the amount of PFAs, the lower is the response. A similar effect is

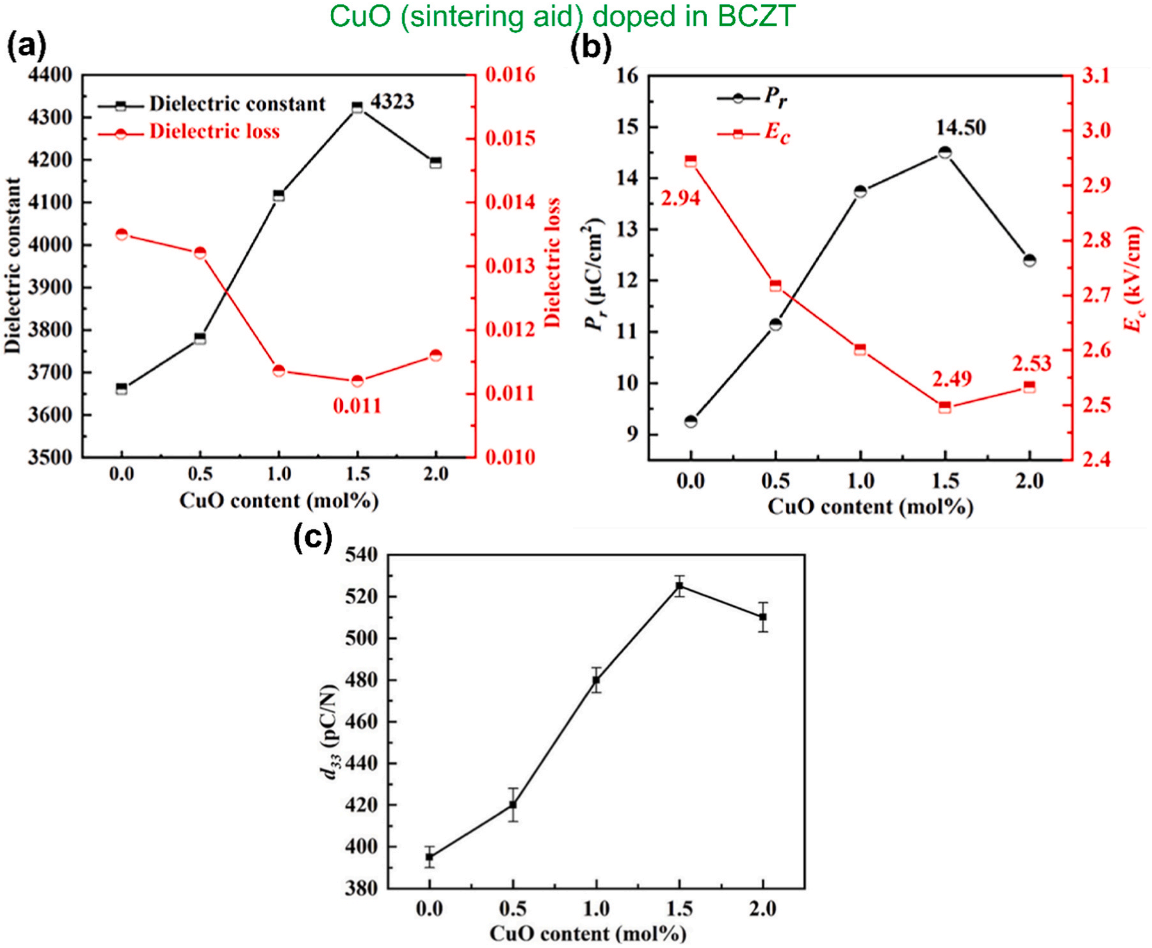

Fig. 39. Effect of sintering aid on the electrical properties. Variation of (a) Permittivity and dielectric loss, (b) Remanent polarization, and (c) Piezoelectric coefficient of BCZT ceramics doped with varying CuO content [184].
Reproduced from Ref.: (a-c) [184], with permission from Elsevier.

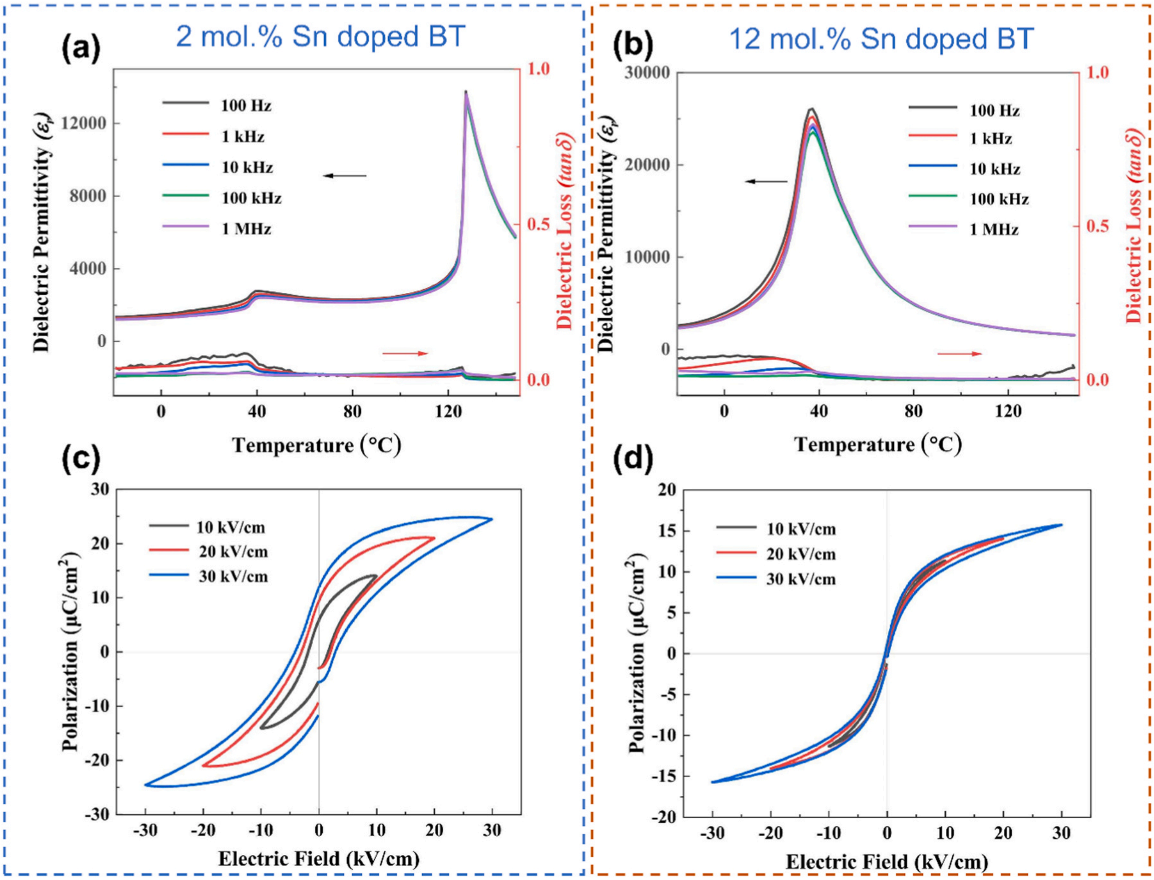

Fig. 40. (a-d) Variation of the dielectric and piezoelectric properties with varying Sn^{4+} content in BT ceramics [167].
Reproduced from Ref.: (a-d) [167], with permission from Elsevier.

observed on increasing the particle size of the PFAs [173].

(vii) Effect of the design

The design of the printed geometries has the potential to significantly alter the functional properties that may not be achieved with conventional shaped geometries. Several studies have reported the effect of the design or the infill density on the properties of the fabricated component.

Hierarchical porous PZT as depicted in Fig. 42(a), with different amounts of ceramic phase exhibit different overall porosities [98]. The ε_r values and the piezoelectric coefficients increase with the increasing the overall fraction of the ceramic phase that actively contributes to the functionality. As evidenced in Fig. 42(b-c), since the decrease/increase in d_{33} was more gradual when compared to ε_r, the g_{33} value decreased with increasing porosity. The authors reported by varying the geometrical porosity (along with the porosity developed due to freeze casting) they could achieve really high d_{33}, g_{33} and better sensitivity.

In another study, authors reported the effect of an open and offset scaffold structure on the electromechanical properties [116]. A significant decrease in the electromechanical properties was observed when comparing the scaffold and offset sample with the powder pressed pellet (Table 7 and Fig. 42(d)). In addition, the offset sample exhibited better properties than the open scaffold. Unlike in the open structure, where the pores are continuous and open, in an offset structure, these pores are closed when the next layer is printed (Fig. 42(e)). As a result, the effective polarizing material is higher in offset structures. The g_{33} is directly proportional to d_{33} and inversely proportional to the ε_r. One can clearly observe from Table 7, that the difference in the ε_r values is larger than the difference in d_{33} values. As a result when considering g_{33} value for figure of merit (FOM), the open scaffolds outperform the offset structures.

A study by Ma *et al.* investigated the electromechanical properties of porous gyroid structures with varying designed porosities (55 vol% – 75 vol%) as shown in Fig. 42(f) [165]. The simulation results indicated that there was minimal difference in the electric field distribution between structures with 60 vol% and 70 vol% porosity. This finding suggests that the electric field distribution in porous structures is more dependent on the geometry of the structure rather than the level of porosity. Additionally, the study revealed that the piezoelectric coefficient d_{33} of the gyroid structure with 50 vol% porosity can approach values similar to those of bulk structures, though only under higher electric fields (Fig. 42(g)). This is due to the fact that porous ceramics require a stronger poling electric field to achieve complete polarization compared to their bulk counterparts. Notably, the d_{33} values remained stable even as porosity increased (Fig. 42(h)). However, the dielectric constant and the polarization showed a significant decrease with higher porosity. Such results prove that the d_{33} is independent of the amount of the porosity in the structure (Fig. 42(i)). The strain however did not exhibit a straightforward relationship but was in the range of 0.07 – 0.1 %.

A recent study exhibited that by increasing the wall thickness of the triply periodic minimal surface (TPMS) structures, the ε_r and d_{33} values increase [192]. Moreover, these TPMS structures exhibited better sensitivities and efficiencies when converting mechanical energy to electrical and vice versa. Such sensitivities and efficiencies were measured by comparing the electromechanical coupling coefficient.

(viii) Effect of properties along different direction

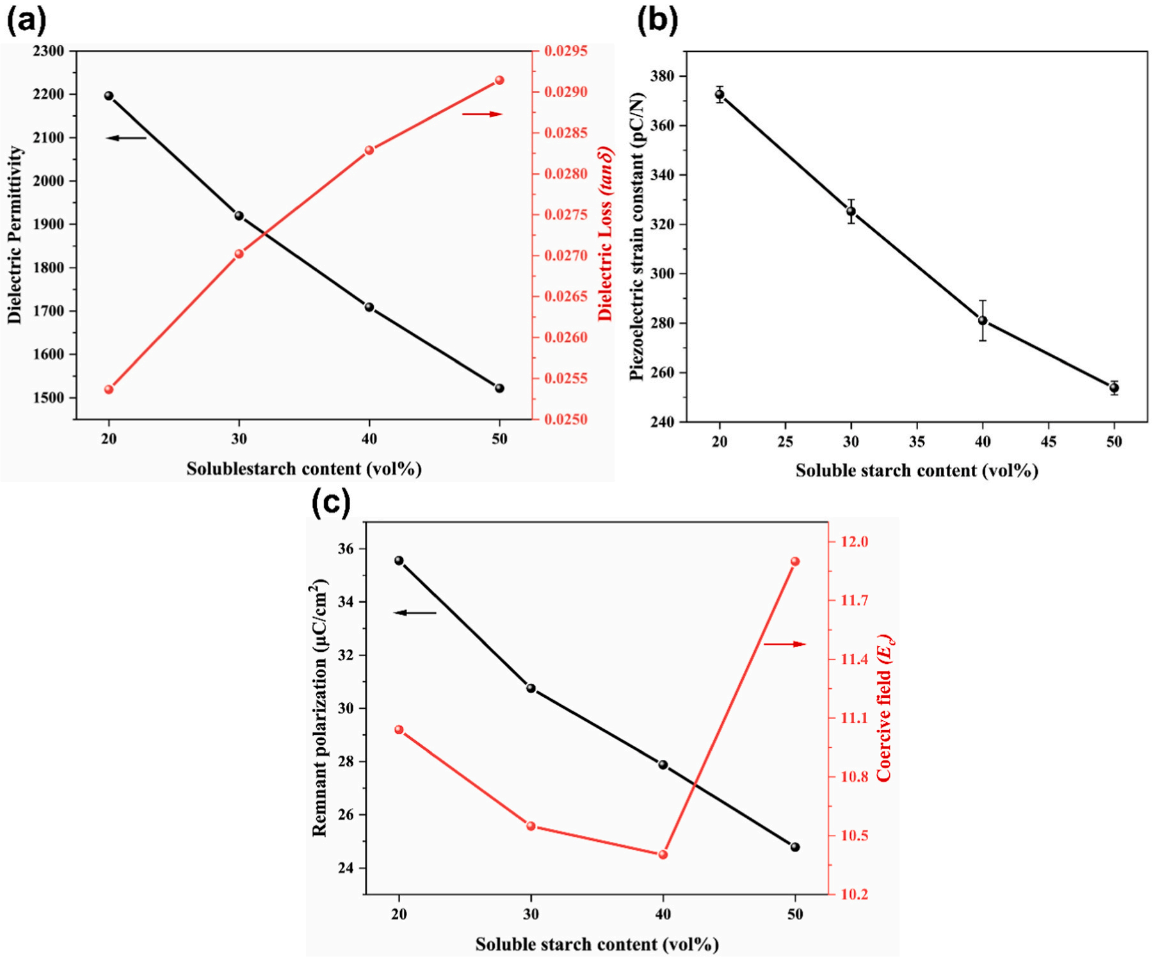

Fig. 41.
Effect of using different amounts of PFAs. (a) Variation of the: (a) Permittivity and dielectric loss, (b) Piezoelectric coefficient, and (c) Remanent polarization of sintered PZT ceramics with varying amount of soluble starch [150]. Reproduced from Ref.: (a-c) [150], with permission from Elsevier.

The dielectric and piezoelectric properties of the sintered samples vary depending on the poling directions or the direction in which they are tested. Ceramics fabricated using BJ technology exhibit high orthotropy due to voids formed during both the fabrication and heat treatment processes. These voids significantly impact several properties of the printed ceramics, especially their functional properties.

Recent findings indicate that the piezoelectric properties of binder jetted BT depend on the testing orientation [200]. Samples tested perpendicular to the printing layers showed a piezoelectric response more than 35 % higher than those tested parallel to the layers. Additionally, the dielectric properties were 20 % better in the samples tested perpendicularly, compared to those tested in parallel. A similar result was reported for PZT samples fabricated by BJT, showing higher piezoelectric properties for samples tested perpendicularly, compared to those tested parallelly [193]. The average piezoelectric response for the parallel samples was 468.5 pC/N, while the perpendicular samples yielded 541.4 pC/N (Fig. 43(a)). In another study on BJ-printed KNN, the d_{33} was measured both parallel and perpendicular to the layer deposition direction [191]. However, the effect of the testing orientation appeared to be minimal. The d_{33} value in the parallel orientation was approximately 84.8 ± 9.2 pC/N, while in the perpendicular orientation it was 89.9 ± 3.8 pC/N.

The differences in dielectric and piezoelectric properties of ceramics in different orientations arise from the anisotropic nature of the binder jetting additive manufacturing process. In the perpendicular orientation, the layer-by-layer fabrication results in a microstructure with oriented porosity that forms a set of capacitors arranged in a parallel circuit (Fig. 43(b)). Consequently, there is no negative impact on the electrical performance. However, in the parallel direction, the porosity forms a series circuit, which lowers the electrical properties of the system (Fig. 43(c)) [200]. In contrast, BJ-printed KNN shows minimal directional differences due to higher densities and uniform internal porosities, maintaining consistent structural integrity despite some preferential porosity orientation [191].

The phenomenon of anisotropy has been also reported for samples fabricated with DIW (Fig. 43(d)) [70]. The anisotropy was more pronounced in samples with lower ceramic loadings (50 vol%) due to their low relative densities after sintering. However, no significant differences were noted in samples with 52 vol% ceramic loading, as they exhibited better densification and limited residual porosity. Similar results were observed for samples fabricated using vat photopolymerization [190]. As the solid loading in the ink increased, the properties of the samples became almost identical in both directions as shown in Fig. 43(e).

Having examined the key parameters that influence piezoelectric and ferroelectric properties, it is essential to now assess the impact of the additive manufacturing process on these properties. When evaluating piezoelectric and ferroelectric characteristics in additive manufacturing (AM), it is critical to consider not only the printing and sintering parameters, but also the properties of the initial powder input. Even minor differences in powder characteristics such as particle size distribution, surface chemistry, purity, and morphology can have a major impact on sintering behaviour and ultimately, material properties. Because of

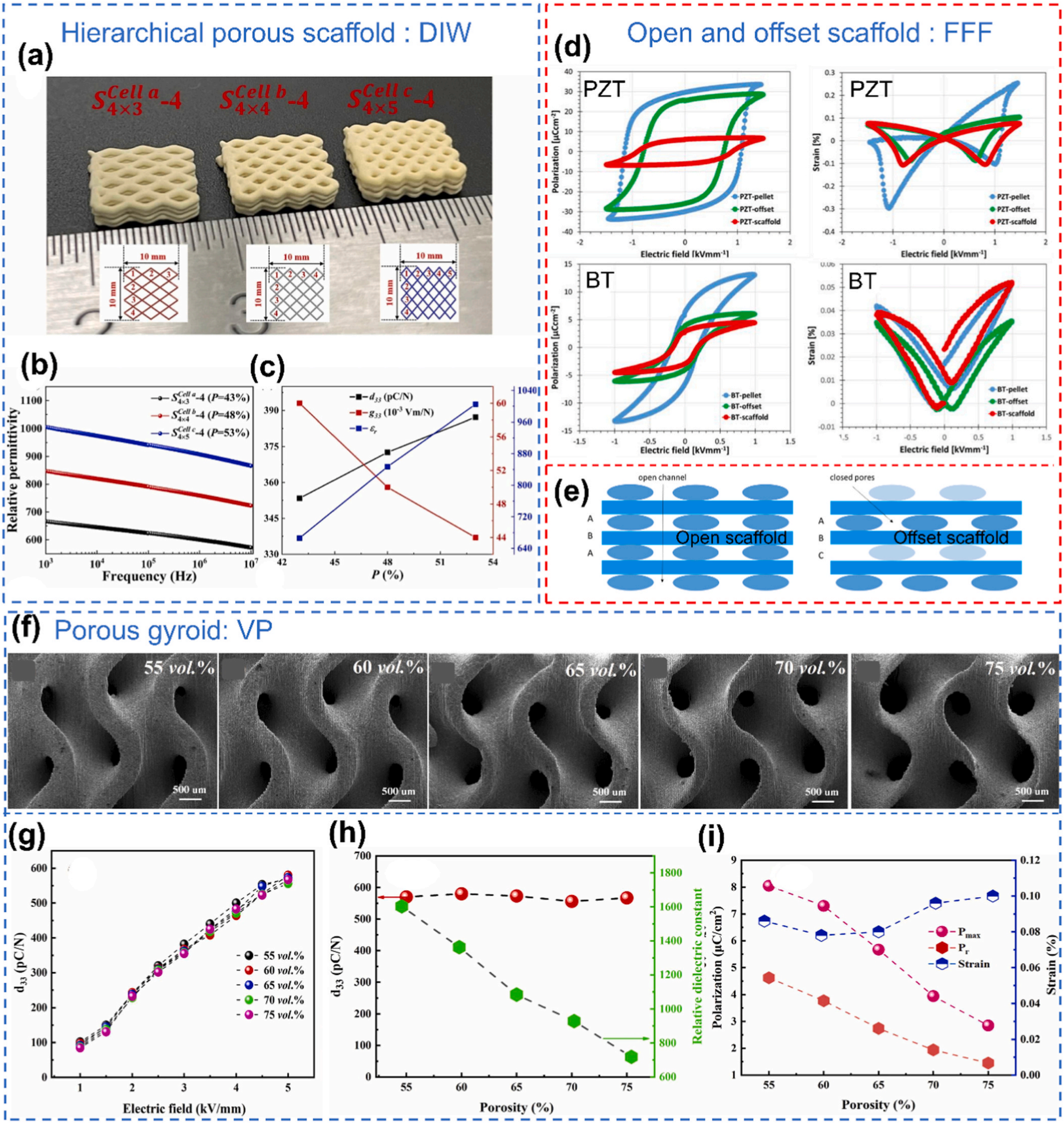

Fig. 42. Design dependent electrical properties. (a) Optical image of the hierarchical porous PZT scaffolds with different infill density. The corresponding evolution of permittivity as a function of frequency, piezoelectric coefficient, $d_{33}$and piezoelectric voltage coefficient, g_{33} has been shown in (b-c) [98]. A comparison of electromechanical properties between powder pressed and 3D printed samples for (d) PZT and BT ceramics. The schematics of two different 3D-printed geometries are schematically shown in (e) [116]. (f) Overview SEM images of the sintered BCZT gyroids with different volume of porosities and their corresponding variation in d_{33}, dielectric constant, polarisation, and strain are shown in (g-i) [165]. Reproduced from Ref.: (a-c) [98], and (f-i) [165], with permission from Elsevier. (d-e) [116], Open access article distributed under the terms of the Creative Commons CC BY license.

these variations, when comparing additive manufacturing processes, it is challenging to distinguish between the effects of the manufacturing process and those of the feedstock. However, we have tried our best to highlight meaningful differences that may arise specifically due to the additive manufacturing process employed. The property gaps observed between piezoelectric ceramics fabricated using different AM methods can be attributed to several key factors, including the particle size of the feedstock, binder content, sintering efficiency, microstructural homogeneity, and anisotropy.

The differences in properties between various AM techniques can be largely attributed to variations in density. For instance, one can clearly notice in Table 11 that the properties of binder-jetted samples are noticeably inferior when compared to those achieved by samples fabricated using DIW or VP. As a stringent requirement for the binder

Table 7
Comparison between pressed pellet and 3D printed open and offset scaffold structures [116]. (Open access article distributed under the terms of the Creative Commons CC BY license.).

	PZT (1.5 kV/mm)			BT (1 kV/mm)		
	Pellet	Scaffold	Offset	Pellet	Scaffold	Offset
d_{33}(pm/V)	384	202	273	142	107	127
ε_r	1405	297	1177	3657	906	1372
S (%)	0.36	0.19	0.18	0.04	0.04	0.04
P_r (μC/cm^2)	29.7	6.2	25.5	6.2	2.9	3.5
g_{33} (mVm/N)	31	77	26	4	13	10
FOM ($d_{33}\times g_{33}$) (fm^2/N)	11904	15554	7098	568	1391	1270

jetting (BJ) process, the powders must be flowable. To achieve this, the initial feedstock often consists of relatively large particle agglomerates, sometimes in the order of 100 μm, which are usually granulates. The powder packing density cannot be very high in the BJ process and the granulates have to be densified during the sintering process. This limits the ability to achieve a densely sintered ceramic.

A similar conclusion regarding the properties can also be drawn for samples fabricated using SLS, as, like BJ, the properties of SLS-processed samples are not particularly favourable. While the density values in Table 6 suggest that these samples are highly densified, the microstructure remains highly inhomogeneous, with numerous defects introduced due to the high-intensity laser used during fabrication, which might lead to inhomogeneous temperature distributions.

The arrangement of porosity in porous samples can give rise to directional properties. This effect is most noticeable in samples fabricated using binder jetting. In contrast, due to the high density achieved in extrusion-based methods and vat photopolymerization, no such anisotropy is observed in the sintered samples. This effect has also been observed in samples fabricated using VP and DIW at lower densities. As the density increases, the differences in properties along different directions diminish, eventually becoming almost identical.

The density achieved in vat photopolymerization (VP) is typically over 95 % in most cases, which can be attributed to the very fine particle size used as feedstock (Tables 4, 10). In contrast, extrusion-based techniques require a feedstock with particle sizes around 1 μm (Tables 2 – 3), where the driving force for sintering is lower (when compared to fine powders used in VP). Despite the binder content being comparable to that of FFF or even higher than that in DIW, the piezoelectric and dielectric properties remain quite impressive.

In summary, the ability to achieve high density and uniform

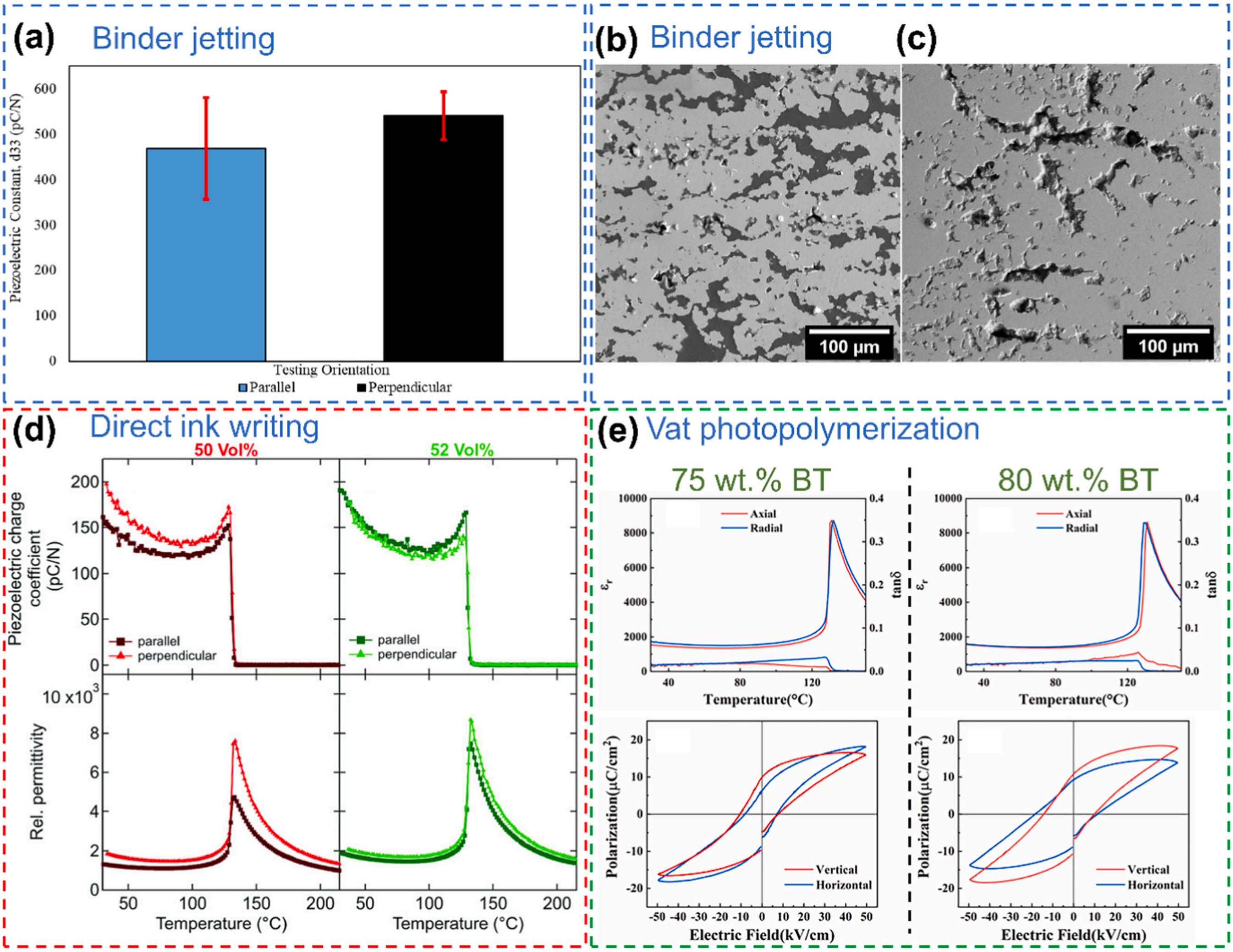

Fig. 43. Directional dependent electrical properties. (a) Piezoelectric coefficient as a function of the testing orientation for sintered PZT ceramics [193]. SEM images of the polished (b) Cross-section perpendicular to the printing direction, and (c) Surface parallel to the printing direction [191]. (d-e) Effect of the ceramic loadings and the measurement direction on the piezoelectric and dielectric behaviour of sintered BT ceramics [70,190].
(a) [193], (d) [70], Open access article distributed under the terms of the Creative Commons CC BY license. Reproduced from Ref.: (b-c) [191], and (e) [70,190], with permission from Elsevier.

microstructure plays a key role in the improved piezoelectric response. Techniques such as DIW and VP provide more homogenous microstructures, greater densities, and enhanced piezoelectric characteristics, while BJ and SLS are more susceptible to inhomogeneous microstructure and flaws that compromise performance. Each AM approach has unique benefits and limitations, and knowing these underlying elements is critical for improving piezoelectric ceramic performance in additive manufacturing. It is important to note that, at this stage, it is challenging to draw definitive conclusions about FFF due to the limited number of studies that deal with sintering and functional characterization of the fabricated components.

If achieving high dielectric and piezoelectric properties is the goal, one should opt for DIW or VP. With VP, there is more design flexibility compared to DIW. However, it is not possible to draw definitive conclusions based solely on the values reported in Tables 8 – 11. A technically sound comparison can only be made if the starting powder and ceramic loading are identical for all AM processes, as even slight deviations can significantly affect the properties. For instance, the initial ceramic loading determines the green density: the higher the green density, the better the densification, and consequently, the better the final properties.

4. Benefits of using AM over powder pressed samples

The preceding sections of this article have been devoted to the analysis of the systematic impact of various parameters on feedstock development and post-processing conditions. However, it is important to point out clearly the distinct advantages that AM offers over conventional manufacturing processes for piezoceramic components.

Commercial piezoelectric devices are often in the form of simple shapes like disks, plates, rods, rings, tubes, cylinders and plates (Fig. 44) [233,234]. These devices are mostly fabricated by using hydraulic presses with desired press molds [234]. In the case of producing devices containing different materials, tape-casting is followed by machining methods to produce the desired geometry [235]. Such machining methods are rather complex and limit the processing possibilities for fabricating complex geometries. Furthermore, the substantial volume of waste produced during the machining process necessitates cautious handling when it comes to recycling or disposal, especially when lead-based formulations are used. In contrast, AM technologies, owing to their layer-by-layer approach, enhance the process efficiency by minimizing the waste generated. This is a step towards a more sustainable manufacturing process. In addition to the flexibility in the designs offered by the AM technologies, the additional benefit of addressing environmental sustainability is worth mentioning.

Material extrusion-based AM techniques have been extensively utilised and harnessed for the production of lattice structures [49–51,54,56,71,83,85,88,92,94–98,104,116,131,133] (Fig. 45). These structures are defined by their repetitive and interconnected framework of extruded struts giving rise to a porous structure (designed porosity) as shown in Fig. 45(a-b), providing numerous benefits in diverse applications. In bone-tissue engineering applications, where piezoceramics can assist with regeneration by providing electrical charges in the bone, which in turn promote growth and repair. In this context, interconnected geometrical porosity is of crucial importance for efficient transportation of the essential nutrients, waste products and migration of the cells for the growth as well as other vital processes (Fig. 45(a-b)) [96,97]. The design of lattice structures can be precisely modified by employing various infill geometries and porosities (Fig. 45(a-h)). For instance, different infill geometries can alter the heating behaviour and heat transfer rate when used as a ceramic heater (Fig. 45(g-h)). [71]. In addition, it can also affect the piezoelectric and dielectric response [98]. Jia *et al.* reported that periodically porous structures exhibited better performance in pulsed-power energy conversion applications when compared to their bulk counterpart [94], thanks to the AM technologies that allow for the fabrication of structures with controlled porosity. In addition, it is also possible to design structures with graded porosity, thus enabling to tailor desired properties to meet specific requirements. The fabrication of a Fresnel zone plate lens (FZPL) serves as great evidence of a graded structure (Fig. 45(i)) [107]. In general, the lattice structures are lightweight and with specialized infill geometry such as a gyroid, a structure with high strength-to-weight ratio can also be obtained.

AM can be used for fabricating geometries with various degrees of connectivity between the active ceramic phase or the passive phase (in this case, the porosity), out of which the 3–0, 3–3 and 2–2 architectures are quite difficult to produce with conventional techniques. Here, the first number refers to the connectivity of the ceramic phase and the second number refers to the connectivity of the geometrical porosity [237]. The electromechanical properties are dictated by the distribution of the two different phases. Specifically, components fabricated with 3–3 connectivity are reported to exhibit enhanced figures of merit (FOM) or improved piezoelectric energy harvesting properties [88,116,133]. In particular, the 2–2 connectivity has been widely used in the reported literature for transducer applications as well (Fig. 45(j)) [99,122]. Moreover, complex architectures have also been successfully fabricated using DIW, where the ink rheology is crucial for the shape retention (Fig. 45(k)) [93].

One prominent and appealing characteristic of extrusion-based techniques is the ability to fabricate structures using multiple materials (depending on the number of nozzles the printer has), thus enabling an extensive array of functionalities and applications. For instance, BT and Ni-BT multilayer structures were successfully printed and sintered under controlled atmosphere conditions to mimic a structure similar to a multilayer capacitor (Fig. 46(a)) [92]. In another study, a multi-layered transducer component was fabricated by depositing hard and soft PZT alternatively in a layer-by-layer fashion [103]. Such multi-material multilayered structures are reported to offer potential benefits in terms of performance, transmittivity and sensitivity. Tube actuators with PMN-PT and silver-palladium electrodes were also developed as a proof-of-concept for enhancing the displacement properties along the tube (Fig. 46(b)) [238].

Some more recent advancements demonstrate that it is possible to fabricated complex twisted spiral structures, in spite of the inherent brittle nature of ceramics (Fig. 47(a-b)) [72]. These structures exhibit a unique macro structure that was previously challenging to fabricate. Modern innovations have led to the creation of even more complex kirigami-origami constructions, which combine the delicate techniques of origami paper folding with the precise principles of Japanese paper cutting (Fig. 47(c-e)) [69]. Such structures can be potentially used in wearable electronics and health monitoring devices. Another example of advancement is the fabrication of free-standing pillars, which can potentially be used for drug delivery, cell cultivation, light emitting diodes, etc. (Fig. 47(f)) [84].

With extrusion-based AM techniques, it is indeed possible to fabricate large components (at least of the order of even a few centimetres). However, the resolution of such printed components is limited by the nozzle size of the extruder, which is typically greater than 400 μm (Tables 2 – 3), with the smallest nozzle size being reported as fine as in the order of 100 – 150 μm [49,88]. In addition, printing structures with large overhangs cannot be printed without support structures, making the post-processing challenging. The samples fabricated using such techniques, often exhibit a rough surface finish, that can be further processed using machining, for samples fabricated with FFF technology. On the contrary, such machining steps cannot typically be carried out on structures fabricated using DIW, as the printed structures are delicate and cannot handle such rough post-processing conditions. It is important to highlight that FFF overperforms DIW in cases where the nozzle has to move repeatedly over the deposited layer. For instance, in order to fabricate small hollow cylinders for transducer applications, FFF is always a better choice as the deposited struts are solidified immediately (and the presence of a cooling fan even makes it faster). This is valid as

Table 8
Post-processing conditionings and functional properties of samples fabricated with Direct ink writing.

Feedstock	Debinding conditions	Sintering conditions	Density (%)	Dielectric constant, ε_r	Dielectric loss, tanδ	Piezoelecetric coefficient, d_{33} (pC/N)	Polarization, P_r (μC/cm^2)	Printed structure	Reference
Hard PZT	0.3 °C/min 600 °C 2 h	5 °C/min 1100 – 1300 °C 2h	~ 93.2 –97.5			~ 268 ± 10		Ring shape	[74]
Barium acetate, TTIP		Argon: 3 °C/min 1200 – 1500 °C 2 h	97.8	533				Honey comb, Lattice, Dense cube	[78]
$BaTiO_3$ Hydrothermally synthesized	3 °C/min 600 °C 2 h	3 °C/min 1320 °C 2 h	~ 96			275	~ 15 – 17	Kirigami-Origami structures	[69]
BCZT	1 °C/min 1500 °C 2 h							Free standing pillars	[84]
BCZT	1 °C/min 800 °C 2 h	3 °C/min 1350 – 1500 °C 2.5h	~ 92 – 93	256 – 1046	0.021 – 0.022	~ 62 – 100	4.11 – 4.56	Log-pile	[51]
$BaTiO_3$	1 °C/min 600 °C 1 h	5 °C/min 1350 °C 3 h	~ 94 – 98	~ 1700 – 2000		165 – 200		Bending bars	[70]
$BaTiO_3$	5 °C/min 600 °C 1 h	5 °C/min 1250 °C 2 h	~ 67.94 – 85.24	~ 1333.07 – 2250		~ 112.2 – 204.61		Hollow cylinder	[58]
$BaTiO_3$	5 °C/min 600 °C 1 h	5 °C/min 1250 °C 2 h	66.95 – 86.75	> 2200		135 – 200			[59]
$BaTiO_3$ doped La, Mn PTC	2 °C/min 350 °C	2 °C/min 1350 °C 2 h	> 99					Honeycomb, square grid, Circular, Elliptical, Square, Rectangular, Graded porous	[71]
PZT	3 °C/min 175 °C, 285 °C, 345 °C, 600 °C, Each step 1 h	3 °C/min 1250 °C 4 h	96.89	1621	0.031	342.6		Wood pile, Helical twentytetrahedral, Cylinder	[85]
$BaTiO_3$		1150 °C						Radial array, Periodic lattice	[49]
$BaTiO_3$	2.8 °C/min 1340 °C 1 h							Radial lattice, Linear lattice	[50]
$Bi_2Mo_2O_9$	1 °C/min 100 °C, 200 °C, 300 °C, 400 °C, 500 °C, Each step 2 h	3 °C/min 640 – 670 °C 2 h	86 – 93	~ 24.5 – 35.7	~ 0.0004 – 0.0006			Honeycomb	[60]
$BaTiO_3$	4 °C/min 600 °C 2 h	4 °C/min 1250 °C 2 h	70.25 – 89.97	1560.2 – 2391.6		175 – 244.5		Dense disc and rectangle	[61]
PZT	5 °C/min 650 °C 1 h	10 °C/min 1250 °C 6 h	~ 90 – 94.9	~ 4132	~ 3.4 %	678		Dense rectangle	[77]
PZT	325 °C, 500 °C, Each step 1 h	1250 °C 2 h	98.36			265		Woodpile structure bent into annulus or twisted to spiral	[72]
PIN-PMN-PT, $BaTiO_3$ platelet	0.1 °C/min 375 °C 9 h	10 °C/min 1050 °C 0h	95			420 – 480		Lattice structue	[91]
$BaTiO_3$, $SrTiO_3$, $BaZrO_3$Ni	350 °C 2 h	N_2 + 200 ppm H_2: 5 °C/min 1350 °C 1 h		1247				Square array	[92]
Nb, Ca, Co- doped $BaTiO_3$	1 °C/min 600 °C 4 h	3 °C/min 1100 °C 4 h	~ 95	~ 1800	~ 0.52 %	~ 260		Disc	[80]
Titanium isopropoxide, MDEA, glycerol, water, BaO	10 °C/h 300 °C 2 h	60 °C/h 1250 – 1350 °C 20 h	94 – 96	1900		159	5.4	Cylindrical object	[73]
$BaTiO_3$	(i) 2 °C/min 200 °C, 500 °C, Each step 30 min (ii) 800 °C, 1 min	5 °C/min 800 °C, 2 °C/min 1200–1300 °C 2 h		462 – 858		201 – 312	1.7 – 2.3	Wood-pile	[88]
PZT	1 °C/min 170 °C, 250 °C, 375 °C, 600 °C, Each step 1 h	3 °C/min 1250 °C 4 h	97.8					Wood-pile	[83][c]
$BaCO_3$, TiO_2	1 °C/min 500 °C, 600 °C, Each step 2 h	1 °C/min 1300 °C 2h, 5 h, 20 h	~ 94	2870 – 4120	0.033	290 – 360		Complex architectures	[93]
		1 °C/min 1300 °C 5h, Step cooling: 1 °C/min 1200 °C, 1100 °C, 1000		4380	0.02	420			

(continued on next page)

Table 8 (*continued*)

Feedstock	Debinding conditions	Sintering conditions	Density (%)	Dielectric constant, ε_r	Dielectric loss, tanδ	Piezoelectric coefficient, d_{33} (pC/N)	Polarization, P_r (μC/cm^2)	Printed structure	Reference
		°C, Each step 5 h							
PZT	1 °C/min 600 °C 2 h	5 °C/min 1250 °C 2 h	98					Scaffolds	[54][c]
PZT95/5 prepared from Pb_3O_4, TiO_2, ZrO_2, Nb_2O_5	1 °C/min 600 °C 2 h	2 °C/min 1330 °C 2 h	83 ± 2	328			33.4 ± 0.4	3D periodically distributed porous structure	[94]
PNZT	2 °C/min 450 °C 3 h	950 – 1050 °C 5 h	60	1265	> 0.04			Square component	[75]
Li, Sb and Ta-doped KNN		3 °C/min 1050 °C, 1100 °C, 1130 °C, 2 h	98	1775		280	18.8	Wood pile	[95]
$BaTiO_3$	5 °C/min 650 °C 1 h	5 °C/min 1100 °C, 1200 °C, 1300 °C, 1400 °C, 3 h	52.5 – 65.3	1580 – 4730	< 0.033	128 – 200		Dense square	[86]
PZT	600 °C 3 h	1250 °C 2 h		~ 1005 – 1533		~ 352 – 382		Hierarchical porous structure	[98]
PZT	3 °C/min 600 °C 2 h	3 °C/min 1275 °C 2 h	~ 98.8					3D periodic structure, V- shaped test structure, 3D radial structure, Porous lattice	[56]
$BaTiO_3$	Debinding and sintering in a single step using different rapid sintering techniuques		~ 72 – 95					Log-pile	[79][d]

A generalized representation for heating rates is as follows: XX °C/min YY °C ZZ h ; where XX denotes heating rate, YY denotes the debinding/sintering temperature, and ZZ denotes the holding time. This representation has been followed in the subsequent Tables 9 – 11 as well.

[c] Sintered samples were embedded in epoxy for the electrical measurements, hence the properties are not reported.

[d] Different rapid sintering techniques employed were: ultra-fast high temperature sintering, pressureless spark plasma sintering and fast firing.

In the debinding/sintering condition, if atmosphere is not mentioned it is in ambient air.

well when depositing struts at different angles. On the other hand, in DIW the presence of the cooling fan is not mandatory and it may distort the structure or hinder the fine tuning of the rheological properties.

Most of the difficulties listed above may be overcome by employing vat photopolymerization. Overhanging structures can be printed quite easily, as the uncured resin provides support during the curing process. The resolution can be of the order of few microns (10 – 100 μm). This means it is practically possible to print fine structures with high resolution. On the other hand, printing large structures (similar to extrusion-based techniques) is quite difficult by this approach, especially considering the limited build volume and the time it takes to print with such fine resolution.

Prominent structures for transducer applications that have been produced using VP are circular/square/rectangular arrays with protruding pillars or features, specifically designed to enhance the performance of the device (Fig. 48(a-f)) [146,147,168,171,179,180,186,224]. The shape of the protruding features can be more flexible, in contrary to the traditional machining methods which could usually shape into square or rectangular features. In addition, the resolution of the protruding feature can be decreased down to the order of microns (Fig. 48 (c, f)). To add to the architectural complexity, the pillars can be inclined at certain desired angles (Fig. 48(f)) [171]. Transducers with several other geometries and configurations have also been reported (Fig. 48 (g-i)) [177,188]. The ability to fabricate overhanging structures are validated in several studies by printing a hollow cube like structure [146,147].

As a proof of concept, often TPMS (Triply periodic minimal surface) structures are employed to validate the flexibility of the printing process (Fig. 49(a-d)) [143,157,158,163,167,169,172,184]. For instance, a P-type TPMS structure with high geometrical porosity (70 %) was fabricated for energy harvesting applications (Fig. 49(e)). Notably, the design and porosity can be adjusted easily to meet specific needs. Often such TPMS structures are embedded in epoxy for practical applications [139,157,158].

The samples fabricated with powder-bed based AM techniques (BJ and SLS) often suffer from low resolution and rough surfaces, as shown in Fig. 50. As a result, these techniques are not used to fabricate piezoelectric device to the same extent as the other techniques evaluated in this work. Most of the published articles only report the fabrication of simple shapes, such as discs as shown in Fig. 50(d), as required for carrying out the electrical measurements [192,194,198,199]. Scaffolds with a possible application in bone tissue engineering were successfully fabricated using BT/HA (Fig. 50(a)) [197]. In addition, TPMS and lattice structures were reported to confirm the viability of complex architectures (Fig. 50(b-c)) [192].

Until now, various complex structures that are fabricated with different AM techniques have been discussed, with more details provided in Tables 8 – 11. Following this, Table 12 highlights the applications of fabricated piezoelectric ceramics across various fields, demonstrating the versatility and potential of these devices.

In summary, the choice of a specific AM technology depends on the specific requirements of the application. For fabricating large components with relatively simple designs, extrusion-based AM techniques are suitable, although there may be a compromise in resolution. In such cases, BJ can also be considered. However, this technique suffers from various disadvantages, including high surface roughness, low green strength and high residual porosity, to name a few. On the other hand, if the design is highly complex with fine features, VP is the most suitable option. The final decision to select the appropriate AM technology depends on factors such as availability and end-use requirements. It is essential to weigh the advantages and disadvantages of each technology to ensure the desired outcomes for the specific application envisioned.

5. Conclusions and outlook

In this review, a comprehensive assessment of the main features,

Table 9
Post-processing conditionings and functional properties of samples fabricated with fused filament fabrication.

Feedstock	Debinding	Sintering	Density (%)	Dielectric constant, ε_r	Dielectric loss, tanδ	Piezoelecetric coefficient, d_{33} (pC/N)	Polarization, P_r (μC/cm^2)	Printed structure	Reference
PZT	30 °C/h 500 °C 4 h							Dome and radial actuator, 2–2 ceramic polymer composite	[99]
PZT-5H	10 °C/h 550 °C	1285 °C 1 h	94 – 96	~ 3100	~ 0.025	~ 650 pC/N		Tube actuator	[121]
PZT-5H	550 °C	1285 °C 1 h	94	2300	0.035	620 – 1270		Dome-shaped actuators	[130]
PZT	30 °C/h 500 °C 2 h	3.5 °C/min 1285 °C 1 h		700		290		2–2 annular ring, 3–3 ladder structure	[120]
PZT	60 °C/h 200 °C, 10 °C/h 550 °C 4 h	3.5 °C/min 1285 °C 1 h	7.7 g/cc	3340	0.023	664 ± 4		2–2 transducer	[122]
BiT powder, BiT platelets	550 °C	1100 °C 1 h							[102]
PZT	10 °C/h 550 °C	1285 °C 1 h						Tube array, Radial, spiral and bellow actuators	[103]
PZT−5HSpray dried	1 °C/min 350 °C 1 h, 1.5 °C/min 550 °C 2 h, 3.5°C/min 800 °C 1 h	3.5 °C/min 1285 °C 1 h						Ladder structure	[104]
PZT	Wick debinding 125 °C, 150 °C, 175 °C, 200 °C, 225 °C	10 K/min 1200 °C 2 h		~ 1873	~ 7.2 %	~ 270		Filament	[118]
$BaTiO_3$ **PZT**	3 °C/min 200 °C, 0.25 °C/min 500 °C 2 h	1350 °C 5 h 1200 °C 2 h						scaffold	[131]
$BaTiO_3$ **PZT**	3 °C/min 200 °C, 0.25 °C/min 500 °C 2 h	1350 °C 5 h 1200 °C 2 h		906 – 1372 297 – 1177		107 – 127 202 – 273	2.9 – 3.5 6.2 – 25.5	Open and offset scaffold	[116]
PZT	600 °C for 60h: Binder removal by capillary forces	150 °C/h 1250 °C 2 h	7.71 g/cc	2060	0.0191	477		Concentric rings	[123]
$BaTiO_3$	2 °C/min 180 °C 30 min, 0.3 °C/min 300 °C 60 min, 0.5 °C/min 550 °C 60 min, 3 °C/min 1000 °C 60 min	10 °C/min 1200 – 1350°C 2 h	~ 58 – 92	1228 – 1472	0.010 – 0.012	196 – 221	11.39 – 12.33	Porous gyroid, log-pile, honeycomb, dense disc, triangular	[113]
PZT 5 H	30 °C/h 550 °C 2 h	3.5 °C/min 1285 °C 1 h						2–2 annular ring, 3–3 ladder structure, C ring actuator	[133]

advantages, and disadvantages of the most commonly used AM technologies employed for fabricating piezoceramic components, such as direct ink writing (DIW), fused filament fabrication (FFF), vat photopolymerization (VP), binder jetting (BJ), and selective laser sintering (SLS) was carried out. AM is one of the most efficient and rapid prototyping techniques that enables the fabrication of complex structures with high precision and desired geometry. Especially concerning piezoelectric ceramics, the functional properties can be easily tailored by the geometry of the fabricated component. This is where 3D printing takes an additional leap forward with respect to other conventional processing techniques, providing a high degree of customization to the users. There are more than 120 publications in the past 20 years related to the above-mentioned technologies, with most of them being reported in the past 2–3 years. These observations suggest that these AM technologies have not been commercialized yet and further developments are required. Additionally, there is a clear trend towards lead-free compositions, which is evident from Fig. 1(c) where the number of papers published on BT surpasses those on lead-based compositions. However, the piezoelectric and ferroelectric properties of lead-based compositions remain significantly superior to those of other materials reported. For instance, as detailed in Tables 8, 9, 10 and 11, the d_{33} values for most lead-based compositions exceed 350 pC/N, with the highest reported value reaching 1270 pC/N. In contrast, compositions based on BT or KNN have d_{33} values up to a maximum of 250 pC/N. Even though researchers are employing various methods such as doping and texturing, the properties still remain significantly below those of lead-based compositions. Nevertheless, with advancements in technology and materials innovation, there is a hope that lead-based materials could eventually be completely replaced by lead-free compositions. Such an accomplishment can be only fulfilled with continuous research and development of the lead-free compositions.

To ensure the successful fabrication of defect-free components, it is essential to carefully formulate a printable feedstock with desired rheology, which in turn affects the piezoelectric performance of the fabricated devices. A typical printable feedstock is composed of ceramic powders, dispersants, solvents, binders and several other additives, depending on the printing technique to be used. concerning VP and DIW of piezoceramic materials, thanks to the availability of affordable and economical printers. The progress of the FFF technology applied to ceramics over the last several years is directly related to the only minor modifications to the cheap and open-source printers that can extrude polymeric materials that are required. While most of the recent advancements in this area have focused on composite polymer-ceramic piezoelectric materials, there is still a great opportunity for optimization and exploration in the realm of pure ceramic devices. On the other hand, because of the inferior product quality and performance, the

Table 10
Post-processing conditionings and functional properties of samples fabricated with vat photopolymerization.

Feedstock	Debinding conditions	Sintering conditions	Density (%)	Dielectric constant, ε_r	Dielectric loss, tanδ	Piezoelecetric coefficient, d_{33} (pC/N)	Polarization, P_r (μC/cm^2)	Printed structure	Reference
PZT-5H	700 °C	1 °C/min 1200 °C	≥ 95	2000					[176]
PMNT	1 °C/min 600 °C 1 h	3 °C/min 1250 °C 1.5 h	97.8 (7)			620 (40)		Hollow spherical cell transducer	[177]
PZT 5 H	1 °C/min 700 °C		95 – 98					Transducer	[178]
BaTiO$_3$	Argon: 600 °C 3 h	1330 °C 4 – 6 h	93.7	1350	0.012	160	2.2 – 7	64 pillar annular segment transducer	[179]
BaTiO$_3$	Argon: 1 °C/min 200 °C, 300 °C, 400 °C, 500 °C, Each step 0.5 h, 600 °C 3 h	3 °C/min 1200 – 1500 °C 4 h	~ 95	920	0.07	87	~ 12	Annular segment transducer array	[168]
KNN	Argon: 1 °C/min 100 °C, 200 °C, 300 °C, 350 °C, 400 °C, 500 °C, 600 °C ,Each step 2 h; Air: 800 °C 3 h	3 °C/ min1050 – 1150 °C 3 h	~ 92	2150	0.08	170	12.1	Annular array for ultrasonic transducer	[180]
BaTiO$_3$	0.5 °C/min 600 °C 2 h	1290 °C 2 h	5.52 – 5.68 g/cc	1829 – 2276	0.036 – 0.094	96 – 166	28.5	Ultrasonic array	[181]
PZT—5A	1 °C/min 280 – 500 °C	1 °C/min 1200 °C 2 h	97 – 98						[164]
BaTiO$_3$	Nitrogen: 600 °C 5 h	1320 °C 3 h	~ 95	2762	0.016	163		9 rod transducer, Hollow cube, Annular ring	[146]
BaTiO$_3$	Nitrogen: 1 °C/ min 300 °C, 0.15 °C/min 400 °C 3 h, 0.15 °C/min 500 °C, 1 °C/min 600 °C 3 h	1300 °C, 1320 °C, 1330 °C 2 h	~ 95.89 – 98.06	~ 2749 – 4423	0.0128 – 0.0188	146 – 206		Hollow cube, Transducer with pillars	[147]
BaTiO$_3$	Nitrogen: 1 °C/ min 200 °C, 300 °C, 400 °C, 450 °C, 500 °C, 600 °C, Each step 1 h; Air: 1 °C/min 450 °C, 600 °C, Each step 2 h	1330 °C 2 h	~ 61.98 – 95.32	948	0.023	168.1	13.1	Octet truss, Gyroid	[139]^e
PZT	Argon: 1 °C/min 100 °C, 200 °C, 300 °C, 350 °C, 400 °C, 500 °C, 600 °C, Each step 2 h; Air: 800 °C 3 h	1200 °C 3 h	6.09 – 6.92 g/cc	2417	0.025	525	17.3	Annular array	[171]
BaTiO$_3$	Air/ Vacuum: 3 °C/min 150 °C 30 min, 1 °C/min 200 °C 30 min, 0.35 °C/min 300 °C, 400 °C, 500 °C, Each step 1 h, 0.35 °C/min 600 °C 2 h	1300 – 1400 °C 2 – 4 h	86.93 – 90.25	1965	0.017	200		Circular disc	[159]
BaTiO$_3$	Inert: 1 °C/min 150 °C, 0.5 °C/ min 150 – 200 °C 3h, 1 °C/min 200 – 350 °C, 0.5 °C/ min 350 – 400 °C 3h, 1 °C/min 400 – 420 °C; Air: 460 °C 3 h	1320 °C 2 h	~ 91 – 95.4	1543	0.0185	180	5 – 10.9	Complex structures	[148]
BaTiO$_3$	Nitrogen: 0.5 °C/ min 300 °C, 400 °C, 450 °C, 500 °C, 600 °C, 700 °C, Each step 1 h;	3 °C/min 1210 – 1330 °C 2 h	~ 87.54 – 95.32	~ 718 – 1512		~ 108.2 – 168.1	7.59 – 20.25	Disc, FCC-structured	[157]

(*continued on next page*)

Table 10 (*continued*)

Feedstock	Debinding conditions	Sintering conditions	Density (%)	Dielectric constant, ε_r	Dielectric loss, $\tan\delta$	Piezoelecetric coefficient, d_{33} (pC/N)	Polarization, P_r (μC/cm^2)	Printed structure	Reference
	Air: 1 °C/min 450 °C, 600 °C, 800 °C, Each step 2 h								
BCZT	Argon: 1 °C/min 150 °C, 0.3 °C/min 180 °C, 400 °C, Each step 2h, 0.5 °C/min 600 °C 2h; Air: 3 °C/min 600 °C 2 h	3 °C/min 1450 – 1525 °C 4 h	~ 93.28 – 95.88	4800	0.025	430	14.38		[149][f]
BaTiO$_3$	12 °C/h 200 °C 1 h, 6 °C/h 300 °C 1 h, 12 °C/h 700 °C 1 h	100 °C/h 1300 °C 1 h	62 – 98	837 – 2426	0.01 – 0.068	5 – 148		Cylinder or rectangular	[182]
KNNLN-Er	Vacuum: 600 °C 4 h, 800 °C 4 h	1120 °C 4 – 8 h	89.6 – 93			97		Disc	[183][g]
PZT	Argon: 0.2 °C/min 200 °C, 310 °C, 395 °C, Each step 2 h	1250 °C 2 h	~ 77.8 – 89.51	1522 – 2196	0.025 – 0.029	254 – 373	24.78 – 35.56	Calibration model	[150]
PMN-PT, BT templates		2.5 °C/min 1200 °C, 1235 °C 4 h	~ 93	2218	0.077	652	19.5	Square	[162]
BaTiO$_3$	Nitrogen: 2 °C/min 100 °C, 200 °C, Each step 2h, 1 °C/min 250 °C, 300 °C, 340 °C, 380 °C, 400 °C, Each step 3h, 2 °C/min 500 °C, 600 °C 2 h; Air600 °C3h	3 °C/min1300 °C3h	78.74 – 91.69 %	5631 – 10009 at T$_c$	~ 0.03 at T$_c$	73 – 151	8.8 – 17.4	Disk	[151]
BaTiO$_3$	Nitrogen: 1 °C/min 200 °C, 300 °C, 400 °C, 450 °C, 500 °C, 600 °C, Each step 1 h; Air: 1 °C/min 450 °C, 600 °C, Each step 2 h	3 °C/min 1250 °C, 1300 °C, 1330 °C, 1350 °C 2 h	~ 90.02 – 95.39	978	0.038	215 ± 13	16.656	TPMS, cylinder	[158]
PZT	Argon: 0.2 °C/min 190 °C, 368 °C, 465 °C, Each step 2 h; Air: 600 °C 2 h	3 °C/min 1250 °C 2 h	~ 85.45 – 87.12	1970 – 2113	0.0256 – 0.0267	340 – 365	32.67 – 34.40	Disk	[152]
BCZT	Argon: 1 °C/min 150 °C, 0.3 °C/min, 180 °C, 400 °C, Each step 2 h, 0.5 °C/min 600 °C 2 h; Air: 3 °C/min 600 °C 2 h	3 °C/min 1450 – 1525 °C 4 h	~ 93.14 – 96.58	4323	0.011	525	14.50	Gyroid	[184][h]
BaTiO$_3$, BT platelets	Inert: 1 °C/min 150 °C, 0.5 °C/min 150–200 °C 3 h, 1 °C/min 200 – 350 °C, 0.5 °C/min 350 – 400 °C 3 h, 1 °C/min 400 – 420 °C; Air: 460 °C 3 h	3 °C/min 1250 °C, 1275 °C, 1300 °C, 1325 °C 3 h		~ 1867	0.037	275	14.88	TPMS	[163]
PZT	0.2 °C/min 250 °C, 375 °C, 480 °C 2h	3 °C/min 1250 °C 2 h	~ 68 – 83.12	868 – 1911	0.027 – 0.032	129 – 308	15.75 – 29.68	TPMS	[172]
BaTiO$_3$	Vacuum: 1 – 8 °C/min 600 °C; Air: 0.5 – 4 °C/min 800 °C	2 °C/min 1450 °C				211		TPMS	[143]
KNN	Argon: 1 °C/min 150 °C, 0.2 °C/min 410 °C, 600 °C Each step 2 h;	5 °C/min 1070 °C, 1080 °C, 1090 °C, 1100 °C 6 h	90.11	460.43 ± 6.05	0.12 ± 0.01	113.67 ± 2.49	19.94(30 kV/cm)	Scaffolds	[144]

(continued on next page)

Table 10 (*continued*)

Feedstock	Debinding conditions	Sintering conditions	Density (%)	Dielectric constant, ε_r	Dielectric loss, tanδ	Piezoelecetric coefficient, d_{33} (pC/N)	Polarization, P_r (μC/cm^2)	Printed structure	Reference
$BaTiO_3$-x$BaSnO_3$	Air: 3 °C/min 600 °C 2 h Inert: 1 °C/min 150 °C, 0.5 °C/min 150 – 200 °C 3 h, 1 °C/min 200 – 350 °C, 0.5 °C/min 350 – 400 °C 3 h, 1 °C/min 400 – 420 °C; Air: 460 °C 3 h	1400 °C 4 h		1767–10532		17 – 283	1.1 – 11.92	Complex strcutures	[167]
$BaTiO_3$		1350 °C 4 h	~ 99					Honeycomb	[185][i]
Barium acetate, Titanium (IV) isopropoxide, Acetic acid, Acrylic acid	5°C/min 90 °C, 250 °C, 385 °C, 655 °C, 900 °C, ramp held for1h	5 °C/min 1330 –1500 °C 1 h	87±1 – 93±1					Complex structures	[175]
PZT 5 H	Vacuum: 600 °C 3 h; Air: 650 °C 3 h	1250 °C 2 h	6.94 – 7.00 g/cc	760 – 1390	0.020 – 0.021	212 – 345		Ceramic array	[186]
PZT855	Argon: 1 °C/min 600 3 h; Air: 600 °C 3 h	1100 °C 3 h	94.7			583	32.4	Micro-curved stave elements, Hemispherical transducers, Helical element, Cylindrical concentric annular arrays, Lattice sensor	[188]
PZT	Argon + Air	1250 °C 3 h	72.98 – 91.43	1256 – 2364	0.0241 – 0.0302	189 – 399	20.44 – 39.72	Complex structures	[145]
$BaTiO_3$	Argon: 0.25 °C/min 400 °C, 460 °C, 550 °C 2 – 3 h, 800 °C 2 h	1 °C/min 450 °C 4 h, 2 °C/min 1000 °C, 1320 °C 3 h	95	1770	0.029	201	18.5	TPMS structures: schwarz, gyroid, I-WP, bodycentred cubic lattice	[140]
PZT, PMMA	Vacuum: 0.5 – 2 °C/min 100 °C, 200 °C, 300 °C, 400 °C, 500°C, Each step 2 h; Air: 600°C 4 h	1200°C 2 h	~ 6.36 – 6.55 g/cm^3					Cylinder	[189]
$BaTiO_3$	Vacuum: 0.5 °C/min 600°C 4 h; Air: 1 °C/min 800 °C 4 h	3°C/min 800 °C, 1°C/min 1320 °C 2 h	94.52 – 95.51	1805 – 2019	0.02 – 0.03	107 – 218	6.31 – 11.05	Square	[190]
Sm-PMN-PT	Argon: 0.5 °C/min 140 °C, 380 °C, 420 °C, Each step 1 h, 1 °C/min 600 °C 1 h	2.5°C/min 600 °C, 1220°C, Each step 2 h	92 – 98	4733 – 6452	0.0430 – 0.0434	1080 – 1230		Hollow cylinder, TPMS: Gyroid, Schwarz_P, Schwarz_D	[141]
BCZT	Nitrogen: 1 °C/min 300 °C, 0.5 °C/min 500	1450 °C3h		718 – 1603		382 – 570		Gyroid	[165]

[e] Best properties reported for the sample with relative density of 95.32 %.

[f] Best properties reported for the sample with sintered at 1500 °C.

[g] Best properties reported for the sample with a holding time of 6 h.

[h] Best properties reported for the sample doped with 1.5 mol.% CuO (relative density 96.58 %).

[i] Sintered samples were embedded in epoxy for the electrical measurements; hence the properties are not reported.

binder jetting technology still remains largely unexplored.

The key distinction between additively manufactured and conventionally manufactured piezoceramics, beyond the unique structural complexity achievable with AM, lies in the differences in density and microstructure in the sintered components. In conventional methods, the application of pressure during the shaping process with limited or without the use of any binder helps in achieving high densities with fine microstructures. In contrary, the residual porosity from the debinding process affects the electrical properties of additively manufactured components in a negative way. Increasing the sintering temperature helps in enhancing the densification process but at the expense of grain growth.

Tables 2 – 6, and 8 – 11 provide an overview of different feedstocks used to fabricate piezoelectric ceramics with complex geometries using AM technologies, along with their sintering and post-processing conditions, as well as their electrical properties. They complement the discussion and assist the reader in formulating their own approach to the fabrication of devices using the AM approach. Examining the tables, one can clearly notice the differences between various additive manufacturing (AM) technologies and their capabilities. If one is concerned about resolution with a limited object size, vat photopolymerization (VP) is the best choice. For applications where resolution

Table 11
Post-processing conditionings and functional properties of samples fabricated with binder jetting.

Feedstock	Debinding	Sintering	Density (%)	Dielectric constant, ε_r	Dielectric loss, tanδ	Piezoelecetric coefficient, d_{33} (pC/N)	Polarization, P_r (μC/cm^2)	Printed structure	Reference
$BaTiO_3$	10 °C/min 600 °C 0.3 h	10 °C/min 1260 °C, 1330 °C, 1400 °C 4h	1.3 – 1.6 g/cc	8.62 – 6.23					[196]
$BaTiO_3$Hydroxyapatite	300 °C 1 h, 500 °C 2 h	600 °C 3 h, 1000 °C 2 h, 1320 °C 1 h	~ approx. 50 % open porosity			3.08 pC/N		Scaffolds (Interconnected cylinder)	[197]
$BaTiO_3$	10 °C/min 600 °C 20 min	10 °C/min 1260 °C, 1330 °C, 1400 °C 4 h	41.4 – 65.2 (60 % binder saturation)	~ 50 – 630	~ 0.01 – 0.81	13.23 – 74.1 pC/N		Dense rectangle	[195]
KNN		2.5 °C/min 1130 °C 2 h	~ 29.5 – 56			~ 74.1 – 89.9		Discs,Triangle with hole at the centre	[191]
$BaTiO_3$	10 °C/min 650 °C 60 min	10 °C/min 1300 °C, 1350 °C, 1400 °C, Each temperature 2 h, 4 h, 6 h	~ 82 – 93	750 (Coarse), 811 (Fine)	0.0553 (Coarse), 0.1159 (Fine)	118 (Coarse), 183 (Fine)		Disc, Lattice structure	[194][j]
$BaTiO_3$	600 °C 60 min	2 °C/min 1200 – 1400 °C 2 h	56 – 66.8	371, 411	< 3 %	105, 110		Disc	[198][k]
BCZT	600 °C 60 min	1400 – 1500 °C, Each temperature 2 h, 4 h, 8 h, 10 h	~ 74 – 91	1909	1.9	152		Disc, TPMS (Gyroid and Schwarz)	[192]
PZT-N	470 °C 4 h	1200 or 1250 °C 2 h	~ 45 – 60	400 – 482		291 – 319		Disc	[199]
$BaTiO_3$	7.5 °C/min 650 °C 1 h	10 °C/min 1250 °C 6 h	36.77	581.6 (Parallel), 698 (Perpendicular)		113 (Parallel), 152 (Perpendicular)			[200][l]
$BaTiO_3$		1260 – 1400 °C		~ 50 – 650					[193][l]
PZT						468.5 pC/N (Parallel), 541.4 (Perpendicular)			

[j] Here, coarse refers to the properties reported for that specific powder fraction, and similarly for fine.
[k] Best properties reported for the sample sintered at 1250 °C.
[l] Parallel and perpendicular refers to the orientation in which the values are measured.

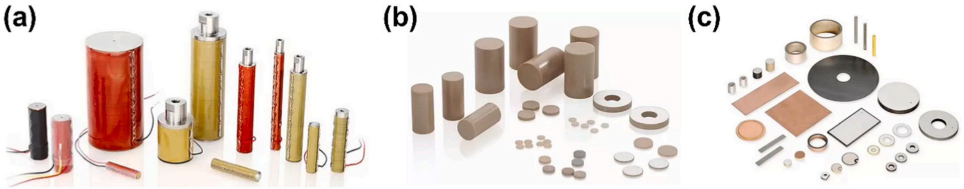

Fig. 44. Commercially used piezoelectric components. (a) Soft PZT for actuators and sensors; (b) Hard PZT for ultrasonic transducers; and (c) Lead-free BNT (Bismuth sodium titanate) suitable for transducers. Note these commercial products are all produced using conventional shaping methods [236].

is not the primary criterion, extrusion-based AM techniques can be used, with fused filament fabrication (FFF) being particularly well-suited for its better shape retention ability owing to the thermoplastic nature of the binder. However, preparing the filaments for the FFF process is time-consuming and requires proper attention. On the other hand, with direct ink writing (DIW), the ink preparation step is relatively easy when compared to FFF. In addition, the limited amount of binder used in DIW is a significant advantage when it comes to the post processing stages. Regardless of the method, samples fabricated with these technologies exhibit acceptable piezoelectric and ferroelectric properties. In contrast, samples fabricated with binder jetting (BJ) exhibit poor resolution and low properties, making them unacceptable for many applications. However, this technology involves high production rate and volume, when compared to other AM technologies reported in this review paper. The choice of AM technology should consider not just the resolution and ease of material preparation but also the specific material properties required for the application, post-processing requirements and the overall cost and scalability of the manufacturing process.

Despite significant advancements in AM technologies for piezoelectric device production, there are some unresolved issues that must be addressed before widespread use and commercialization can occur. These concerns need attention and should be regarded as the goals for future growth and development of the field.

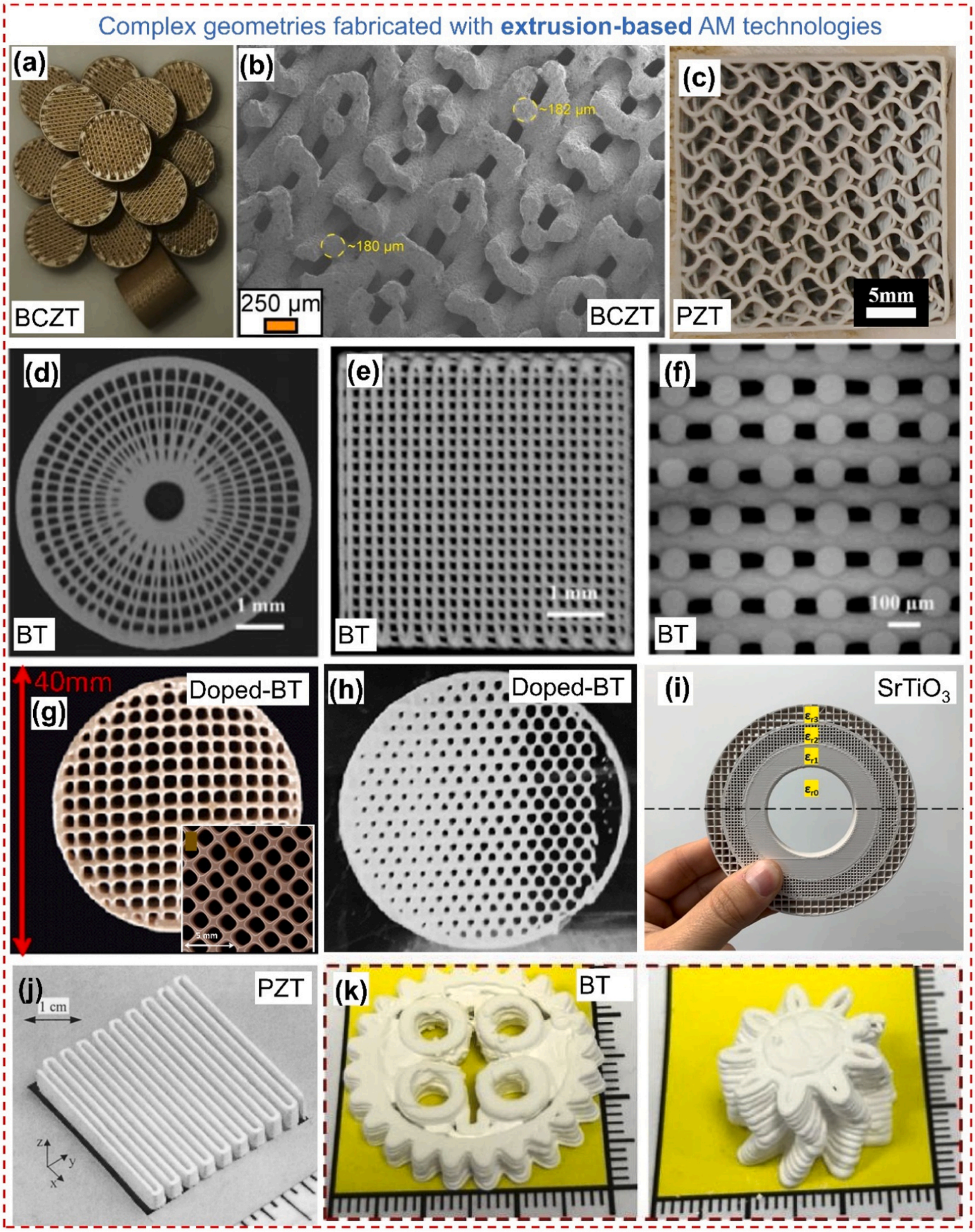

Fig. 45. Optical images of: (a-b) BCZT scaffolds for bone graft substitute with the corresponding SEM image of the fracture surface [97], (c) Helical twenty tetrahedral structure fabricated using PZT ceramics [85], (d) 3D radial array, and (e-f) 3D periodic lattice printed using a 100 µm nozzle with BT nanoparticle ink, with the cross-sectional over-view [49], (g) Sintered BT honeycomb heating element. The inset shows a magnified optical micrograph of a sintered square grid structure [71], (h) 3D printed green sample with graded porous structure for possible use in heating elements [71], (i) Fresnel zone plate lens fabricated using FFF [107], (j) PZT array [122], and (k) BT green body from milled precursors with complex architectures [93].

(a-b) [97] Open access article distributed under the terms of the Creative Commons CC BY license. Reproduced from Ref.: (c) [85], (g-h) [71], (i) [107], (j) [122], and (k) [93], with permission from Elsevier. (d-e) [49], with permission from John Wiley and Sons.

(i) Use of simple piezoceramic powders

Pure piezoceramic powders, such as PZT, BT, KNN, PNN-PZT and PMNT, have been used for AM in the majority of the articles that have been published so far. There are few studies concerning doped compositions. This means such formulations are still beyond the reach of the AM technologies. In such a scenario, where the trend is to shift from lead-based to lead-free piezoceramics, it is necessary to employ doped compositions in lead-free formulations to enhance the functional properties. The best doped composition should be shared to the industrial

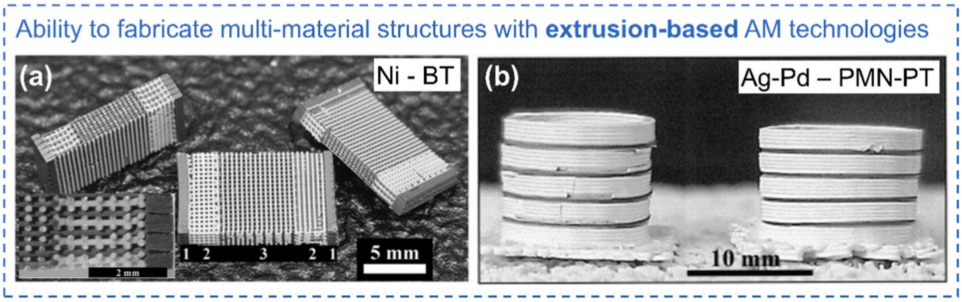

Fig. 46. (a) Isometric view of multilayer Ni-BT structures. The inset shows the cross-section [92]. (b) Multilayer tube actuators made of PMN–PT and electrode materials (silver-palladium) [238].
Reproduced from Ref.: (a) [92], with permission from John Wiley and Sons. (b) [238], with permission from Elsevier.

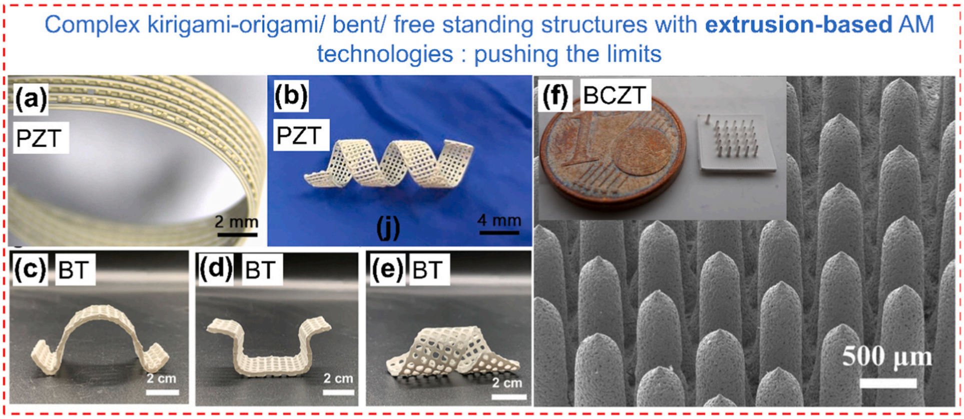

Fig. 47. Optical photos of printed green bodies (a) Bent into an annular structure, and (b) Twisted into ribbon spiral [72]. (c-e) Photographs of sintered kirigami–origami structures with different configurations [69]. (f) Representative optical image of the free-standing pillars with their corresponding SEM micrographs [84].
Reproduced from Ref.: (a-b) [72], and (f) [84], with permission from Elsevier. (c-e) [69] Open access article distributed under the terms of the Creative Commons CC BY license.

partners for production in bulk quantities.

(ii) Limited use of texturing

It is widely established that texturing through templated grain growth significantly enhances the piezoelectric properties. The manufacturing technique for the platelets, on the other hand, is highly time demanding and calls for high levels of control over the stoichiometry. For such reasons, the production of the platelet powders has not been widely commercialized yet. Moreover, achieving a fully aligned distribution of platelets within additively manufactured parts using currently available technologies is still a challenge. This restricts the further usage of the concept of texturing in the field of AM.

(iii) Ability to fabricate multi-material structures

The concept of multi-material fabrication using piezoceramics is still in its early stages. The integration of various piezoceramic materials or piezoceramics with other materials, such as metals, polymers or other ceramics, can be made possible by multi-material AM. Enhanced sensitivity and better mechanical properties are two examples of enhanced performance attributes that may result from this.

(iv) Hybridization of technologies

Hybridization in AM refers to the integration and exploitation of the unique advantages of several production techniques. To enhance the quality of piezoceramics, one possible approach is to combine Direct Ink Writing (DIW) with stereolithography (SLA) to create components with enhanced flexibility. Such hybridization has been recently reported by several authors [240,241] and could be translated to piezoceramic components as well.

(v) Limited size

AM techniques are often restricted by the build volume of the available printers. This is particularly challenging when a large component is desired. For example, the debinding of large components is time-consuming and can lead to delamination or warping during the thermal treatment process. Internal stresses during the printing can also increase when fabricating large components. In addition, the time required to print large structures can lead to an economic constraint. There is often a compromise between the dimensions of the component and the level of resolution or detail that can be attained. When dealing with larger components, it may be necessary to use thicker layers in order to keep the printing time reasonable. However, this might result in a loss of detail and a less smooth surface quality.

(vi) Rapid post processing

Efficient post-processing techniques are crucial for enhancing productivity and minimising the production time. Rapid sintering techniques, such as spark plasma sintering, ultra-fast high temperature sintering etc., which aim at decreasing the sintering temperature and time drastically, have not been well implemented yet. The microstructure is strongly affected by the heating and cooling rates, with rapid

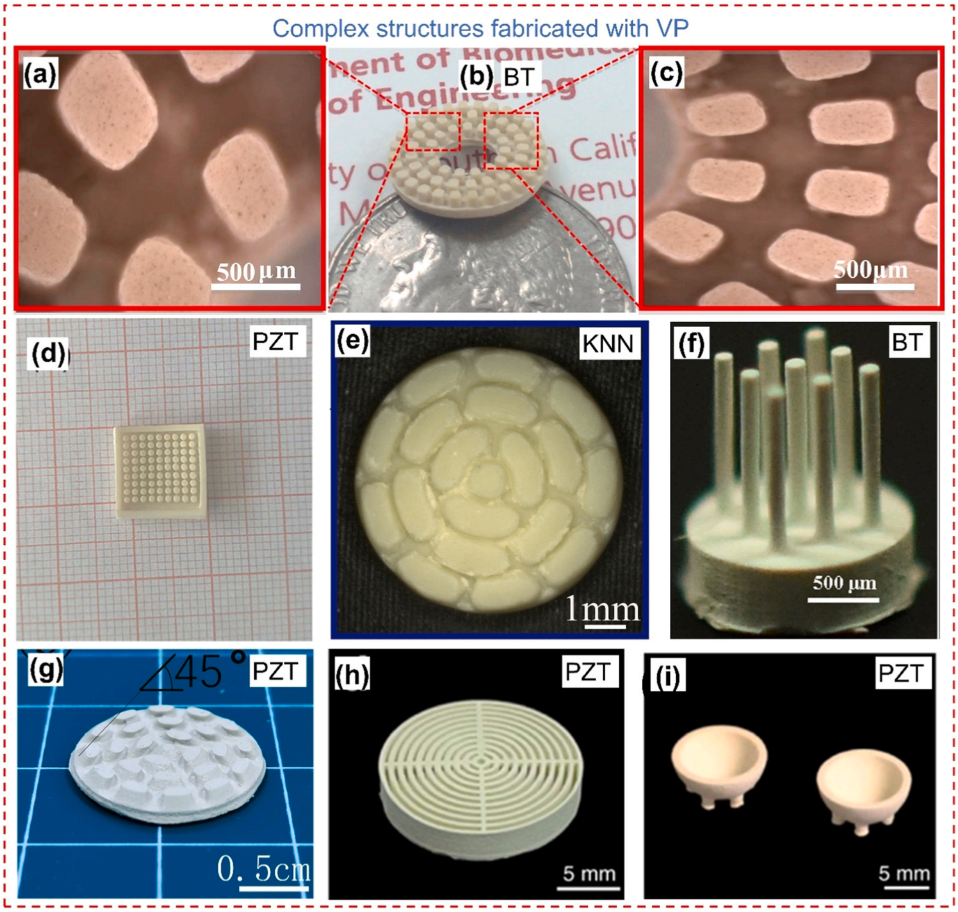

Fig. 48. Optical microscopy images of different types of sintered arrays that can be used for several applications [146,171,179,180,186,188].
Reproduced from Ref.: (a-c) [179], (d) [186], (e) [180], (f) [146], (g) [171], with permission from Elsevier. (h-i) [188], Open access article distributed under the terms of the Creative Commons CC BY license.

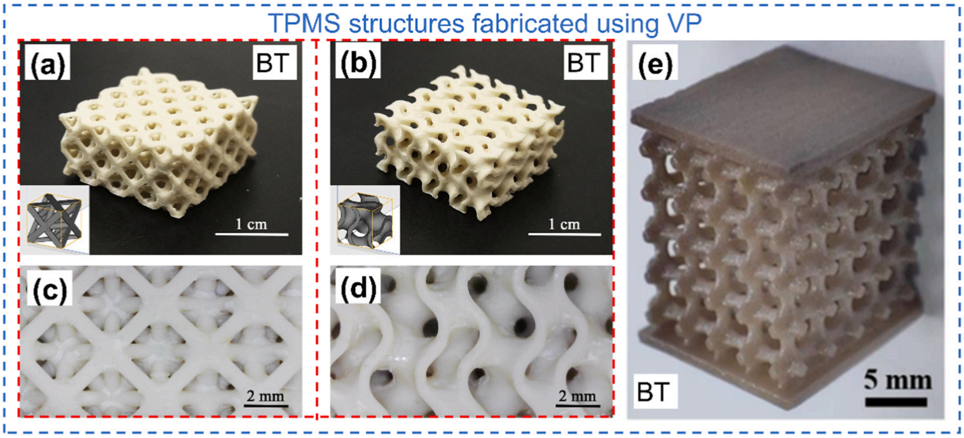

Fig. 49. Optical images of complex TPMS structures [139,143].
Reproduced from Ref.: (a-d) [139], with permission from Elsevier. (e) [143], Open access article distributed under the terms of the Creative Commons CC BY license.

heating and cooling rates often leading to finer microstructures. It is also important to keep in mind the sintering atmosphere, as it plays a important role and hence it should be carefully chosen.

(vii) Unavailability of commercial piezoceramic filaments or slurries (for DIW or VP)

The absence of easily accessible commercial piezoceramic filaments or slurries for Direct Ink Writing (DIW) or Vat Photopolymerization (VP) is an important challenge that restricts the industrial use of AM technologies. This slows down the development process as a lot of time is required in optimizing the piezoceramic formulation. Manufacturing piezoceramic materials internally may result in variations in both quality and performance due to variations in raw materials, processing conditions and handling.

To summarize, AM technologies open up new opportunities for the

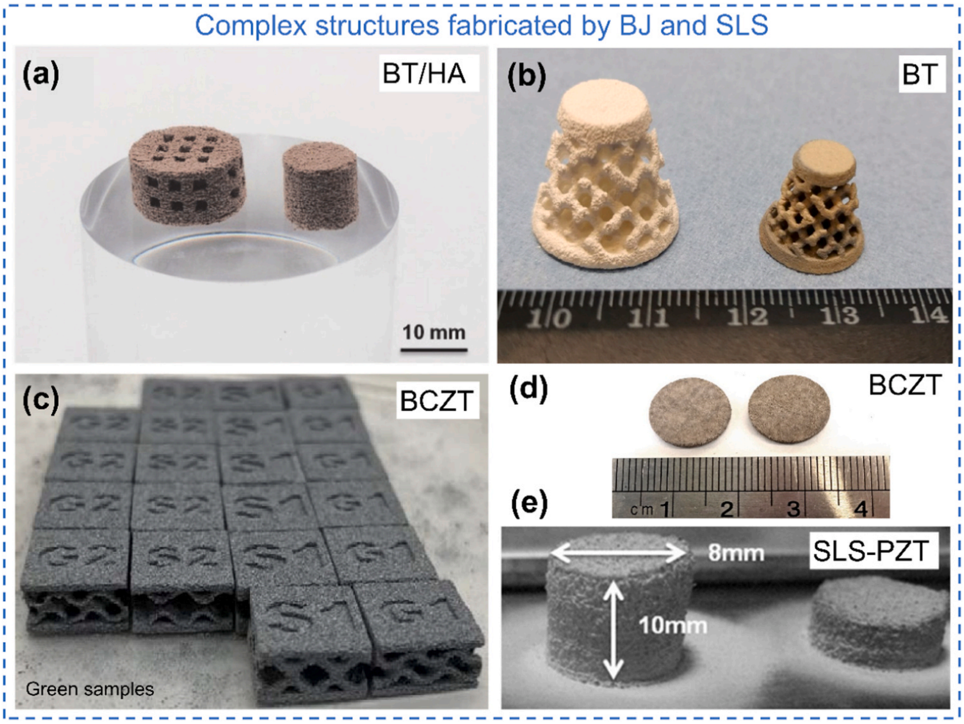

Fig. 50. (a-d) Optical images of scaffold structures fabricated using binder jetting [191,192,194,197]. The circular samples showed in (d) are typically usually used for the property measurements, which holds true for other AM techniques as well. (e) Simple cylinder fabricated using SLS [210].
(a) [197], (b) [194], (c-d) [192], Open access article distributed under the terms of the Creative Commons CC BY license. Reproduced from Ref. (e) [210], with permission from Elsevier.

Table 12
Classification of the additively manufactured piezoceramic components according to their application.

Additive manufacturing	Material	Applications
Direct ink writing	BST	Bone tissue engineering [96]
	BT -based	Heating element[71]
	PZT	Transducer [83], Sensor [54,69,98]
	BCZT	Bone graft substitute [97]
Fused filament fabrication	PZT	Actuator [99,103,130,133], Transducer [122]
	BST	Antenna [126]
	BT	Antenna [110], Bioactive scaffolds [111]
Vat photopolymerization	PZT, PMNT	Transducer [142,176,188,239], sensor [188]
	BT, KNN	Transducers [146,147,168,179,180,186], Ultrasonic array [224], Energy harvesting [169,184], Bone scaffolds [144]
Binder jetting	BT	Bone tissue engineering [217]

fabrication of complex and high-precision piezoceramic parts with properties almost similar to the conventional ones. Despite several challenges, this field is rapidly progressing with notable developments. These technological breakthroughs are enabling the exploration of new opportunities in the fields of sensors, actuators and energy harvesting systems. As research and development progresses, the possibility of AM revolutionising the production and functioning of piezoceramic materials becomes more and more real, holding the promise for improved performance and the introduction of new capabilities in several key sectors.

CRediT authorship contribution statement

Gaurav Vajpayee: Writing – original draft, Funding acquisition. **Subhadip Bhandari:** Writing – original draft, Methodology, Funding acquisition, Formal analysis, Data curation, Conceptualization, Writing – review & editing. **Manuel Hinterstein:** Writing – review & editing, Validation, Supervision, Funding acquisition. **Lucas Lemos da Silva:** Writing – review & editing, Funding acquisition. **Paolo Colombo:** Writing – review & editing, Supervision, Project administration, Methodology, Conceptualization. **Giorgia Franchin:** Writing – review & editing, Validation, Supervision, Project administration.

Declaration of Competing Interest

The authors declare the following financial interests/personal relationships which may be considered as potential competing interests. Subhadip Bhandari reports financial support was provided by Foundation of the Savings Bank of Padua and Rovigo (CARIPARO). Manuel Hinterstein, Gaurav Vajpayee, Lucas Lemos da Silva reports financial support was provided by Fraunhofer Internal Programs for financial support under grant no. Attract 40-04857. If there are other authors, they declare that they have no known competing financial interests or personal relationships that could have appeared to influence the work reported in this paper.

Acknowledgement

Subhadip Bhandari gratefully acknowledges the CARIPARO foundation for the PhD scholarship. Manuel Hinterstein, Gaurav Vajpayee, and Lucas Lemos da Silva thank the Fraunhofer Internal Programs for financial support under grant no. Attract 40–04857.

Data availability

Data will be made available on request.

References

[1] World – World Energy Balances: Overview – Analysis - IEA, (n.d.).

[2] A. Smirnov, S. Chugunov, A. Kholodkova, M. Isachenkov, A. Vasin, I. Shishkovsky, Progress and challenges of 3D-printing technologies in the manufacturing of piezoceramics, Ceram. Int. 47 (2021) 10478–10511, https://doi.org/10.1016/J.CERAMINT.2020.12.243.

[3] M. Safaei, H.A. Sodano, S.R. Anton, M. Habib, I. Lantgios, K. Hornbostel, A review of ceramic, polymer and composite piezoelectric materials, J. Phys. D. Appl. Phys. 55 (2022) 423002, https://doi.org/10.1088/1361-6463/AC8687.

[4] G.H. Haertling, Ferroelectric ceramics: History and technology, J. Am. Ceram. Soc. 82 (1999) 797–818, https://doi.org/10.1111/J.1151-2916.1999.TB01840.X.

[5] A.J. Bell, O. Deubzer, Lead-free piezoelectrics—The Environmental and regulatory issues, MRS Bull. 43 (2018) 581–587, https://doi.org/10.1557/mrs.2018.154.

[6] EU, DIRECTIVE 2002/95/EC OF THE EUROPEAN PARLIAMENT AND OF THE COUNCIL of 27 January 2003 on the restriction of the use of certain hazardous substances in electrical and electronic equipment, Off. J. Eur. Union (2003) 12–25, - Google Search, (n.d.).

[7] Directive - 2002/96 - EN - EUR-Lex, (n.d.). https://doi.org/http://data.europa.eu/eli/dir/2002/96/oj.

[8] T.R. Shrout, S.J. Zhang, Lead-free piezoelectric ceramicS: Alternatives for PZT, J. Electroceram. 19 (2007) 111–124, https://doi.org/10.1007/S10832-007-9047-0/FIGURES/23.

[9] Y. Saito, H. Takao, T. Tani, T. Nonoyama, K. Takatori, T. Homma, T. Nagaya, M. Nakamura, Lead-free piezoceramics, Nature 432 (2004) 84–87, https://doi.org/10.1038/nature03028.

[10] E. Cross, Lead-free at last, Nat 2004 4327013 432 (2004) 24–25, https://doi.org/10.1038/nature03142.

[11] J. Rödel, K.G. Webber, R. Dittmer, W. Jo, M. Kimura, D. Damjanovic, Transferring lead-free piezoelectric ceramics into application, J. Eur. Ceram. Soc. 35 (2015) 1659–1681, https://doi.org/10.1016/J.JEURCERAMSOC.2014.12.013.

[12] M. Acosta, N. Novak, V. Rojas, S. Patel, R. Vaish, J. Koruza, G.A. Rossetti, J. Rödel, BaTiO3-based piezoelectrics: fundamentals, current status, and perspectives, Appl. Phys. Rev. 4 (2017), https://doi.org/10.1063/1.4990046.

[13] J. Koruza, P. Groszewicz, H. Breitzke, G. Buntkowsky, T. Rojac, B. Malič, Grain-size-induced ferroelectricity in NaNbO3, Acta Mater. 126 (2017) 77–85, https://doi.org/10.1016/J.ACTAMAT.2016.12.049.

[14] C.A. Randall, N. Kim, J.P. Kucera, W. Cao, T.R. Shrout, Intrinsic and extrinsic size effects in fine-grained morphotropic-phase-boundary lead zirconate titanate ceramics, J. Am. Ceram. Soc. 81 (1998) 677–688, https://doi.org/10.1111/J.1151-2916.1998.TB02389.X.

[15] G. Picht, N.H. Khansur, K.G. Webber, H. Kungl, M.J. Hoffmann, M. Hinterstein, Grain size effects in donor doped lead zirconate titanate ceramics, J. Appl. Phys. 128 (2020) 214105, https://doi.org/10.1063/5.0029659.

[16] L. Lemos Da Silva, K.Y. Lee, S. Petrick, M. Etter, A. Schökel, C.G. Chaves, N. Oliveira Da Silva, K.V. Lalitha, G. Picht, M.J. Hoffmann, M. Hinterstein, Uncovering the symmetry of the induced ferroelectric phase transformation in polycrystalline barium titanate, J. Appl. Phys. 130 (2021), https://doi.org/10.1063/5.0068703.

[17] B. Wang, F. Li, L.-Q. Chen, B. Wang, L.-Q. Chen, F. Li, Inverse domain-size dependence of piezoelectricity in ferroelectric crystals, Adv. Mater. 33 (2021) 2105071, https://doi.org/10.1002/ADMA.202105071.

[18] A.K. Batra, A. Alomari, Fundamentals of Ferroelectric Materials, Power Harvest. via Smart Mater. (2017) 1–32, https://doi.org/10.1117/3.2268643.ch2.

[19] H. Takahashi, Y. Numamoto, J. Tani, S. Tsurekawa, Piezoelectric properties of BaTiO3 ceramics with high performance fabricated by microwave sintering, Jpn. J. Appl. Phys., Part 1 Regul. Pap. Short. Notes Rev. Pap. 45 (2006) 7405–7408, https://doi.org/10.1143/JJAP.45.7405/XML.

[20] D. Ghosh, A. Sakata, J. Carter, P.A. Thomas, H. Han, J.C. Nino, J.L. Jones, Domain wall displacement is the origin of superior permittivity and piezoelectricity in BaTiO 3 at intermediate grain sizes, Adv. Funct. Mater. 24 (2014) 885–896, https://doi.org/10.1002/adfm.201301913.

[21] H. Takahashi, Development of lead-free BaTiO3 ceramics possessing enhanced piezoelectric properties, Electron. Commun. Jpn. 95 (2012) 20–26, https://doi.org/10.1002/ECJ.10418.

[22] Y. Tan, J. Zhang, Y. Wu, C. Wang, V. Koval, B. Shi, H. Ye, R. McKinnon, G. Viola, H. Yan, Unfolding grain size effects in barium titanate ferroelectric ceramics, Sci. Rep. 2015 51 5 (2015) 1–9, https://doi.org/10.1038/srep09953.

[23] Z. Zhao, V. Buscaglia, M. Viviani, M.T. Buscaglia, L. Mitoseriu, A. Testino, M. Nygren, M. Johnsson, P. Nanni, Grain-size effects on the ferroelectric behavior of dense nanocrystalline BaTiO3 ceramics, Phys. Rev. B - Condens. Matter Mater. Phys. 70 (2004) 024107, https://doi.org/10.1103/PHYSREVB.70.024107/FIGURES/5/MEDIUM.

[24] S. Tsunekawa, S. Ito, T. Mori, K. Ishikawa, Z. Li, Y. Kawazoe, Critical size and anomalous lattice expansion in nanocrystalline particles, Phys. Rev. B - Condens. Matter Mater. Phys. 62 (2000) 3065–3070, https://doi.org/10.1103/PhysRevB.62.3065.

[25] G.L. Messing, S. Poterala, Y. Chang, T. Frueh, E.R. Kupp, B.H. Watson, R. L. Walton, M.J. Brova, A.K. Hofer, R. Bermejo, R.J. Meyer, Texture-engineered ceramics—Property enhancements through crystallographic tailoring, 2017 3217, J. Mater. Res. 32 (2017) 3219–3241, https://doi.org/10.1557/JMR.2017.207.

[26] S. Wada, K. Takeda, T. Muraishi, H. Kakemoto, T. Tsurumi, T. Kimura, Preparation of [110] grain oriented barium titanate ceramics by templated grain growth method and their piezoelectric properties, Japanese J. Appl. Physics, Part 1 Regul. Pap. Short Notes Rev. Pap. 46 (2007) 7039–7043. https://doi.org/10.1143/JJAP.46.7039/XML.

[27] E. Kobayashi, S. Ueno, K. Nakashima, N. Kumada, T.S. Suzuki, T. Uchikoshi, Y. Sakka, I. Fujii, S. Wada, Fabrication of (111)-oriented tetragonal BaTiO3 ceramics by an electrophoretic deposition in a high magnetic field, Trans. Mater. Res. Soc. Jpn. 40 (2015) 223–226, https://doi.org/10.14723/TMRSJ.40.223.

[28] D. Vriami, D. Damjanovic, J. Vleugels, O. Van der Biest, Textured BaTiO3 by templated grain growth and electrophoretic deposition, J. Mater. Sci. 50 (2015) 7896–7907, https://doi.org/10.1007/S10853-015-9322-4/FIGURES/16.

[29] M. Özen, M. Mertens, F. Snijkers, G.Van Tendeloo, P. Cool, Texturing of hydrothermally synthesized BaTiO3 in a strong magnetic field by slip casting, Ceram. Int. 42 (2016) 5382–5390, https://doi.org/10.1016/J.CERAMINT.2015.12.073.

[30] J.F. Fernández, P. Durán, C. Moure, Microstructure development of tape casting BaTiO3 ceramics, Http://Dx.Doi.Org/10.1080/00150199208223348 127 (2011) 65–70. https://doi.org/10.1080/00150199208223348.

[31] L. Zhang, J. Zhai, X. Yao, Dielectric Properties of Electrophoretically Deposited and Isothermally Pressed BaTiO3 Thick Films, J. Am. Ceram. Soc. 91 (2008) 2075–2077, https://doi.org/10.1111/J.1551-2916.2008.02385.X.

[32] I. Stanimirović, Z. Stanimirović, Piezoelectric ceramics by powder injection molding, 2010 27th Int. Conf. Microelectron. MIEL 2010 - Proc. (2010) 231–233, https://doi.org/10.1109/MIEL.2010.5490494.

[33] A. Zocca, P. Colombo, C.M. Gomes, J. Günster, Additive Manufacturing of Ceramics: Issues, Potentialities, and Opportunities, J. Am. Ceram. Soc. 98 (2015) 1983–2001, https://doi.org/10.1111/JACE.13700.

[34] C.A. Goat, R.W. Whatmore, The Effect of Grinding Conditions on Lead Zirconate Titanate Machinability, J. Eur. Ceram. Soc. 19 (1999) 1311–1313, https://doi.org/10.1016/S0955-2219(98)00426-9.

[35] C. Chen, X. Wang, Y. Wang, D. Yang, F. Yao, W. Zhang, B. Wang, G.A. Sewvandi, D. Yang, D. Hu, Additive Manufacturing of Piezoelectric Materials, Adv. Funct. Mater. 30 (2020) 2005141, https://doi.org/10.1002/ADFM.202005141.

[36] Y. Lakhdar, C. Tuck, J. Binner, A. Terry, R. Goodridge, Additive manufacturing of advanced ceramic materials, Prog. Mater. Sci. 116 (2021) 100736, https://doi.org/10.1016/j.pmatsci.2020.100736.

[37] A. Sotov, A. Kantyukov, A. Popovich, V. Sufiiarov, A Review on Additive Manufacturing of Functional Gradient Piezoceramic, Micromachines 13 (2022), https://doi.org/10.3390/mi13071129.

[38] J. Park, D.G. Lee, S. Hur, J.M. Baik, H.S. Kim, H.C. Song, A Review on Recent Advances in Piezoelectric Ceramic 3D Printing, Vol. 12, Page 177, Actuators 2023 12 (2023) 177, https://doi.org/10.3390/ACT12040177.

[39] D. Sun, Y. Lu, T. Karaki, Review of the applications of 3D printing technology in the field of piezoelectric ceramics, Resour. Chem. Mater. 2 (2023) 128–142, https://doi.org/10.1016/J.RECM.2023.02.001.

[40] A. Shahzad, I. Lazoglu, Direct ink writing (DIW) of structural and functional ceramics: recent achievements and future challenges, Compos. Part B Eng. 225 (2021) 109249, https://doi.org/10.1016/J.COMPOSITESB.2021.109249.

[41] L. del-Mazo-Barbara, M.P. Ginebra, Rheological characterisation of ceramic inks for 3D direct ink writing: a review, J. Eur. Ceram. Soc. 41 (2021) 18–33, https://doi.org/10.1016/J.JEURCERAMSOC.2021.08.031.

[42] S. Lamnini, H. Elsayed, Y. Lakhdar, F. Baino, F. Smeacetto, E. Bernardo, Robocasting of advanced ceramics: ink optimization and protocol to predict the printing parameters - A review, Heliyon 8 (2022), https://doi.org/10.1016/J.HELIYON.2022.E10651.

[43] J.M.F. Ferreira, S.M. Olhero, A. Kaushal, Is the ubiquitous presence of barium carbonate responsible for the poor aqueous processing ability of barium titanate? J. Eur. Ceram. Soc. 33 (2013) 2509–2517, https://doi.org/10.1016/J.JEURCERAMSOC.2013.05.010.

[44] S.M. Olhero, A. Kaushal, J.M.F. Ferreira, Preventing hydrolysis of BaTiO3 powders during aqueous processing and of bulk ceramics after sintering, J. Eur. Ceram. Soc. 35 (2015) 2471–2478, https://doi.org/10.1016/J.JEURCERAMSOC.2015.03.007.

[45] A. Kaushal, S.M. Olhero, J.M.F. Ferreira, Lead-free 0.5Ba(Zr0.2Ti0.8)O3-0.5(Ba 0.7Ca0.3)TiO3 powder surface treated against hydrolysis-a key for a successful aqueous processing, J. Mater. Chem. C. 1 (2013) 4846–4853, https://doi.org/10.1039/C3TC30741G.

[46] T. Bakarič, B. Budič, B. Malič, D. Kuščer, The influence of pH dependent ion leaching on the processing of lead-zirconate-titanate ceramics, J. Eur. Ceram. Soc. 35 (2015) 2295–2302, https://doi.org/10.1016/J.JEURCERAMSOC.2015.02.021.

[47] Thermal shock cracking resistant multilayer ceramic capacitor termination compositions, (1992).

[48] Zeta potential | Anton Paar Wiki, (n.d.).

[49] Q. Li, J.A. Lewis, Nanoparticle Inks for Directed Assembly of Three-Dimensional Periodic Structures, Adv. Mater. 15 (2003) 1639–1643, https://doi.org/10.1002/ADMA.200305413.

[50] S.S. Nadkarni, J.E. Smay, Concentrated barium titanate colloidal gels prepared by bridging flocculation for use in solid freeform fabrication, J. Am. Ceram. Soc. 89 (2006) 96–103, https://doi.org/10.1111/j.1551-2916.2005.00646.x.

[51] B. Nan, S. Olhero, R. Pinho, P.M. Vilarinho, T.W. Button, J.M.F. Ferreira, Direct ink writing of macroporous lead-free piezoelectric Ba0.85Ca0.15Zr0.1Ti0.9O3, J. Am. Ceram. Soc. 102 (2019) 3191–3203, https://doi.org/10.1111/JACE.16220.

[52] R.L. Walton, M.A. Fanton, R.J. Meyer, G.L. Messing, Dispersion and rheology for direct writing lead-based piezoelectric ceramic pastes with anisotropic template

particles, J. Am. Ceram. Soc. 103 (2020) 6157–6168, https://doi.org/10.1111/JACE.17350.

[53] J.H. Adair, J. Crampo, M.M. Mandanas, E. Suvaci, The role of material chemistry in processing BaTiO 3 in aqueous suspensions, J. Am. Ceram. Soc. 89 (2006) 1853–1860, https://doi.org/10.1111/J.1551-2916.2006.01021.X.

[54] J. Li, M. Yan, Y. Zhang, Z. Li, Z. Xiao, H. Luo, X. Yuan, D. Zhang, Optimization of polarization direction on 3D printed 3-3 piezoelectric composites for sensing application, Addit. Manuf. 58 (2022) 103060, https://doi.org/10.1016/j.addma.2022.103060.

[55] T. Swift, L. Swanson, M. Geoghegan, S. Rimmer, The pH-responsive behaviour of poly(acrylic acid) in aqueous solution is dependent on molar mass, Soft Matter 12 (2016) 2542–2549, https://doi.org/10.1039/C5SM02693H.

[56] J.E. Smay, J. Cesarano, J.A. Lewis, Colloidal inks for directed assembly of 3-D periodic structures, Langmuir 18 (2002) 5429–5437, https://doi.org/10.1021/la0257135.

[57] G.M. Channell, C.F. Zukoski, Shear and compressive rheology of aggregated alumina suspensions, AIChE J. 43 (1997) 1700–1708, https://doi.org/10.1002/AIC.690430707.

[58] A. Renteria, J.A. Diaz, B. He, I.A. Renteria-Marquez, L.A. Chavez, J.E. Regis, Y. Liu, D. Espalin, T.L. Tseng, Y. Lin, Particle size influence on material properties of BaTiO3 ceramics fabricated using freeze-form extrusion 3D printing, Mater. Res. Express 6 (2019), https://doi.org/10.1088/2053-1591/ab4a36.

[59] A. Renteria, H. Fontes, J.A. Diaz, J.E. Regis, L.A. Chavez, T.L. Tseng, Y. Liu, Y. Lin, Optimization of 3D printing parameters for BaTiO3 piezoelectric ceramics through design of experiments, Mater. Res. Express 6 (2019), https://doi.org/10.1088/2053-1591/ab200e.

[60] A. Goulas, G. Chi-Tangyie, S. Zhang, D. Wang, A. Ketharam, B. Vaidhyanathan, I. M. Reaney, D.A. Cadman, W. Whittow, J. (Yiannis) C. Vardaxoglou, D. S. Engstrøm, Direct ink writing of bismuth molybdate microwave dielectric ceramics, Ceram. Int. 47 (2021) 7625–7631, https://doi.org/10.1016/j.ceramint.2020.11.102.

[61] A. Renteria, L.F. Garcia, V.H. Balcorta, D. Ortiz, L.C. Delfin, J. Regis, M. Marcos-Hernández, D. Espalin, T.L. (Bill) Tseng, Y. Lin, Influence of bimodal particle distribution on material properties of BaTiO3 fabricated by paste extrusion 3D printing, Ceram. Int. 47 (2021) 18477–18486, https://doi.org/10.1016/j.ceramint.2021.03.171.

[62] Z. Zhou, M.J. Solomon, P.J. Scales, D.V. Boger, The yield stress of concentrated flocculated suspensions of size distributed particles, J. Rheol. (N. Y. N. Y 43 (1999) 651–671, https://doi.org/10.1122/1.551029.

[63] A.S. Mueller, E.W. Llewellin, H.M. Mader, S.P. Mathematical, E. Sciences, The rheology of suspensions of solid particles Linked references are available on JSTOR for this article, Rheol. Suspens. Solid Part. 466 (2010) 1201–1228, https://doi.org/10.1007/BF01432034.

[64] P. D'Haene, J. Mewis, Rheological characterization of bimodal colloidal dispersions, Rheol. Acta 33 (1994) 165–174, https://doi.org/10.1007/BF00437301/METRICS.

[65] S. Pednekar, J. Chun, J.F. Morris, Bidisperse and polydisperse suspension rheology at large solid fraction, J. Rheol. (N. Y. N. Y). 62 (2018) 513–526. https://doi.org/10.1122/1.5011353/16137306/513_1_ACCEPTED_MANUSCRIPT.PDF.

[66] J.P. Hong, S.W. Yoon, T. Hwang, J.S. Oh, S.C. Hong, Y. Lee, J.Do Nam, High thermal conductivity epoxy composites with bimodal distribution of aluminum nitride and boron nitride fillers, Thermochim. Acta 537 (2012) 70–75, https://doi.org/10.1016/J.TCA.2012.03.002.

[67] W. Pabst, E. Gregorová, C. Berthold, Particle shape and suspension rheology of short-fiber systems, J. Eur. Ceram. Soc. 26 (2006) 149–160, https://doi.org/10.1016/J.JEURCERAMSOC.2004.10.016.

[68] I. Santamaría-Holek, C.I. Mendoza, The rheology of concentrated suspensions of arbitrarily-shaped particles, J. Colloid Interface Sci. 346 (2010) 118–126, https://doi.org/10.1016/J.JCIS.2010.02.033.

[69] Z. Wang, D. Ma, Y. Wang, Y. Xie, Z. Yu, J. Cheng, L. Li, L. Sun, S. Dong, H. Wang, Kirigami–Origami-Inspired Lead-Free Piezoelectric Ceramics, Adv. Sci. 10 (2023) 2207059, https://doi.org/10.1002/ADVS.202207059.

[70] M. Lorenz, A. Martin, K.G. Webber, N. Travitzky, Electromechanical Properties of Robocasted Barium Titanate Ceramics, Adv. Eng. Mater. 22 (2020) 1–10, https://doi.org/10.1002/adem.202000325.

[71] W. Rowlands, B. Vaidhyanathan, Additive manufacturing of barium titanate based ceramic heaters with positive temperature coefficient of resistance (PTCR), J. Eur. Ceram. Soc. 39 (2019) 3475–3483, https://doi.org/10.1016/J.JEURCERAMSOC.2019.03.024.

[72] Z. Li, J. Li, H. Luo, X. Yuan, X. Wang, H. Xiong, D. Zhang, Direct ink writing of 3D piezoelectric ceramics with complex unsupported structures, J. Eur. Ceram. Soc. 42 (2022) 3841–3847, https://doi.org/10.1016/j.jeurceramsoc.2022.03.038.

[73] C. Gadea, T. Spelta, S.B. Simonsen, V. Esposito, J.R. Bowen, A.B. Haugen, Hybrid inks for 3D printing of tall BaTiO3-based ceramics, Open Ceram. 6 (2021) 3–10, https://doi.org/10.1016/j.oceram.2021.100110.

[74] S.S. Hossain, S. Jang, S. Park, C.J. Bae, Understanding ink design and printing dynamics of extrusion-based 3D printing: Defect-free dense piezoelectric ceramics, J. Manuf. Process. 92 (2023) 1–11, https://doi.org/10.1016/j.jmapro.2023.02.018.

[75] S.L. Morissette, J.A. Lewis, P.G. Clem, J. Cesarano, D.B. Dimos, Direct-Write Fabrication of Pb(Nb,Zr,Ti)O3 Devices: Influence of Paste Rheology on Print Morphology and Component Properties, J. Am. Ceram. Soc. 84 (2001) 2462–2468, https://doi.org/10.1111/J.1151-2916.2001.TB01036.X.

[76] W.H. Herschel, R. Bulkley, Konsistenzmessungen von Gummi-Benzollösungen, Kolloid-Z. 39 (1926) 291–300, https://doi.org/10.1007/BF01432034/METRICS.

[77] S.E. Hall, J.E. Regis, A. Renteria, L.A. Chavez, L. Delfin, S. Vargas, M. R. Haberman, D. Espalin, R. Wicker, Y. Lin, Paste extrusion 3D printing and characterization of lead zirconate titanate piezoelectric ceramics, Ceram. Int. 47 (2021) 22042–22048, https://doi.org/10.1016/j.ceramint.2021.04.224.

[78] T. Rosental, S. Magdassi, A New Approach to 3D Printing Dense Ceramics by Ceramic Precursor Binders, Adv. Eng. Mater. 21 (2019) 1–8, https://doi.org/10.1002/adem.201900604.

[79] S. Bhandari, O. Hanzel, P. Veteška, M. Janek, E. De Bona, V.M. Sglavo, M. Biesuz, G. Franchin, From rapid prototyping to rapid firing: on the feasibility of high-speed production for complex BaTiO3 components, J. Am. Ceram. Soc. (2024), https://doi.org/10.1111/JACE.19950.

[80] R. Damamme, L. Seveyrat, A. Borta-Boyon, V.C. Nguyen, M.Q. Le, P.J. Cottinet, 3D printing of doped barium-titanate using robocasting - Toward new generation lead-free piezoceramic transducers, J. Eur. Ceram. Soc. 43 (2023) 3297–3306, https://doi.org/10.1016/j.jeurceramsoc.2023.02.054.

[81] A. M`Barki, L. Bocquet, A. Stevenson, Linking rheology and printability for dense and strong ceramics by direct ink writing, Sci. Rep. 2017 71 7 (2017) 1–10, https://doi.org/10.1038/s41598-017-06115-0.

[82] T. Mori, Y. Hori, H. Fei, I. Inamine, K. Asai, T. Kiguchi, J. Tsubaki, Experimental study about the agglomeration behavior in slurry prepared by adding excess polyelectrolyte dispersant, Adv. Powder Technol. 23 (2012) 661–666, https://doi.org/10.1016/J.APT.2011.08.004.

[83] K. Liu, Q. Zhang, C. Zhou, Y. Shi, C. Sun, H. Sun, C. Yin, J. Hu, S. Zhou, Y. Zhang, Y. Fu, 4D Printing of lead zirconate titanate piezoelectric composites transducer based on direct ink writing, Front. Mater. 8 (2021) 1–11, https://doi.org/10.3389/fmats.2021.659441.

[84] B. Nan, F.J. Galindo-Rosales, J.M.F. Ferreira, 3D printing vertically: Direct ink writing free-standing pillar arrays, Mater. Today 35 (2020) 16–24, https://doi.org/10.1016/j.mattod.2020.01.003.

[85] K. Liu, Y. Xia, Q. Zhang, Y. Du, Y. Shi, S. Joshi, C. Yan, Y. Wu, S. Huang, H. Sun, Effect of the slurry composition on the piezoelectric properties of PZT ceramics fabricated via materials extrusion 3D printing, Ceram. Int. 49 (2023) 20024–20033, https://doi.org/10.1016/j.ceramint.2023.03.124.

[86] H. Kim, A. Renteria-Marquez, M.D. Islam, L.A. Chavez, C.A. Garcia Rosales, M. A. Ahsan, T.L.B. Tseng, N.D. Love, Y. Lin, Fabrication of bulk piezoelectric and dielectric BaTiO 3 ceramics using paste extrusion 3D printing technique, J. Am. Ceram. Soc. 102 (2019) 3685–3694, https://doi.org/10.1111/jace.16242.

[87] E. Koos, N. Willenbacher, Capillary forces in suspension rheology, Science 80 (331) (2011) 897–900, https://doi.org/10.1126/science.1199243.

[88] D. Menne, L. Lemos da Silva, M. Rotan, J. Glaum, M. Hinterstein, N. Willenbacher, Giant functional properties in porous electroceramics through additive manufacturing of capillary suspensions, ACS Appl. Mater. Interfaces 14 (2022) 3027–3037, https://doi.org/10.1021/acsami.1c19297.

[89] J. Dittmann, E. Koos, N. Willenbacher, Ceramic capillary suspensions: novel processing route for macroporous ceramic materials, J. Am. Ceram. Soc. 96 (2013) 391–397, https://doi.org/10.1111/jace.12126.

[90] M. Pospischil, J. Specht, M. König, M. Hörteis, C. Mohr, F. Clement, D. Biro, Paste rheology correlating with dispensed finger geometry, IEEE J. Photovolt. 4 (2014) 498–503, https://doi.org/10.1109/JPHOTOV.2013.2278657.

[91] R.L. Walton, M.J. Brova, B.H. Watson, E.R. Kupp, M.A. Fanton, R.J. Meyer, G. L. Messing, Direct writing of textured ceramics using anisotropic nozzles, J. Eur. Ceram. Soc. 41 (2021) 1945–1953, https://doi.org/10.1016/j.jeurceramsoc.2020.10.021.

[92] J.E. Smay, S.S. Nadkarni, J. Xu, Direct writing of dielectric ceramics and base metal electrodes, Int. J. Appl. Ceram. Technol. 4 (2007) 47–52, https://doi.org/10.1111/j.1744-7402.2007.02118.x.

[93] X. Wei, Y. Liu, D. Zhao, S.S. Ge, 3D printing of piezoelectric barium titanate with high density from milled powders, J. Eur. Ceram. Soc. 40 (2020) 5423–5430, https://doi.org/10.1016/j.jeurceramsoc.2020.06.021.

[94] J. Jia, H. Nie, X. He, C. Feng, M. Zhu, C. Wu, G. Wang, X. Dong, Significantly decreased depolarization hydrostatic pressure of 3D-printed PZT95/5 ceramics with periodically distributed pores, J. Am. Ceram. Soc. 105 (2022) 412–418, https://doi.org/10.1111/jace.18080.

[95] Y. Li, L. Li, B. Li, Direct ink writing of three-dimensional (K, Na)NbO3-based piezoelectric ceramics, Materials 8 (2015) 1729–1737, https://doi.org/10.3390/ma8041729.

[96] T. Tariverdian, A. Behnamghader, P. Brouki Milan, H. Barzegar-Bafrooei, M. Mozafari, 3D-printed barium strontium titanate-based piezoelectric scaffolds for bone tissue engineering, Ceram. Int. 45 (2019) 14029–14038, https://doi.org/10.1016/j.ceramint.2019.04.102.

[97] L. Nedelcu, J.M.F. Ferreira, A.C. Popa, L. Amarande, B. Nan, L.M. Bălescu, C. D. Geambașu, M.C. Cioangher, L. Leonat, M. Grigoroscuță, D. Cristea, H. Stroescu, R.C. Ciocoiu, G.E. Stan, Multi-parametric exploration of a selection of piezoceramic materials for bone graft substitute applications, Mater. (Basel) 16 (2023) 1–23, https://doi.org/10.3390/ma16030901.

[98] J. Ye, H. Gong, Y. Zhang, Q. Xu, X. Zhou, M. Yan, D. Zhai, K. Zhou, D. Zhang, C. Bowen, Piezoelectric ceramics with hierarchical macro- and micro-pore channels for sensing applications, Addit. Manuf. 79 (2024) 103915, https://doi.org/10.1016/j.addma.2023.103915.

[99] T.F. McNulty, F. Mohammadi, A. Bandyopadhyay, D.J. Shanefield, S.C. Danforth, A. Safari, Development of a binder formulation for fused deposition of ceramics, Rapid Prototyp. J. 4 (1998) 144–150, https://doi.org/10.1108/13552549810239012.

[100] N. Venkataraman, S. Rangarajan, M.J. Matthewson, A. Safari, S.C. Danforth, A. Yardimci, Mechanical and rheological properties of feedstock material for

fused deposition of ceramics and metals (FDC and FDMet) and their relationship to process performance, Solid Free. Fabr. Proc. August 1999 (1999) 351–359.
[101] N. Venkataraman, S. Rangarajan, M.J. Matthewson, B. Harper, A. Safari, S. C. Danforth, G. Wu, N. Langrana, S. Guceri, A. Yardimci, Feedstock material property - Process relationships in fused deposition of ceramics (FDC), Rapid Prototyp. J. 6 (2000) 244–252, https://doi.org/10.1108/13552540010373344.
[102] M. Allahverdi, B. Jadidian, Y. Ito, A. Safari, Fabrication of Bismuth Titanate components with oriented microstructures via FDC and TGG, IEEE Int. Symp. Appl. Ferroelectr. 1 (2000) 385–388, https://doi.org/10.1109/isaf.2000.941577.
[103] A. Safari, S.C. Danforth, M. Jafari, M. Allahverdi, B. Jadidian, F. Mohammadi, Processing and properties of piezoelectric actuators developed by fused deposition technique, IEEE Int. Symp. Appl. Ferroelectr. 1 (2000) 79–82, https://doi.org/10.1109/isaf.2000.941516.
[104] A. Bandyopadhyay, R.K. Panda, V.F. Janas, M.K. Agarwala, S.C. Danforth, A. Safari, Processing of piezocomposites by fused deposition technique, J. Am. Ceram. Soc. 80 (1997) 1366–1372, https://doi.org/10.1111/j.1151-2916.1997.tb02993.x.
[105] Y. Wu, D. Isakov, P.S. Grant, Fabrication of composite filaments with high dielectric permittivity for fused deposition 3D printing, Materials 10 (2017), https://doi.org/10.3390/ma10101218.
[106] B. Khatri, K. Lappe, M. Habedank, T. Mueller, C. Megnin, T. Hanemann, Fused deposition modeling of ABS-barium titanate composites: a simple route towards tailored dielectric devices, Polymers 10 (2018), https://doi.org/10.3390/polym10060666.
[107] A. Goulas, S. Zhang, J.R. McGhee, D.A. Cadman, W.G. Whittow, J.C. Vardaxoglou, D.S. Engstrøm, Fused filament fabrication of functionally graded polymer composites with variable relative permittivity for microwave devices, Mater. Des. 193 (2020) 108871, https://doi.org/10.1016/j.matdes.2020.108871.
[108] H. Kim, F. Torres, D. Villagran, C. Stewart, Y. Lin, T.L.B. Tseng, 3D printing of BaTiO3/PVDF composites with electric in situ poling for pressure sensor applications, Macromol. Mater. Eng. 302 (2017) 1–6, https://doi.org/10.1002/mame.201700229.
[109] R. Tao, J. Shi, F. Granier, M. Moeini, A. Akbarzadeh, D. Therriault, Multi-material fused filament fabrication of flexible 3D piezoelectric nanocomposite lattices for pressure sensing and energy harvesting applications, Appl. Mater. Today 29 (2022) 101596, https://doi.org/10.1016/J.APMT.2022.101596.
[110] R. Colella, F.P. Chietera, A. Greco, F. Montagna, L. Catarinucci, 3D-printed tunable UHF RFID PIFA realized with BaTiO3enhanced PLA for multipurpose applications, 2020 33rd Gen. Assem. Sci. Symp. Int. Union Radio Sci. URSI GASS 2020 (2020), https://doi.org/10.23919/URSIGASS49373.2020.9232412.
[111] P. Sikder, P. Nagaraju, H.P.S. Naganaboyina, 3D-printed piezoelectric porous bioactive scaffolds and clinical ultrasonic stimulation can help in enhanced bone regeneration, Bioengineering 9 (2022), https://doi.org/10.3390/bioengineering9110679.
[112] P. Parsons, Z. Larimore, M. Mirotznik, G. Mitchell, Composite materials development for fused filament fabrication of RF systems, Appl. Comput. Electromagn. Soc. J. 35 (2020) 1278–1279, https://doi.org/10.47037/2020.ACES.J.351108.
[113] S. Bhandari, P. Veteška, G. Vajpayee, M. Hinterstein, Z. Bača, Z. Hajdúchová, G. Špitalský, M. Franchin, Janek, Material-extrusion based additive manufacturing of BaTiO3 ceramics: from filament production to sintered properties, Addit. Manuf. 88 (2024) 104238, https://doi.org/10.1016/J.ADDMA.2024.104238.
[114] C. Aumnate, A. Pongwisuthiruchte, P. Pattananuwat, P. Potiyaraj, Fabrication of ABS/Graphene oxide composite filament for fused filament fabrication (FFF) 3D Printing, Adv. Mater. Sci. Eng. 2018 (2018), https://doi.org/10.1155/2018/2830437.
[115] H. Kim, J. Johnson, L.A. Chavez, C.A. Garcia Rosales, T.L.B. Tseng, Y. Lin, Enhanced dielectric properties of three phase dielectric MWCNTs/BaTiO3/PVDF nanocomposites for energy storage using fused deposition modeling 3D printing, Ceram. Int. 44 (2018) 9037–9044, https://doi.org/10.1016/j.ceramint.2018.02.107.
[116] T. Sebastian, M. Bach, A. Geiger, T. Lusiola, L. Kozielski, F. Clemens, Investigation of electromechanical properties on 3-d printed piezoelectric composite scaffold structures, Mater. (Basel) 14 (2021), https://doi.org/10.3390/ma14205927.
[117] M. Bach, T. Sebastian, M. Melnykowycz, T. Lusiola, D. Scharf, F. Clemens, Industrializing Additive Manufacturing - Proceedings of Additive Manufacturing in Products and Applications - AMPA2017, Ind. Addit. Manuf. - Proc. Addit. Manuf. Prod. Appl. - AMPA2017 2 (2018), https://doi.org/10.1007/978-3-319-66866-6.
[118] L. Gorjan, T. Lusiola, D. Scharf, F. Clemens, Kinetics and equilibrium of Eco-debinding of PZT ceramics shaped by thermoplastic extrusion, J. Eur. Ceram. Soc. 37 (2017) 5273–5280, https://doi.org/10.1016/j.jeurceramsoc.2017.04.063.
[119] I. Özden, A. Iveković, A. Kocjan, Additive manufacturing of ceramics from thermoplastic feedstocks, Open Ceram. 6 (2021), https://doi.org/10.1016/j.oceram.2021.100129.
[120] T.F. McNulty, D.J. Shanefield, S.C. Danforth, A. Safari, Dispersion of lead zirconate titanate for fused deposition of ceramics, J. Am. Ceram. Soc. 82 (1999) 1757–1760, https://doi.org/10.1111/j.1151-2916.1999.tb01996.x.
[121] A.M. Umarji, A.L. Kholkin, T.F. McNulty, S.C. Danforth, A. Safari, Development of tube actuators by Fused Deposition of Ceramics, IEEE Int. Symp. Appl. Ferroelectr. (1998) 269–272. https://doi.org/10.1109/isaf.1998.786685.
[122] G.M. Lous, I.A. Cornejo, T.F. Mcnulty, A. Safari, S.C. Danforth, Fabrication of piezoelectric ceramic / polymer composite transducers using fused deposition of ceramics, Mater. Res. Soc. Symp. - Proc. 542 (1999) 105–110, https://doi.org/10.1557/proc-542-105.
[123] 3D Printing of PZT Piezoelectric Transducer Elements, (n.d.).
[124] N. Venkataraman, S. Rangarajan, B. Harper, M.J. Matthewson, A. Safari, S. C. Danforth, Process-property-performance relationship for fused deposition of ceramics (FDC) feedstock materials, Mater. Res. Soc. Symp. - Proc. 625 (2000) 203–210, https://doi.org/10.1557/PROC-625-203/METRICS.
[125] R.J. Hunter, Foundations of colloid sciennce, Second, Oxford university press, 2001.
[126] A. Goulas, J.R. McGhee, T. Whittaker, D. Ossai, E. Mistry, W. Whittow, B. Vaidhyanathan, I.M. Reaney, J. (Yiannis) C. Vardaxoglou, D.S. Engstrøm, Synthesis and dielectric characterisation of a low loss BaSrTiO3/ABS ceramic/polymer composite for fused filament fabrication additive manufacturing, Addit. Manuf. 55 (2022) 1–8, https://doi.org/10.1016/j.addma.2022.102844.
[127] F. Castles, D. Isakov, A. Lui, Q. Lei, C.E.J. Dancer, Y. Wang, J.M. Janurudin, S. C. Speller, C.R.M. Grovenor, P.S. Grant, Microwave dielectric characterisation of 3D-printed BaTiO3/ABS polymer composites, Sci. Rep. 6 (2016) 1–8, https://doi.org/10.1038/srep22714.
[128] Ferdinand P. Beer, J.T.D. Jr, E. Russell Johnston, Mechanics Of Materials SI Unit Fourth Edition, (2006) 1–796.
[129] N. Venkataraman, T. Mcnulty, S. Rangarajan, M. Vidaic, M.J. Matthewson, N. Langrana, A. Safari, S.C. Danforth, Mechanical Properties Of Feedstock Material For Fused Deposition Of Ceramics N. Venkataraman, T. McNulty, S. Rangarajan, M. Vidaic, M.J. Matthewson, N. Langrana, A. Safari, and S.C. Danforth Rutgers University, Department of Ceramic and Materials Engineer, 542 (n.d.) 111–117.
[130] F. Mohammadi, A. Kholkin, S.C. Danforth, A. Safari, Processing and electromechanical properties of dome-shaped actuators fabricated by Fused Deposition of Ceramics, IEEE Int. Symp. Appl. Ferroelectr. (1998) 273–276, https://doi.org/10.1109/isaf.1998.786686.
[131] M. Bach, T. Sebastian, M. Melnykowycz, T. Lusiola, D. Scharf, F. Clemens, Additive manufacturing of piezoelectric 3-3 composite structures, Ind. Addit. Manuf. - Proc. Addit. Manuf. Prod. Appl. - AMPA2017 (2018) 93–103, https://doi.org/10.1007/978-3-319-66866-6_9.
[132] D.V. Isakov, Q. Lei, F. Castles, C.J. Stevens, C.R.M. Grovenor, P.S. Grant, 3D printed anisotropic dielectric composite with meta-material features, Mater. Des. 93 (2016) 423–430, https://doi.org/10.1016/j.matdes.2015.12.176.
[133] A. Bandyopadhyay, R.K. Panda, T.F. McNulty, F. Mohammadi, S.C. Danforth, A. Safari, Piezoelectric ceramics and composites via rapid prototyping techniques, Rapid Prototyp. J. 4 (1998) 37–49, https://doi.org/10.1108/13552549810200285.
[134] X. Song, Y. Chen, T. Woo, S. Wu, L. Cheng, Ceramic fabrication using Mask-Image-Projection-based Stereolithography integrated with tape-casting, J. Manuf. Process. 20 (2015) 456–464, https://doi.org/10.1016/j.jmapro.2015.06.022.
[135] E. Stefan, T. Didriksen, T. Olav, S. Marie, L. Fontaine, H. Ræder, P.M. Rørvik, Effects of powder properties on the 3D printing of - BaTiO 3 ceramic resins by stereolithography, Prog. Addit. Manuf. (2023), https://doi.org/10.1007/s40964-023-00431-w.
[136] S. Zakeri, M. Vippola, E. Levänen, A comprehensive review of the photopolymerization of ceramic resins used in stereolithography, Addit. Manuf. 35 (2020) 101177, https://doi.org/10.1016/J.ADDMA.2020.101177.
[137] C.-J. Bae, A. Ramachandran, K. Chung, S. Park, C.-J. Bae, A. Ramachandran, K. Chung, S. Park, Ceramic stereolithography: additive manufacturing for 3D complex ceramic structures, J. Korean Ceram. Soc. 54 (2017) 470–477, https://doi.org/10.4191/KCERS.2017.54.6.12.
[138] M.L. Griffith, J.W. Halloran, Scattering of ultraviolet radiation in turbid suspensions, J. Appl. Phys. 81 (1997) 2538–2546, https://doi.org/10.1063/1.364311.
[139] K. Liu, C. Zhou, J. Hu, S. Zhang, Q. Zhang, C. Sun, Y. Shi, H. Sun, C. Yin, Y. Zhang, Y. Fu, Journal of the European Ceramic Society Fabrication of barium titanate ceramics via digital light processing 3D printing by using high refractive index monomer, 41 (2021) 5909–5917. https://doi.org/10.1016/j.jeurceramsoc.2021.04.044.
[140] S. Chen, R. Wang, H. Li, H. Ye, J. Cheng, S. Wu, X. He, B. Jian, R. Tao, Q. Ge, High-precision BaTiO3 piezoelectric ceramics via vat photopolymerization 3D printing, J. Eur. Ceram. Soc. 44 (2024) 116706, https://doi.org/10.1016/J.JEURCERAMSOC.2024.116706.
[141] W. Ma, K. Zheng, Y. Quan, Q. Lian, J. Zhuang, C. Qi, S. Qi, J. Zhang, H. Li, W. Liu, T. Zhao, C. Fei, W. Ren, D. Li, High-precision complex structured Sm-PMN-PT ceramics with large piezoelectric response manufactured by vat photopolymerization, Addit. Manuf. 84 (2024) 104116, https://doi.org/10.1016/j.addma.2024.104116.
[142] O. Dufaud, S. Corbel, Stereolithography of PZT ceramic suspensions 8 (2002) 83–90, https://doi.org/10.1108/13552540210420952.

[143] D. Zhang, Y. Yang, Parameter Optimization for Printing Barium Titanate Piezoelectric Ceramics through Digital Light Processing, (2023).

[144] M. Pan, Y. Chen, J. Wu, G. Fan, X. Zhang, Preparation and properties of K 0. 48 Na 0. 52 NbO 3 ceramics for bone scaffolds via digital light processing, Ceram. Int. 49 (2023) 38519–38526, https://doi.org/10.1016/j.ceramint.2023.09.182.

[145] C.-L. Liu, Q. Du, J.-M. Wu, G. Zhang, Y.-S. Shi, Preparation of porous lead zirconate titanate piezoelectric ceramics via vat photopolymerization combined with burnt polymer spheres technique, Addit. Manuf. (2024) 104326, https://doi.org/10.1016/J.ADDMA.2024.104326.

[146] W. Wang, J. Sun, B. Guo, X. Chen, K.P. Ananth, J. Bai, Journal of the European Ceramic Society Fabrication of piezoelectric nano-ceramics via stereolithography of low viscous and non-aqueous suspensions, J. Eur. Ceram. Soc. 40 (2020) 682–688, https://doi.org/10.1016/j.jeurceramsoc.2019.10.033.

[147] X. Chen, J. Sun, B. Guo, Y. Wang, S. Yu, W. Wang, J. Bai, Effect of the particle size on the performance of BaTiO 3 piezoelectric ceramics produced by additive manufacturing, Ceram. Int. 48 (2022) 1285–1292, https://doi.org/10.1016/j.ceramint.2021.09.213.

[148] C. Liu, Q. Du, C. Zhang, J. Wu, G. Zhang, Fabrication and properties of BaTiO 3 ceramics via digital light processing for piezoelectric energy harvesters, Addit. Manuf. 56 (2022) 102940, https://doi.org/10.1016/j.addma.2022.102940.

[149] Z.X. He, X.T. Gong, C.L. Liu, Q.P. Du, J.M. Wu, G.Z. Zhang, Y.S. Shi, Preparation and properties of (Ba0.85Ca0.15)(Ti0.9Zr0.1)O3 lead-free ceramics via vat photopolymerization, Addit. Manuf. 59 (2022) 103170, https://doi.org/10.1016/J.ADDMA.2022.103170.

[150] C. Liu, Q. Du, H. Zhou, S. Chen, J. Wu, 3D printing of lead zirconate titanate piezoelectric ceramics via digital light processing (DLP, Ceram. Int. 49 (2023) 28492–28499, https://doi.org/10.1016/j.ceramint.2023.06.106.

[151] C. Chen, X. Wang, Y. Wang, H. Gu, W. Zhao, W. Zhang, G. Asha, Digital light processing 3D printing of barium titanate / 1, 6 - ethylene glycol diacrylate / polyethylene glycol (400) diacrylate nanocomposites, Adv. Compos. Hybrid. Mater. 6 (2023) 1–9, https://doi.org/10.1007/s42114-022-00617-w.

[152] C. Liu, Q. Du, H. Zhou, J. Wu, G. Zhang, Y. Shi, Jo u rn a of, Addit. Manuf. (2023) 103857. https://doi.org/10.1016/j.addma.2023.103857.

[153] I.L. de Camargo, M.M. Morais, C.A. Fortulan, M.C. Branciforti, A review on the rheological behavior and formulations of ceramic suspensions for vat photopolymerization, Ceram. Int. 47 (2021) 11906–11921, https://doi.org/10.1016/J.CERAMINT.2021.01.031.

[154] J.H. Jang, S. Wang, S.M. Pilgrim, W.A. Schulze, Preparation and characterization of barium titanate suspensions for stereolithography, J. Am. Ceram. Soc. 83 (2000) 1804–1806, https://doi.org/10.1111/J.1151-2916.2000.TB01467.X.

[155] C. Qian, K. Hu, J. Li, P. Li, Z. Lu, The effect of light scattering in stereolithography ceramic manufacturing, J. Eur. Ceram. Soc. 41 (2021) 7141–7154, https://doi.org/10.1016/J.JEURCERAMSOC.2021.07.017.

[156] M.L. Griffith, J.W. Halloran, Freeform fabrication of ceramics via stereolithography, J. Am. Ceram. Soc. 79 (1996) 2601–2608, https://doi.org/10.1111/J.1151-2916.1996.TB09022.X.

[157] K. Liu, J. Hu, Y. Du, Y. Shi, Y. Sun, S. Zhang, R. Tu, Q. Zhang, S. Huang, H. Sun, Influence of particle size on 3D-printed piezoelectric ceramics via digital light processing with furnace sintering, Int. J. Appl. Ceram. Technol. 19 (2022) 2461–2471, https://doi.org/10.1111/IJAC.14074.

[158] K. Liu, Y. Sun, H. Sun, Y. Du, C. Sun, Y. Shi, C. Yan, Journal of the European Ceramic Society Effect of particle grading on the properties of photosensitive slurry and BaTiO 3 piezoelectric ceramic via digital light processing 3D printing, J. Eur. Ceram. Soc. 43 (2023) 3266–3274, https://doi.org/10.1016/j.jeurceramsoc.2023.02.021.

[159] A. Sotov, A. Kantyukov, A. Popovich, V. Sufiiarov, LCD-SLA 3D printing of BaTiO 3 piezoelectric ceramics 47 (2021) 30358–30366, https://doi.org/10.1016/j.ceramint.2021.07.216.

[160] B. Iverson, H.J. Kim, E. Slamovich, K. Bowman, Texture evolution in tape cast lead metaniobate, J. Eur. Ceram. Soc. 28 (2008) 863–869, https://doi.org/10.1016/J.JEURCERAMSOC.2007.07.025.

[161] H.J. Kim, M.J.M. Krane, K.P. Trumble, K.J. Bowman, Analytical fluid flow models for tape casting, J. Am. Ceram. Soc. 89 (2006) 2769–2775, https://doi.org/10.1111/J.1551-2916.2006.01163.X.

[162] K. Zheng, D. Ding, Y. Quan, J. Zhuang, C. Fei, J. Zhao, L. Wang, T. Zhao, Z. Wang, M. Liu, Z. Jiang, Z. Jiang, L. Wen, S. Wu, W. Ren, Journal of the European Ceramic Society 3D printing orientation controlled PMN-PT piezoelectric ceramics, J. Eur. Ceram. Soc. 43 (2023) 2408–2416, https://doi.org/10.1016/j.jeurceramsoc.2023.01.007.

[163] Q. Du, C. Zhang, C. Liu, W. Zhou, F. Zeng, K. Li, Highly < 001 > -textured BaTiO 3 ceramics with high piezoelectric performance prepared by vat photopolymerization, Addit. Manuf. 66 (2023) 103454, https://doi.org/10.1016/j.addma.2023.103454.

[164] J. Cha, J.W. Lee, B. Bae, S. Lee, C. Yoon, Communication Fabrication and Characterization of PZT Suspensions for Stereolithography based on 3D Printing, 56 (2019) 360–364.

[165] W. Ma, X. Zhou, H. Gao, C. Wang, H. Tan, C. Samart, J. Wang, N.M.A. Tran, C. Yan, Y. Hu, J. Wang, H. Zhang, Structure-reinforced periodic porous piezoceramics for ultrahigh electromechanical response manufactured by vat photopolymerization, Addit. Manuf. 93 (2024) 104446, https://doi.org/10.1016/j.addma.2024.104446.

[166] C. Sun, X. Zhang, Experimental and numerical investigations on microstereolithography of ceramics, J. Appl. Phys. 92 (2002) 4796–4802, https://doi.org/10.1063/1.1503410.

[167] C.L. Liu, Q. Du, J.M. Wu, G. Zhang, Y.S. Shi, High piezoelectricity of 3D printed BaTiO3-xBaSnO3 piezoceramics via vat photopolymerization, J. Eur. Ceram. Soc. 44 (2024) 4639–4645, https://doi.org/10.1016/J.JEURCERAMSOC.2024.01.085.

[168] X. Song, Z. Chen, L. Lei, K. Shung, Q. Zhou, Y. Chen, Piezoelectric component fabrication using projection-based stereolithography of barium titanate ceramic suspensions, Rapid Prototyp. J. 23 (2017) 44–53, https://doi.org/10.1108/RPJ-11-2015-0162.

[169] C.L. Liu, Q. Du, C. Zhang, J.M. Wu, G. Zhang, Y.S. Shi, Fabrication and properties of BaTiO3 ceramics via digital light processing for piezoelectric energy harvesters, Addit. Manuf. 56 (2022) 102940, https://doi.org/10.1016/J.ADDMA.2022.102940.

[170] I. Kim, S. Kim, A. Andreu, J. Kim, Y. Yoon, Influence of dispersant concentration toward enhancing printing precision and surface quality of vat photopolymerization 3D printed ceramics, Addit. Manuf. 52 (2022) 102659, https://doi.org/10.1016/j.addma.2022.102659.

[171] X. Hu, X. Li, K. Yan, X. Qi, W. Chen, D. Wu, Fabrication of porous PZT ceramics using micro-stereolithography technology, Ceram. Int. 47 (2021) 32376–32381, https://doi.org/10.1016/j.ceramint.2021.08.137.

[172] C. Liu, Q. Du, H. Zhou, Y. Wang, S. Chen, J. Wu, G. Zhang, Y. Shi, Influence of polyethylene content on preparation and properties of lead zirconate titanate piezoelectric ceramics via vat photopolymerization, Ceram. Int. (2023), https://doi.org/10.1016/j.ceramint.2023.10.119.

[173] C.L. Liu, Q. Du, H. Zhou, J.M. Wu, G. Zhang, Y.S. Shi, Effect of the polystyrene particle size on dielectric and piezoelectric properties of PZT piezoelectric ceramics via vat photopolymerization (VPP), Addit. Manuf. 78 (2023) 103857, https://doi.org/10.1016/J.ADDMA.2023.103857.

[174] I. Kim, A. Andreu, Y. Yoon, Materials & Design A digital light processing 3D printing approach for tuning the interfacial properties of pore forming agents for porous ceramics, Mater. Des. 233 (2023) 112247, https://doi.org/10.1016/j.matdes.2023.112247.

[175] T. Rosental, S. Mizrahi, A. Kamyshny, S. Magdassi, Particle-free compositions for printing dense 3D ceramic structures by digital light processing, (2021). https://doi.org/10.1080/17452759.2021.1922121.

[176] P. Singh, L.S. Smith, M. Bezdecny, M. Cheverton, J.A. Brewer, V. Venkataramani, Additive manufacturing of PZT-5H piezoceramic for ultrasound transducers, IEEE Int. Ultrason. Symp. 2023 (2011) 1111–1114, https://doi.org/10.1109/ULTSYM.2011.0273.

[177] 2015 Physica Status Solidi a - 2015 - Woodward - Additively-manufactured piezoelectric devices.pdf, (n.d.).

[178] M. Cheverton, P. Singh, L.S. Smith, K.P. Chan, J.A. Brewer, V. Venkataramani, Ceramic-Polymer Additive Manufacturing System for Ultrasound Transducers, (n.d.) 863–875.

[179] Z. Chen, X. Song, L. Lei, X. Chen, C. Fei, C.T. Chiu, X. Qian, T. Ma, Y. Yang, K. Shung, Y. Chen, Q. Zhou, 3D printing of piezoelectric element for energy focusing and ultrasonic sensing, Nano Energy 27 (2016) 78–86, https://doi.org/10.1016/J.NANOEN.2016.06.048.

[180] W. Chen, F. Wang, K. Yan, Y. Zhang, D. Wu, Micro-stereolithography of KNN-based lead-free piezoceramics, Ceram. Int. 45 (2019) 4880–4885, https://doi.org/10.1016/j.ceramint.2018.11.185.

[181] J. Cheng, Y. Chen, J. Wu, X. Ji, S. Wu, 3D Printing of BaTiO 3 Piezoelectric Ceramics for a Focused Ultrasonic Array, (2019).

[182] A. Smirnov, S. Chugunov, A. Kholodkova, M. Isachenkov, A. Tikhonov, The Fabrication and Characterization of BaTiO 3 Piezoceramics Using SLA 3D Printing at 465 nm Wavelength, (2022).

[183] Y. Chen, D. Zhang, H. Luo, Z. Peng, L. Zeng, M. Yuan, X. Ji, 3D printed Er3+ doped KNNLN piezoelectric ceramics for transparent ultrasonic transducer application, Ceram. Int. 50 (2024) 9979–9984, https://doi.org/10.1016/J.CERAMINT.2023.08.256.

[184] Z. He, G. Mao, J. Wu, G. Zhang, Y. Shi, Effects of CuO additive on properties of high-performance (Ba 0. 85 Ca 0. 15, Ceram. Int. 49 (2023) 38973–38981, https://doi.org/10.1016/j.ceramint.2023.09.233.

[185] Y. Zeng, L. Jiang, Y. Sun, Y. Yang, Y. Quan, S. Wei, 3D-Printing Piezoelectric Composite with Honeycomb Structure for Ultrasonic Devices, (n.d.).

[186] Y. Chen, X. Bao, C. Wong, J. Cheng, H. Wu, H. Song, X. Ji, S. Wu, PZT ceramics fabricated based on stereolithography for an ultrasound transducer array application, Ceram. Int. 44 (2018) 22725–22730, https://doi.org/10.1016/j.ceramint.2018.09.055.

[187] S. Chugunov, I. Shishkovsky, A. Smirnov, A. Kholodkova, A. Tikhonov, O. Dubinin, Evaluation of Stereolithography-Based Additive Manufacturing Technology for BaTiO3 Ceramics at 465 nm, Appl. Sci. 12 (2022), https://doi.org/10.3390/app12010412.

[188] H. Lu, H. Cui, G. Lu, L. Jiang, R. Hensleigh, Y. Zeng, A. Rayes, M.K. Panduranga, M. Acharya, Z. Wang, A. Irimia, F. Wu, G.P. Carman, J.M. Morales, S. Putterman, L.W. Martin, Q. Zhou, 3D Printing and processing of miniaturized transducers

with near-pristine piezoelectric ceramics for localized cavitation, (2023) 1–11. https://doi.org/10.1038/s41467-023-37335-w.

[189] I. Kim, Y.J. Yoon, Digital light processing 3D printing of porous ceramics: A systematic analysis from a debinding perspective, Addit. Manuf. 93 (2024) 104409, https://doi.org/10.1016/j.addma.2024.104409.

[190] Z. Cheng, L. Chen, Y. Liao, M. Yuan, L. Zeng, F. Zuo, Y. Chen, X. Ji, The effect of solid content on the anisotropy for 3D printed barium titanate piezoelectric ceramics, Ceram. Int. (2024) 1–7, https://doi.org/10.1016/j.ceramint.2024.09.414.

[191] M. Mariani, R. Beltrami, E. Migliori, L. Cangini, E. Mercadelli, C. Baldisserri, C. Galassi, N. Lecis, Additive manufacturing of lead-free KNN by binder jetting, J. Eur. Ceram. Soc. 42 (2022) 5598–5605, https://doi.org/10.1016/j.jeurceramsoc.2022.05.075.

[192] V. Sufiiarov, A. Kantyukov, A. Popovich, A. Sotov, Synthesis of spherical powder of lead-free BCZT piezoceramics and binder jetting additive manufacturing of triply periodic minimum surface lattice structures, Materials 15 (2022), https://doi.org/10.3390/ma15186289.

[193] L.A. Chavez, P. Ibave, B. Wilburn, D. Alexander, C. Stewart, R. Wicker, Y. Lin, The influence of printing parameters, post-processing, and testing conditions on the properties of binder jetting additive manufactured functional ceramics, Ceramics 3 (2020) 65–77, https://doi.org/10.3390/ceramics3010008.

[194] V. Sufiiarov, A. Kantyukov, A. Popovich, A. Sotov, Structure and properties of barium titanate lead-free piezoceramic manufactured by binder jetting process, Mater. (Basel) 14 (2021), https://doi.org/10.3390/ma14164419.

[195] S.M. Gaytan, M.A. Cadena, H. Karim, D. Delfin, Y. Lin, D. Espalin, E. MacDonald, R.B. Wicker, Fabrication of barium titanate by binder jetting additive manufacturing technology, Ceram. Int. 41 (2015) 6610–6619, https://doi.org/10.1016/J.CERAMINT.2015.01.108.

[196] S.M. Gaytan, M. Cadena, M. Aldaz, E. Herderick, F. Medina, R. Wicker, Analysis of ferroelectric ceramic fabricated by binder jetting technology, 24th Int. SFF Symp. - Addit. Manuf. Conf. SFF 2013 (2013) 859–868.

[197] C. Polley, T. Distler, R. Detsch, H. Lund, A. Springer, A.R. Boccaccini, H. Seitz, 3D printing of piezoelectric barium titanate-hydroxyapatite scaffolds with interconnected porosity for bone tissue engineering, Materials 13 (2020), https://doi.org/10.3390/MA13071773.

[198] D.R. Schipf, G.H. Yesner, L. Sotelo, C. Brown, M.D. Guild, Barium titanate 3–3 piezoelectric composites fabricated using binder jet printing, Addit. Manuf. 55 (2022) 102804, https://doi.org/10.1016/j.addma.2022.102804.

[199] M. Mariani, E. Mercadelli, L. Cangini, C. Baldisserri, C. Galassi, C. Capiani, N. Lecis, Additive manufacturing of piezoelectric niobium-doped lead zirconate titanate (PZT-N) by binder jetting, Crystals 13 (2023), https://doi.org/10.3390/cryst13060883.

[200] L.A. Chavez, B.R. Wilburn, P. Ibave, L.C. Delfin, S. Vargas, H. Diaz, C. Fulgentes, A. Renteria, J. Regis, Y. Liu, R.B. Wicker, Y. Lin, Fabrication and characterization of 3D printing induced orthotropic functional ceramics, Smart Mater. Struct. 28 (2019) 125007, https://doi.org/10.1088/1361-665X/AB4E0A.

[201] A.N. Chen, J.M. Wu, K. Liu, J.Y. Chen, H. Xiao, P. Chen, C.H. Li, Y.S. Shi, High-performance ceramic parts with complex shape prepared by selective laser sintering: a review, Adv. Appl. Ceram. 117 (2018) 100–117, https://doi.org/10.1080/17436753.2017.1379586.

[202] C. Shuai, G. Liu, Y. Yang, F. Qi, S. Peng, W. Yang, Z. Liu, Construction of an electric microenvironment in piezoelectric scaffolds fabricated by selective laser sintering, Ceram. Int. 45 (2019) 20234–20242, https://doi.org/10.1016/j.ceramint.2019.06.296.

[203] F. Qi, N. Chen, Q. Wang, Dielectric and piezoelectric properties in selective laser sintered polyamide11/BaTiO3/CNT ternary nanocomposites, Mater. Des. 143 (2018) 72–80, https://doi.org/10.1016/j.matdes.2018.01.050.

[204] F. Qi, N. Chen, Q. Wang, Preparation of PA11/BaTiO3 nanocomposite powders with improved processability, dielectric and piezoelectric properties for use in selective laser sintering, Mater. Des. 131 (2017) 135–143, https://doi.org/10.1016/j.matdes.2017.06.012.

[205] X. Zhang, F. Wang, Z. Wu, Y. Lu, X. Yan, M. Nastasi, Y. Chen, Y. Hao, X. Hong, B. Cui, Direct selective laser sintering of hexagonal barium titanate ceramics, J. Am. Ceram. Soc. 104 (2021) 1271–1280, https://doi.org/10.1111/jace.17568.

[206] Z.S. Macedo, M.H. Lente, J.A. Eiras, A.C. Hernandes, Dielectric and ferroelectric properties of Bi4Ti 3O12 ceramics produced by a laser sintering method, J. Phys. Condens. Matter 16 (2004) 2811–2818, https://doi.org/10.1088/0953-8984/16/16/005.

[207] N. Basile, M. Gonon, F. Petit, F. Cambier, Interaction between laser beam and BaTiO 3 powders in selective laser sintering treatments, J. Eur. Ceram. Soc. 32 (2012) 3303–3311, https://doi.org/10.1016/j.jeurceramsoc.2012.04.033.

[208] E.Y. Tarasova, G.V. Kryukova, A.L. Petrov, I.V. Shishkovsky, Structure and properties of porous PZT ceramics synthesized by selective laser sintering method, Laser Appl. Microelectron. Optoelectron. Manuf. V 3933 (2000) 502. https://doi.org/10.1117/12.387590.

[209] R.S. Silva, A.C. Hernandes, Laser sintering of BaTiO3 ceramics obtained from nanometric powders, Mater. Sci. Forum 514–516 (2006) 1216–1220, https://doi.org/10.4028/www.scientific.net/msf.514-516.1216.

[210] S.A. Bernard, V.K. Balla, S. Bose, A. Bandyopadhyay, Direct laser processing of bulk lead zirconate titanate ceramics, Mater. Sci. Eng. B 172 (2010) 85–88, https://doi.org/10.1016/j.mseb.2010.04.022.

[211] D.M. Gureev, R.V. Ruzhechko, I.V. Shishkovskiĭ, Selective laser sintering of PZT ceramic powders, Tech. Phys. Lett. 26 (2000) 262–264, https://doi.org/10.1134/1.1262811.

[212] Z. Lotfizarei, A. Mostafapour, A. Barari, A. Jalili, A.E. Patterson, Overview of debinding methods for parts manufactured using powder material extrusion, Addit. Manuf. 61 (2023) 103335, https://doi.org/10.1016/J.ADDMA.2022.103335.

[213] S. Zhou, G. Liu, C. Wang, Y. Zhang, C. Yan, Y. Shi, Thermal debinding for stereolithography additive manufacturing of advanced ceramic parts: A comprehensive review, Mater. Des. 238 (2024) 112632, https://doi.org/10.1016/J.MATDES.2024.112632.

[214] K. Catyb, D. Chen, J. Counsel, T. Tambolleo, Y. Zhong, Binder Burnout Investigation on Lanthanum Strontium Manganite, (2020).

[215] S. Masia, P.D. Calvert, W.E. Rhine, H.K. Bowen, Effect of oxides on binder burnout during ceramics processing, J. Mater. Sci. 24 (1989) 1907–1912. https://doi.org/10.1007/BF02385397/METRICS.

[216] S. Nugroho, Z.C. Chen, A. Kawasaki, M.O.D. Jarligo, Solid-state synthesis and formation mechanism of barium hexaaluminate from mechanically activated Al2O3-BaCO3 powder mixtures, J. Alloy. Compd. 502 (2010) 466–471, https://doi.org/10.1016/j.jallcom.2010.04.198.

[217] V. Rehn, J. Hötzer, W. Rheinheimer, M. Seiz, C. Serr, B. Nestler, Phase-field study of grain growth in porous polycrystals, Acta Mater. 174 (2019) 439–449, https://doi.org/10.1016/J.ACTAMAT.2019.05.059.

[218] R.M. Glaister, H.F. Kay, An investigation of the cubic-hexagonal transition in barium titanate, Proc. Phys. Soc. 76 (1960) 763–771, https://doi.org/10.1088/0370-1328/76/5/317.

[219] A. Rečnik, D. Kolar, Exaggerated Growth of Hexagonal Barium Titanate under Reducing Sintering Conditions, J. Am. Ceram. Soc. 79 (1996) 1015–1018, https://doi.org/10.1111/j.1151-2916.1996.tb08541.x.

[220] J.L. Jones, The effect of crystal symmetry on the maximum polarization of polycrystalline ferroelectric materials, Mater. Sci. Eng. B 167 (2010) 6–11, https://doi.org/10.1016/j.mseb.2010.01.019.

[221] L. Lemos da Silva, M. Hinterstein, Size Effect on Ferroelectricity in Nanoscaled BaTiO$_3$, in: A.K. Alves (Ed.), Technol. Appl. Nanomater., Springer Nature Switzerland AG, 2022, pp. 123–133, https://doi.org/10.1007/978-3-030-86901-4_7.

[222] F.K. Lotgering, Topotactical reactions with ferrimagnetic oxides having hexagonal crystal structures—I, J. Inorg. Nucl. Chem. 9 (1959) 113–123, https://doi.org/10.1016/0022-1902(59)80070-1.

[223] T. Chen, T. Zhang, G. Wang, J. Zhou, J. Zhang, Y. Liu, Effect of CuO on the microstructure and electrical properties of Ba 0.85Ca 0.15Ti 0.90Zr 0.10O 3 piezoceramics, J. Mater. Sci. 47 (2012) 4612–4619. https://doi.org/10.1007/S10853-012-6326-1/FIGURES/14.

[224] J. Cheng, Y. Chen, J.W. Wu, X.R. Ji, S.H. Wu, 3D Printing of BaTiO3 Piezoelectric Ceramics for a Focused Ultrasonic Array, Vol. 19, Page 4078, Sensors 2019 (19) (2019) 4078, https://doi.org/10.3390/S19194078.

[225] Y. Zhang, M. Xie, J. Roscow, C. Bowen, Dielectric and piezoelectric properties of porous lead-free 0.5Ba(Ca0.8Zr0.2)O3-0.5(Ba0.7Ca 0.3)TiO3 ceramics, Mater. Res. Bull. 112 (2019) 426–431, https://doi.org/10.1016/J.MATERRESBULL.2018.08.031.

[226] Y.N. Huang, Y.N. Wang, H.M. Shen, Internal friction and dielectric loss related to domain walls, Phys. Rev. B 46 (1992) 3290, https://doi.org/10.1103/PhysRevB.46.3290.

[227] A. Grnebohm, M.E. Gruner, P. Entel, Domain Structure in the Tetragonal Phase of BaTiO3– from Bulk to Nanoparticles, Ferroelectrics 426 (2012) 21–30, https://doi.org/10.1080/00150193.2012.671090.

[228] P. Zheng, J.L. Zhang, Y.Q. Tan, C.L. Wang, Grain-size effects on dielectric and piezoelectric properties of poled BaTiO3 ceramics, Acta Mater. 60 (2012) 5022–5030, https://doi.org/10.1016/J.ACTAMAT.2012.06.015.

[229] V. Buscaglia, C.A. Randall, Size and scaling effects in barium titanate. An overview, J. Eur. Ceram. Soc. 40 (2020) 3744–3758, https://doi.org/10.1016/j.jeurceramsoc.2020.01.021.

[230] W.R. BUESSEM, L.E. CROSS, A.K. GOSWAMI, Phenomenological Theory of High Permittivity in Fine-Grained Barium Titanate, J. Am. Ceram. Soc. 49 (1966) 33–36, https://doi.org/10.1111/j.1151-2916.1966.tb13144.x.

[231] E.J. Huibregtse, D.R. Young, Triple Hysteresis Loops and the Free-Energy Function in the Vicinity, Phys. Rev. 103 (1956) 1705–1711.

[232] W.J. Merz, The electric and optical behavior of BaTiO3 single-domain crystals, Phys. Rev. 76 (1949) 1221–1225, https://doi.org/10.1103/PhysRev.76.1221.

[233] Piezoceramic components | Products | CTS Ferroperm, (n.d.).

[234] Piezo Elements Made by Pressing Technology, (n.d).

[235] Piezoelectric Ceramics Manufacturing Technology | CTS, (n.d).

[236] Piezoceramic Materials, (n.d).

[237] A. Safari, E.K. Akdogan, Rapid prototyping of novel piezoelectric composites, Ferroelectrics 331 (2006) 153–179, https://doi.org/10.1080/00150190600737727.

[238] M. Allahverdi, S.C. Danforth, M. Jafari, A. Safari, Processing of advanced electroceramic components by fused deposition technique, J. Eur. Ceram. Soc. 21 (2001) 1485–1490, https://doi.org/10.1016/S0955-2219(01)00047-4.

[239] D.I. Woodward, C.P. Purssell, D.R. Billson, D.A. Hutchins, S.J. Leigh, Additively-manufactured piezoelectric devices, Phys. Status Solidi Appl. Mater. Sci. 212 (2015) 2107–2113, https://doi.org/10.1002/pssa.201532272.

[240] K. Huang, A. De Marzi, G. Franchin, P. Colombo, UV-assisted robotic arm freeforming of SiOC ceramics from a preceramic polymer, Addit. Manuf. 83 (2024), https://doi.org/10.1016/j.addma.2024.104051.

[241] A. De Marzi, M. Vibrante, M. Bottin, G. Franchin, Development of robot assisted hybrid additive manufacturing technology for the freeform fabrication of lattice structures, Addit. Manuf. 66 (2023), https://doi.org/10.1016/j.addma.2023.103456.

Subhadip Bhandari is currently enrolled as a PhD student of Industrial Engineering at the University of Padova, Italy under the supervision of Dr. Giorgia Franchin and Prof. Paolo Colombo. Prior to that he graduated in Ceramic technology from Government College of Engineering and Ceramic Technology, Kolkata, India in 2018. Subsequently, he worked for a year with Bharat Aluminium Company Limited (BALCO) as an assistant manager before moving on to do his master's (2021) in Materials Science and Engineering from Indian Institute of Technology (IIT) Patna, India. His current research focuses on coupling extrusion-based additive manufacturing of oxide ceramics with non-conventional sintering techniques. He is also dedicated to developing and optimizing feedstocks specifically for extrusion-based processes, aiming to enhance both the printing quality and final properties of the ceramic components. Prior to this, he worked at Forschungszentrum Jülich, where he gained valuable experience in flash sintering of ceramics. He is also the recipient of several awards that includes the Gold medal for the best graduate student at IIT Patna, DAAD scholarship (for master's thesis at Forschungszentrum Jülich), the National Scholarship Programme (NSP) of the Slovak Republic (STU Bratislava during PhD), and several travel grants from the European ceramic society, and the American ceramic society. Recently he was awarded with the Best poster award at the young ceramist additive manufacturing forum (yCAM 2024) and the ICACC 2024 organized by the American ceramic society for his work on additive manufacturing of piezoceramics.

M.Sc. Gaurav Vajpayee is a Research Assistant at Fraunhofer Institute for Mechanics of Materials (IWM) and a PhD student at the Institute for Applied Materials (IAM) at the Karlsruhe Institute of Technology (KIT). His research is centered on the Additive Manufacturing of Barium Titanate (BT), with a key focus on understanding and optimizing structure-property relationships. Gaurav's work spans from preparing novel porous inks using capillary suspensions of BT to 3D printing via Direct Ink Writing (DIW) and Fused Filament Fabrication (FFF), followed by detailed electromechanical characterization of the printed structures. He also explores incorporating texturing in ceramics through additive manufacturing to further enhance their properties. In addition, Gaurav is advancing the field by integrating in-situ electron and neutron experiments, allowing for real-time analysis of BT materials under operational conditions. This approach enhances the application of additive manufacturing technologies in functional ceramics. Gaurav's experience with BT began during his master's thesis, which he completed at the Institute for Applied Materials (IAM), Karlsruhe Institute of Technology (KIT), as a recipient of the prestigious DAAD scholarship. He holds a master's degree from the Indian Institute of Technology (IIT), Patna, where he developed a strong foundation in materials science. His master's work focused on the production and flash sintering of BT, combined with in-depth electromechanical testing and in-situ experiments. This foundation has enabled him to push forward with innovative research that bridges additive manufacturing and advanced real-time characterization techniques.

M.Sc. Lucas Lemos da Silva is a researcher at the Fraunhofer Institute for Mechanics of Materials (IWM) in Freiburg, Germany, since 2023. His research focuses on the structure-property-relationships of functional ferroelectric ceramics, particularly in BT-based systems. Combining a broad range of sintering methods with diversified approaches he is able to tailor piezoelectric properties designing microstructures, controlling grain size distribution, and porosity. He has extensive experience in electromechanical characterization of both dense and porous additive manufactured (DIW) ferroelectric ceramics. In addition, he possesses expertise in the production of ceramic micro- and nanofibers using the electrospinning method, as well as in capillary suspension-based techniques for fabricating highly porous structures. His work also includes *in situ* analysis of local structures through X-rays and Neutron total scattering, utilizing Pair Distribution Function (PDF) analysis. In 2014, he obtained his Bachelor's degree in Engineering Physics at the State University of Mato Grosso do Sul (UEMS), Dourados, Brazil. He obtained his Master's degree from the Ceramic Materials Laboratory (LACER) of the Federal University of Rio Grande do Sul (UFRGS), Porto Alegre, Brazil, in 2017. He started his PhD thesis at the Institute for Applied Materials (IAM) at the Karlsruhe Institute of Technology (KIT), Karlsruhe, Germany, in 2018.

Dr. Manuel Hinterstein is a group leader at the Fraunhofer Institute for Material Mechanics and a lecturer at the University of Freiburg since 2022. His research focusses on the structure-properties-relationships of functional materials and the development of complex materials and systems for energy conversion. A special focus lies on the multi-hierarchical metastructuring of ferroelectric and piezoelectric ceramics as well as the structural and dielectric characterization of these electroceramics. He published 88 research articles and 3 book chapters. He developed sample environments for in situ and operando experiments as a beamline scientist at the Deutsches Elektronensynchrotron in Hamburg, Germany (2007–2013). As a Feodor Lynen Fellow of the Alexander von Humboldt foundation, DECRA Fellow of the Australian Research Council and Senior Adjunct Lecturer, he continued his research at the University of New South Wales in Sydney, Australia (2013–2022) and as an Emmy Noether group leader at the Karlsruhe Institute of Technology in Karlsruhe, Germany (2016–2022). Among his awards are the Young Scientist Award of the European Crystallographic Association (2014), the Discovery Early Career Researcher Award of the Australian Research Council (2015), The Emmy Noether Research Group of the German Research Council (2016) and the Fraunhofer Attract Group of the Fraunhofer Society (2022).

Dr. Giorgia Franchin is an Associate Professor of Materials Science and Technology at the University of Padova. She holds a PhD in industrial engineering from the University of Padova. During her PhD studies, she worked with the Mediated Matter group at the Massachusetts Institute of Technology (MIT) Media Lab (Cambridge, MA). She was also a Visiting Scientist at the Bundesanstalt für Materialforschung und -prüfung (BAM) (Berlin, DE) from 2018 to 2021. Her main research interests lie in the Additive Manufacturing of ceramics and glass, particularly in the development of hybrid and advanced processes exploiting liquid feedstocks (preceramic polymers, geopolymers, sol-gel formulations).

Professor Paolo Colombo is a professor of Materials Science and Technology at the Department of Industrial Engineering, University of Padova, Italy. He is also an adjunct professor of Materials Science and Engineering at the Pennsylvania State University, a visiting professor in the Department of Mechanical Engineering of University College London, UK, and a member of the EPSRC Peer Review College (UK). He is an Academician of the World Academy of Ceramics, the European Academy of Sciences, Academia Europaea and the Italian Academy of Engineering and Technology, and a Fellow of the American Ceramic Society, the Institute of Materials, Minerals and Mining and the European Ceramic Society. He was awarded a Fulbright Scholarship for the Pennsylvania State University, the Pfeil Award (Institute of Materials, Minerals and Mining), the Global Star Award (American Ceramic Society), the Edward C. Henry Award (American Ceramic Society), the Verulam Medal & Prize (Institute of Materials, Minerals and Mining), the Global Ambassador Award (American Ceramic Society), the Polish Ceramic Society Award, the Bridge Building Award (American Ceramic Society) and the ECerS-ACerS Joint Award (European Ceramic Society-American Ceramic Society). He is Past President of the International Ceramic Federation (ICF) and Editor-in-Chief of Open Ceramics (Elsevier). He has published over 350 papers in peer-reviewed journals (h index Google Scholar = 76; Citations = 23418). He is co-editor of a book on polymer-derived ceramics, and a book on cellular ceramics and 11 proceedings books. He is in the editorial board of 10 international scientific journals and has co-organized >130 international conferences and has given >70 invited talks in the field of porous ceramics, polymer-derived ceramics and additive manufacturing of ceramics. His research interests include the development of ceramic components from preceramic polymers and geopolymers, novel processing routes to porous glasses and ceramics (now additive manufacturing in particular).